

ANALYSIS OF FIRST KATRIN DATA AND SEARCHES FOR KEV-SCALE STERILE NEUTRINOS

Zur Erlangung des akademischen Grades eines
DOKTORS DER NATURWISSENSCHAFTEN

von der KIT-Fakultät für Physik
des Karlsruher Instituts für Technologie
genehmigte

DISSERTATION

von

M. Sc. Anton Huber

aus Karlsruhe

Erstgutachter: Prof. Dr. Guido Drexlin
Institut für Experimentelle Teilchenphysik, KIT

Zweitgutachter: Dr. habil. Thierry Lasserre
IRFU, CEA, Université Paris-Saclay

Tag der mündlichen Prüfung: 10. Juli 2020

Declaration of authorship

I declare that I have developed and written the enclosed thesis in hand completely by myself, and have not used sources or means without any declaration in the text.

Erklärung der Selbstständigkeit

Hiermit versichere ich, die vorliegende Arbeit selbstständig angefertigt, alle dem Wortlaut oder Sinn nach entnommenen Inhalte anderer Werke an den entsprechenden Stellen unter Angabe der Quellen kenntlich gemacht und keine weiteren Hilfsmittel verwendet zu haben.

.....
Anton Huber

Karlsruhe, den 11. Januar 2021

Introduction

Since their postulation by Wolfgang Pauli in 1930 [1], neutrinos became one of the most extensively studied particles of the *Standard Model of Particle Physics* (SM). It took 23 years until the first experimental observation of a neutrino in a laboratory experiment was made [2]. With the discovery of the muon neutrino in 1962 [3] and the tau neutrino in 2000 [4], it was made evident that neutrinos are organized in three flavor generations, analogous to the other SM particles. The discovery of neutrino oscillation in 2001 [5] set another milestone in the history of particle physics. It proved that neutrinos, contrary to their formulation in the SM, have a finite mass. This finding has far-reaching consequences for particle physics as well as for cosmology. Since neutrinos are the most abundant particles in our Cosmos, their influence on the evolution and structure formation of the Universe depends crucially on their mass. [10]

There have been numerous attempts to determine the neutrino mass in the last decades (for example [7, 8]). The current upper limit on the effective antineutrino mass of $m_{\bar{\nu}_e} < 1.1$ eV (90 % C.L.) is set by the Karlsruhe Tritium Neutrino (KATRIN) experiment [9]. The ultimate goal of the KATRIN experiment is to directly measure the effective antineutrino mass with a sensitivity of 0.2 eV (90 % C.L.) after 5 years of data taking [10].

In order to achieve this, the KATRIN experiment measures the tritium β -decay spectrum in a high-precision spectroscopic approach. The neutrino mass will manifest as a small distortion of the spectral shape in close vicinity to the kinematic endpoint. [10]

Besides the excellent spectroscopic precision, the KATRIN experiment is equipped with several unique features. One is the high-luminosity tritium source with an activity of 100 GBq, stable on the permille level [11]. The high decay rate in combination with the precise rate stability enables the KATRIN experiment to enhance its scientific program, for example to search for sterile neutrinos on the keV mass scale [12].

Besides the three light active neutrinos, the SM can be extended by additional sterile neutrinos [6]. These particles would not interact via any SM interaction, however, could have a small admixture with their active partners [13]. Sterile neutrinos can help to solve several problems in particle physics and cosmology: Heavy sterile neutrinos on the GeV and TeV mass scale can explain the very small masses of the active SM neutrinos via the see-saw mechanisms [14]. If the mass of the sterile neutrinos would be on the order of keV, they could significantly contribute to the Dark Matter content of our Universe and solve structure formation problems of the Λ CDM model [13]. Anomalies observed in short-baseline neutrino oscillation experiments could be explained by active-to-sterile mixing of sterile neutrinos on the eV mass scale [15].

A sterile neutrino in the keV mass range would manifest as a kink-like distortion in the β -decay spectrum [12]. If the KATRIN experiment is used to search for keV-scale sterile neutrinos, the tritium β -decay spectrum needs to be measured on an extended energy range down to several keV below the endpoint. This arises certain challenges: deeper in the spectrum, the signal electron count rate exceeds the limits of the KATRIN Fo-

cal Plane Detector (FPD). Furthermore, additional systematic effects occur, for example transmission losses due to non-adiabatic electron motion [16].

As a consequence, the following approach was chosen for the search for keV-scale sterile neutrinos with the KATRIN experiment:

The TRISTAN project develops a new detector system that is able to resolve high count rates of up to 10^8 cps. This enables a high statistics sterile neutrino search with a sensitivity on the mixing amplitude of up to $\sin^2 \theta < 10^{-6}$. [17]

Until the new detector system is available (earliest 2025), the KATRIN experiment can be used with only minor modifications for a first sterile neutrino search. This has the potential to improve the current laboratory limits on the active-to-sterile mixing amplitude by up to one order of magnitude on a mass range of several keV. This thesis focuses on the realization of such a measurement.

The main objectives are:

- To find an optimized setting of the KATRIN experiment that takes into account all technical limits as well as all systematic effects that occur if the spectrum is measured further away from the endpoint.
- To extend the KATRIN β -decay model which is optimized for an endpoint analysis in order to search for keV-scales sterile neutrinos in the data of the *First Tritium Campaign*.
- To develop future strategies that guide the way towards a high statistics sterile neutrino measurement with the KATRIN experiment.

The work is structured as follows:

Chapter 1 gives a brief overview of the history of neutrino physics. The framework of the SM is introduced with focus on the electroweak sector and the particular position of the neutrino among the other particles. The principle of neutrino oscillation is described and its consequences for the neutrino properties are explained. The last part focuses on past and current approaches to determine the neutrino mass.

In chapter 2, the KATRIN experiment is presented. In the first part of the chapter, the underlying measurement principle is explained, followed by the description of the different sections of the experimental setup. The second part covers a brief introduction of the analysis strategies and shows the concept of how the sensitivity on the neutrino mass is derived.

Chapter 3 focuses on sterile neutrinos. It shows how the hypothetical particle can be embedded in the SM by a minimal extension. Furthermore, it is explained which role sterile neutrinos on the keV-mass scale play in cosmology and how they can help to solve major problems of our present understanding of the evolution of the Universe. Subsequently, limits from cosmological observations as well as laboratory experiments on the sterile neutrino parameter space are presented. In the last part of the chapter, the concept of a search for sterile neutrinos with the KATRIN experiment is introduced and the objectives of the thesis are defined.

Chapter 4 presents detailed studies on how the current KATRIN setup can be adjusted in order to search for sterile neutrinos. The rate limit on the FPD is defined and methods to lower the signal rate are discussed. A second challenge that arises if the retarding potential is lowered are transmission losses in the main spectrometer. Due to their chaotic nature,

they can be of great harm if the tritium spectrum is measured several keV below the endpoint. After a discussion of the concept of adiabatic electron transport, three methods are developed to regain fully-adiabatic transmission over a large energy range. At the end of the chapter, several measurement scenarios are defined based on optimized KATRIN settings.

Chapter 5 presents the first comprehensive study of all yet known systematic effects that are relevant for deep spectral scans with the KATRIN experiment and their impact on the sensitivity of a sterile neutrino measurement is derived. Furthermore, countermeasures are identified and recommendations for future improvements are documented.

The information gained so far in the thesis is used for a first sterile neutrino measurement with the KATRIN experiment. Chapter 6 presents the analysis of data taken during the KATRIN *First Tritium Campaign* in 2018. The tritium β -decay model that is used in the standard KATRIN neutrino mass analysis is extended by systematic effects derived in the previous chapter.

In chapter 7, future strategies and perspectives for a keV-scale sterile neutrino search with the KATRIN experiment are developed and discussed. Besides other hardware modifications, the TRISTAN detector system is briefly introduced. As a conclusion of all the studies of this thesis, a proposal is made for a next sterile neutrino measurement with the KATRIN experiment.

Finally, chapter 8 summarizes the results of the thesis and gives an outlook.

Contents

Introduction	v
1 Neutrino Physics	1
1.1 History of Neutrino Physics	1
1.2 Neutrinos in the Standard Model of Particle Physics	2
1.2.1 Introduction to the Standard Model	2
1.2.2 The electroweak Sector - Neutrinos in the SM	3
1.3 Neutrino Oscillation	5
1.3.1 The Solar Neutrino Problem and its Solution	5
1.3.2 Theory of Neutrino Oscillation	7
1.3.3 Neutrino Oscillation Parameters	8
1.3.4 Consequences of Neutrino Oscillation	8
1.4 Massive Neutrinos	10
1.4.1 Dirac and Majorana Massterm	10
1.4.2 Seesaw Mechanism	11
1.4.3 Possible Masses of Sterile Neutrinos	12
1.5 Absolute Neutrino Mass Measurements	13
1.5.1 Cosmological Observations	13
1.5.2 Double Beta Decay Experiments	14
1.5.3 Single Beta Decay Experiments	16
2 The KATRIN Experiment	19
2.1 The Measurement Principle	19
2.2 The Experimental Setup	21
2.2.1 Tritium Source	21
2.2.2 Transport Section	23
2.2.3 Spectrometer Section	24
2.2.4 Focal Plane Detector	26
2.3 Sensitivity on the Neutrino Mass	26
3 Sterile Neutrinos on the keV Mass Scale	29
3.1 Motivation for keV-scale Sterile Neutrinos	29
3.1.1 From Particle Physics	30
3.1.2 From Cosmology	30
3.2 Cosmological constraints on the Sterile Neutrino Parameters m_{ν_s} and $\sin^2 \theta$	33
3.3 Laboratory Search for keV-scale Sterile Neutrinos	35
3.4 Search for keV-scale Sterile Neutrinos with KATRIN	38
4 Search for keV-scale sterile Neutrinos with KATRIN	41
4.1 Reducing the Signal Rate	42
4.1.1 Rate Limits of the FPD	42
4.1.2 Lowering the Source Strength	43

4.1.3	Modification of the Source Magnetic Field Setting	45
4.1.4	Modification of the Detector Magnetic Field Setting	47
4.1.5	Conclusion	49
4.2	Main Spectrometer Transmission at high Surplus Energies	51
4.2.1	Adiabatic Electron Transport	51
4.2.2	Increase of the LFCS Field	53
4.2.3	Reduced Entrance Fluxtube Radius	56
4.2.4	Ring-wise Transmission Properties	56
4.2.5	Conclusion	57
4.3	Optimized Measurement Settings	57
4.3.1	Adiabatic Setting	59
4.3.2	Nominal Field Setting	60
4.3.3	Intermediate Setting	62
4.4	Conclusion and Outlook	65
5	Systematic Effects of a KATRIN keV-scale sterile Neutrino integral Measurement	67
5.1	Analysis Strategy	68
5.2	Backscattering on the Rear Wall	70
5.3	Electron Scattering in the Source	78
5.4	Magnetic Traps in the Source	87
5.5	Source Fluctuations	95
5.6	Detection Efficiency	97
5.6.1	Electron Loss due to Backscattering	99
5.6.2	Rate dependent Pile-up Loss	102
5.7	Theoretical Corrections of the Spectrum	107
5.7.1	Final State Distribution	107
5.7.2	Other theoretical Corrections	110
5.8	Minor Effects	115
5.8.1	Retarding Potential Dependent Background Rate	116
5.8.2	HV Instabilities	116
5.8.3	Doppler Broadening	117
5.8.4	Synchrotron Radiation	117
5.8.5	Plasma Potential	119
5.9	Summary and Conclusion	119
6	Search for keV-scale sterile Neutrinos with KATRIN during the 2018 First Tritium Campaign	123
6.1	The 2018 First Tritium Campaign	124
6.2	Data taking Strategy	124
6.3	Data Selection and Analysis	125
6.4	Additional Model Corrections	126
6.5	Systematic Effects and Uncertainties	129
6.6	Results	133
6.7	Conclusion and Outlook for Future Measurements	133
7	Future Strategies	137
7.1	The TRISTAN Project	138
7.1.1	Purpose and Design	138
7.1.2	Prototype Measurements and Schedule	139
7.2	Upgraded LFCS	140
7.2.1	Purpose and Design	140

7.2.2	Transmission Properties	141
7.3	Beryllium Rear Wall	142
7.4	SSC-Sterile: A new β -Decay Model for sterile Neutrino Searches	146
7.5	Using KATRIN without Hardware Modifications in the Future	147
7.6	Conclusion	151
8	Summary and Outlook	153
Appendix		157
A	Transmission Studies with the KATRIN Simulation Framework <i>KASPER</i> .	157
B	Relation between Non-Adiabaticity and Chaos	158
C	Simulation of secondary Photon Emission at the Detector Chamber	161
D	Backscattering Probability and Energy Distribution of backscattered Electrons	162
E	Validation of <i>GEANT4</i> Backscattering Simulations and Uncertainty Estimation	165
F	Simulation of Energy and Angular Distribution of escaped Electrons	168
G	Theoretical Correction Terms of the Tritium β -Spectrum	169
H	Measurements at Troitsk Nu-Mass Experiment	174
	List of Figures	179
	List of Tables	183
	Bibliography	185
	Danksagung	207

CHAPTER 1

Neutrino Physics

With at least four Nobel prizes directly connected to neutrino physics [18, 19, 20, 21], this field of research always had strong potential to help understanding the Universe and the matter that forms it. The discovery of neutrino oscillation in 2001 [5, 22] proved that neutrinos have to be massive and that the *Standard Model of Particle Physics* (SM) is incomplete and needs to be extended (see for example [23]).

This chapter gives a brief introduction to the history of neutrino physics and its theoretical description in the framework of the SM (section 1.1 and 1.2). The massive neutrino that is required to explain the phenomenon of neutrino oscillation (section 1.3) could be introduced to the SM by adding a new particle, the sterile neutrino (section 1.4). In section 1.5 it is shown how the mass of neutrinos can be experimentally determined.

1.1 History of Neutrino Physics

In 1896, Henry Becquerel discovered radioactivity by studying the phosphorescence of uranium [24]. Three years later, Ernest Rutherford showed that the emitted radiation can be separated in two different kinds: α - and β -radiation [25]. In 1914, Frederick Soddy proposed that these decays correspond to a transformation of mother-atoms to daughter-atoms by postulating that chemical elements decay into elements with lower atomic number by emitting β -radiation [26]. Similar to the observed α and γ radiation the spectrum of the β -radiation was expected to be monoenergetic [6].

First hints of anomalies in the β -spectrum were found by Lise Meitner, Otto Hahn, and Otto von Baeyer in 1911 [27]. With the help of a magnetic spectrometer James Chadwick proved in 1914 that the spectrum of the emitted β -decay electrons is indeed continuous, which gave a puzzling challenge to the physics community of the early 20th century [28]. Not only the conservation of energy, but also of angular momentum seemed violated.

In 1930, Wolfgang Pauli postulated a new particle – the *neutrino* – to explain the shape of the β -decay spectrum [1]¹. Pauli claimed that the neutrino needs to be a spin $S = \frac{1}{2}$ particle to regain the conservation of angular momentum and carries parts of the decay energy so that total energy is also conserved. Furthermore, the particle needs to be massless, or at least of very small mass, to explain the shape of the spectrum close to the endpoint [1]. In the years after Pauli's postulation, Enrico Fermi formulated a theory that describes the β -decay as a pointlike one-vertex decay with four particles taking part

$$n \rightarrow p + e^{-} + \bar{\nu}_e \quad [29]. \quad (1.1)$$

¹Originally Pauli named the particle *neutron*. However Enrico Fermi renamed it in 1931 to *neutrino*, due to the simultaneously discovery of the neutron as the counterpart of the proton [29].

It took another 20 years to experimentally observe the neutrino. In 1956, Clyde Cowan and Frederick Reines demonstrated via the inverse β -decay

$$\bar{\nu}_e + p \rightarrow e^+ + n \quad (1.2)$$

the existence of the neutrino. They derived a cross section in the order of $\sigma \sim 10^{-43} \text{ cm}^2$. [2] Frederick Reines was awarded with the Nobel Prize in Physics 1995 for the first detection of the neutrino, Clyde Cowan unfortunately passed away 1974 [30].

A second neutrino type, the ν_μ was found 1962 by Jack Steinberger, Melvin Schwartz, and Leon Lederman at the Brookhaven Synchrotron. The group used the decay of the π -meson

$$\pi^+ \rightarrow \mu^+ + \nu_\mu, \quad (1.3)$$

to show that there is an additional neutrino flavor, different from the electron neutrino.[3] After the discovery of the charged τ -lepton in 1975 it was believed that there has to be a third neutrino flavor, the ν_τ [31]. This assumption was supported by the measurement of the decay width of the Z^0 -boson which affirmed three generations of neutrinos [32]. The ν_τ was finally measured in 2000 by the DONUT experiment [4].

1.2 Neutrinos in the Standard Model of Particle Physics

The *Standard Model of Particle Physics* (SM) is the result of many decades of theoretical and experimental research. Even though it has been tested to a level of high precision, it faces some major challenges that arose from experimental results such as neutrino oscillation [5] or the existence of Dark Matter [33]. Section 1.2.1 gives an introduction to the SM, its general concept and content, and difficulties with observations and other theoretical models. In section 1.2.2, a focus on the electroweak sector and especially the neutrino is laid.

The following two sections are a summary of the basic concept of modern particle physics. The used formulation, as well as similar formulations can be found in most textbooks on introductions to particle physics. It is well described for example in [34] chapters 10-14.

1.2.1 Introduction to the Standard Model

The SM describes the properties and interactions of all known elementary particles via three of the four fundamental forces (electromagnetic, weak, and strong force, gravity is not included). The interactions between the fermionic matter particles (quarks and leptons with spin $S = \frac{1}{2}$.) are mediated by gauge bosons (the gluon, photon, W^\pm -/ Z^0 -bosons with spin $S = 1$). Via coupling to the scalar Higgs boson (spin $S = 0$), the masses of the particles are generated. The photon, gluon, and the neutrinos remain massless. [34]

The SM is formulated as a gauge quantum field theory. It describes the dynamics and interactions of a particle with a renormalized² Lagrange formalism for fields. The particles are represented as quantized fields, their kinematics and interactions are summarized in a Lagrangian density \mathcal{L} . The Lagrangian is invariant under a local $SU(3)_C \times SU(2)_{T_3} \times U(1)_{Y_W}$ symmetry, which leads to certain conserved charges³: the color charge C of the strong interaction resulting from the $SU(3)_C$ -symmetry, the weak isospin T_3 and hypercharge Y_W of the electroweak interaction, coming from $SU(2)_{T_3}$ and the $U(1)_Y$ symmetry. [34]

²To avoid infinities (or divergences) arising in calculations using a certain theory it needs to be renormalized. This is achieved by redefining parameters in such a way that the calculations show no divergences anymore. The original, non-renormalized parameters are so called *bare* parameters [35].

³In gauge theory, certain sets of transformations are summarized under symmetry groups. The equations of motion do not change under these transformations. Following the Noether Theorem, every symmetry generates a conservation quantity [36].

The resulting Lagrangian of the SM consists of several terms, which describe the fundamental interactions between the particles: The theory of quantum chromodynamics (QCD) was developed in the 1970 by Harald Fritzsch, Heinrich Leutwyler and Murray Gell-Mann [37] and is based on the 1954 published work of Chen Ning Yang and Robert Mills [38]. It defines the strong interaction of the quarks via gluon transition. Leptons are color uncharged and do not take part in the strong interaction.

The electroweak sector is the unified description of the theory of quantum electrodynamics (QED) [39] and the weak interaction [29] and was formulated in the 1960's mainly by Sheldon Lee Glashow, Steven Weinberg, and Abdus Salam [40, 41, 42]. It describes the weak interaction, in which all fermions of the SM take part, and the electromagnetic interactions of all electrically charged particles.

The SM is experimentally studied with high precision. With the discovery of the Higgs boson in 2012 [43, 44] another milestone of particle physics was reached that demonstrated once more the consistency of the SM.

However, the SM also has some major inadequacies, for example:

- The model does not include the fourth fundamental interaction: gravity [45].
- It is incompatible with the *Standard Model of Cosmology* (Λ CDM⁴) since it fails to describe Dark Energy, matter-antimatter asymmetry, and does not provide a candidate for Dark Matter [46]. It only describes 4.6% of the energy density in the Universe [33].
- In the weak sector it leaves several open questions, for example the existence of a non-vanishing neutrino mass [23].

Figure 1.1 shows an overview of the elementary particles that are combined in the SM.

The course of this chapter addresses some of the open questions and shows ways to extend the SM to solve them. The following section focuses on the electrically and color-uncharged neutrinos that only interact via weak interaction.

1.2.2 The electroweak Sector - Neutrinos in the SM

The electroweak interaction underlays the weak isospin $SU(2)_{T_3}$ and the weak hypercharge symmetry $U(1)_{Y_W}$ (combined as the $SU(2)_{T_3} \times U(1)_{Y_W}$ symmetry group). It is mediated by the W^{\pm} , Z^0 - and γ -bosons. [34]

The Higgs mechanism describes the spontaneous symmetry breaking of the $SU(2)_{T_3} \times U(1)_{Y_W}$ to the electromagnetic $U(1)_{em}$ symmetry. According to the Goldstone Theorem [49], three would-be Goldstone bosons appear, which are absorbed by the W^{\pm} - and Z^0 -bosons and generate their masses while the γ -boson remains massless.[50]

The SM leptons played a keyrole in investigating the electroweak interaction especially the neutrinos. In 1956, Chien-Shiung Wu used the ${}^{60}_{27}\text{Co}$ β -decay to show that the weak interaction violates the parity conservation: Weak gauge bosons only interact with left-handed particles (and right-handed antiparticles)[51].

Representing the left-handed leptons as $SU(2)_{T_3}$ doublets

$$\begin{pmatrix} \nu_e \\ e^- \end{pmatrix}_L \quad \begin{pmatrix} \nu_\mu \\ \mu^- \end{pmatrix}_L \quad \begin{pmatrix} \nu_\tau \\ \tau^- \end{pmatrix}_L \quad (1.4)$$

and their right-handed partners as $SU(2)_{T_3}$ singlets

$$(e^-)_R \quad (\mu^-)_R \quad (\tau^-)_R \quad (1.5)$$

⁴ Λ stands for the cosmological constant and CDM for Cold Dark Matter. For details see section 1.5.1.

	I	II	III		
mass	2.16 MeV/c ²	1.27 GeV/c ²	172.9 GeV/c ²	0	125.10 GeV/c ²
spin	$\frac{2}{3}$	$\frac{2}{3}$	$\frac{2}{3}$	0	0
charge	$\frac{1}{2}$	$\frac{1}{2}$	$\frac{1}{2}$	1	0
	u	c	t	g	H
quarks					scalar bosons
	4.67 MeV/c ²	93 MeV/c ²	4.18 GeV/c ²	0	
	$-\frac{1}{3}$	$-\frac{1}{3}$	$-\frac{1}{3}$	0	
	$\frac{1}{2}$	$\frac{1}{2}$	$\frac{1}{2}$	1	
	d	s	b	γ	
	0.51 MeV/c ²	105.66 MeV/c ²	1.78 GeV/c ²	91.19 GeV/c ²	
	-1	-1	-1	0	
	$\frac{1}{2}$	$\frac{1}{2}$	$\frac{1}{2}$	1	
	e	μ	τ	Z	
leptons					
	0	0	0	80.38 GeV/c ²	
	0	0	0	± 1	
	$\frac{1}{2}$	$\frac{1}{2}$	$\frac{1}{2}$	1	
	ν_e	ν_μ	ν_τ	W	gauge bosons

Figure 1.1: The *Standard Model of Particle Physics*: The matter particles consist of quarks and leptons (fermions) and constitute of three generations (column 1 - 3). The gauge bosons (column 4) mediate the interactions between the particles, while the Higgs boson (column 5) gives them mass. The figure is adapted from [47] figure 2.2. with values from [48].

assures that only the left handed leptons interact with the weak-interaction bosons. [6] One year later Maurice Goldhaber determined a helicity of $h_\nu = 1.0 \pm 0.3$ for neutrinos, which means that they only appear as left-handed particles (respectively antineutrinos as right-handed) [52].

The SM charged leptons l generate their mass via Yukawa coupling y_l [53] to the Higgs doublet ϕ

$$\phi = \begin{pmatrix} \phi_+ \\ \phi_0 \end{pmatrix} \quad \text{with} \quad \begin{aligned} \phi_+ &= \frac{1}{\sqrt{2}}(\phi_1 + i\phi_2) \\ \phi_0 &= \frac{1}{\sqrt{2}}(\phi_3 + i\phi_4) \end{aligned} \quad (1.6)$$

and the Lagrangian

$$\mathcal{L}_Y = -y_l \left[\begin{pmatrix} \bar{\nu}_l \\ \bar{l} \end{pmatrix}_L \phi l_R \right] + h.c.. \quad (1.7)$$

By expanding around the Higgs vacuum expectation value

$$\langle \phi_0 \rangle = \frac{1}{\sqrt{2}} \begin{pmatrix} 0 \\ v \end{pmatrix}, \quad (1.8)$$

the mass terms for the charged leptons

$$\mathcal{L}_Y = -m_l [\bar{l}_R l_L + \bar{l}_L l_R], \quad (1.9)$$

with the charged lepton mass $m_l = y_l \frac{v}{\sqrt{2}}$, can be derived. As a consequence of equation (1.5) neutrinos remain massless in the SM. [13]

The fact that neutrinos are massless in the SM are not their only exceptional property. Since neutrinos are not charged under any unbroken gauge symmetry (U(1)_{em}) they could

be their own antiparticle. Particles that fulfill this requirement are called *Majorana particles*. [54] A Majorana neutrino would violate lepton number conservation which is not allowed in the SM [6].

1.3 Neutrino Oscillation

The discovery of neutrino oscillation was groundbreaking, both for neutrino and particle physics [5, 22]. It reveals once more the far reaching significance of neutrino properties to the understanding of the SM and its underlying physical processes. Section 1.3.1 briefly discusses the history of neutrino oscillation discovery, followed by a theoretical description of the mechanism (section 1.3.2). It is shown that flavor-changing processes necessarily require the neutrino to have a non-zero mass and point out other challenges to the SM that come up with the existence of this phenomenon.

1.3.1 The Solar Neutrino Problem and its Solution

With the solar neutrino flux being approximately $\Phi_{\nu}^{\text{sol}} \sim 6.6 \cdot 10^{10} \text{cm}^{-2}\text{s}^{-1}$, the Sun is the strongest natural source of neutrinos observed on Earth. Electron neutrinos are generated in fusion processes with the main contribution coming from helium fusion (pp-chain)



The solar neutrino energy spectrum is composed of several continuous and monoenergetic spectra and was first investigated in detail by John Bahcall as a result of his Standard Solar Model (SSM) (see figure 1.2) [55].

In 1964, Ray Davis proposed a low background experiment in a mine in Homestake with the purpose to measure the neutrino flux of ${}^7\text{Be}$ coming from fusion processes in the sun [56].

The neutrinos were captured via the inverse β -decay of chlorine to excited argon



After a fixed measurement interval of 60 days, the argon was separated. It de-excited via electron capture to excited states of chlorine which again decayed via Auger electron emission to a chlorine groundstate. The electrons were measured in a proportional counter. [57] This process of determining the number of captured neutrinos is known as the radiochemical detection method [6].

After two decades of measurement the determined neutrino flux showed a significant deficit to the prediction of the SSM. Only about a third of the expected electron neutrinos were measured. [58] In the upcoming years, several other observations confirmed this so-called *solar neutrino problem*, for example the GALLEX [59] or the SAGE experiment [60].

The foundations of an approach to explain the electron neutrino deficit was already formulated by Bruno Pontecorvo in 1957 [62, 63]. He proposed a neutrino-antineutrino mixing analog to kaon oscillation. His idea was further developed by himself and by Ziro Maki, Masami Nakagawa and Shoichi Sakata to a theory of flavor transition of neutrinos, today known as *neutrino oscillation* [64].

The problem was finally solved in 2001 by the SNO experiment. It used an experimental technique that allowed for a measurement of not only electron neutrinos but neutrinos of all flavors. The D_2O target detected charged current (CC) and neutral current (NC) interactions on deuterium as well as elastic electron scattering (ES)



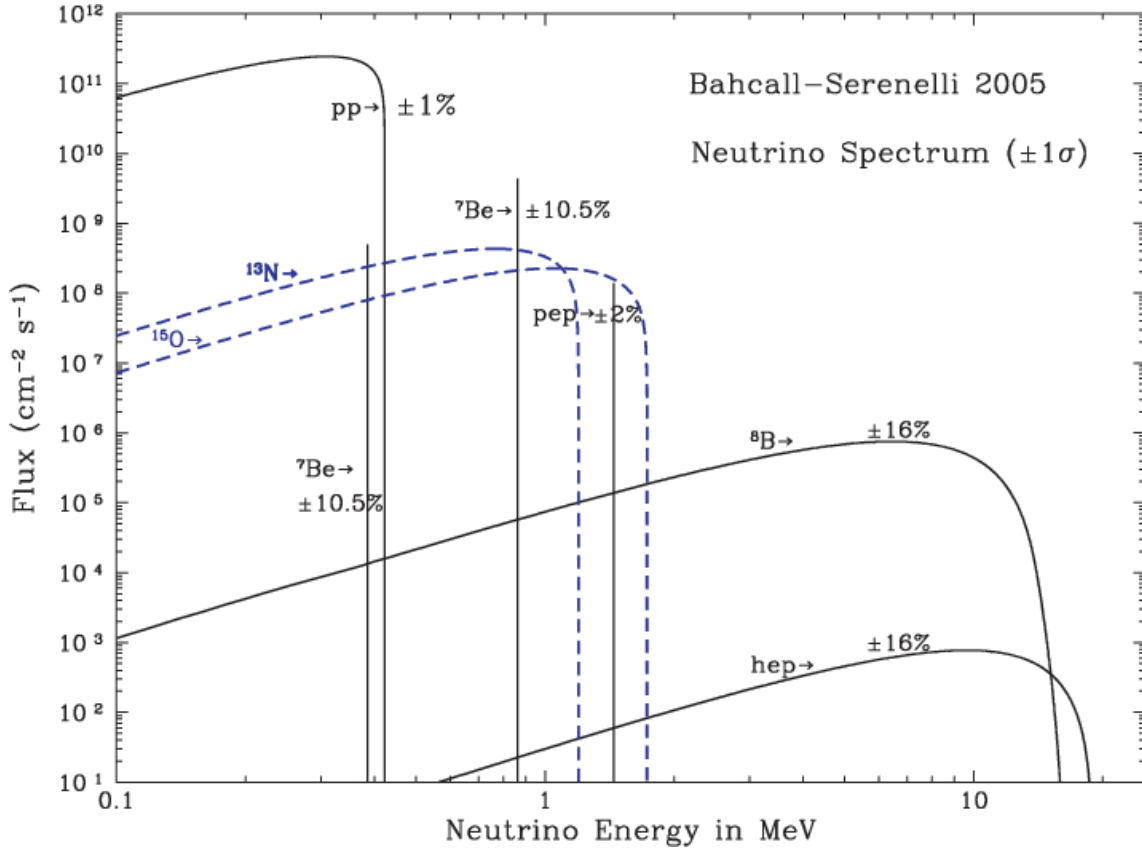


Figure 1.2: The Solar Neutrino Spectrum in a double-logarithmic representation derived by [61]. The figure summarizes the fluxes of neutrinos originating from different fusion processes in the sun. The dashed lines correspond to the neutrino-flux coming from the CNO-cycle, the solid black lines from the pp-chain. Depending on the corresponding decay, the emitted neutrinos are monoenergetic or have a continuous energy spectrum. The percentage numbers are the uncertainties on the size of the fluxes. The figure is reprinted from [61] with the kind permission of the American Astronomical Society and the author.

The measured solar neutrino flux, when consisting of all three flavors ($l = e, \mu, \tau$), confirmed the predictions of the SSM, while the electron neutrino flux showed the same behavior as the other solar neutrino experiments. This result could only be explained by neutrino oscillation. [5]

The spokesperson of the SNO collaboration Arthur McDonald was awarded the Nobel Prize of Physics together with his colleague Takaaki Kajita from the Super-Kamiokande collaboration, an experiment that simultaneously confirmed neutrino oscillation for atmospheric neutrinos [22].

1.3.2 Theory of Neutrino Oscillation

The following formalism of neutrino oscillation can be found in most textbooks on introduction to neutrino physics or related topics. One good example can be found in [6] section 8.1.

The concept of neutrino oscillation is an outcome of a gauge theory for massive neutrinos [6]. There exists a mixing matrix analogous to the CKM⁵-matrix for quark mixing [65] that transforms the neutrino mass eigenstates ν_i (with $i = 1, 2, 3$) to flavor eigenstates ν_α (with $l = e, \mu, \tau$)

$$|\nu_l\rangle = \sum_i U_{li} |\nu_i\rangle \quad \text{and vice versa} \quad |\nu_i\rangle = \sum_l U_{li}^* |\nu_l\rangle, \quad (1.15)$$

where U_{li} is the so-called PMNS⁶-matrix [64, 6]. This unitary 3×3 matrix can be interpreted as a rotation matrix

$$U = \begin{bmatrix} U_{e1} & U_{e2} & U_{e3} \\ U_{\mu1} & U_{\mu2} & U_{\mu3} \\ U_{\tau1} & U_{\tau2} & U_{\tau3} \end{bmatrix} [13]. \quad (1.16)$$

If neutrinos are Dirac particles, the PMNS-matrix is defined by the three mixing angles θ_{ij} and the CP-violating Dirac phase δ and can be written as

$$U^D = \begin{bmatrix} c_{12}c_{13} & s_{12}c_{13} & s_{13}e^{-i\delta} \\ -s_{12}c_{23} - c_{12}s_{13}s_{23}e^{i\delta} & c_{12}c_{23} - s_{12}s_{13}s_{23}e^{i\delta} & c_{13}s_{23} \\ s_{12}s_{23} - c_{12}c_{23}s_{13}e^{i\delta} & -c_{12}s_{23} - s_{12}s_{13}c_{23}e^{i\delta} & c_{13}c_{23} \end{bmatrix}, \quad (1.17)$$

with $s_{ij} = \sin \theta_{ij}$ and $c_{ij} = \cos \theta_{ij}$ [13].

For Majorana neutrinos, the mixing matrix needs to be extended by two Majorana phases $\alpha_{1,2}$

$$U^M = U^D \cdot S \quad (1.18)$$

with

$$S = \begin{bmatrix} e^{i\alpha_1/2} & 0 & 0 \\ 0 & e^{i\alpha_2/2} & 0 \\ 0 & 0 & 1 \end{bmatrix} [13]. \quad (1.19)$$

The oscillation probability $P_{\alpha\beta}$ can be derived via the time evolution of an initial $|\nu_\alpha(t)\rangle$ to a final neutrino flavor state $|\nu_\beta\rangle$

$$|\nu_\alpha(t)\rangle = \sum_i U_{\alpha i}^* \cdot \exp(-iE_i t) |\nu_i\rangle \neq |\nu_\alpha(t=0)\rangle [6]. \quad (1.20)$$

⁵Cabibbo-Kobayashi-Maskawa.

⁶Pontecorvo-Maki-Nakagawa-Sakata.

The mass eigenstates $|\nu_i\rangle$ propagate through space-time with energy E_i . The oscillation probability $P_{\alpha\beta}$ is given by the transition amplitude

$$\begin{aligned}
P_{\alpha\beta} &= |\langle \nu_\beta | \nu_\alpha(t) \rangle|^2 = \left| \sum_i U_{\alpha i}^* U_{\beta i} \cdot \exp(-iE_i t) \right|^2 \\
&= \sum_{i,j} U_{\alpha i}^* U_{\beta i} U_{\alpha j} U_{\beta j}^* \cdot \exp(-i(E_i - E_j)t) \quad [6].
\end{aligned} \tag{1.21}$$

For relativistic neutrinos with $p \gg m$ the mass eigenstate energy is

$$E_i = \sqrt{p^2 + m_i^2} \approx E + \frac{m_i^2}{2E} \tag{1.22}$$

which leads to the final expression.

$$P_{\alpha\beta}(L, E) = \sum_{i,j} U_{\alpha i}^* U_{\beta i} U_{\alpha j} U_{\beta j}^* \cdot \exp\left(-i \frac{\Delta m_{ij}^2 L}{2E}\right), \tag{1.23}$$

with $\Delta m_{ij}^2 = m_i^2 - m_j^2$ the mass differences of the mass eigenstates, L the distance of propagation, and E the neutrino energy. [6]

1.3.3 Neutrino Oscillation Parameters

The mixing angles θ_{ij} and mass splittings Δm_{ij}^2 are experimentally accessible. θ_{12} and Δm_{12}^2 are historically connected to solar neutrino observations (e.g. [5, 59, 60]) and have been well cross-checked by reactor experiments [66, 67, 68]. The parameters θ_{23} and Δm_{23}^2 are mainly determined by atmospheric neutrino observations measuring ν_μ generated in the Earth's atmosphere by μ^\pm -decays [6]. The flagship is the Super-Kamiokande experiment, which uses Cherenkov detection techniques to measure ν_e and ν_μ [69].

θ_{31} was only recently determined by the Daya Bay short-baseline reactor experiment [70], figure 1.3 shows the result of the measurements.

In [23] a broad overview of all oscillation experiments can be found. The values of the oscillation parameters are given in table 1.1.

The sign of the mass splitting Δm_{32}^2 relative to Δm_{12}^2 is still unknown, which leads to two different scenarios of neutrino mass ordering:

$$\begin{aligned}
\text{Normal ordering:} & \quad m_1 < m_2 \ll m_3 \\
\text{Inverted ordering:} & \quad m_3 \ll m_1 < m_2.
\end{aligned} \tag{1.24}$$

The global analysis of all oscillation experiment data favors a normal over an inverted ordering, with a statistical significance of 3.2σ . [23, 71]

While neutrino oscillation experiments are able to measure the Δm_{ij}^2 the absolute mass of the neutrino m_i can not be accessed [13].

1.3.4 Consequences of Neutrino Oscillation

The formalism of the leptonic sector in the SM stands in great contradiction to the theory of neutrino oscillation. It necessarily postulates non-zero neutrino masses and measurements even provide bounds and relations due to the measured mass splittings. The SM does not contain a mechanism to generate neutrino masses and it has to be extended to allow for neutrino oscillation. [6] Once introduced, massive neutrinos are of special interest to explain the cosmological observations of *Dark Matter* (as described for example in [14]). For more information see section 1.5.1.

Table 1.1: The neutrino oscillation parameters as listed by the particle data group [48]. The parameters are the best fit values $\pm 1\sigma$. They are sorted by normal and inverted ordering according to equation (1.24).

Parameter	Normal ordering	Inverted Ordering
$\sin^2 \theta_{12}$	$0.307^{+0.013}_{-0.012}$	$0.307^{+0.013}_{-0.012}$
$\sin^2 \theta_{23}$	$0.417^{+0.025}_{-0.028}$	$0.421^{+0.033}_{-0.025}$
$\sin^2 \theta_{31}$	$0.021^{+0.001}_{-0.001}$	$0.021^{+0.001}_{-0.001}$
$\frac{\Delta m_{12}^2}{10^{-5} \text{ eV}^2}$	$7.53^{+0.18}_{-0.18}$	$7.53^{+0.18}_{-0.18}$
$\frac{\Delta m_{32}^2}{10^{-3} \text{ eV}^2}$	$+2.51^{+0.05}_{-0.05}$	$2.56^{+0.04}_{-0.04}$

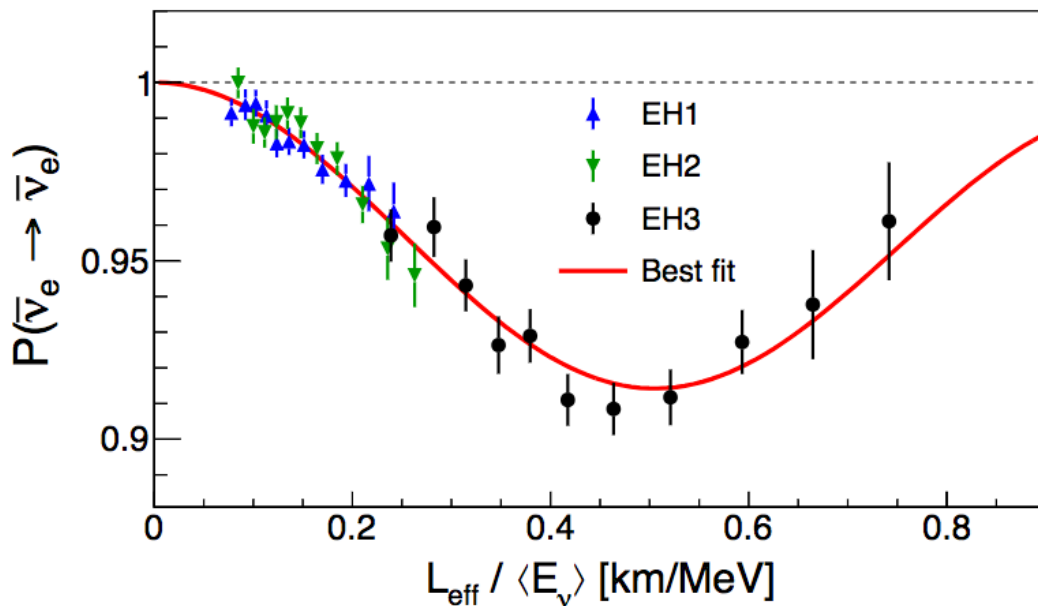


Figure 1.3: Survival probability $P(\bar{\nu}_e \rightarrow \bar{\nu}_e)$ of electron antineutrinos versus the effective propagation distance L_{eff} divided by the average antineutrino energy $\langle E_\nu \rangle$, measured by the Daya Bay experiment [70]. The data points are the ratios of the measured antineutrino flux to the one predicted without oscillation. EH1-3 stand for the three different experimental halls. By varying $L_{\text{eff}}/\langle E_\nu \rangle$ an oscillation pattern appears in the survival probability as predicted by theory. The figure is reprinted from [70] with the friendly permission of the author and the American Physical Society.

Furthermore, equations (1.17) and (1.19) implement CP-violating phases to the weak interaction. The violation of CP-Symmetry in the quark sector is a well-studied phenomenon [72, 20] and can help to explain the matter-antimatter asymmetry in our universe to a certain (however not sufficient) degree [73, 74]. The additional CP-violating phases, introduced by neutrino oscillation, could play a crucial role in explaining this discrepancy [13].

1.4 Massive Neutrinos

In this section several mechanisms to introduce massive neutrinos to the SM are discussed, all of them require an extension. In section 1.4.1, the neutrino mass is added analog to the charged lepton masses (equations (1.7)-(1.9)) by coupling to the SM Higgs doublet. Depending on the Dirac or Majorana nature of the neutrino, the mechanism splits up in two ways. Both models require a very small Yukawa coupling (about five orders of magnitude smaller than for the charged leptons). This unnatural discrepancy can be avoided by the so-called *seesaw mechanism* which is discussed in section 1.4.2. [13]

All three ways have one thing in common, which is of great importance in the scope of this thesis: They require to add another group of particles to the SM – the *sterile neutrinos*. The right-handed partners of the active neutrinos do not interact via any SM interaction and imprint themselves only via mixing with the active neutrinos. [13]

For the sake of completeness it should be mentioned that there are also other possibilities to generate neutrino masses for example via radiative quantum corrections [75, 76, 77], Froggatt-Nielsen type models [78], and models with approximate lepton number conservation [79, 80, 81].

1.4.1 Dirac and Majorana Massterm

To formulate a neutrino mass term analogous to equation (1.9) a right-handed neutrinos need to be introduced to the SM. Identically to right-handed charged leptons they are formulated as SU(2) singlets with $T_3 = 0$ and $Y_W = 0$ and can not interact with weak W- and Z⁰-bosons

$$(\nu_e)_R \quad (\nu_\mu)_R \quad (\nu_\tau)_R \cdot [13] \quad (1.25)$$

The Dirac massterms are derived via Yukawa coupling to the SM Higgs doublet from equation (1.6):

$$\mathcal{L}_D = -m_D(\bar{\nu}_L \nu_R + \bar{\nu}_R \nu_L) [13]. \quad (1.26)$$

The Dirac mass of the neutrino is given by

$$m_D = y_D \frac{v}{\sqrt{2}}, \quad (1.27)$$

where v is the Higgs vacuum expectation value. The lepton number is conserved. With $v = 246$ GeV the Dirac-Yukawa coupling has to be in the order of $y_D \leq 10^{-11}$ and would be five orders of magnitude smaller than for the charged leptons due to the large mass difference. [13]

Assuming that the neutrino is a Majorana particle, the neutrino spinors are directly connected to their own CP-conjugate (antiparticle). In this case, the mass term can be written as

$$\mathcal{L}_M = -\frac{1}{2}M_L(\bar{\nu}_L \nu_R^C + \bar{\nu}_R^C \nu_L) - \frac{1}{2}M_R(\bar{\nu}_R \nu_L^C + \bar{\nu}_L^C \nu_R). [13] \quad (1.28)$$

This coupling of neutrinos and antineutrinos would violate lepton conservation and can not be described by the SM Higgs mechanism. One way to realize it is by coupling to a

Higgs triplet or higher-dimensional operations including two Higgs doublets [82]. The Dirac and Majorana mass terms can be combined to

$$\mathcal{L}_\nu = -\frac{1}{2}(\bar{\nu}_L \bar{\nu}_L^C) \begin{pmatrix} M_L & m_D \\ m_D & M_R \end{pmatrix} \begin{pmatrix} \nu_R^C \\ \nu_R \end{pmatrix} + \text{h.c.} \quad [13] \quad (1.29)$$

One way to explain the neutrino mass and avoid unnaturally small Yukawa couplings, is a special case of equation (1.29) where the Majorana mass for the left-handed neutrinos is set to zero $M_L = 0$. This so called *minimal type-I seesaw mechanism* is explained in the following section. [13] A graphical interpretation of the three different coupling scenarios can be found in figure 1.4.

1.4.2 Seesaw Mechanism

The seesaw mechanism is a well studied theory, to introduce a small neutrino mass by adding n right-handed sterile neutrinos to the SM. Over the past years, it has been the topic of many different investigations for example [83, 84, 85, 86, 87, 88]. The limitation of the new mass eigenstates depends on the mechanism type, but is in general arbitrary [13]. The masses can be chosen in a way to potentially explain the matter-antimatter asymmetry [74], the reactor antineutrino anomaly observed in short-baseline neutrino oscillation experiments [89], or Dark Matter on the keV mass scale [90]. It allows a mixing of active and sterile neutrinos which makes an experimental observation possible [13].

As an example, the *minimal type-I seesaw mechanism* is considered, which describes a special case of equation (1.29) with $M_L = 0$ and $M_R \gg m_D$ with the Lagrangian

$$\mathcal{L}_\nu = -\frac{1}{2}(\bar{\nu}_L \bar{\nu}_L^C) \begin{pmatrix} 0 & m_D \\ m_D & M_R \end{pmatrix} \begin{pmatrix} \nu_R^C \\ \nu_R \end{pmatrix} + \text{h.c.} \quad [6, 13]. \quad (1.30)$$

By diagonalizing the 2×2 matrix, two eigenvalues which correspond to two Majorana neutrinos are derived

$$m_{\nu_a} \sim \frac{m_D^2}{M_R}, \quad m_{\nu_s} \sim M_R, \quad (1.31)$$

with m_{ν_a} the active and m_{ν_s} the sterile neutrino mass eigenvalue [13].

The name seesaw mechanism refers to the fact that $m_{\nu_a} \sim m_{\nu_s}^{-1}$. The heavier the sterile neutrino mass, the lighter the active SM neutrino. Both neutrinos mix with the amplitude

$$|\theta| \sim \frac{m_D}{M_R} \sim \sqrt{\frac{m_{\nu_a}}{m_{\nu_s}}}, \quad (1.32)$$

which makes the sterile state observable. [13]

The Yukawa coupling is given by

$$y_D = \frac{\sqrt{m_{\nu_a} m_{\nu_s}}}{v}. \quad (1.33)$$

By choosing very large sterile neutrino masses the problem of an unnaturally small Yukawa coupling can be solved. [13]

As mentioned above, the mass M_R and subsequently m_{ν_s} is of arbitrary scale. In the following section several scenarios for different sterile neutrino masses are discussed. For some of them, the *minimal type-I seesaw mechanism* presented here does not meet the requirements in regard of number of sterile neutrinos. Therefore it is important to mention, that there are several other seesaw models, which allow for more than one sterile neutrino, such as the *Neutrino Minimal Standard Model* ν MSSM, which is presented in chapter 3. [14]

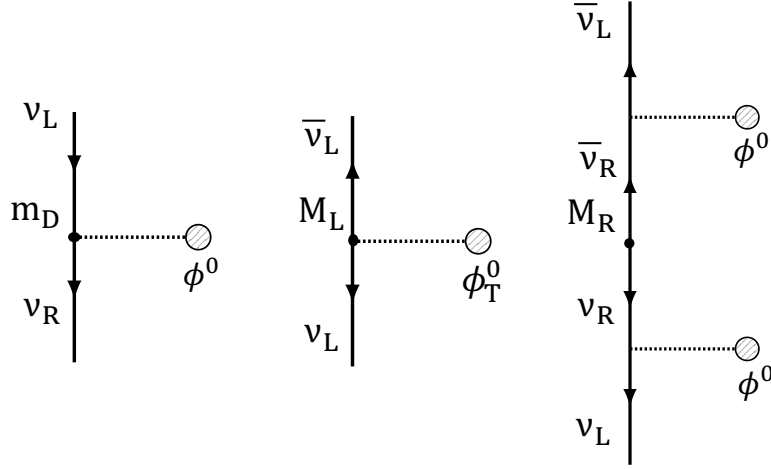


Figure 1.4: The three ways of neutrino mass generation discussed in this paragraph visualized in a Feynman diagram-like representation (idea with modifications from [91]). **Left:** Generation of Dirac mass via Yukawa coupling to a neutral component of a Higgs doublet ϕ^0 (corresponds to equation (1.26)). **Center:** The Majorana case with coupling to a Higgs triplet ϕ_T^0 . The Majorana mass could also be generated by a coupling to two Higgs doublets via a higher-dimensional operator (see [13].) **Right:** Majorana mass generation via the seesaw mechanism type-I by a Yukawa coupling to two Higgs-doublets ϕ^0 . All three cases are generic examples. [13]

1.4.3 Possible Masses of Sterile Neutrinos

In principle, the sterile neutrino mass m_{ν_s} can be of any value [13]. However, there are some favored mass scales that imply different seesaw scenarios. The resulting sterile neutrinos could have great influence on several processes of particle physics and cosmology. Furthermore, the method to detect them also strongly depends on the mass-scale. In [13] the different mass scales are listed as follows:

- $m_{\nu_s} = \mathcal{O}(\text{eV})$: Many short-baseline neutrino oscillation experiments such as LSND [92] and MiniBooNE [93] observed an anomaly in the $\bar{\nu}_e$ disappearance channel that could be referred to an active-to-sterile neutrino mixing [94, 95]. The *minimal-mini-seesaw model* with $m_D \ll m_{\nu_s} \sim \mathcal{O}(\text{eV})$ and $M_L = 0$ yields reasonable values for the active-to-sterile mixing and the active and sterile masses [96, 97]. Sterile neutrinos in the eV-mass range could be detectable in β -decay spectra [98]. [13]

- $m_{\nu_s} = \mathcal{O}(\text{keV})$: Sterile neutrinos in the keV-mass range are favored Dark Matter candidates, with the production mechanism determining whether they are cold, warm or hot DM [99]. If the sterile neutrino would act as Warm Dark Matter it could help to solve structure problems in the universe [100, 101, 102] (detailed discussion in chapter 3). [13]

The simplest way to introduce keV-scale sterile neutrinos is via the *Neutrino Minimal Standard Model* (νMSM), which adds three sterile neutrinos to the SM, one of them on the keV-scale [14].

Sterile neutrinos in the keV mass range are experimentally accessible, either via active-to-sterile mixing in β -decay experiments [12] or through their decay channel $\nu_s \rightarrow \gamma \nu_a$ in astrophysical observations [103, 104, 13] Both cases are discussed in more detail in chapter 3.

- $m_{\nu_s} = \mathcal{O}(\text{MeV} - \text{TeV})$: In the above mentioned νMSM , two heavy sterile neutrinos appear [14]. If their mass is constrained to 150 MeV – 100 GeV, the baryonic matter-antimatter asymmetry could be explained via active-to-sterile neutrino oscillation-

induced leptogenesis, converted to baryon asymmetry via sphaleron transition [105, 13].

- $m_{\nu_s} \gg \mathcal{O}(\text{TeV})$: For maximally heavy sterile neutrinos from the TeV to the Planck scale, the Yukawa coupling y_D is in the same order as the coupling for quarks and charged leptons, and solves the mass-hierarchy problem in the SM [13]. This scenario is favored by supersymmetric models and could be visible in sneutrino exchange processes [106, 13].

This thesis lays focus on the search for keV-scale sterile neutrinos with the KATRIN experiment. Chapter 3 gives a broader introduction on how sterile neutrinos on this specific mass scale can be detected via β -decay spectroscopy. Limits on their parameter space, already given by cosmological and experimental observations, are discussed and an introduction on the history of keV-scale sterile neutrino investigation and the current status is given.

1.5 Absolute Neutrino Mass Measurements

The nature of the neutrino and especially the phenomenon of neutrino oscillation is of great interest for modern physics. The absolute neutrino mass is a new parameter in the SM whose scale has significant influence on, for example, the structure formation of our Universe [107]. There are several approaches to determine the neutrino mass. This section presents an overview of the main principles sub-divided into two groups (as, for example, formulated in [10])

- Measurements that dependent on underlying models represent the first group of absolute neutrino mass determination experiments. The study of the hypothetical neutrinoless double β -decay measuring the Majorana neutrino mass $m_{\beta\beta}$ and the determination of the absolute sum of masses $\sum_i m_i$ via cosmological observations is explained in section 1.5.1 and 1.5.2.
- Model-independent measurements which study the pure kinematics of single β -decays make use of the relativistic energy momentum relation⁷. The study of the tritium β -decay is used in the KATRIN experiment in order to determine the effective electron antineutrino mass m_β . Details are discussed in section 1.5.3.

It is important to emphasize that all approaches are sensitive to a different effective neutrino mass [10].

1.5.1 Cosmological Observations

The Λ CDM model is a cosmological model that describes the evolution of the Universe since its beginning in the *Big Bang* [46]. With only six free parameters it is one of the most basic and at the same time most accurate models and is therefore often referred to as the *Standard Model of Cosmology* (for example in [13, 108]). It describes with high consistency the existence and structure of the *Cosmic Microwave Background* (CMB), the large-scale structure distribution of galaxies and voids, and the accelerated expansion of the Universe [46]. The six parameters of the Λ CDM are mainly derived by detailed studies of the multipole expanded power spectrum of the CMB. Their values determined by the *Planck* satellite experiment are listed in table 1.2 [33].

The baryon density parameter $\Omega_b h^2$ implies that the contribution of baryonic matter to the energy density of the Universe is only about 4.86 % while 26.8 % is Dark Matter. Since neutrinos only interact weakly and gravitationally they could contribute as so-called Hot

⁷ $E^2 = p^2 c^2 + m_0^2 c^4$ with the energy E , the momentum p , and m_0 the rest mass of the particle.

Table 1.2: The main parameters of the Λ CDM-model [46]. Values taken from the results from the *Planck* collaboration [33].

Description	Parameter	Value
baryon density	$\Omega_b h^2$	0.02236 ± 0.00015
dark matter density	$\Omega_c h^2$	0.1202 ± 0.0014
reionization optical depth	τ	$0.054^{+0.007}_{-0.0081}$
curvature fluctuation amplitude	A_s	$(2.101^{+0.031}_{-0.034}) \cdot 10^{-9}$
scalar spectral index	n_s	0.9649 ± 0.0044
acoustic scale angle	$100\theta_{MC}$	1.04090 ± 0.00031

Dark Matter [109].

The Λ CDM predicts a *Cosmic Neutrino Background* (CvB) similar to the CMB that consists of relic neutrinos which decoupled only one second after the Big Bang from the baryonic matter [107]. The relic neutrino density is predicted to be 339 cm^{-3} with a present black body temperature of 1.95 K [6]. Due to their small energy in the sub-eV range the CvB has not been experimentally confirmed yet [110]. Its total energy density $\Omega_\nu h^2$ is given by the sum of the neutrino masses $\sum m_i$ derived from parameters that can be found in table 1.2

$$\Omega_\nu h^2 = \frac{\sum_i m_i}{93.14 \text{ eV} c^{-2}} [6]. \quad (1.34)$$

The neutrino mass $\sum_i m_i$ can be estimated from astrophysical observations. The relevant observables are the power spectrum of the CMB temperature anomalies as in [33] or the matter power spectrum observed by galaxy surveys, for example the Sloan Digital Survey [111].

The *Planck* Collaboration published an upper limit on the total neutrino mass in 2018 with

$$\sum_i m_i < 0.12 \text{ eV} c^{-2} \text{ (95 \% C.L.) [33]}. \quad (1.35)$$

Since the limit on the neutrino mass derived by cosmological observations is model-dependent it can not be directly compared to laboratory experiments [10]. However, it is important to understand the immense influence of the neutrino mass on the evolution of our Universe and its matter content as it is described, for example, in [6].

1.5.2 Double Beta Decay Experiments

The Bethe-Weizsäcker formula underlays a semi-empirical model that describes the binding energy of atomic nuclei and their resulting decay scheme [112]. The binding energy is depending quadratically on the proton number Z as shown on the left side of figure 1.5. A β -decay transmutes an even-even in an energetically preferred odd-odd state by converting a neutron in a proton (or vice versa). Sometimes the daughter nucleus has a higher binding energy and the decay is energetically forbidden. The double β -decay ($2\nu\beta\beta$) is a second order weak interaction process that can be experimentally observed in such cases. [6] It was first formulated by Maria Goeppert-Mayer in 1935 [113]. The double β -decay describes

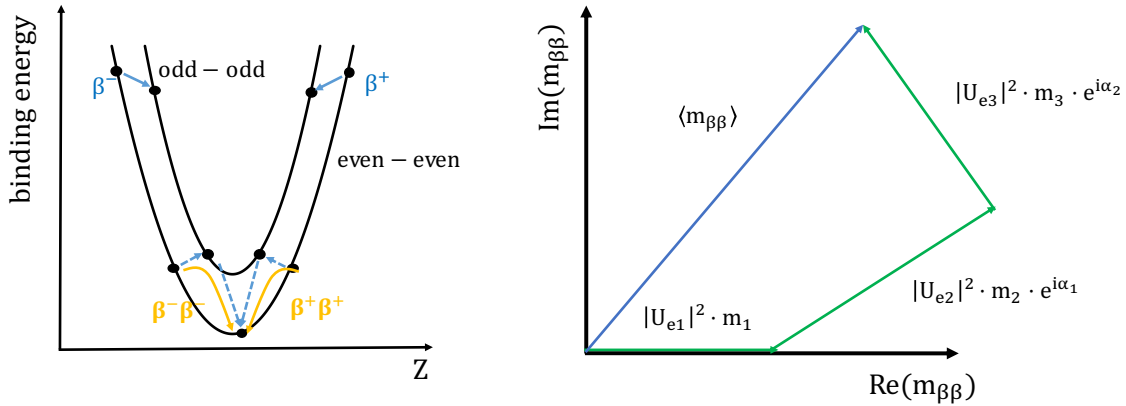


Figure 1.5: **Left:** The binding energy (mass) of different atomic nuclei as a function of the number of protons derived by the Bethe-Weizsäcker formula. In some cases the single β -decay is energetically forbidden and the double β -decay is necessary to reach the minimum of the mass parabola. **Right:** The coherent sum of the mass eigenstates in the case of a Majorana neutrino. If the complex phases are $\alpha_j \neq n \cdot \pi$ the summation leads to cancellations. [6]

two simultaneous transmutations of two neutrons in two protons under the emission of two electrons and two electron antineutrinos⁸



A graphical interpretation of the decay can be found in the center of figure 1.6. Sections 1.2, 1.3.2 and 1.4.1 already point out, that neutrinos could be Majorana particles so that $\nu = \bar{\nu}$ [54]. In this case, the neutrino generated in one decay vertex could be absorbed at the other and there would be no neutrino in the final state. This process is called neutrinoless double β -decay ($0\nu\beta\beta$):



and was first proposed by G. Racah in 1937. [115]

In this decay the lepton number conservation would be violated by $\Delta L = 2$ why it is forbidden in the SM. In addition to the Majorana nature of the neutrino, the $0\nu\beta\beta$ requires the neutrino to be massive. The electron antineutrino in one vertex would be emitted as right-handed $\bar{\nu}_R$ and needs to be absorbed as a left-handed neutrino ν_L . This spin flip (change of sign of helicity⁹) requires $m_\nu > 0$. The sum of the energies carried away by the electrons is constant in contrast to the $2\nu\beta\beta$, where always some energy is carried by the neutrinos. It would imprint itself as a comparatively small mono-energetic peak at the endpoint of the decay. The $0\nu\beta\beta$ is strongly suppressed compared to $2\nu\beta\beta$ due to the smaller phase space. An exemplary spectrum can be seen on the left side of figure 1.7. [6] In $0\nu\beta\beta$ the effective Majorana mass $\langle m_{\beta\beta} \rangle$ of the neutrino can be determined via measuring the half-life $T_{1/2}^{0\nu\beta\beta}$ of the decay

$$\left(T_{1/2}^{0\nu\beta\beta}\right)^{-1} = G^{0\nu\beta\beta} \left|M^{0\nu\beta\beta}\right|^2 \frac{\langle m_{\beta\beta} \rangle^2}{m_e^2}, \quad (1.38)$$

⁸The $\beta^+\beta^+$ decay with two protons decaying in two neutrons is also possible and was observed in the ^{78}Kr decay [114]. However, the β^+ -decay competes most of the time with electron capturing and is therefore very rare [6].

⁹Projection of the spin onto the momentum vector.

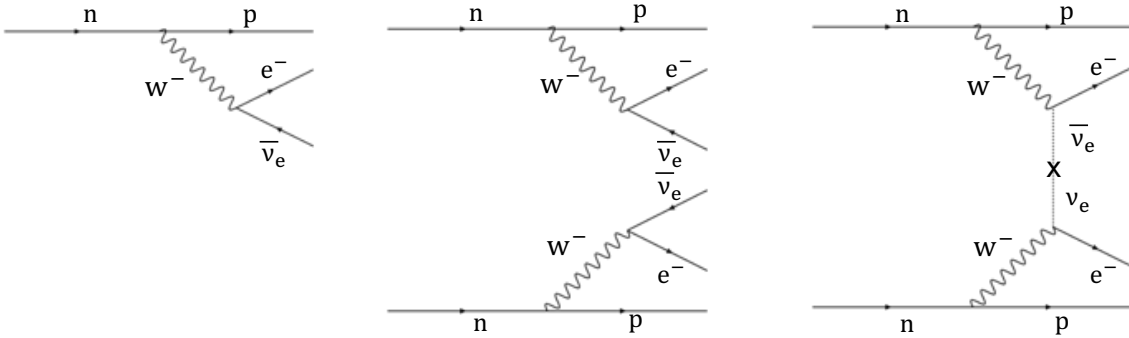


Figure 1.6: The Feynman diagrams of the single β -decay (left) and the two neutrino (middle) and neutrinoless double β -decay (right). The latter case requires the neutrino to be a Majorana particle and to be massive [6].

where $|M^{0\nu\beta\beta}|$ is the nuclear transition matrix element and $G^{0\nu\beta\beta}$ a phase space factor [6]. The effective Majorana mass is given by

$$\langle m_{\beta\beta} \rangle = \left| \sum_i^3 U_{ei}^2 m_i \right| = \left| \sum_{j,i}^{2,3} |U_{ei}|^2 m_i e^{i\alpha_j} \right|, \quad (1.39)$$

which is the coherent sum of the neutrino mass eigenstates with the CP-violating Majorana phase α_j from equation (1.19). [6, 116]

The right side of figure 1.5 graphically interprets the summation of the neutrino masses and the influence of the complex Majorana phases α_j . It is possible that the α_j lead to cancellations which could result in a negative effective Majorana mass $\langle m_{\beta\beta} \rangle < \sum_i m_i$. [6] There are several experiments that are investigating the neutrinoless double β -decay for example the MAJORANA [117], the KamLAND-Zen [118] and the GERDA experiment [119]. All experiments require a very low background rate why they are located in underground laboratories [6].

The current limit on $T_{1/2}^{0\nu\beta\beta}$ is given by the latest results of the GERDA experiment¹⁰ from March 2018

$$T_{1/2}^{0\nu\beta\beta} > 8.0 \cdot 10^{25} \text{ a (90\% C.L.)}, \quad (1.40)$$

which corresponds to a Majorana mass limit of

$$\langle m_{\beta\beta} \rangle < (0.12 - 0.26) \text{ eV [119]}. \quad (1.41)$$

The result strongly depends on the transmission matrix elements $|M^{0\nu\beta\beta}|$, which display the highest theoretical uncertainty as well as the underlying model-dependencies [120].

1.5.3 Single Beta Decay Experiments

In a β^- -decay a neutron decays into a proton under the emission of an electron and an electron antineutrino¹¹

$$(A, Z) \rightarrow (A, Z + 1) + e^- + \bar{\nu}_e \text{ [6]}. \quad (1.42)$$

The formulation of the decay via a Feynman graph can be seen on the left side of figure 1.6.

The released energy that is set free in this decay splits mainly between the two leptons since the mass of the daughter nucleus is very large compared to the electron and the

¹⁰observing the decay: $^{76}\text{Ge} \rightarrow ^{76}\text{Se} + 2e^-$ [119].

¹¹In the following only referred to as *neutrino*.

neutrino (some energy goes into the recoil of the mother nucleus). The neutrino energy is given by

$$E_\nu = \sqrt{m_\nu^2 c^4 + p_\nu^2 c^2} \quad [6], \quad (1.43)$$

with the rest mass of the neutrino m_ν and its momentum p_ν . Since neutrinos have a non-vanishing rest mass, they always carry some of the released energy, so that the maximum observed electron energy of this decay is given by

$$E_e^{\max} = E_0 - E_\nu(p_\nu = 0) \quad [6]. \quad (1.44)$$

The differential electron spectrum of the β -decay can be expressed by Fermi's Golden Rule [29] and is given by

$$\begin{aligned} \frac{dN}{dE_e} = & \frac{G_F}{2\pi^3} \cos^2 \Theta_C |M|^2 \cdot F(E, Z) \cdot \\ & \cdot p_e \cdot (E_e + m_e c^2) \cdot (E_0 - E_e) \cdot \sqrt{(E_0 - E_e)^2 - c^4 \sum_i |U_{ei}|^2 m_{\nu_i}^2}, \end{aligned} \quad (1.45)$$

where G_F is the Fermi constant, Θ_C the Cabbibo angle, M the nuclear transition matrix and $F(E, Z)$ the Fermi function [121]. The right side of figure 1.7 shows the spectral shape with the focus on the endpoint region and the influence of the neutrino mass on the spectrum.

The expression

$$m_{\bar{\nu}_e}^2 = \sum_i |U_{ei}|^2 m_{\nu_i}^2 \quad (1.46)$$

describes the effective electron antineutrino mass and is the incoherent sum of the three neutrino mass eigenstates. In contrast to the $0\nu\beta\beta$ no cancellations can occur due to CP-violating phases and the Majorana or Dirac nature of the neutrino is not of importance. [6] All effects that modify the shape of the spectrum, for example the final states of the daughter nucleus have to be taken into account in β -spectroscopy. Therefore, A very high energy resolution is required to reach the sub-eV sensitivity on $m_{\bar{\nu}_e}^2$. [121]

The tritium β -decay



has several advantages over other β -decays. The most important advantages are the energy independent transision matrix element, the relatively simple atomic-shell structure and the short half-life of $T_{1/2} \approx 12.3$ a. [10] The current limit on $m_{\bar{\nu}_e}^2$ was recently published by the KATRIN collaboration in [9] and is

$$m_{\bar{\nu}_e}^2 < 1.1 \text{ eV} (90\% \text{ C.L.}). \quad (1.48)$$

In the next chapter the KATRIN experiment is introduced. With its high-luminosity source and a precise MAC-E filter it has the potential to push the limit of the neutrino mass by another factor of five, to finally reach the sub-eV scale for the absolute electron neutrino mass [10].

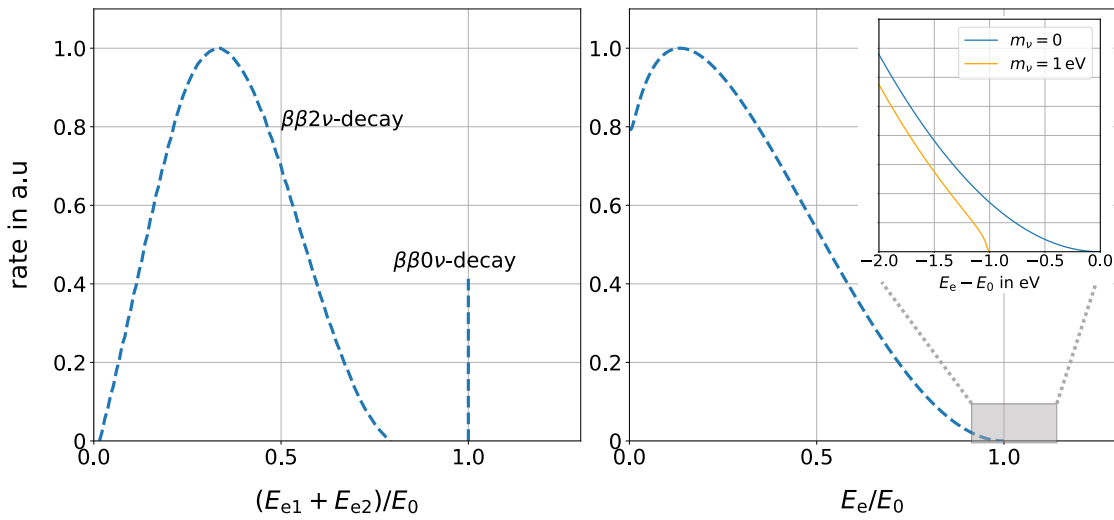


Figure 1.7: Left: The spectra of both electrons emitted in a double β -decay with and without neutrino emission. While the $2\nu\beta\beta$ generates a continuous spectrum from 0 to E_0 , the $0\nu\beta\beta$ appears as a monoenergetic peak at the endpoint. The size of the neutrinoless double β -decay spectrum is figured exaggerated. **Right:** The electron spectrum from a single β -decay. The neutrino mass is visible close to the endpoint by a shift towards lower energies.

CHAPTER 2

The KATRIN Experiment

The objective of the Karlsruhe Tritium Neutrino (KATRIN) experiment is to determine the effective mass of the electron antineutrino in a direct and model-independent measurement. This is achieved by measuring the β -decay spectrum of tritium close to the kinematic endpoint via high-precision spectroscopy. With an aimed sensitivity of $m_{\bar{\nu}_e} < 200$ meV (at 90% C.L.) and a 5σ discovery potential of $m_{\bar{\nu}_e} = 350$ meV KATRIN intends to improve the laboratory limits of previous experiments by one order of magnitude. [10]

This chapter gives a short introduction to the measurement principle in section 2.1 followed by the experimental setup and the main components in section 2.2. Section 2.3 gives a brief overview of the analysis technique and the aimed sensitivity of KATRIN on the neutrino mass.

2.1 The Measurement Principle

As introduced in paragraph 1.5.3 the effective electron antineutrino mass squared

$$m_{\bar{\nu}_e}^2 = \sum_{i=1}^3 |U_{ei}|^2 m_{\nu_i}^2 \quad (2.1)$$

can be determined by analyzing the shape of the tritium β -decay in close vicinity to the kinematic endpoint.

Compared to the two predecessor experiments in Troitsk [8] and Mainz [7], the KATRIN experiment aims to improve the current sensitivity on the neutrino mass of $m_{\bar{\nu}_e} < 2$ eV (at 90% C.L.) by a factor of 10 and probe the sub-eV range. In order to achieve this ambitious goal, the energy of the emitted electrons needs to be determined with a resolution of $\Delta E < 1$ eV. This is achieved by a spectroscopic measurement method called **M**agnetic **A**diabatic **C**ollimation with an **E**lectrostatic filter (MAC-E filter). This principle was first tested in 1980 in [122] and later used in many experiments (for example in [8, 7, 123]). [10] Its concept will be explained in the following.

MAC-E Filter Setup

The principle of a MAC-E filter in the context of the KATRIN and its predecessor experiments has been described in multiple works. Good examples can be found in [124, 125, 126] or the KATRIN design report [10].

In a MAC-E filter, electrons are guided magnetically from their point of generation to their point of detection. The energy is determined in the center of a spectroscope. By applying

a negative electrostatic potential qU_{ret}^1 parallel to the guiding magnetic field lines, only electrons with sufficient energy are able to overcome the potential (high pass filter). [124] Caused by the Lorentz force, the electrons move in cyclotron trajectories. The total kinetic energy of the electrons E_{tot} splits up in a transversal and a longitudinal component

$$E_{\text{tot}} = E_{\perp} + E_{\parallel}. \quad (2.2)$$

The angular between both components is θ . [124]

However, only the longitudinal energy E_{\parallel} can be analyzed by the electrostatic potential. Consequently, the transversal energy E_{\perp} needs to be transformed to longitudinal energy E_{\parallel} before the signal electrons reach the analyzing plane². This is achieved by a process called *Magnetic Adiabatic Collimation* (MAC):

The polar angle of the electron is proportional to the strength of the magnetic field, $\theta \sim B$. By reducing the magnetic field the polar angle and correspondingly the transversal energy E_{\perp} decreases and transforms into longitudinal energy E_{\parallel} . To assure an adiabatic transition, the magnetic field gradient needs to be small within one cyclotron length. Details on adiabatic electron propagation in MAC-E filters can be found in section 4.2. [124]

A MAC-E filter has two characteristic parameters: the maximum acceptance angle θ_{max} and the energy resolution ΔE which are introduced and determined for the KATRIN MAC-E filter in the following.

Maximum Acceptance Angle θ_{max}

If an electron experiences an increasing magnetic field, the polar angle gets steeper until a maximum angle of $\theta = 90^\circ$ is reached and the electron gets magnetically reflected. The ratio of the starting and the maximum magnetic field at a MAC-E filter (pinch magnet) defines a maximum polar angle θ_{max} under which β -electrons can start in the source without being magnetically reflected. The maximum acceptance angle can be calculated as follows:

If the transition is fully adiabatic, the orbital magnetic moment is conserved in first order

$$\mu = \frac{E_{\perp}}{B} = \text{const}, \quad (2.3)$$

which leads to

$$\frac{E_{s,\perp}}{B_s} = \frac{E_{\text{pch},\perp}}{B_{\text{pch}}}, \quad (2.4)$$

with the starting transversal energy $E_{s,\perp}$ and magnetic field B_s as well as the transversal energy $E_{\text{pch},\perp}$ at the pinch magnet B_{pch} . [126]

Replacing the transversal energy by its decomposition of the total energy

$$\frac{E_{s,\text{tot}} \cdot \sin^2 \theta_s}{B_s} = \frac{E_{\text{pch},\text{tot}} \cdot \sin^2 \theta_{\text{pch}}}{B_{\text{pch}}} \quad (2.5)$$

and assuming that the electron gets reflected at the pinch magnet ($\sin^2 \theta_{\text{pch}} = 1$), the maximum acceptance angle can be derived

$$\theta_{\text{max}} = \sin^{-1} \sqrt{\frac{B_s}{B_{\text{pch}}}}. \quad [124] \quad (2.6)$$

¹If not explicitly stated different, the retarding voltage U_{ret} as well as the retarding potential qU_{ret} are expressed as their positive absolute value through out the entire thesis ($|U_{\text{ret}}| = U_{\text{ret}}$, $q|U_{\text{ret}}| = qU_{\text{ret}}$).

²The analyzing plane is usually situated in the center of the spectrometer and is the point where the magnetic field reaches its minimum and the retarding potential its maximum. The ratio of both values defines the energy resolution (see equation (2.8)). [124] In order to reduce the spectrometer background approaches to shift the analysis plane are currently investigated [127].

Electrons with a larger polar angle than θ_{\max} are magnetically reflected at the pinch magnet.

For the KATRIN design values of $B_s = 3.6\text{ T}$ and $B_{\text{pch}} = 6.0\text{ T}$ [128] the maximum acceptance angle is $\theta_{\max} \approx 51^\circ$.

Energy Resolution ΔE

Since the magnetic field at the analyzing plane is non-zero, some of the electron's energy remains in the transversal component $E_{a,\perp}^{\min}$, which leads to the energy resolution of the MAC-E filter

$$\Delta E = E_{a,\perp}^{\min}. \quad [124] \quad (2.7)$$

The minimum transversal kinetic energy at the analyzing plane corresponds to a maximum transversal kinetic energy at the pinch magnet which is the kinematic endpoint of the tritium β -decay $E_0 = 18.575\text{ keV}$. Following equation (2.4), the energy resolution of the KATRIN main spectrometer is given by

$$\Delta E = E_0 \frac{B_a}{B_{\text{pch}}} \approx 0.93\text{ eV}, \quad [124] \quad (2.8)$$

with the nominal magnetic field at the analyzing plane $B_a = 3 \cdot 10^{-4}\text{ T}$ and the maximum magnetic field that is reached at the pinch magnet $B_{\text{pch}} = 6.0\text{ T}$ [128]. Throughout the entire process, the magnetic flux is conserved

$$\Phi = \int_A \vec{B} \cdot d\vec{A} = \text{const}. \quad [124] \quad (2.9)$$

With the design value of the magnetic flux $\Phi = 191\text{ Tcm}^2$, the fluxtube reaches a maximum radius of $r_{\max} = 4.5\text{ m}$ in the small field of the analyzing plane of $B_a = 3 \cdot 10^{-4}\text{ T}$ explaining the dimensions of the KATRIN main spectrometer [10].

2.2 The Experimental Setup

On October 14th, 2016 the first electrons generated at the KATRIN rear wall were successfully transported through the 70 m long beamline to the detector [129, 130]. This milestone was followed by the First Tritium (FT) measurement campaign in May 2018 [131] and the official inauguration on June 11th, 2018. These were the final steps of more than a decade long construction work of KATRIN, which mainly took place at the experimental site at the Karlsruhe Institute of Technology (KIT).

The experimental setup can be divided in four sections: the source, transport, spectrometer and detector section. All experimental components and their working principles are described in the following sections 2.2.1-2.2.4. A graphical overview of the experiment can be seen in figure 2.1.

2.2.1 Tritium Source

KATRIN uses the tritium β -decay to determine the neutrino mass. Tritium has several advantages over other β -emitters. The superallowed transition ${}^3\text{H} \rightarrow {}^3\text{He}$ has a short half-life of only $T_{1/2} = 12.3\text{ yr}$ which assures a high rate of decays for a small amount of source material [132]. With a low nuclear charge of $Z = 1$, the theoretical description of the decay is rather easily, which reduces the systematic uncertainties [133, 134, 135].

In order to make use of all the benefits, the KATRIN source needs to meet several requirements concerning temperature and stability. The source is designed for a working

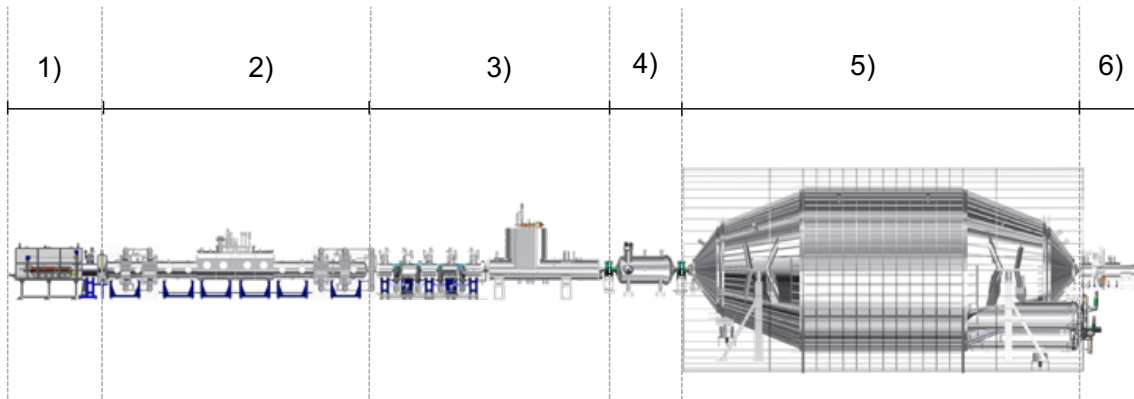


Figure 2.1: Overview of the 70 m long experimental setup of KATRIN. The rear section (1) monitors the decay activity and defines a homogeneous potential of the source (2), where the tritium β -decays takes place. The electrons are guided magnetically through the transport section (3) consisting of a differential and cryogenic pumping unit that removes tritium gas and helium ions. The spectrometer section consists of two components, the pre-spectrometer (4) and the main spectrometer (5) which work as high-pass filters (MAC-E principle). At the focal plane detector (6) the signal electrons that overcome the spectrometer potential are counted. [124] The figure was provided by the engineering department of the IKP at KIT and is adapted from [9].

temperature at 30 K with a stability of 0.1 % reached with a two-phase neon cooling system [136, 11]. A low temperature is favored, in order to minimize the uncertainty caused by the Doppler effect of the moving tritium molecules [11].

Figure 2.2 shows a conceptual overview of the KATRIN tritium loop. The nominal column density of $\rho d = 5 \cdot 10^{17}$ molecules/cm² needs to be stable on the permille level which is achieved first of all by a low and constant inlet pressure of $3 \cdot 10^{-3}$ mbar provided by a pressure controlled buffer vessel [137, 138]. Most of the gas (> 99 %) is pumped out at the WGTS by turbo molecular pumps [139]. To ensure that no impurities arising for example from the turbo molecular pumps reach the WGTS, it is purified by a palladium-silver membrane which is only permeable to hydrogen isotopes [140]. The gas composition is determined via Laser Raman spectroscopy (LARA) [141]. The gas amount which is mainly lost in the transport section is fed back by the *mix* buffer vessel into vessel *B*. The impured gas that is separated at the permeator is sent back to the infrastructure of the Tritium Laboratory Karlsruhe, where the tritium is extracted. The same holds for the pumped out gas from the transport section. [131]

The β -electrons are guided magnetically from the source to the transport section. The required field of up to 3.6 T is provided by three super conducting magnets and a solenoid surrounding the source. Four additional solenoids, two at the back end and two at the front end of the source provide the rear section magnetic field (nominal 3.6 T) as well as the transition field to the transport section with values up to 5.6 T. [128]

The WGTS cryostat has a length of 16 m and a total weight of 26 t [124]. The center piece of the WGTS is the central source tube with a total length of 10 m and a diameter of 90 mm. It is the component where the tritium is injected and the decay of the molecules takes place. [11]

On the back end of the WGTS is the rear section. It consists of the gold-plated rear-wall disc that provides an uniform work function and a constant source potential [142]. The rear section is equipped with a monitoring system that determines the stability of the

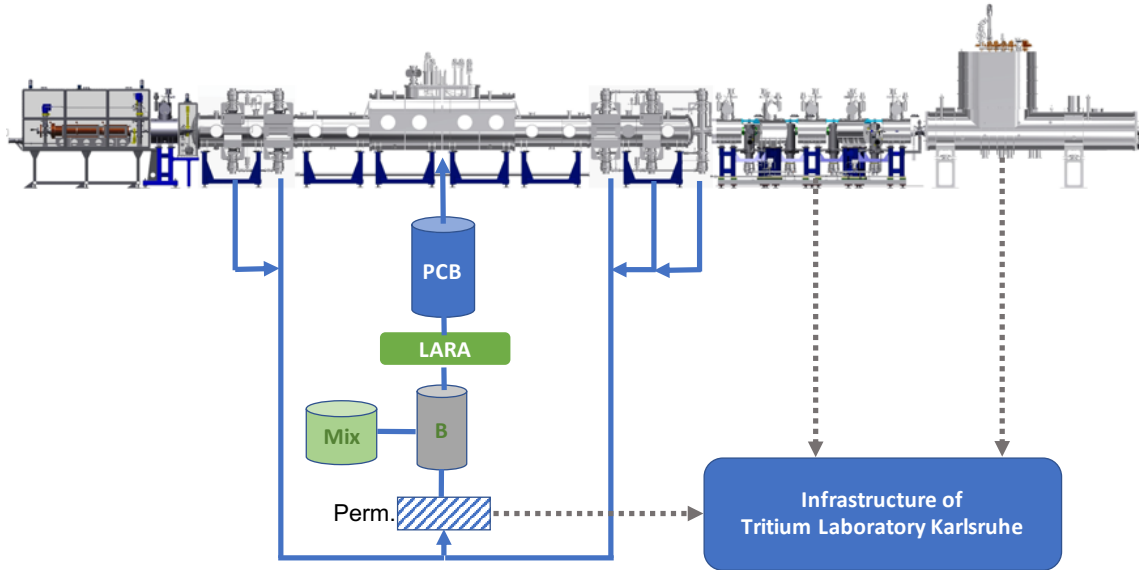


Figure 2.2: A schematic overview of the KATRIN tritium loop as described in the text. The gas is injected to the source by the pressure controlled buffer vessel (PCB). The return gas is purified by a palladium-silver permeator (Perm) and combined with the pre-defined hydrogen gas mixture (Mix). During the entire process, the gas composition is monitored via Laser Raman spectroscopy (LARA). All impure gas is redirected to the facility of the Tritium Laboratory Karlsruhe where it is purified and stored. [131] The figure is adapted from [131].

source activity by measuring the X-ray spectrum generated by source electrons scattering at the gold plate via β -induced X-ray spectroscopy (BIXS) [143, 144]. Another task of the rear section is the angular selective electron gun (e-gun) that provides mono-energetic electrons both for commissioning (for example the energy loss function) and monitoring (for example the column density) measurements [145].

2.2.2 Transport Section

The main tasks of the transport section are to adiabatically guide the electrons from the source to the spectrometers and to reduce the neutral tritium gas flow by at least 14 orders of magnitude on that way, in order to avoid tritium-induced background in the spectrometers. This large suppression is achieved by the combination of a differential (DPS) and cryogenic pumping section (CPS). Furthermore, another device to monitor the source activity is situated at the end of the CPS, the forward beam monitor (FBM). [10] For detailed descriptions of all components the reader is referred to [146, 147].

Differential Pumping Section

While the DPS1-F at the end of the source section already reduces the tritium flow by two orders of magnitude, the main differential pumping is performed at the DPS [148]. It consists of five superconducting solenoids surrounding the beam tubes that are each tilted by 20° . Signal electrons are guided by the up to 5.6 T strong magnetic field through the chicanes, while the heavier neutral tritium molecules scatter with the walls and are pumped out by six TMPs. The DPS reduces the tritium flux by five orders of magnitude [149]. [10]

Positive helium ions that are generated in the β -decay in the source are unaffected by the differential pumping and have the potential to contribute to the background if they reach the spectrometer section [150]. These ions are removed by three dipole electrodes that

cause an $\vec{E} \times \vec{B}$ -drift towards the DPS walls. Since electrons are 10^4 times lighter, they are not affected by the electrodes. For additional ion safety reasons, a ring-shaped blocking electrode with a positive potential of up to +100 V forms the downstream end of the DPS. [151] Details on ion removal can also be found in [152].

Cryogenic Pumping Section

The adjoining CPS reduces the tritium flow by more than seven orders of magnitude [153]. Tritium molecules are adsorbed by an argon frost layer via cryo-sorption. In order to increase the desorption time of the adsorbed neutral tritium, the CPS inner surface is operated at 3 K. Similar to the DPS, the four beam tube elements of the CPS are aligned in 15° tildes. β -Electrons are guided by the magnetic field of superconducting solenoids while the neutral tritium molecules stick to the argon frost. When the argon surface layer is saturated it needs to be replaced and regenerated by removing the tritiated molecules by heating it up. At continuous operation mode, the regeneration needs to be done approximately every 60 days. [154]

Forward Beam Monitor

Another monitoring device is located at the end of the KATRIN transport section. The forward beam monitor (FBM) measures the source activity via a PIN diode³ detector [155, 156, 157]. It is positioned at the outer part of the magnetic fluxtube, which allows to operate it simultaneously during regular measurements without blocking the fluxtube visible by the KATRIN focal plane detector. The FBM is located on a two meter long manipulator that moves it to any position in the fluxtube with a accuracy of 0.1 mm. [158] After an integrated measurement time of 60 s it is able to monitor the β -electron flux with a precision of 0.1% [157].

2.2.3 Spectrometer Section

The spectrometer section consists of two electrostatic filters: the pre- and the main spectrometer. While the pre-spectrometer works as a first filter for electrons with energies up to 18.3 keV (nominal setting) the energy determination of electrons close to the kinematic endpoint region is performed in the main spectrometer. [10]

As described in section 2.1, the high resolution of $\Delta E = 0.93$ eV at 18.6 keV of the KATRIN MAC-E filter requires a magnetic field in the analyzing plane of a few mT. In order to fine shape this small field and to compensate the earth magnetic field, the main spectrometer is surrounded by an air coil system [159].

In the following, all three components of the spectrometer section are introduced, followed by a description of another spectrometer that is used to monitor the retarding voltage setpoint and stability.

Pre-Spectrometer

The pre-spectrometer has a length of 3.4 m and a maximum diameter of 1.7 m. It can be operated as a high-pass energy filter with a nominal potential barrier of $U_{\text{ret}} = 18.3$ kV. To avoid ionization in the sensitive area of the main spectrometer, the pre-spectrometer works as a pre-filter and reduces the overall electron flux by up to seven orders of magnitude. [10] Studies showed that if it is operated at too high potential a Penning trap can

³The PIN (positive intrinsic negative) diode has recently been replaced by a seven pixel silicon drift detector (a prototype of the TRISTAN detector [17]).

be formed between the electric potentials of the pre- and the main spectrometer storing electrons that are generated between both potentials [160]. The electrons accumulated in this trap can lead to sudden discharges that increase the background and endanger the detector system [160]. By assuring an ultra-high vacuum and lowering the retarding potential of the pre-filter by a few keV, the trap can be reduced and its contribution to the background is neglectable [161]. As a supplement, a penning wiper system is installed [162].

Electrons are guided by the two pre-spectrometer magnets, generating a maximum magnetic field of 4.5 T [128]. At the center of the spectrometer the field drops to a minimal value of $2 \cdot 10^{-2}$ T which corresponds to an energy resolution of $\Delta E \approx 70$ eV following equation (2.7) [10].

Main Spectrometer

The magnetic flux conservation in combination with the precise energy resolution of the KATRIN main spectrometer, result in the large dimensions of this most prominent component of the KATRIN experiment. With a total length of 23.3 m and a diameter of 10 m the main spectrometer pushes the MAC-E filter technique to the limit of feasibility. [10] The main contribution to the magnetic field is generated by the second magnet of the pre-spectrometer (4.5 T) and the strongest magnet of the KATRIN setup located at the exit of the main spectrometer - the pinch magnet (6 T) [128].

Because of its large volume and functionality, the main spectrometer has the highest vulnerability to background causing processes of the entire beamline. To avoid and reduce background generation it is equipped with several tools. A two layer electrode system with more than 24 000 wires serve as a shield for muon-induced background, generated at the walls of the vessel. By operating the wires at a nominal offset of $U_{\text{offset}} = -200$ V, the electrons that are generated at the spectrometer walls by muon ionization are reflected back to their point of generation. [163, 164, 165, 166]

In order to reduce the background caused by ionization of residual gas inside the spectrometer volume, the main spectrometer is operated at an ultra high vacuum below 10^{-10} mbar [167]. This is achieved by six cascade TMPs and three getter pumps performing at a combined pumping speed of 10^6 ℓ /s and regular bake-out phases [167].

Air Coil System

As described in section 2.1, the MAC-E filter requires a magnetic field of only $3 \cdot 10^{-4}$ T at the center of the main spectrometer. The fine-shaping of this field is realized by an air coil system (**Low-Field Coil System**, LFCS) consisting of 14 coils surrounding the main spectrometer. With values of approximately 10^{-6} T the Earth's magnetic field contributes significantly to the fine-shaping of the small field as well. 16 vertical and 10 horizontal cosine coils form the **Earth Magnetic Compensation System** (EMCS). [159]

The LFCS system has recently been upgraded. Details on the upgrade can be found in section 7.2.

Monitor Spectrometer

The retarding potential of the main spectrometer is applied by a high-precision voltage divider [168]. To monitor the stability, a third spectrometer is directly connected to the main spectrometer high voltage [169]. It is also used in a MAC-E filter setup. The former spectrometer of the Mainz neutrino mass experiment scans the mono-energetic spectrum

of ^{83}Kr with a precision on the ppm level and is therefore sensitive to subtle drifts of the main spectrometer potential. [10] For details the reader is referred to [170, 171, 172].

2.2.4 Focal Plane Detector

Electrons that pass the main spectrometer potential are focused via re-acceleration and detected by the focal plane detector (FPD). The detector wafer with a radius of 4.5 cm consists of a monolithic PIN diode and is segmented in 148 pixels, all of equal surface area. The detector wafer is surrounded by the detector magnet, which is usually operated at a field strength of 3.6 T [128]. The segmentation allows for an event-wise exact field line reconstruction by the detector. [173]

A custom-designed read-out system connects the detector with the data acquisition system of KATRIN. In order to reduce the noise level, the preamplifiers are directly mounted inside an ultra-high vacuum system. To shield the detector from γ background it is surrounded by 3 cm thick cylindrical lead shells. Incoming muons are tagged by a veto system. [174]

In KATRIN, the energy resolution is determined by the main spectrometer configuration and the FPD only counts electrons. However, the detector has a designed energy resolution of $\Delta E \sim 1.6 \text{ keV}$ which is necessary for detector noise and pile-up discrimination in the analysis [175].

Before the electrons hit the detector surface, they are accelerated by the $U_{\text{PAE}} = +10 \text{ keV}$ post-acceleration electrode (PAE). The increased incident energy helps to discriminate the signal from detector background at lower energies, caused by intrinsic γ -background. [174] By accelerating the electrons, the longitudinal energy increases which respectively declines the impact angle and the uncertainty caused by electrons scattering back on the detector surface [173] (for a detailed discussion of electron backscattering at the detector see section 5.6.1).

The detector section is equipped with two calibration sources providing γ -radiation and photoelectrons [174].

2.3 Sensitivity on the Neutrino Mass

In order to determine the neutrino mass from the measured data, the measurement needs to be compared to a predicted tritium β -decay spectrum. Systematic effects influence the shape of the spectrum and need to be modeled in a response function. In the following, $R(E, qU_{\text{ret}})$ is a general expression to connect the theoretical spectrum with the predicted spectrum that is compared with the observed data. [10] Details on response function modeling can be found for example in section 5.3.

The upcoming derivation follows mainly [124] section 2.3 which apparently has been adapted from [10] section 11.6.

The KATRIN experiment measures the integrated tritium β -decay spectrum by measuring the signal electron count rates N_s at the detector for different retarding potentials qU_{ret}

$$N_s(qU_{\text{ret}}, E_0, m_{\nu_e}^2) = N_T \cdot t_{qU_{\text{ret}}} \int_{qU_{\text{ret}}}^{E_0} \frac{dN}{dE}(E_0, m_{\nu_e}^2) \cdot R(E, qU_{\text{ret}}) dE, \quad (2.10)$$

with N_T the number of tritium molecules in the source, $t_{qU_{\text{ret}}}$ the measurement time spent at each retarding potential, and $\frac{dN}{dE}(E_0, m_{\nu_e}^2)$ the differential tritium β -decay spectrum [124].

In order to get the predicted count rate at the detector, a constant, energy-independent and Poisson distributed⁴ background is added

$$N_{\text{pred}}(R_s, R_{\text{bkg}}, qU_{\text{ret}}, E_0, m_{\bar{\nu}_e}^2) = R_s \cdot N_s(qU_{\text{ret}}, E_0, m_{\bar{\nu}_e}^2) + R_{\text{bkg}} \cdot N_{\text{bkg}}, \quad (2.11)$$

with the amplitudes of the signal and background rates R_s and R_{bkg} [124]. This predicted spectrum is now fit to a measured spectrum $N_{\text{meas}}(qU_{\text{ret},i})$ by minimizing the χ^2 function

$$\chi^2(R_s, R_{\text{bkg}}, E_0, m_{\bar{\nu}_e}^2) = \sum_i \left(\frac{N_{\text{meas}}(qU_{\text{ret},i}) - N_{\text{pred}}(R_s, R_{\text{bkg}}, qU_{\text{ret},i}, E_0, m_{\bar{\nu}_e}^2)}{\sqrt{N_s + N_{\text{bkg}}}} \right)^2. \quad (2.12)$$

The signal and background related amplitudes R_s and R_{bkg} as well as the endpoint energy E_0 and the effective neutrino mass squared $m_{\bar{\nu}_e}^2$ are free fit parameters and are result of the minimization process. [124]

With the design parameters of KATRIN and a cumulated measurement time of 3 years, a statistical uncertainty of

$$\sigma_{\text{stat}} = 0.018 \text{ eV}^2 \quad (2.13)$$

is reached [124].

Due to the complex setup and the challenging measurement technique there are a number of systematic uncertainties that have to be taken into account for a proposition of an experimental sensitivity. The KATRIN design report [10] lists most of them and derives a systematic uncertainty budget of

$$\sigma_{\text{sys}} = 0.017 \text{ eV}^2. \quad (2.14)$$

Adding both uncertainties leads to the total uncertainty of

$$\sigma_{\text{tot}} = \sqrt{\sigma_{\text{stat}}^2 + \sigma_{\text{sys}}^2} = 0.025 \text{ eV}^2 \text{ [124]}. \quad (2.15)$$

Taking into account this budget, KATRIN has a 5σ discovery potential for a neutrino mass of $m_{\bar{\nu}_e} = 350 \text{ meV}$ or an upper limit on the mass of $m_{\bar{\nu}_e} < 200 \text{ meV}$ at a 90% confidence level [10].

⁴As recent studies imply, there is a significant non-Poissonian contribution to the background [176] as well as a slight dependence on the retarding potential [177]. Both effect are considered in the analysis but for the sake of simplicity are not included here.

CHAPTER 3

Sterile Neutrinos on the keV Mass Scale

Right-handed neutrinos are a minimal and well-motivated extension of the *Standard Model of Particle Physics* (SM) in order to introduce masses for active neutrinos. They are not charged under any SM gauge symmetry therefore they only interact gravitationally. This property could make sterile neutrinos a pivotal particle in cosmology, concerning the unknown nature of Dark Matter. As shown in section 1.4.3, the mass scale of sterile neutrinos is arbitrary. [13] This thesis focuses on the search for sterile neutrinos on the keV-scale which would be observable in the tritium β -decay measured by the KATRIN experiment. KATRIN is equipped with one of the strongest tritium sources for scientific use [10]. This feature, among others, makes the KATRIN experiment also expandable for investigations of other physical parameters and phenomena beside the effective electron antineutrino mass $m_{\bar{\nu}_e}$. Several studies have shown that KATRIN has the potential to reach high-statistical sensitivity to search for keV-scale sterile neutrinos [178, 16, 12].

This chapter presents a general motivation for keV-scale sterile neutrinos from a particle physics (section 3.1.1) and cosmological (section 3.1.2) point of view. The constraints on the sterile neutrino parameter space linked to cosmological (section 3.2) or laboratory observations (section 3.3) are discussed. Section 3.4 focuses on the laboratory search for keV-scale sterile neutrinos via β -decay experiments, in particular the KATRIN experiment. Two different measurement programs are discussed, one that requires major hardware modifications and another that uses KATRIN with only minor adjustments.

3.1 Motivation for keV-scale Sterile Neutrinos

The SM is an extensively tested theory for describing the particle content of our Universe and the underlying fundamental interactions (with the exception of gravity). Among others, it has two major ambiguities: the non-zero mass of the neutrinos and the absence of a Dark Matter candidate. [34] One possible extension that has the potential to solve both problems is called the *Neutrino Minimal Standard Model* (ν MSM). It was first formulated in 2005 by Mikhail Shaposhnikov and Takehiko Asaka [179]. The ν MSM introduces three right-handed neutrinos to the SM: Two heavy sterile neutrinos on the electroweak scale (\sim GeV) and one keV-scale sterile neutrino. The introduction of the ν MSM is mainly built on two arguments:

1. The masses of the two heavy sterile neutrinos are chosen in a way to coincide with the observed mass splittings of the active SM neutrinos via a minimal-type-I seesaw mechanism and to explain baryon asymmetry (see section 1.4.2).

2. The keV-scale sterile neutrino acts as a candidate for Warm Dark Matter (WDM). [179]

The following subsections 3.1.1 and 3.1.2 discuss these two arguments in detail and underline the importance of a model-independent laboratory experiment to search for sterile neutrinos on the keV mass scale. A detailed introduction of the ν MSM can be found in [179].

3.1.1 From Particle Physics

The discovery and study of neutrino oscillations requires the SM neutrinos to have a non-vanishing mass (see section 1.3) [34]. The most consistent way to introduce neutrino masses to the SM is the seesaw mechanism type-I (section 1.4.2) which explains the mass generation without unnatural small Yukawa couplings (derived in equation (1.31)) [13]. All of the seesaw models require right-handed neutrinos which do not participate within the SM interactions, however, do mix with the active neutrinos [84].

The ν MSM includes three sterile neutrinos so that the number of right-handed neutrinos is equal to the number of fermionic generations [179]. A graphical overview of the ν MSM is displayed in figure 3.1. In the ν MSM, the SM Lagrangian is extended by

$$\delta\mathcal{L} = i\bar{\nu}_R \not{\partial} \nu_R - \bar{\ell}_L F \nu_R \tilde{\Phi} - \tilde{\Phi}^\dagger \bar{\nu}_R F^\dagger \ell_L - \frac{1}{2} \left(\bar{\nu}_R^C M_M \nu_R + \bar{\nu}_R M_M^\dagger \nu_R^C \right), \quad (3.1)$$

with the newly introduced right-handed neutrino ν_R , the left-handed SM lepton doublet $\ell_L = (\nu_L, e_L)^\top$, the Higgs doublet Φ (with $\tilde{\Phi} = i\sigma_2 \cdot \Phi^*$), and the Yukawa interaction matrix F . [13]

The formulation of ν_R as a singlet allows the Majorana mass term with M_M . Beside the three additional Majorana masses, the model adds three Yukawa couplings, six mixing angles, and CP-violating phases respectively. By choosing the three Majorana masses to be

$$\begin{aligned} M_1 &\sim \mathcal{O}(\text{keV}), \\ M_{2,3} &> 1 \text{ GeV}, \end{aligned} \quad (3.2)$$

the active neutrino masses can be fixed to

$$\begin{aligned} m_1 &\sim \mathcal{O}(10^{-5} \text{ eV}), \\ m_2 &= (9.05_{-0.1}^{+0.2}) \cdot 10^{-3} \text{ eV}, \\ m_3 &= (4.8_{-0.5}^{+0.6}) \cdot 10^{-2} \text{ eV}, \end{aligned} \quad (3.3)$$

assuming the normal mass hierarchy. This does not only provide a keV-scale sterile neutrino with a lifetime long enough to serve as a Dark Matter particle (due to a small Yukawa coupling) but explains baryon asymmetry of the Universe and is consistent with neutrino oscillation experiments¹. [14, 179]

3.1.2 From Cosmology

The Λ CDM model parameterises the Big Bang cosmological model, assuming an expanding Universe (with Λ being the cosmological constant) caused by Dark Energy [46]. It includes non-relativistic Cold Dark Matter (CDM) with small free-streaming lengths [46]. Due to

¹The ν MSM can also be used to explain the origin of the baryon asymmetry, which is another fundamental open question in cosmology and particle physics. The GeV-scale sterile neutrinos decay out-of-equilibrium (third Sakharov condition) and generate a sizable lepton asymmetry. [179] During the early phase of the Universe, shortly after the electroweak symmetry breaking, the lepton asymmetry can be converted into a baryon asymmetry via sphaleron transition [105].

	I	II	III		
mass	2.16 MeV/c ²	1.27 GeV/c ²	172.9 GeV/c ²	0	125.10 GeV/c ²
charge	$\frac{2}{3}$	$\frac{2}{3}$	$\frac{2}{3}$	0	0
spin	$\frac{1}{2}$	$\frac{1}{2}$	$\frac{1}{2}$	1	0
	u	c	t	g	H
	left right	left right	left right		
	d	s	b	γ	
quarks	left right	left right	left right		
	4.67 MeV/c ²	93 MeV/c ²	4.18 GeV/c ²	0	
	$-\frac{1}{3}$	$-\frac{1}{3}$	$-\frac{1}{3}$	0	
	$\frac{1}{2}$	$\frac{1}{2}$	$\frac{1}{2}$	1	
	e	μ	τ	Z	
	left right	left right	left right		
	0.51 MeV/c ²	105.66 MeV/c ²	1.78 GeV/c ²	91.19 GeV/c ²	
	-1	-1	-1	0	
	$\frac{1}{2}$	$\frac{1}{2}$	$\frac{1}{2}$	1	
	ν_e	ν_μ	ν_τ	W	
leptons	left right	left right	left right		
	$< 1.1 \text{ eV}/c^2$	$< 0.19 \text{ MeV}/c^2$	$< 18.2 \text{ MeV}/c^2$	80.38 GeV/c ²	
	0	0	0	± 1	
	$\frac{1}{2}$	$\frac{1}{2}$	$\frac{1}{2}$	1	
	N_1	N_2	N_3		
	left right	left right	left right		

scalar bosons

gauge bosons

Figure 3.1: The ν MSM extends the leptonic sector of the SM by three right-handed sterile neutrinos. The sterile neutrinos have almost the same quantum mechanical properties as their active partners. However, due to the zero isospin, they do not interact weakly. The figure is adapted from [47] figure 2.6. with values from [9] and [48].

its consistency with observations (for example the *Cosmic Microwave Background* [33]) and the simple formulation with only six free parameters, it is frequently referred to as the *Standard Model of Cosmology* for example in [13, 108]. Physics beyond the SM provide CDM candidates, the most prominent is the lightest supersymmetric particle [180].

While the Λ CDM model accounts for a number of observations on the large scale structure of the Universe, from a few Gpc (scale of CMB) down to a few Mpc (galaxy clusters), it fails to explain small-scale structures in the sub-Mpc range. In recent years, an alternative Dark Matters candidate was proposed, helping to solve the small-scale Λ CDM tensions: A so-called Warm Dark Matter (WDM) particle would be ultra-relativistic at the time of decoupling with typical free-streaming lengths of $\lambda_{\text{fs}} < 0.1$ Mpc. On a large scale, WDM models produce very similar structures and are indistinguishable from CDM, however, on a small scale, the WDM properties improve the sub-Mpc structure formation to favor observations. Sterile neutrinos in the keV-mass range are plausible WDM candidates. [13] A model such as the ν MSM provides a sterile neutrino that would be in the correct mass range and behave as WDM [179].

In the following paragraphs, the three main small-scale tensions of the Λ CDM model are presented. Several solutions are discussed with the focus on keV-scale sterile neutrino WDM. The ideas presented in this discussions are mainly based on [13] pages 48-59 where further information and references can be found.

Missing Dwarf Galaxies Problem

The *missing dwarf galaxy problem*, which is also called *missing satellite problem*, arises from Λ CDM N-body simulations (excluding baryons and DM self-interactions) [181]. Due to the small free-streaming lengths of $\lambda_{\text{fs}} < 0.1$ pc, CDM starts to cluster on small scales in a bottom-up scenario [46]. For scales larger than galaxy clusters (> 1 Mpc) the Λ CDM simulations fit the observations, however, the simulated number of dwarf galaxies is one

order of magnitude higher than observed [181]. While there are 59 confirmed dwarf galaxies² that are gravitational bound to the Milky Way, simulations predict up to 500 satellite galaxies [192]. [13]

There are two well studied approaches to solve the problem, which in turn cause further issues themselves. The first one predicts a large number of small but low-luminosity DM halos that have not attracted enough baryonic matter to create a visible dwarf galaxy [181]. With masses of $M \lesssim 5 \cdot 10^9 M_\odot$ those invisible DM halos are in the mass range of dwarf galaxies and could explain the non-observable abundance of satellite galaxies in the Λ CDM model. The discovery of eight ultra-faint satellite galaxies in 2007 by the Keck-observatory supports this hypothesis [193]. However, these small-scale DM halos would require cusp-like density profiles (steeply increasing density for small radii), which contradict observations (see next paragraph *cusp-core problem*) [194]. [13]

Baryonic feedback is another possibility to explain the missing dwarf galaxies [195]. Different baryon-involved cosmological processes can alter the gravitational potential on small-scale structure and cause an adiabatic contraction of DM halos [195]. Outflow processes (for example supernovae) rip the baryon cluster apart. Both processes could cause a heating of the DM which results in a washout of the small structures. However, at higher redshifts the densities of galaxies and respectively their escape velocity increase, which make the feedback processes inefficient. [13]

The existence of WDM would naturally solve the *missing dwarf galaxy problem*. The free streaming length scales with the mass of the DM particle and is directly linked to its wash-out scale in the early Universe. [13]

Cusp-Core Problem

Besides a large number of dwarf galaxies, Λ CDM simulations predict inner density profiles of DM halos with power-law shape $\rho \sim r^{-\alpha}$ with $\alpha \approx 1$ [196]. Those cusp-density profiles are a result of non-baryonic, collisionless Λ CDM N-body simulations, first published by J. Navarro, C. Frenk and S. White (so called NFW-Profiles) [196], and are consistent with recent, higher resolution simulations, for example as shown in reference [197]. [13]

There have been many efforts of measuring the DM profiles: Typical research objects are dwarf galaxies due to their abundance of neutral hydrogen, since the gas profiles provide direct information on the DM distribution. However, studies from 2011 using data of THINGS³ observe core-like inner density profiles with $\alpha = 0.29 \pm 0.07$ [194]. The core-like profiles are also confirmed by studies of dwarf spheroidal (dSph) [198] and low surface brightness galaxies (LSB) [199, 200, 201]. Baryonic feedback, including star formation and supernova-driven outflows, is one way to explain the washing out of cusp inner density profiles resulting in core-like distributions that fit the measurements. However, the large radii and simultaneous low baryonic matter density of LSB galaxies are naturally resistant to any feedback mechanism, as star formation is inefficient with low gas densities. Additionally, supernova wind outflows in low densities cannot provide the baryonic feedback effect as required to redistribute the DM profile significantly. Even if baryonic feedback is able to explain the core-like profiles of dwarf galaxies, no sufficient approach to explain the erase of cusps in LSB galaxies have been found yet [202]. [13]

Sterile neutrino WDM on the keV-scale would automatically provide core-like profiles due to a finite phase space density that does not allow for an accumulation of the DM particles in a small volume over time [13, 203] (see also section 3.2).

²The references for the dwarf galaxy observations are [182, 183, 184, 185, 186, 187, 188, 189, 190, 191].

³The **HI** **N**earby **G**alaxy **S**urvey, a measurement performed at the very large array of the National Radio Astronomy Observatory in New Mexico, U.S. [194].

Too-Big-To-Fail Problem

The *too-big-to-fail* (TBTF) problem is a combination of the *missing dwarf galaxy* and the *cuspy-core problem*. It describes the problem that the amount of satellite galaxies cannot be conciliated with their inner kinematics. In order to describe the observed numbers of satellite galaxies, they need to be hosted in very large DM halos, which would show different kinematics as measured. Observations of the kinematics of Milky Way (MW) satellite populations lead to the first observation of the TBTF problem [204, 205]. Later, other galaxies such as M31 Andromeda [206] confirmed the problem. Studies based on SDSS⁴ data showed that the Milky Way satellite populations are representative of galaxies of this size, suggesting that the TBTF problem is likely to be observed in many other MW-like galaxies [207]. [13]

One approach to solve the TBTF problem is a mechanism called tidal stripping, which is closely related to the baryonic feedback explained above [208]. This mechanism uses hydrodynamic simulations and combines stellar feedback with tidal effects caused, for example, by supernova shock waves, to strip apart the cusp density profiles and small DM halos. However, these processes only show agreement with satellite dwarf galaxies and not with isolated ones [209, 210, 211]. [13]

Similar to the missing galaxy and cuspy-core problem, WDM has been regarded as a promising solution to the TBTF problem. A typical WDM power spectrum suppresses the formation of small-scale structures while simultaneously providing the correct kinematics. [13]

3.2 Cosmological constraints on the Sterile Neutrino Parameters m_{ν_s} and $\sin^2 \theta$

Cosmological observations provide bounds on the sterile neutrino parameter space. Most of them are model-dependent and depend, for example, on the production mechanism⁵. The following paragraphs list the most important constraints, that either limit only the sterile neutrino mass (phase space density and Lyman- α forest observations) or both parameters (x-ray observations).

An overview of the cosmological limits are displayed in figure 3.2. The ideas presented in the discussions are mainly based on [13] pages 39-42 and 64-80 where further information and references can be found.

Maximal Phase Space Density of Fermions

If Dark Matter would be made of sterile neutrinos, two general constraints on the sterile neutrino parameters appear: 1. the mean lifetime of the particle must be greater than the age of the Universe and 2. the particle temperature and compactness must be small enough to allow an accumulation on the galactic scale of sub-Mpc [13]. The latter argument leads to a constraint on the sterile neutrino mass. It is valid for all possible fermionic Dark Matter. The derivation is taken from [13] equation (4.1) et. seq.

⁴Sloan Digital Sky Survey, a large dimensioned spectroscopic redshift survey [207].

⁵A distinction is mainly made between two production mechanisms: 1. The sterile neutrinos are generated in the early Universe analogous to the active SM neutrinos. This scenario requires an early decoupling and subsequent dilution to match the present DM density; 2. No sterile neutrinos exist in the early Universe and they have to be generated thermally by mixing with the active SM neutrinos [13]. The second scenario requires the seesaw mechanism as it is used in the ν MSSM and therefore is the favored scenario in the framework of keV-scale sterile neutrinos [179].

In good approximation, the galactic velocity distribution of Dark Matter with mass m_{DM} can be described by a Maxwell distribution

$$F_{\text{DM}}(\vec{v}) = \frac{1}{(\sqrt{2\pi}m_{\text{DM}}\sigma(\vec{x}))^3} \cdot \exp\left(-\frac{\vec{v}^2}{2\sigma^2(\vec{x})}\right), \quad (3.4)$$

with the position-dependent velocity dispersion $\sigma(\vec{x})$ and the velocity \vec{v} . Since sterile neutrinos are fermions the *Pauli Principle* forbids the maximum of the phase space density

$$F_{\text{DM}}^{\text{max}}(\vec{v}, \vec{x}) = \frac{\rho(\vec{x})}{m_{\text{DM}}} F_{\text{DM}}(\vec{v} = 0), \quad (3.5)$$

to be greater than the critical value

$$F_{\text{DM}}^{\text{crit}} = \frac{g_{\text{DM}}}{(2\pi)^3}, \quad (3.6)$$

where g_{DM} is the number of intrinsic degrees of freedom, which equals 2 in the case of a sterile neutrino, and $\rho(\vec{x})$ is the Dark Matter mass density. [13]

Deriving the equation

$$F_{\text{DM}}^{\text{max}}(\vec{v}) \leq F_{\text{DM}}^{\text{crit}}, \quad (3.7)$$

the lower mass limit is

$$\frac{(2\pi)^{3/8}}{g_{\text{DM}}^{1/4}} \left(\frac{\rho(\vec{x})}{\sigma(\vec{x})}\right)^{1/4} \leq m_{\text{DM}}. \quad (3.8)$$

For sterile neutrino Dark Matter this limits the lower mass bound to $m_{\nu_s} \gtrsim 1$ keV. [13] Depending on the studied object, the value can vary between $m_{\nu_s} \gtrsim (0.41 - 2.79)$ keV [212]. This limit is also known as the Tremaine-Gunn bound named after the mechanism derived in [213].

Lyman- α Forest Observations

Another lower bound on the sterile neutrino Dark Matter mass arises from Lyman- α forest observations. The Lyman- α forest is a series of absorption lines caused by Lyman- α hydrogen transitions ($n = 1 \longleftrightarrow n = 2$) [214]. The spectra from far away objects, such as quasars, are absorbed and shifted by interactions with the intergalactic medium at different redshifts, causing a typical spectrum with multiple Lyman- α absorption lines [214, 215, 216]. Observations of the spectra and comparison to N-body simulations or semi-analytical calculations lead to conclusions about the free streaming length of Dark Matter particles λ_{fs} depending on the mass (and temperature) of the Dark Matter particle [13]. However, the resulting mass limit strongly depends on the composition of the Dark Matter (mixing ratio of WDM and CDM particles for example) and the production mechanism and leading to a lower mass limit of $m_{\nu_s} \gtrsim (0.75 - 14)$ keV [217, 218].

Non-Observation of Sterile Neutrino Decays

An upper limit on the sterile neutrino mass and mixing can be obtained by a discussion of its decays to active neutrinos. A keV-scale sterile neutrino can decay via Z-exchange to three active neutrinos $\nu_s \rightarrow \nu_\alpha + \nu_\beta + \bar{\nu}_\beta$, where α and β are arbitrary lepton flavors. This is possible since the leptonic weak neutral current is non-diagonal in mass eigenstates if a sterile neutrino is added to the leptonic sector. The decay width is given by

$$\Gamma_{\nu_s \rightarrow \nu_\alpha + \nu_\beta + \bar{\nu}_\beta} = \frac{1}{4.7 \cdot 10^{10} \text{ s}} \left(\frac{m_{\nu_s}}{50 \text{ keV}}\right)^5 \sin^2 \theta. \quad [13, 219, 220] \quad (3.9)$$

The maximum mixing angle is

$$\sin^2 \theta < 1.1 \cdot 10^{-7} \left(\frac{50 \text{ keV}}{m_{\nu_s}} \right)^5, \quad (3.10)$$

assuming that mean lifetime of the sterile neutrino is greater than the age of the Universe [13].

A second decay channel is the one-loop mediated radiative decay $\nu_s \rightarrow \gamma + \nu_\alpha$. This decay would lead to a monochromatic x-ray line-spectrum which allows an observation. The total decay width is

$$\Gamma_{\nu_s \rightarrow \gamma + \nu_\alpha} = \frac{1}{8.3 \cdot 10^{20} \text{ s}} \left(\frac{m_{\nu_s}}{50 \text{ keV}} \right)^5 \sin^2 \theta, \quad (3.11)$$

and shows a strong suppression compared to the decay width displayed in equation (3.9), which makes a detection demanding even in Dark Matter dominated objects. [13, 221] The non-observation of a contribution of the radiative decay to the diffuse x-ray background sets a lower limit on the mixing parameter depending on the present sterile neutrino Dark Matter density Ω_s

$$\sin^2 \theta < 6.5 \cdot 10^{-5} \left(\frac{50 \text{ keV}}{m_{\nu_s}} \right)^5 \Omega_s^{-1} [13]. \quad (3.12)$$

The 3.5 keV X-Ray Line

Recent *XMM-Newton* measurements claimed to identify a $E_\gamma \approx 3.5 \text{ keV}$ x-ray line from stacked spectra of galaxy clusters [103], the Andromeda galaxy [104], and the Galactic center region [222]. The signal, with a statistical significance of up to $\sim 4\sigma$, hints at a possible decay of a sterile neutrino with $m_{\nu_s} \approx 7.1 \text{ keV}$ and a active-to-sterile mixing amplitude of $\sin^2 \theta \approx 7 \cdot 10^{-11}$ [104]. However, other studies explain the observed signal via different atomic plasma lines [223] or incomplete underlying background models [224]. Some exclude the line with a significance of $> 5\sigma$ [225]. [13]

The 2016 launched x-ray observation satellite *Htnomi* (also known as *ASTRO-H*) had the potential to bring further progress to this topic [226]. Due to a technical problem, the satellite lost contact to the ground station during the commissioning phase and was probably destroyed by entering the Earth's atmosphere three months after its launch [227].

3.3 Laboratory Search for keV-scale Sterile Neutrinos

There are several approaches to detect sterile neutrinos in model-independent laboratory experiments. Analogous to other Dark Matter direct searches (for example WIMP searches), the relic sterile neutrino background could be measured directly via scattering or capturing processes using existing Dark Matter experiments such as XENON [229]. [13]

Another way is to produce the particle directly in the laboratory and detect it indirectly via decay kinematics [12]. The latter approach is historically more probed and is part of recent experiments, for example via tritium β -decay (KATRIN [12]) or electron capturing of holmium (EHC0 [230]).

Both methods are presented in the following section.

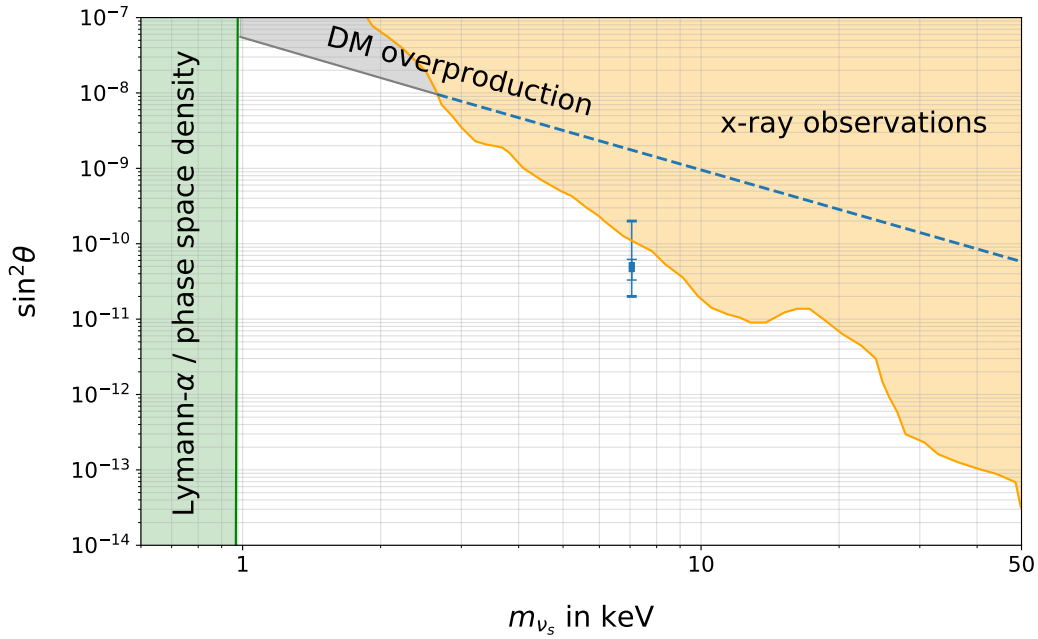


Figure 3.2: Limits on the active-to-sterile mixing $\sin^2 \theta$ and sterile neutrino mass m_{ν_s} gained by cosmological investigations. The non-observation of a sterile neutrino signal in Lyman- α forest surveys of quasars as well as the maximum fermionic phase space density, leads to a lower mass limit of $m_{\nu_s} \gtrsim 1$ keV (green area). Another bound is given by the absence of a sterile neutrino decay signal that would be visible as an x-ray line (orange area). The blue data point marks a possible measurement of a 7.1 keV sterile neutrino, which was not confirmed by other measurements (the data point and the uncertainties are taken from [104]). If the sterile neutrino would be produced thermally by coherent scattering of active neutrinos at primeval plasma, another limit on the mass and mixing can be introduced (gray line and area) [228]. The data was extracted from figure 19 in [13] where further references are stated.

Direct Search for relic Sterile Neutrinos

A direct detection of relic sterile neutrinos in a laboratory experiment is possible via elastic scattering

$$\nu_s \xrightarrow{\sin^2 \theta} \nu_a + e^- \rightarrow \nu_a + e^-, \quad (3.13)$$

or inverse β -decay

$$\nu_s \xrightarrow{\sin^2 \theta} \nu_a + N(A, Z) \rightarrow N'(A, Z \mp 1) + e^\pm, \quad (3.14)$$

where a sterile neutrino mixes with the amplitude $\sin^2 \theta$ with an active neutrino that scatters with an electron or is captured by a β -decaying nucleus. Elastic scattering could be observed in the electron spectrum with a signal that corresponds to an electron with a momentum $p_e \approx m_{\nu_s}$. The inverse β -decay would imprint as a monoenergetic peak in the spectrum with a distance $\Delta E_e \approx m_{\nu_s}$ above the endpoint E_0 . [13]

Both interactions are leading order processes, however, are strongly suppressed by the active-to-sterile mixing amplitude [13].

If all of the local Dark Matter density of $\rho_{\text{DM}} = 0.3 \text{ GeV cm}^{-3}$ correspond to sterile neutrinos, the expected signal rate for the elastic scattering on a 1 t xenon target would be

$$\Gamma_{\text{ES}} \simeq 0.5 \text{ yr}^{-1} \left(\frac{\sin^2 \theta}{10^{-6}} \right) \left(\frac{m_{\nu_s}}{10 \text{ keV}} \right) \left(\frac{M}{10^3 \text{ kg}} \right), \quad (3.15)$$

and the capture rate of relic sterile neutrinos via inverse β -decay with tritium would be

$$\Gamma_{\beta^{-1}} \simeq 0.3 \text{ yr}^{-1} \left(\frac{\sin^2 \theta}{10^{-6}} \right) \left(\frac{m_{\nu_s}}{10 \text{ keV}} \right)^{-1} \left(\frac{M}{10^3 \text{ kg}} \right), \quad (3.16)$$

assuming 10 kg target material, which corresponds to the majority of the worldwide tritium supply. Beside the small rates, both experiments would have to handle several experimental challenges, for example a precise modeling of the background. [13]

Search for Sterile Neutrinos in Decay Kinematics

In 1980, years before finding evidence for neutrino oscillation and a non-vanishing neutrino mass, R. Shrock proposed the possibility of searching for neutrino mass states m_i in β -decay spectra [231]. Each mass state would be visible as a kink signature at $E_0 - m_i$, with the height of the discontinuity being directly proportional to the mixing amplitude $|U_{ei}|^2$. The idea was employed by several experiments, attempting to find heavy sterile and active neutrino states. [232] The following description focuses only on the study of sterile mass eigenstates:

The first experiment used a magnetic spectrometer to study the β^+ and β^- -decays of ^{64}Cu and set a limit of $|U_{e4}|^2 < 8 \cdot 10^{-3}$ for a mass range of $110 \text{ keV} < m_4 < 450 \text{ keV}$ [233]. In 1985, the group of J. Simpson observed a signal in the tritium β -decay spectrum, corresponding to a heavy neutrino mass of $m_4 \approx 17.1 \text{ keV}$ with a mixing probability of 3% [234]. The surprising result was soon confirmed by other experiments that studied various β -decays using semiconductor spectrometers [235, 236]. Shortly after, the possible discovery was ruled out with high statistical significance as a systematic error by using other magnetic spectrometer techniques⁶ [237]. Current laboratory limits on the active-to-sterile mixing are on the order of $\sin^2 \theta \lesssim 10^{-3}$ for a mass range of $m_{\nu_s} \approx 1 - 100 \text{ keV}$

⁶The first experiment that found a false signal (Simpson et al. [234]) used tritium implanted into a Si(Li) detector. The systematic effect that lead to the false sterile neutrino signature with 3% mixing was caused by scattering of the β -decay electrons at the Si(Li)-diaphragm [13].

with the effective electron neutrino mass $m_{\nu_e}^2 = \sum_{i=1}^3 |U_{ei}|^2 m_{\nu_i}^2$ and the mass of the fourth mass eigenstate $m_4 = m_{\nu_s}$ which is referred to as the *sterile neutrino* in the rest of this thesis. The amplitude $|U_{e4}| = \sin^2 \theta$ denotes the mixing between the active and the sterile eigenstate. An example of a resulting signal in a differential tritium β -decay spectrum can be seen in figure 3.4. [12]

There are several arguments for using the KATRIN experiment to search for keV-scale sterile neutrinos. First of all, all benefits of the tritium β -decay that are listed in 2.2.1 also apply for a sterile neutrino search. Furthermore, with the kinematic endpoint of $E_0 \approx 18.6$ keV, the interesting sterile neutrino mass range of a few eV up to $m_{\nu_s} \lesssim 18.6$ keV can be studied. The KATRIN experiment provides a strong and stable tritium source. With its high luminosity, the WGTS is able to provide a total signal rate of up to 10^{10} cps [10]. Assuming three years of data taking at full source strength, the KATRIN experiment would be statistically able to reach a sensitivity on the active-to-sterile mixing amplitude of up to $\sin^2 \theta < 10^{-8}$. [12]

The KATRIN experiment is designed to measure in the close vicinity to the kinematic endpoint region. For sterile neutrino studies, the spectrum needs to be scanned over a wider range. This leads to several challenges: deep scans of the spectrum cause larger signal rates at the detector and higher surplus energies of the signal electrons with respect to the retarding potential of the main spectrometer (see sections 2.2.3 and 2.2.4). Both cases require a modification of the current setting (*phase-0*) or new hardware (*phase-1*). [12]

The following paragraph describes the two measurement phases which are proposed for the usage of the KATRIN experiment to search for keV-scale sterile neutrinos. The further course of this work focuses on the *phase-0* measurement that faces the challenge of using KATRIN with only minor modifications. This first low statistics sterile neutrino search has the potential to improve the current laboratory limits on the active-to-sterile mixing amplitude by one order of magnitude on an extended energy range as will be shown in the course of this work.

The Measurement Phases

The high activity of the KATRIN source is one of the key parameters in the search for keV-scale sterile neutrinos. In order to achieve a high sensitivity to the small distortion in the β -decay spectrum caused by a sterile neutrino, a measurement with high statistical significance is necessary. The KATRIN focal plane detector with 148 pixels is able to resolve count rates up to 10^5 cps⁷ and is designed to measure the β -decay spectrum in an interval of $E_0 - 90$ eV $< qU_{\text{ret}} < E_0 + 5$ eV (where E_0 is the endpoint energy and qU_{ret} is the retarding energy of the main spectrometer) [10].

A keV-scale sterile neutrino measurement requires an extension of the measurement interval to cover a larger part of the spectrum by lowering the retarding potential of the main spectrometer to smaller values. Consequently, the number of electrons that reach the detector will increase with a maximum value of approximately 10^{10} cps at full source strength and no retarding potential applied to the main spectrometer [12]. This high rate exceeds the limit of the focal plane detector by five orders of magnitude.

The TRISTAN project has the goal to build a new detector system for the KATRIN experiment. It is designed to measure count rates up to 10^8 cps with a multi-pixel silicon drift detector with a total number of 3500 pixels. The TRISTAN detector is currently under construction and it is planned to operate in 2025 (details can be found in chapter 7.1). With the new detector system a high statistics deep scan of the tritium β -decay

⁷Details on the rate limits of the FPD can be found in section 4.1.1

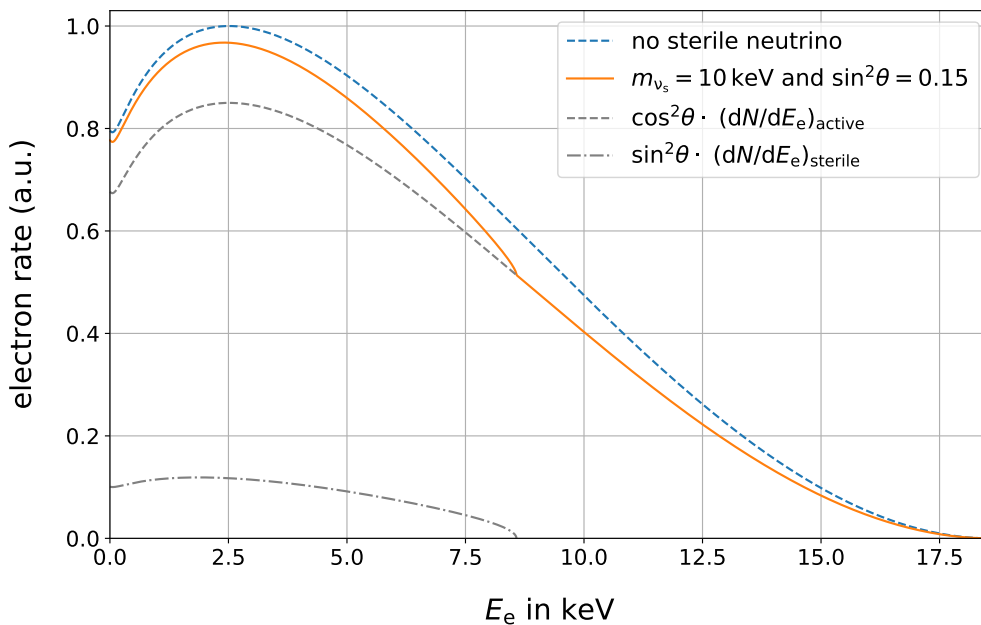


Figure 3.4: Tritium β -decay spectra for two scenarios: 1. The blue dashed line presents the spectrum with no additional mass eigenstate; 2. the orange solid line is a spectrum with a sterile neutrino with a mass of $m_{\nu_s} = 10$ keV and an exaggerated mixing amplitude of $\sin^2\theta = 0.15$. As indicated in equation (3.17), the spectrum including a sterile neutrino is an admixture of a spectral component caused by the active neutrinos, and a component generated by the sterile mass eigenstate (both components are displayed in grey dashed lines). The latter arises at electron energies of $E_e < E_0 - m_{\nu_s}$.

spectrum will be possible and it is aimed to probe the sterile neutrino phase space with mixing amplitudes down to $\sin^2\theta < 10^{-6}$. [17]

This work presents the idea of using KATRIN 'as is' to search for keV-scale sterile neutrinos and allowing only minor modifications of the experimental setup. A combination of a lower source strength and changed magnetic field setting provides the opportunity to cover a significant range of the tritium β -decay spectrum with statistical potential to improve the current laboratory limits by one order of magnitude.

CHAPTER 4

Search for keV-scale sterile Neutrinos with KATRIN

As explained in detail in the previous chapter, right-handed (sterile) neutrinos do not interact within any SM interaction, however, they mix with left-handed neutrinos via mass eigenstate oscillation. This active-to-sterile mixing would manifest itself as a kink-like distortion in the electron spectrum of β -decays (see figure 3.4), enabling a laboratory search for the particle. [13] Tritium β -decay provides several advantages for such an experimental study which are listed in section 3.4.

The concept of using the KATRIN experiment to search for keV-scale sterile neutrinos was first formulated in the design report in 2004 [10]. In 2012, a study specified the experimental requirements and showed that with the full KATRIN source strength, a high statistical sensitivity on the active-to-sterile mixing of $\sin^2 \theta < 10^{-8}$ can be reached after three years of data taking [12]. However, major hardware modifications, for example a new detector system, are required for the realization of such a measurement [17].

This work presents the idea of using KATRIN with only minor experimental adjustments and without any hardware modifications for a first search for sterile neutrinos on the keV mass scale. It is shown in chapter 4 and 5 that on a short-term, KATRIN has the potential to improve the current laboratory limits by at least one order of magnitude¹.

If the KATRIN experiment is used to search for keV-scale sterile neutrinos, the tritium β -spectrum needs to be measured over an extended energy range compared to neutrino mass measurements, in order to maximize the accessible parameter space. This results in two major challenges:

1. The signal electron rate rapidly increases when the main spectrometer retarding potential is lowered and exceeds the FPD counting limits.
2. The growing surplus energy of the electrons with respect to the retarding potential can lead to an uncontrolled transmission loss due to non-adiabatic electron transmission conditions in the main spectrometer.

This chapter presents a description of both effects and how they can be addressed by an adjustment of the source strength and magnetic field setting (section 4.1 and 4.2). By combing the results of both studies, several scenarios that make a search for keV-scale sterile neutrinos with the current KATRIN experimental setup possible, are presented (section 4.3).

¹Compared to the limits displayed in figure 3.3, which are based on [244, 245, 246, 247, 248].

4.1 Reducing the Signal Rate

The KATRIN signal electrons are generated in a high-luminosity gaseous tritium source with a rate of up to 10^{11} decays per second at full source strength (see section 2.2.1) [10]. In order to determine the neutrino mass, the KATRIN experiment studies the endpoint region of the tritium β -decay spectrum. Only a fraction of approximately 10^{-10} of the signal electrons are in the last 10 eV below the endpoint, which makes the high source activity necessary. Lowering the retarding potential leads to a rapid increase of the signal electron rate. The KATRIN focal plane detector (FPD) is designed to resolve rates up to 10^5 cps [174]. At full source strength, this rate limit is already exceeded at energies of approximately 400 eV below the endpoint. In order to maximize the accessible parameter space of a sterile neutrino search, a method to reduce the signal electron rate is required. This section discusses the limit on the highest possible rate the FPD can resolve (section 4.1.1) and presents two methods to lower the signal rate to the required values, using a modified source activity (section 4.1.2) and magnetic field setting (section 4.1.3 and 4.1.4).

4.1.1 Rate Limits of the FPD

The FPD is a monolithic PIN diode segmented into 148 individual pixels [173]. The detector and read-out system are described in section 2.2.4. The maximum rate of signal electrons that can be resolved at the FPD is limited by two properties: the data read-out speed and the probability for event pile-up.

Read-Out Speed and Data Processing

An 18.6 keV electron generates a signal of $\Delta U \approx 10$ V with a pulse length of $\Delta t \approx 20$ ns at room temperature in the FPD silicon wafer [173]. The detection, amplification, and digitalization of the signal requires a customized read-out and data acquisition (DAQ) system which has been developed over many years and is operated at the KATRIN experiment [131, 174].

The FPD is equipped with three DAQ modes, which differ mainly in the amount of recorded information for each detected event. The read-out speed is limited by the amount of information that needs to be stored, therefore, it is directly related to the maximum resolvable rate combined for all pixels. [174]

The *energy mode* is the primary data-taking mode that records event-wise information on the energy and timing, and is able to resolve rates up to 108 kcps. If the individual ADC waveforms of the single events are required in the analysis, the detector can be operated in *trace mode*, where the rate is limited to 8 kcps. This mode is usually used for commissioning measurements. If no information on the timing of the event is necessary, the FPD can be operated in *histogram mode* and resolves rates up to 3.3 Mcps by storing the events in a 2048-bin energy histogram during a set time frame. This mode does not allow event-based analysis. [174]

For a keV-scale sterile neutrino search event-wise information is required, therefore, the FPD needs to be operated in the *energy mode*. The maximum integrated rate is limited to approximately 100 kcps.

Limits due to Signal Pile-Up

If the detector is operated at high rates and the time between two incoming electrons Δt is smaller than the shaping length L of the detector or the characteristic discharging time τ of the preamplifier, the two signals are combined and piled up which leads to a

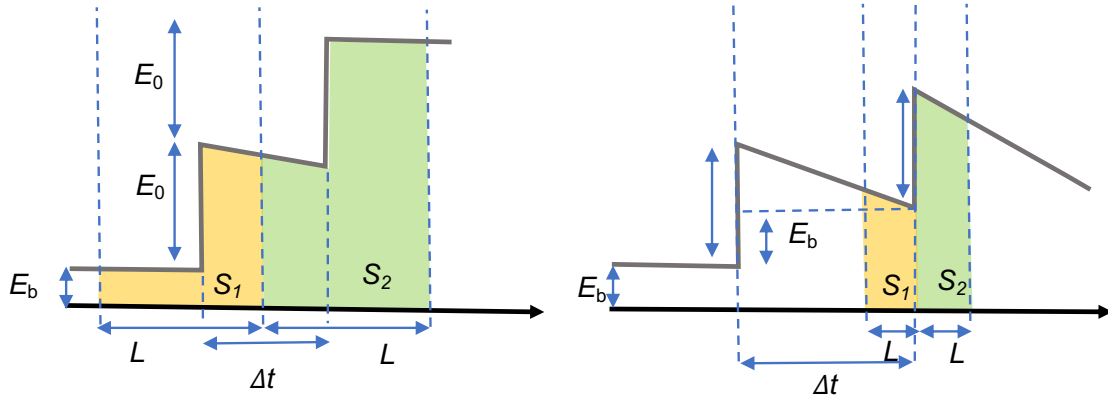


Figure 4.1: A graphical interpretation of peak (left) and tail pile-up (right). If two signals S_1 and S_2 occur within a time difference Δt smaller than the shaping length L , both signals are stacked up to a single event. Tail pile-up appears if Δt is smaller than the preamplifier needs to discharge. The baseline energy E_b is different for both signals which leads to an underestimation of the energy of the second event. [173] The figures are based on illustrations in [173] and [251].

detection of the wrong energy. A distinction is made between two different types of pile-up effects: peak and tail pile-up. Figure 4.1 shows a schematic representation of both effects. [173]

The probability of pile-up scales with the signal rate. For tritium β -decay measurements, pile-up leads to an unreconstructible distortion of the spectrum and should be avoided or kept to a minimum. [173]

In addition to the rate limit caused by the maximum read-out speed, pile-up leads to a pixel-wise rate limit. Studies show that for signal rates of up to 1 kcps per pixel, pile-up is small and the caused systematic effect can be modeled as a correction of the detection efficiency (see section 5.6.2) [249, 250].

In summary, the FPD is limited to a maximum rate of 1 kcps per pixel and 100 kcps for the integrated detector rate. It is important to note that if the FPD is operated close to the 1 kcps limit on the per pixel rate, the integrated rate of the detector would exceed the 100 kcps read-out speed limit (148 pixels). However, individual segments of the detector can be turned off to limit the read-out rate to the required value.

4.1.2 Lowering the Source Strength

As described in the previous paragraph, the FPD maximum integrated rate is limited to 100 kcps which occurs at approximately 400 eV below the endpoint. However, if KATRIN is used to search for keV-scale sterile neutrinos, the spectrum has to be measured over a wider energy range. Therefore, the electron rate at the detector has to be reduced by up to a factor of $f_{\text{red}} = 10^5$. One effective way to lower the signal electron rate is to reduce the source strength.

The total number of tritium molecules in the source

$$N_{\text{tot}} = \epsilon_{\text{T}} \cdot \rho d \cdot A, \quad (4.1)$$

with the source cross-sectional area A , the column density ρd , and the tritium purity ϵ_{T} , is a direct measure of the source activity [10].

The two parameters which can be used to modify the source strength are ρd and ϵ_T . The rate reduction factor due to a lower column density is defined as

$$f_{\text{red}}^{\rho d}(\rho d_{\text{red}}) = \frac{\rho d_{\text{nom}}}{\rho d_{\text{red}}}, \quad (4.2)$$

where ρd_{red} is the reduced, and $\rho d_{\text{nom}} = 5 \cdot 10^{17} \text{ cm}^{-2}$ is the nominal column density.

A further reduction of the source strength can be achieved by lowering the tritium purity ϵ_T . In nominal KATRIN operations the source gas is composed of an admixture of the isotopologues $T_2 (> 95 \%)$, $DT (< 5 \%)$, $HT (< 5 \%)$, and traces of D_2 , HD , and H_2 which leads to a nominal tritium purity of $\epsilon_{T,\text{nom}} \approx 0.95$ [9]. By replacing the radioactive with non-radioactive isotopologues, ϵ_T and respectively the decay rate can be reduced. This defines a rate reduction factor

$$f_{\text{red}}^T(\epsilon_{T,\text{red}}) = \frac{\epsilon_{T,\text{nom}}}{\epsilon_{T,\text{red}}}, \quad (4.3)$$

with the reduced tritium purity $\epsilon_{T,\text{red}}$.

A total reduction is given by the product $f_{\text{red}} = f_{\text{red}}^{\rho d} \cdot f_{\text{red}}^T$.

Maximum Source Strength Reduction

By maximizing $f_{\text{red}}^{\rho d}$ and f_{red}^T , the accessible parameter space of deep spectral scans can be increased.

Maximizing $f_{\text{red}}^{\rho d}$: In order to maximizing $f_{\text{red}}^{\rho d}$, the lowest stable column density needs to be determined. At a constant source temperature, the pressure inside the pressure controlled buffer vessel (PCB) can be directly translated to the column density stability (for details of the tritium loop system see section 2.2.1) [252]. The lowest stable pressure inside the PCB was determined in a dedicated measurement. Figure 4.2 shows the measured pressure over a time period of 1 hour. The values fluctuate around the setpoint of 0.5 mbar within an accuracy of 0.1% over the full time interval (peak to peak). During the measurement, the WGTS beamtube was operated at 80 K. The corresponding column density is estimated to be $1.7 \cdot 10^{14} \text{ cm}^{-2}$ which is equivalent to a rate reduction factor of $f_{\text{red}}^{\rho d} = 2.9 \cdot 10^3$ [253]. This setting would allow an operation of the main spectrometer up to energies of 3.7 keV below the endpoint before the signal rate exceeds the FPD limit².

Maximizing f_{red}^T : In order to maximize f_{red}^T , the tritium purity needs to be reduced to a minimum. During the *First Tritium Campaign* the KATRIN source was operated at a reduced tritium purity of $\epsilon_{T,\text{red}} = 5.0 \cdot 10^{-3}$ (1% DT admixture to the D_2 carrier gas)[131]. If all tritium scans are combined, the uncertainty on the DT-concentration and respectively the tritium purity was found to be $\sim 0.08 \%$ [131, 254].

This setting is the lowest stable gas composition KATRIN has been operated with to date. It corresponds to a reduction of the tritium purity by a factor of $f_{\text{red}}^T \approx 190$ which allows to measure down to a retarding potential of 1.67 keV from the endpoint.

Both reduction factors can be combined. Figure 4.3 shows the lowest retarding potential with which the spectrum can be measured within the limits of the FPD, as a function of the column density for different tritium purities. If the source would be operated at 80 K with the lowest stable column density of $\rho d_{\text{min}} = 1.7 \cdot 10^{14} \text{ cm}^{-2}$ and the same gas

²If the source is operated at the nominal temperature of 30 K the same inlet pressure corresponds to a higher value of $\rho d \approx 9.1 \cdot 10^{14} \text{ cm}^{-2}$ due to the temperature dependent conductance. The corresponding reduction factor is $f_{\text{red}}^{\rho d} = 0.6 \cdot 10^3$. [253]

composition as used during the *First Tritium Campaign* of $\epsilon_{T,\text{red}} = 5.0 \cdot 10^{-3}$, the full tritium β -spectrum would be experimentally accessible.

4.1.3 Modification of the Source Magnetic Field Setting

Another possibility to reduce the signal rate at the detector is to lower the source magnetic field. As defined in equation (2.6), the maximum initial angle under which an electron can start in the source and reach the detector without being magnetically reflected at the pinch magnet is given by

$$\theta_{\text{max}} = \sin^{-1} \sqrt{\frac{B_s}{B_{\text{pch}}}}, \quad (4.4)$$

where B_s is the source magnetic field and B_{pch} is the pinch magnetic field [124]. If the source magnetic field is reduced, the maximum acceptance angle decreases which leads to a rate reduction³.

The rate reduction factor caused by this effect is a function of the reduced source magnetic field $B_{s,\text{red}}$

$$f_{\text{red}}^{\theta_{\text{max}}}(B_{s,\text{red}}) = \frac{N_{\theta_{\text{max}},\text{nom}}}{N_{\theta_{\text{max}},\text{red}}(B_{s,\text{red}})}, \quad (4.5)$$

where $N_{\theta_{\text{max}},\text{red}}$ is the reduced and $N_{\theta_{\text{max}},\text{nom}}$ is the nominal fraction of electrons that are able to reach the detector without being magnetically reflected.

Since the β -decay electrons are emitted isotropically, the solid angle in forward direction

$$\frac{\Delta\Omega}{4\pi} = \frac{1 - \cos\theta_{\text{max}}}{2} \quad (4.6)$$

can be used to calculate $N_{\theta_{\text{max}},\text{nom}}$ and $N_{\theta_{\text{max}},\text{red}}$ [10].

With the definitions from equation (4.4) and (4.6) the reduction factor is

$$f_{\text{red}}^{\theta_{\text{max}}}(B_{s,\text{red}}) = \frac{1 - \cos\theta_{\text{max,nom}}}{1 - \cos\theta_{\text{max}}(B_{s,\text{red}})}. \quad (4.7)$$

Using the relation

$$\cos[\sin^{-1}(\sqrt{x})] = \sqrt{1-x}, \quad (4.8)$$

equation (4.7) can be written as

$$f_{\text{red}}^{\theta_{\text{max}}}(B_{s,\text{red}}) = \frac{1 - \sqrt{1 - \frac{B_{s,\text{nom}}}{B_{\text{pch,nom}}}}}{1 - \sqrt{1 - \frac{B_{s,\text{red}}}{B_{\text{pch,nom}}}}}, \quad (4.9)$$

where $B_{s/\text{pch,nom}}$ are the nominal source and pinch magnetic field values.

The blue line in figure 4.4 shows the reduction factor $f_{\text{red}}^{\theta_{\text{max}}}$ as a function of the source magnetic field. If the source magnetic field is reduced to $B_{s,\text{red}} = 10^{-2}$ T a rate reduction of up to $f_{\text{red}}^{\theta_{\text{max}}} = 440$ could be achieved.

Technical Limitations of reducing B_s

The WGTS contains of seven super conducting magnets that are assembled in a straight line. The magnet modules are grouped in three sections, the center WGTS/C (M4, M5), the rear WGTS/R (M1, M2, M3) and the front WGTS/F (M6, M7) group. For nominal KATRIN operations, the WGTS-C and WGTS-R modules are operated at the same value

³The same effect could be gained by increasing the pinch magnetic field, however, it is already operated at its maximum value.

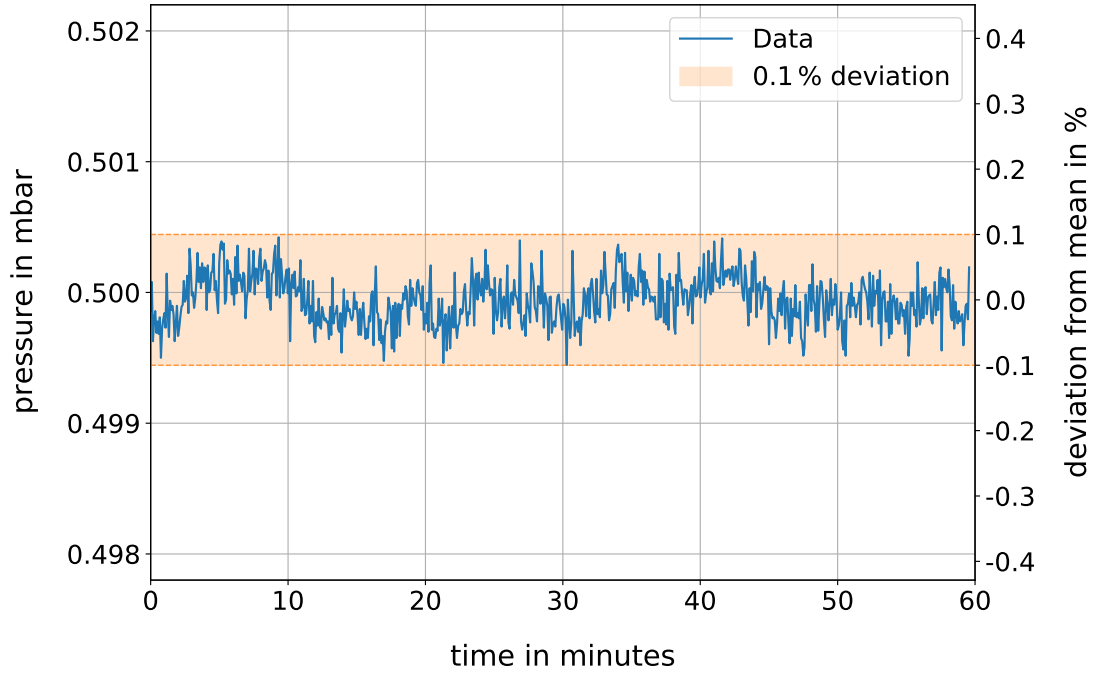


Figure 4.2: To determine the lowest stable pressure inside the PCB, a setpoint of 0.5 mbar was chosen. The pressure was monitored during a time interval of 1 hour. It fluctuates within a deviation of 0.1% (orange shaded area) throughout the entire measurement which can be directly translated into a column density stability of the same order. The sinusoidal oscillations are caused by the regulation system. The measurement took place on 19th March, 2020, and is documented under the internal E-Log-ID KNM3/3.

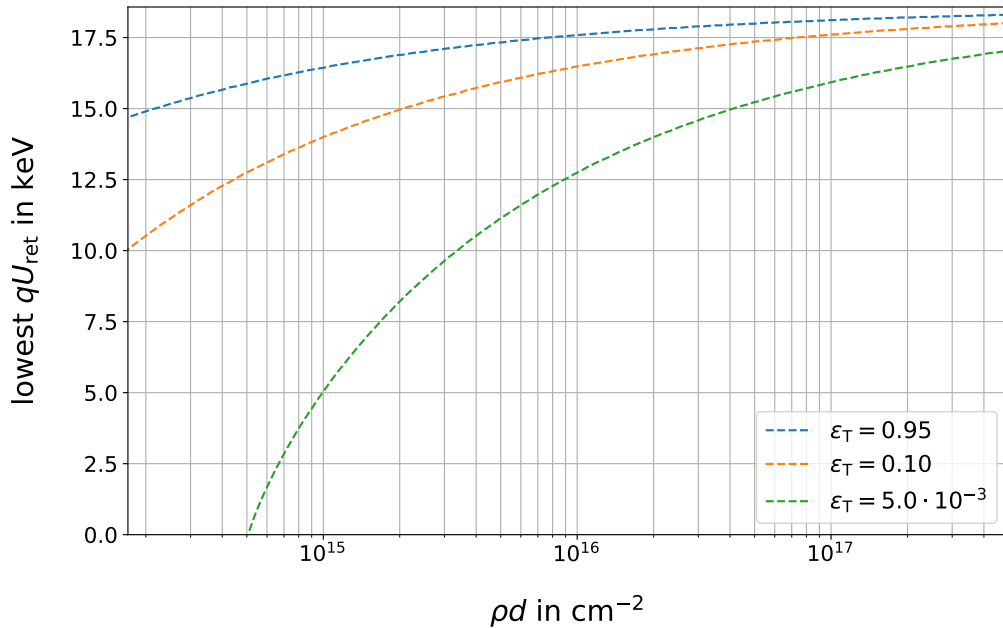


Figure 4.3: The lowest possible retarding potential for sterile neutrino searches as a function of the column density. The blue line is the nominal KATRIN setting. Assuming a lowest technically feasible column density of $\rho d = 1.7 \cdot 10^{14} \text{ cm}^{-2}$ (at a source temperature of 80 K) the spectrum can be scanned to a minimum retarding potential of $qU_{\text{ret}} = 14.9 \text{ keV}$. By reducing the tritium purity of the source gas ϵ_T from the nominal to lower values, the possible measurement range extends. For $\epsilon_T = 5.0 \cdot 10^{-3}$ the full spectrum can be measured within the FPD limitations.

of 3.6 T and the WGTS-F at a higher field of 5.6 T. [128] All three modules can be accessed and controlled separately, although, within certain restrictions⁴.

A deviation from their nominal source magnetic field can cause several effects:

Increased cyclotron radii at the source tube: Electrons with charge e , velocity \vec{v} , and polar angle θ propagate through electromagnetic fields (\vec{E} and \vec{B}) in cyclotron motion caused by the Lorentz force

$$\vec{F}_L = e \cdot (\vec{E} + \vec{v} \times \vec{B}). \quad (4.10)$$

The radius of the cyclotron motion (*Larmor radius*) is given by

$$r_L = \frac{m_e c \cdot \sqrt{\gamma_0^2 - 1}}{eB}, \quad (4.11)$$

with the magnetic field strength B and the relativistic correction factor

$$\gamma_0 = 1 + \frac{E_\perp}{m_e c^2} \quad (4.12)$$

with the transversal kinetic energy of the electron

$$E_\perp = E \cdot \sin \theta. \quad [255] \quad (4.13)$$

As equations (4.11) - (4.13) imply, a reduction of the magnetic field strength leads to an increase of the Larmor radius r_L of the electron trajectories. For fields on the order of 10^{-2} T, r_L can be up to 1 cm. The center of the WGTS consists of a 10 m long beam tube with a radius at $r_s = 4.5$ cm. Electrons that start on a distance to the tube wall smaller than $r_s - r_L$ will eventually scatter with the wall and lose energy. Since the Larmor radius depends on the starting energy of the electron, the scattering effect is energy dependent, which leads to a spectral distortion. In order to avoid this, the detector magnetic field must be lowered with respect to the source magnetic field to reduce the radius of the *visible fluxtube* (details can be found in section 4.1.4). By doing so, the detector only observes a volume within the source that does not contain electrons scattering on the tube walls.

Adiabatic electron transport in the WGTS: If the source magnetic field is reduced, non-adiabatic transmission between the source and the transport section can occur analogous to the main spectrometer (for details see section 4.2). This can be avoided by adjusting the WGTS/F field to reduce the magnetic field gradient between the source and the transport section by an intermediate step. Since this depends on the specific source magnetic field setting, the value has to be obtained for each individual setting (with a simulation).

4.1.4 Modification of the Detector Magnetic Field Setting

Another option to lower the signal electron rate with an adjusted magnetic field setting is the reduction of the *visible fluxtube*. Due to the conservation of the magnetic flux

$$\phi = \int_A \vec{B} \cdot d\vec{A} = \text{const.}, \quad (4.14)$$

the radii of the fluxtube in two different locations x_1 and x_2 are connected via

$$r_{x_1}^2 \cdot B_{x_1} = r_{x_2}^2 \cdot B_{x_2}. \quad [10] \quad (4.15)$$

⁴Superconducting magnets operated in close proximity to each other require careful tuning of the field settings. The restrictions depend on the desired settings and are assessed on a case-by-case basis.

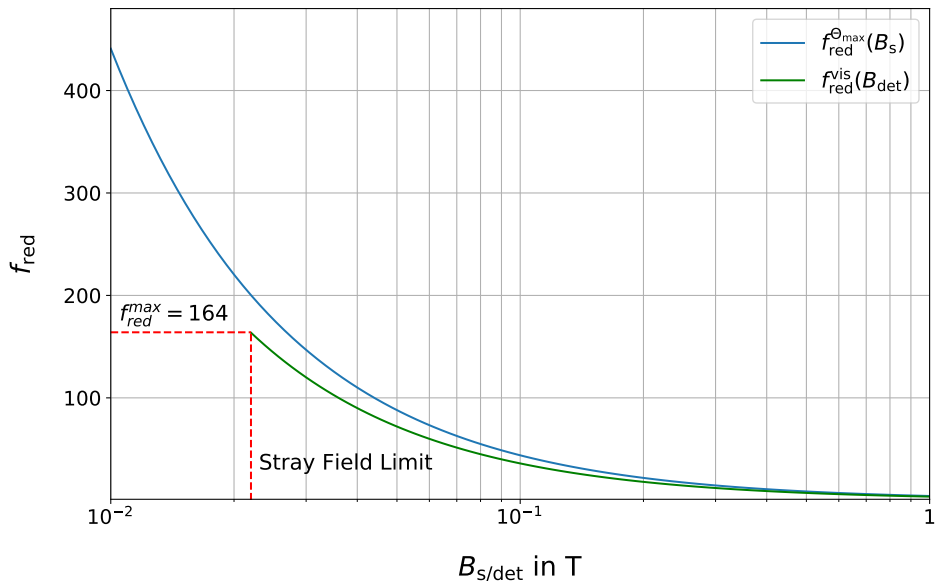


Figure 4.4: The rate reduction factors corresponding to reduced source and detector magnetic fields as calculated in equation (4.9) and (4.18). On both curves one field was varied while the other was fixed to the nominal value. The reduction of the source magnetic field is more efficient than the detector field reduction which is also technically limited by the stray field of the pinch $B_{\text{pch}}^{\text{stray}} = 2.2 \cdot 10^{-2}$ T. A further reduction would require a reversal of the current of the super-conducting detector magnet.

If the detector magnetic field is reduced, the fluxtube widens at the position of the FPD. As a consequence, the source volume that is visible to the wafer, and respectively the number of observable β -decays, decreases.

The radius of the *visible fluxtube* is a function of the source and detector magnetic field

$$r_{\text{vis}} = r_{\text{waf}} \cdot \sqrt{\frac{B_{\text{det}}}{B_{\text{s}}}}, \quad (4.16)$$

where r_{waf} is the radius of the detector wafer.

For the radially homogeneous KATRIN source, the rate reduction resulting from a decreased visible fluxtube is given by the ratio of the areas of the fluxtube and the detector wafer

$$f_{\text{red}}^{\text{vis}}(r_{\text{vis}}) = \frac{r_{\text{waf}}^2}{r_{\text{vis}}^2}. \quad (4.17)$$

From equation (4.16) follows

$$f_{\text{red}}^{\text{vis}}(B_{\text{det,red}}) = \frac{B_{\text{s}}}{B_{\text{det,red}}}. \quad (4.18)$$

The green line in figure 4.4 shows the rate reduction as a function of the detector magnetic field. The reduction of the detector magnetic field is less effective than that of the source magnetic field. Furthermore, it is technically limited, as described in the following.

Technical Limitations of reducing B_{det}

The detector magnet can be operated independently from all other magnets. Due to its close proximity to the pinch magnet, the detector magnetic field strength is technically limited by the pinch magnet stray field to a minimum of $2.2 \cdot 10^{-2} \text{ T}$ (for the nominal pinch magnetic field of $B_{\text{pch}} = 6.0 \text{ T}$, the value has been determined in a simulation). This corresponds to a maximum reduction factor of $f_{\text{red}}^{\text{vis}} = 164$. A further reduction would require a pole reversal in order to compensate the stray field.

A deviation from the nominal detector magnetic field setting can cause two effects:

Secondary photon emission at the detector chamber: If the fluxtube is widened due to a reduced detector magnetic field, most of the field lines on which electrons are transported from the source to the detector section, are mapped on the stainless steel detector chamber. These electrons induce secondary photon emission due to bremsstrahlung and contribute to the detector γ -background. If the detector magnet is turned off and the source magnet is operated at its nominal value, the relative background contribution to the observed signal electron rate is in the order of 10^{-6} . A detailed simulation study of the effect can be found in appendix C.

Increased cyclotron radii: Analogous to the source magnetic field, a reduced detector magnetic field leads to larger *Larmor radii* within the detector section. The influence of this effect is mainly relevant for signal electron backscattering from the detector which is discussed in detail in section 5.6.1.

4.1.5 Conclusion

When the tritium β -spectrum is used to search for keV-scale sterile neutrinos, it needs to be measured over an energy range as wide as possible. Therefore, the main spectrometer retarding potential needs to be lowered several keV below the kinematic endpoint. This leads to an increase of the signal electron rate at the detector. As described in section 4.1.1, the FPD can be operated with rates up to 1 kcps per pixel (limited by pile-up) or 100 kcps integrated rate over all pixels (limited by the read-out speed). If the detector is operated close to the 1 kcps per pixel limit, some of the pixels need to be turned off to keep within the integrated rate limit.

If the KATRIN experiment is operated at its nominal setting, the signal electron rate already exceeds the technical limits of the FPD at approximately 400 eV below the endpoint. One way to reduce the signal electron rate is to operate the tritium source with a reduced column density and a modified gas composition. Both methods have been already successfully tested and would enable to measure the full β -spectrum.

Another way to reduce the signal rate requires a modification of the source or the detector magnetic field. The first approach makes use of the magnetic reflection of electrons at higher magnetic fields, the latter technique decreases the size of the fluxtube and respectively the decay volume in the source that is mapped on the detector. All effects can be combined as displayed in figure 4.5.

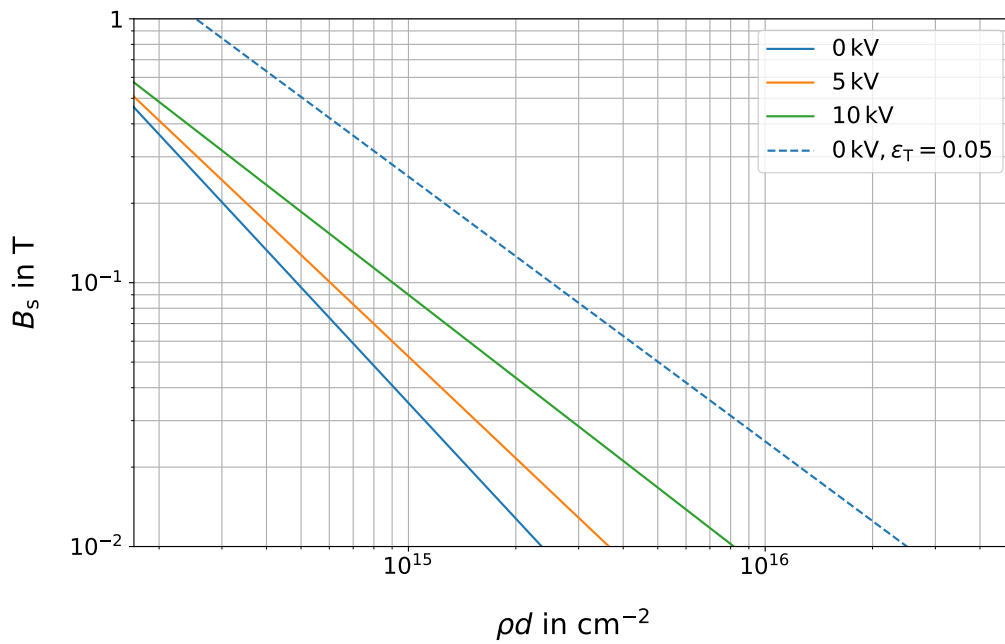


Figure 4.5: The combination of a reduced column density and lowered source magnetic field. The contours correspond to the lowest possible retarding potential before the rate exceeds the read-out speed of the detector system. The detector magnet was fixed to the same value as the source magnetic field. The blue dashed line shows a scenario with an additionally reduced tritium purity of $\epsilon_T = 0.05$. If the source is operated at a column density of $\rho d = 1.0 \cdot 10^{15} \text{ cm}^{-2}$ and a tritium purity of $\epsilon_T = 0.05$, the source magnetic field needs to be approximately 0.2 T in order to measure the entire energy range of the tritium β -decay spectrum.

4.2 Main Spectrometer Transmission at high Surplus Energies

The KATRIN main spectrometer is designed to provide a high energy resolution of up to 0.93 eV for electrons in the tritium β -decay endpoint region of $E_0 = 18.6$ keV. In order to reach this precision, a small magnetic field in the order of a few 10^{-4} T at the analyzing plane and a large field of up to 6 T at the exit of the main spectrometer is required (see section 2.1). This results in a large magnetic field gradient. [10]

When KATRIN is used to search for keV-scale sterile neutrinos, the main spectrometer needs to be operated at low retarding potentials. As a consequence, the surplus energy of the electrons with respect to the retarding potential

$$E_{\text{sur}} = E_e - qU_{\text{ret}} \quad (4.19)$$

increases. The combination of high surplus energies and a large magnetic field gradient leads to non-adiabatic transport conditions inside the main spectrometer and a transmission loss of signal electrons. (see for example [161])

Beside all other systematic effects that occur when the tritium β -decay spectrum is measured over a wide energy range, non-adiabatic transmission loss has a special position. Due to the chaotically nature of the underlying processes⁵, small variations of the experimental conditions have a large influence on the size and shape of the transmission loss. This makes a modeling of the effect and a treatment in the analysis particularly challenging [125].

If no countermeasures are taken, this effect sets a strong limit on the accessible parameter space when KATRIN is used to search for a keV-scale sterile neutrinos.

The upcoming section gives an introduction to the concept of adiabatic electron transport and explains why high surplus energies lead to a transmission breakdown (section 4.2.1). The introduction is followed by a presentation of three different countermeasures: an increase of the LFCS field (section 4.2.2), a reduction of the detector magnetic field (section 4.2.3), and the utilization of the radial dependency of the main spectrometer transmission (section 4.2.4).

The presented studies are mainly based on *KASPER* simulations. All details to the simulation settings and analyses, as well as a brief introduction to the concept of the *KASPER* simulation framework can be found in appendix A.

Several former works studied (non-)adiabatic electron transport in the context of the KATRIN (or predecessor) experiment for example [125, 126, 161]. A first investigation of the impact of non-adiabatic transmission in the main spectrometer on a keV-scale sterile neutrino search can be found in [16]. Especially the countermeasure of an increased LFCS field was topic of the investigations in [16] (master thesis of the author).

4.2.1 Adiabatic Electron Transport

An electron with charge e and velocity \vec{v} propagates through electromagnetic fields in cyclotron motion as described by equations (4.11)-(4.13). If the particle experiences a variation of the magnetic field during its propagation, the resulting angular change can be calculated by the relation

$$\sin^2 \theta_1 \cdot B_2 = \sin^2 \theta_2 \cdot B_1 [10]. \quad (4.20)$$

⁵A study that investigates the chaotic nature of non-adiabatic electron motion can be found in appendix B and in [125].

For a positive magnetic field gradient, θ increases. If it gets steeper than 90° the direction flips and the electron propagates towards its original position (*magnetic mirror effect*). For any starting magnetic field, equation (4.4) defines a maximum initial angle θ_{\max} under which an electron is able to pass a second field without being magnetically reflected. Relations (4.4) and (4.20) are only valid, if the gradient of the electric and magnetic field

$$\vec{\nabla}E = \frac{\Delta E}{E} \ll 1, \quad (4.21)$$

$$\vec{\nabla}B = \frac{\Delta B}{B} \ll 1, \quad (4.22)$$

is small within one cyclotron length

$$l_{\text{cycl}} = 2\pi \frac{\gamma_0 m_e}{eB} v_{\parallel} [161]. \quad (4.23)$$

If equations (4.21) and (4.22) are fulfilled, the motion is adiabatic⁶.

In the main spectrometer, the magnetic field drops from the entrance to the center by up to four orders of magnitude over a distance of about 12 m. For nominal KATRIN operations, the electrons have low surplus energies (for example during the *KNM1 Campaign* up to 200 eV [9]) and the magnetic field gradient per cyclotron length is small enough to fulfill the adiabatic conditions.

If the retarding potential is further lowered, as is required for a keV-scale sterile neutrino search, a growing number of electrons pass the spectrometer with surplus energies of up to several keV. For these electrons, the cyclotron length defined in equation (4.23) increases. As a consequence, the electrons experience a larger field gradient within one cyclotron length and the probability to violate the adiabatic conditions (4.21) and (4.22) increases as well.

Instead of a controlled angular transition as described by equation (4.20), the polar angle of the electrons changes chaotically which leads to an increased reflection probability at the pinch magnet. As a consequence, the transmission probability for electrons with high surplus energies through the main spectrometer decreases as displayed in figure 4.6. [125, 16] The values shown in the figure relate to the nominal KATRIN magnetic field setting as stated in table A.1. Even if the energies of the electrons are large enough to overcome the retarding potential, the transmission probabilities decrease down to 40 % for $E_{\text{sur}} > 10.0$ keV.

The effect of non-adiabatic transmission does not only scale with the surplus energy of the electrons but also depends on their propagation path through the main spectrometer. The magnetic field inside the main spectrometer is axially symmetric. If electrons propagate through the main spectrometer on the symmetry axis, the magnetic field is approximately uniform. For off-axis electrons, the cyclotron motion leads to an asymmetric field, which has an influence on the radius of curvature of the electrons trajectory. This asymmetry leads to an azimuthal drift which increases with the electron surplus energy E_{sur} , polar angle θ , and distance to the main spectrometer symmetry axis [257, 258]. The latter parameter is related to the electrons entrance radius r_{ent} . The higher E_{sur} , θ , and r_{ent} , the larger is the azimuthal drift as well as the magnetic field gradient that is experienced within one cyclotron length [126]. This leads to a correlation between the three parameters and the occurrence of non-adiabaticity as shown in figure 4.7.

⁶The definition of the term *adiabatic* used here follows the *adiabatic theorem* formulated by M. Born and V. Fock. It defines an adiabatic transformation as a process in which the physical state remains in its instantaneous eigenstate if the perturbation is acting on it slowly enough [256].

Due to the chaotic nature of non-adiabatic electron motion, the effect varies a lot for small variations of the initial conditions [125]. This makes a modeling challenging, and is why countermeasures are particularly important.

In the following, three methods are introduced which help to regain adiabatic electron transport even for surplus energies of several keV.

4.2.2 Increase of the LFCS Field

One of the most effective ways to regain adiabaticity is to increase the magnetic field inside the main spectrometer⁷. This is for two reasons:

1. An increase of the overall magnetic field strength reduces the magnetic field gradient. As a consequence, fulfillment of the adiabatic conditions from equation (4.21) and (4.22) is assured for higher surplus energies.
2. As stated in equation (4.15), the size of the magnetic fluxtube radius scales with the magnetic field strength. An increase of the LFCS field leads to a decrease of the magnetic fluxtube inside the main spectrometer as displayed in figure 4.8. This reduces the distance of the electron trajectories to the symmetry axis which in return reduces the probability for non-adiabaticity.

As introduced in section 2.2.3, the LFCS consists of 15 large air coils; 6 with 14 turns (double layer coils) and 9 with 8 turns (single layer coils). The generated magnetic field is linearly proportional to the coil current and the number of turns [16]. The number of turns cannot be increased without a major hardware modification, however, the coil current can be enhanced within a certain range.

The increase is limited due to temperature dependent oxidation that can occur if a too high current is applied to the coils. A dedicated measurement determined a limit on the single layer coils of $I_{\max}^{\text{single}} = 120$ A and on the double layer coils of $I_{\max}^{\text{double}} = 95$ A⁸.

Three different air coil settings are compared to study the influence of an increased LFCS field on the adiabatic transmission: The nominal KATRIN setting which is optimized for standard neutrino mass analysis, the *max. LFCS* setting, where the coils are operated at the currently highest possible coil current, and a hypothetical scenario, where the coil current is set to 400 A for all coils (the latter value has first been determined in [16]). All settings are displayed in table A.1.

In figure 4.9 the transmission probabilities for the three scenarios are shown. An increase of the coil current leads to gain in transmission. The *max. LFCS* setting shows a distinct improvement compared to the nominal KATRIN setting. If the coils would be operated at $I_{\text{coil}} = 400$ A, adiabaticity can be gained on the full energy scale.

Simultaneously with the completion of this study an upgrade of the LFCS has been installed at the main spectrometer. The main purpose is to reduce the main spectrometer background [127]. During the upgrade, five additional coils have been added to the setup and all single layer coils have been upgraded to double layer coils. Section 7.2 presents the design of the upgrade and studies the transmission conditions that can be reached.

⁷The effect of an increased LFCS magnetic field on the transmission conditions of electrons with high surplus energies has first been studied in the author's master thesis [16].

⁸Details on the measurement can be found in the KATRIN e-log under the e-log ID mainspectrometer/1648.

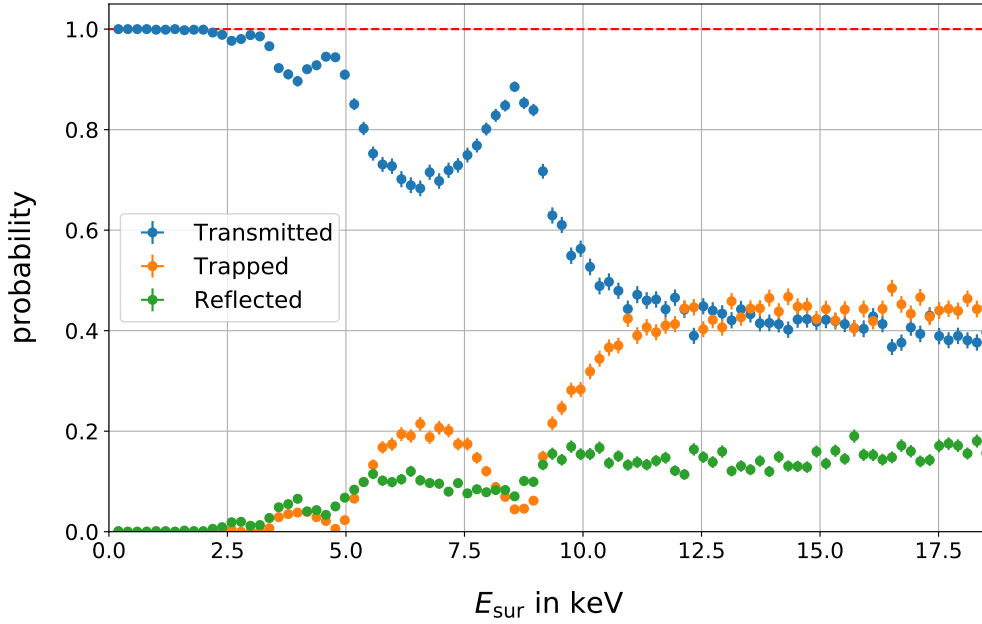


Figure 4.6: The transmission probability starts to drop for surplus energies larger than $E_{\text{sur}} > 2 \text{ keV}$ (blue markers). The electrons that cannot be transmitted are either trapped in the spectrometer (the simulation terminates the tracks after 10 turns) or reflected back to the source (orange and green markers). Details on the simulation setting and analysis can be found in appendix A. Figure is adapted from [16] figure 4.8.

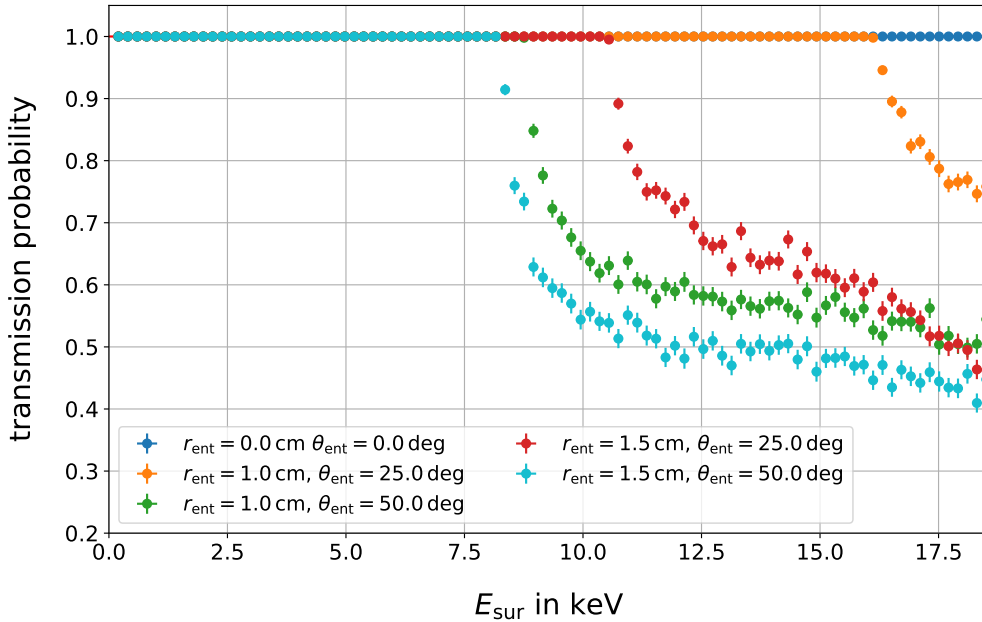


Figure 4.7: The transmission probability as a function of the surplus energy for various entrance radii r_{ent} and polar angles θ_{ent} . The further away from the symmetry axis ($r = 0 \text{ cm}$) the faster the transmission breaks down. This effect is caused by an azimuthal drift of the electrons that lead to an increased field gradient within one cyclotron length. The effect increases with increasing polar angle.

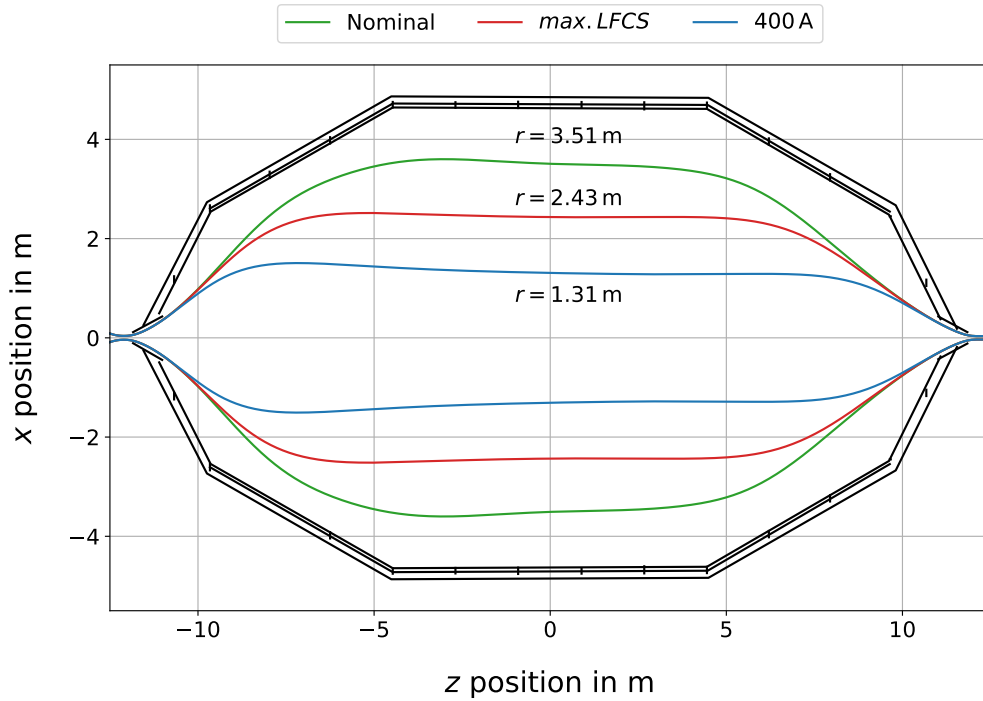


Figure 4.8: The outer lines of the fluxtube visible by the focal plane detector for three magnetic field settings. An enhanced coil current leads to an increased magnetic field inside the main spectrometer according to equation (4.15).

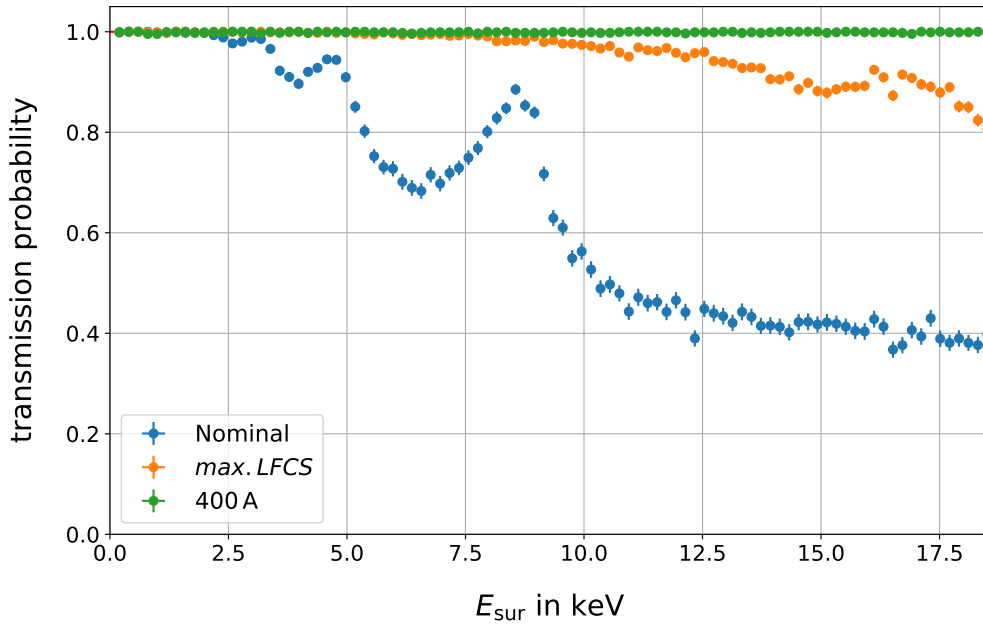


Figure 4.9: The electron transmission through the main spectrometer for the three studied LFCS settings. For higher currents the transmission probability increases. With a coil current of 400 A full transmission for all surplus energies would be reached within an uncertainty of approximately 10^{-3} . For the *max. LFCS* setting the transmission loss exceeds the 1% level at surplus energies larger than 8.0 keV within the statistical significance of the simulation. The probabilities are averaged over all detector rings.

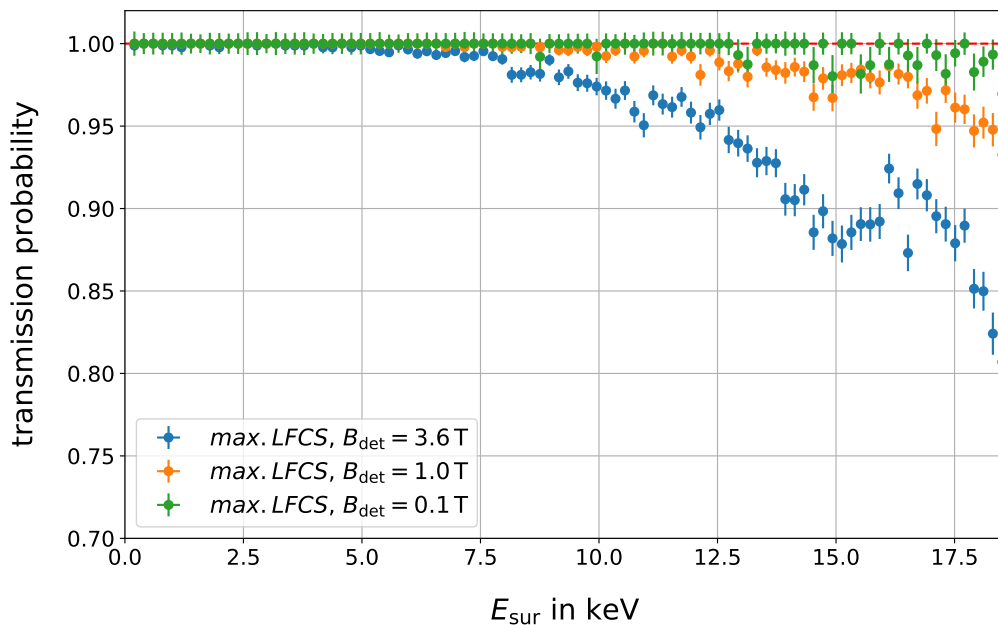


Figure 4.10: If the detector magnetic field is reduced, the transmission probability increases for higher surplus energies. In combination with an increased LFCS field, adiabatic transmission can be gained even for electrons with several keV surplus energy. Within an uncertainty of 1%, the setting with $B_{\text{det}} = 3.6$ T enables adiabatic motion for surplus energies of up to $E_{\text{sur}} = 8.0$ keV. When the detector magnetic field is lowered to $B_{\text{det}} = 1.0$ T, the range of adiabatic transport is extended to $E_{\text{sur}} = 12.1$ keV and for $B_{\text{det}} = 0.1$ T even to $E_{\text{sur}} = 13.1$ keV.

4.2.3 Reduced Entrance Fluxtube Radius

Another countermeasure requires the reduction of the detector magnetic field. According to equation (4.14) the fluxtube radius inside the second pre-spectrometer magnet with the field B_{PS2} (entrance of the main spectrometer) is given by

$$r_{\text{PS2}} = r_{\text{ent}} = \sqrt{\frac{B_{\text{det}}}{B_{\text{PS2}}}} \cdot r_{\text{waf}}, \quad (4.24)$$

with the radius of the detector wafer r_{waf} .

Lowering the detector magnetic field B_{det} reduces the radius of the fluxtube at the entrance of the main spectrometer, observed by the detector. Accordingly, the distance of the measured electrons to the main spectrometer symmetry axis decreases, which in turn improves the adiabatic transmission.

Figure 4.10 shows three combinations of an increased LFCS and reduced detector magnetic field. For the *max. LFCS* setting and a detector magnetic field of $B_{\text{det}} = 0.1$ T, the spectrum could be measured up to surplus energies of $E_{\text{sur}} = 8.7$ keV for transmission losses smaller than 10^{-3} , and $E_{\text{sur}} = 13.1$ keV for 10^{-2} losses.

4.2.4 Ring-wise Transmission Properties

The radial dependency of the effect can be used to define fiducial detector segments, depending on the specific electromagnetic setting. Only data taken in these detector segments observe a fully adiabatic transmission.

Figure 4.11 displays the adiabatic area of the detector in green and the detector area with expected transmission losses in red. The values are calculated for the *max. LFCS* setting

and the nominal detector magnetic field. By using only the most inner detector ring, the β -decay spectrum could be measured up to 8.6 keV below the endpoint.

It is important to point out, that the total statistics gained in a measurement depends on the number of pixels that have been actively used during the data taking. With the maximum rate of 1 kcps per pixel, the integrated rate is given by

$$R_{\max}^{\text{det}} = (4 + 12 \cdot n_{\text{rings}}) \cdot 1 \text{ kcps}, \quad (4.25)$$

with the number of active detector rings n_{rings} (the bullseye ($n_{\text{rings}} = 0$) consists of 4, all other rings of 12 pixels). The integrated rate at the detector is limited to 100 kcps. If the detector is operated at the per pixel limit, and $n_{\text{rings}} < 8$, the total statistics that can be gained in a measurement are reduced by a factor

$$s_{\text{red}} = \frac{(4 + 12 \cdot n_{\text{rings}}) \cdot 1 \text{ kcps}}{100 \text{ kcps}}. \quad (4.26)$$

For the *max. LFCS* setting, the highest statistics can be reached for a measurement down to 1.1 keV below the endpoint, where all rings including ring 8 can be used (displayed in the detector map on the top left of figure 4.11).

4.2.5 Conclusion

Non-adiabatic transmission conditions of the main spectrometer can cause a dominant systematic uncertainty and set strong limits on the accessible parameter space when the KATRIN experiment is used to search for keV-scale sterile neutrinos. The required reduction of the MAC-E filter voltage increases the surplus energy and respectively the velocity of the signal electrons. Inside the main spectrometer, the magnetic field drops over a short length scale by up to four orders of magnitude. Electrons that experience a high magnetic field gradient within one cyclotron length are likely to change their polar angle in a non-adiabatic and chaotic way. This leads to a transmission loss, depending on the surplus energy, position, and polar angle of the electron at the entrance of the main spectrometer. Since the effect scales with the distance of the electron's propagation path to the symmetry axis, it can be reduced by increasing the LFCS, as well as by lowering the detector magnetic field. Both lead to a decrease of the magnetic fluxtube radius inside the main spectrometer observed by the detector and therefore an improvement of the transmission. If fully-adiabatic transmission cannot be gained for the full detector area, it is recommended to use the radial dependency of the effect to define fiducial segments. It is important to keep in mind, that if less than 8 detector rings are used in the measurement, the statistical sensitivity is decreased by the factor s_{red} defined in equation (4.26).

4.3 Optimized Measurement Settings

The information gained in sections 4.1 and 4.2 are combined to derive three KATRIN settings, which provide the opportunity to search for keV-scale sterile neutrinos without any hardware modifications. In the course of this section, the advantages and disadvantages of the respective settings are discussed and their potential is shown in terms of the maximum achievable statistical sensitivity of a sterile neutrino measurement.

The three settings can be distinguished according to their different objectives. Details of the complete setting can be found in tables 4.1, 4.2, and 4.3.

1. **Adiabatic setting:** By lowering the source and detector as well as simultaneously increasing the LFCS magnetic field strength, the KATRIN setting is optimized to measure the tritium β -spectrum as deep as possible.

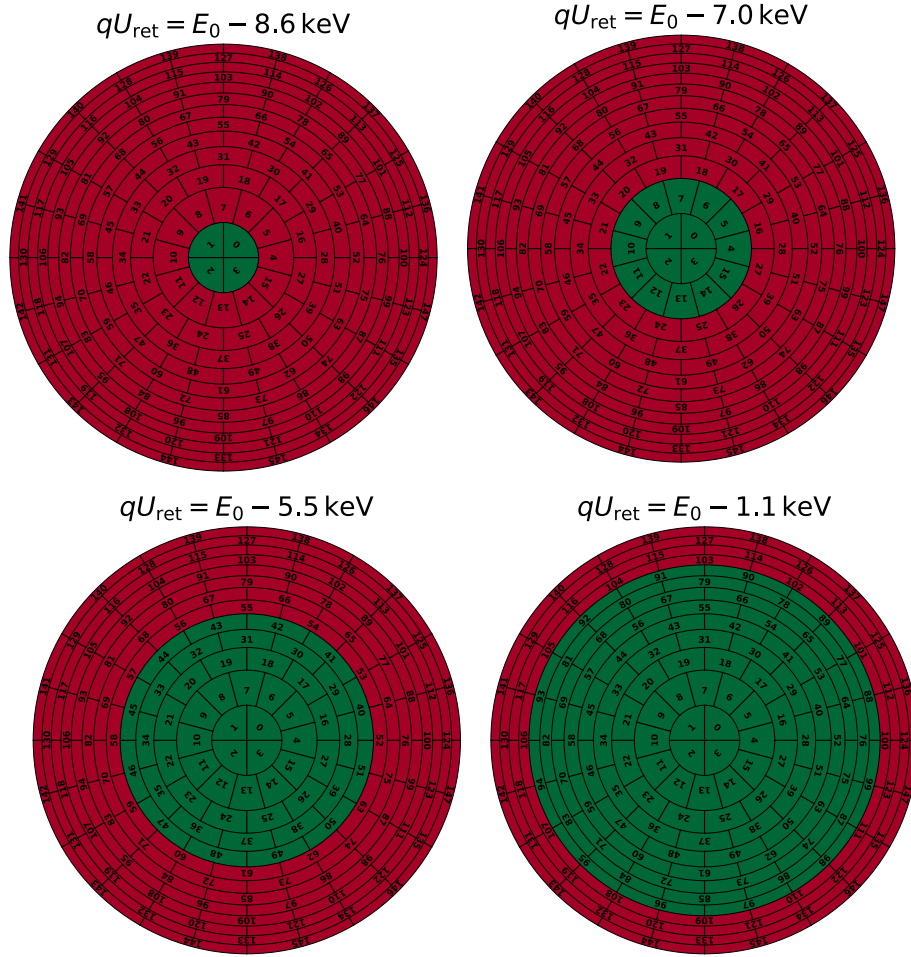


Figure 4.11: The fully-adiabatic areas projected onto the focal plane detector (green) and the detector rings where transmission losses are expected (red) for different applied retarding potentials qU_{ret} . If the spectrum is measured 1.1 keV below the endpoint, only the three outer rings have to be rejected. For high surplus energies up to 8.6 keV the only fiducial detector segment is the bullseye. All values are within a statistical uncertainty of 10^{-4} and calculated for the *max. LFCS* setting and the nominal source and detector magnetic field.

2. **Nominal field setting:** Depending on the measurement time available, it is useful to define a setting, where the KATRIN experiment is operated as close as possible to the nominal setting. In this scenario, the magnetic fields are kept at the nominal KATRIN values, except the LFCS, which is operated at its maximum. To maintain the FPD limits, the source strength is reduced to values close to the minimum defined in section 4.1.2.
3. **Intermediate setting:** A combination of both other settings. The source and detector magnetic field strengths are reduced to a value of $B_{\text{det}} \approx B_s = 2.0 \text{ T}$, while the LFCS is operated at the *max. LFCS* setting. The source is operated at a reduced activity to stay within the FPD limits.

All settings are sub-divided in three scenarios that differ mainly in the observed energy interval. An important characteristic of each scenario is the statistical sensitivity on the sterile neutrino parameter space that can be statistically reached. In order to determine the sensitivity, the $\Delta\chi^2$ (90% C.L.) contours are calculated for a hypothetical 7-day reference measurement. Details on the method and the reference measurement can be found in section 5.1. All statements about fully-adiabatic transmission refer to a statistical uncertainty of 10^{-4} .

4.3.1 Adiabatic Setting

The adiabatic scenarios requires significant changes of the source and detector magnetic field setting. To keep the observed fluxtube inside the main spectrometer as small as possible, the source magnetic field is lowered to $B_s = 0.045 \text{ T}$. To ensure an adiabatic transition between the source and the transport section, the WGTS/F field needs to be ramped down to $B_{\text{WGTS/F}} = 0.2 \text{ T}$. Due to the large cyclotron radii of electrons in the source, the magnetic field at the detector is set to $B_{\text{det}} = 0.039 \text{ T}$. In order to ensure the low source and detector field, all other magnets, except the pinch magnet, must be reduced as well.

The combined rate reduction due to the adjusted magnetic field setting is $f_{\text{red}}^{\text{mag}} = 112.31$ which requires an additional decrease of the source activity. The setting is divided in three scenarios that differ in the measurement window and respectively in the required source strength reduction. Table 4.1 shows an overview of the adjusted parameters.

For scenario 1 a) and b), the source can be operated at a column density of $\rho d = 5 \cdot 10^{16} \text{ cm}^{-2}$ which relates to 10% of the nominal setting. To access the lowest retarding potential of $qU_{\text{ret}}^{\text{min}} = 9.2 \text{ keV}$ for the detector's bullseye, a further reduction of the column density to 4% of the nominal value is required. All scenarios use a tritium purity of $\epsilon_T = 0.1$ which can be achieved by different gas compositions.

Main Spectrometer Transmission

Due to the high LFCS and reduced source and detector magnetic field the fluxtube in the main spectrometer is comparably small, which leads to an adiabatic transmission for the entire detector, on an energy scale down to 6.4 keV from the endpoint.

A further lowering of the retarding potential leads to an increase of non-fiducial detector areas and consequently a reduction of the statistics. The detector bullseye can measure electrons with a surplus energy of up to 9.4 keV at fully-adiabatic transmission.

Statistical Sensitivity on the keV-scale sterile Neutrino Parameter Space

The statistical sensitivity on the keV-scale sterile neutrino mass and mixing angle is displayed in figure 4.12. Scenario 1 c) covers the largest parameter space in terms of sterile neutrino mass with $m_{\nu_s} < 9.4 \text{ keV}$. If the full detector is used, as in scenario 1 a), the accessible mass parameter space is limited to $m_{\nu_s} < 6.4 \text{ keV}$, however, at the maximum possible integrated rate of 100 kcps. Consequently, scenario 1 a) covers the largest parameter space in terms of mixing angle with $\sin^2 \theta < 1.36 \cdot 10^{-4}$. The second scenario 1 b), describes a midway case, where detector rings 0 – 4 are operated at a maximum integrated rate of 52 kcps. The reduced statistics lower the sensitivity on the mixing angle to $\sin^2 \theta < 1.82 \cdot 10^{-4}$, but increases the mass parameter space to $m_{\nu_s} < 7.0 \text{ keV}$.

Conclusion

The adiabatic setting describes a case with a fundamental change of the magnetic field settings. As a benefit, the spectrum can be scanned down to a retarding potential of 9.4 keV below the endpoint. Especially scenario 1 a) obtains a large sterile neutrino parameter space, both in mass and mixing amplitude.

Since the KATRIN experiment has never been operated in such a magnetic field configuration, considering this scenario would require careful commissioning.

4.3.2 Nominal Field Setting

The second setting follows the idea of using KATRIN in its nominal magnetic field settings and only adjusts the LFCS magnetic field to increase the adiabaticity. In order to reduce the signal electron rate, the source is operated at a low activity.

This has two major benefits: 1. it only uses magnetic field settings KATRIN has already been successfully operated with; 2. the modification of the source strength can be prepared beforehand and applied on the time scale of hours, which makes it simple to accommodate the measurement before or after a nominal operation of the experiment⁹.

In order to reduce the signal electron rate at the detector, the source strength needs to be adjusted accordingly. Scenario 2 a) scans the spectrum to values of 1.1 keV below the endpoint for inner detector rings up to ring 8. This high statistics scenario requires a column density of $5 \cdot 10^{16} \text{ cm}^{-2}$ (10 % of the nominal value) and a reduction of the tritium purity to $\epsilon_T = 0.25$. If the spectrum is scanned deeper, as in scenario 2 b) and c), the column density and gas composition needs to be further reduced. Scenario 2 c) requires operation of the source at 1 % column density and a tritium purity of $\epsilon_T = 5.0 \cdot 10^{-3}$. An overview of the corresponding settings can be found in table 4.2.

Main Spectrometer Transmission

The only way to improve the adiabatic transmission through the main spectrometer is the increase of the LFCS magnetic field. Even though the bullseye area of the detector can be used to measure electrons with surplus energies up to $E_{\text{sur}} < 8.6 \text{ keV}$, the non-adiabaticity increases with growing radial position of the detector segments. In the maximum statistics scenario 2 a), the spectrum can only be scanned to energies of 1.1 keV below the endpoint.

⁹It is important to note, that a deviation of ϵ_T from the nominal setting could require time consuming preparation that may include the purging of the entire tritium loop beforehand.

Table 4.1: Overview of the magnetic field and source settings. The maximum rate is derived by the number of fiducial pixels multiplied with the maximum rate per pixel of 1 kcps. If the number of pixels that are used is larger than 100 (ring 0 - 8), the maximum rate is fixed to 100 kcps due to the read-out speed limit of the detector. The source and detector magnetic field strength is reduced by approximately two orders of magnitude compared to the nominal KATRIN setting, which provides the possibility to operate the spectrometer at a minimum retarding voltage of $U_{\text{ret}} = 12.2 \text{ kV}$ by simultaneously ensuring an adiabatic transmission of signal electrons for all detector segments. To stay within the FPD limits, the source strength is reduced to various column densities between $\rho d = (2.0 - 5.0) \cdot 10^{15} \text{ cm}^{-2}$ with tritium purity of $\epsilon_{\text{T}} = 0.1$.

Parameter	scenario 1 a)	scenario 1 b)	scenario 1 c)
fiducial det. rings	full detector	0 - 4	bullseye
maximum rate in kcps	100	52	4
$U_{\text{ret}}^{\text{min}}$ in kV	12.2	11.6	9.2
B_{s} in T	0.045	0.045	0.045
B_{det} in T	0.039	0.039	0.039
LFCS setting	<i>max.</i>	<i>max.</i>	<i>max.</i>
ρd in cm^{-2}	$5 \cdot 10^{16}$	$5 \cdot 10^{16}$	$2 \cdot 10^{16}$
ϵ_{T}	0.1	0.1	0.1

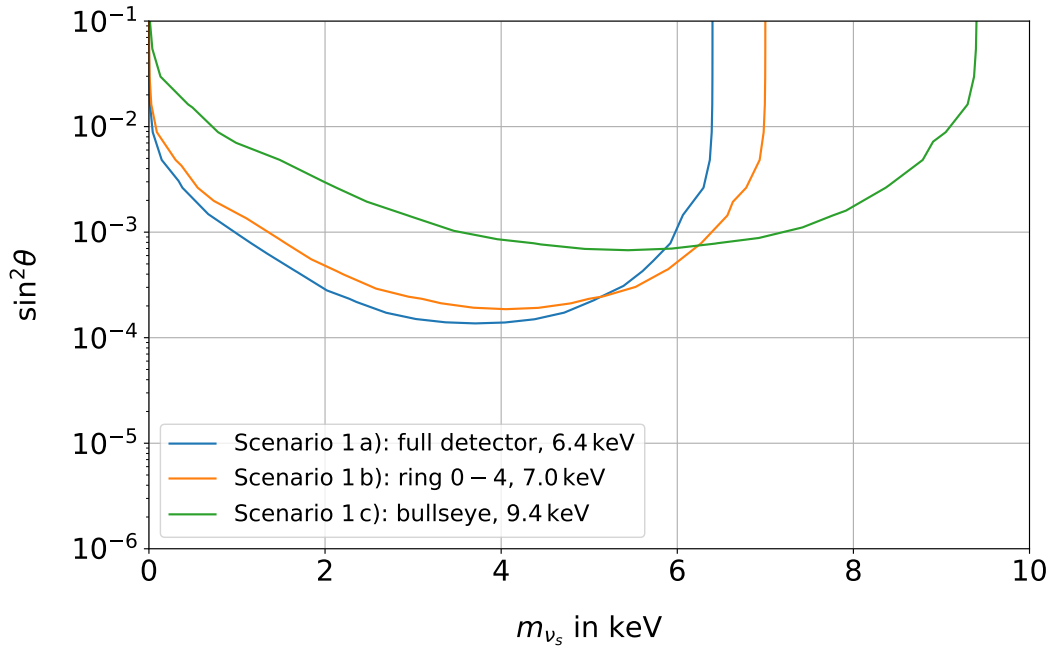


Figure 4.12: The coverage of the sterile neutrino parameter space depends on the minimal retarding potential and statistics of the measurement. For scenario 1 c) the mass parameter sensitivity reaches its maximum at $m_{\nu_s} = 9.4 \text{ keV}$. The gained statistic and therefore the sensitivity on the mixing angle is the largest for scenario 1 a) with a statistical sensitivity on the mixing angle of up to $\sin^2 \theta < 1.36 \cdot 10^{-4}$.

Statistical Sensitivity on the keV-scale sterile Neutrino Parameter Space

The statistical sensitivity on the keV-scale sterile neutrino parameter space is shown in figure 4.13. Scenario 2 c) covers the largest parameter space of sterile neutrino mass. The measurement is sensitive for masses up to $m_{\nu_s} < 8.6 \text{ keV}$ with a sensitivity on the mixing angle of up to $\sin^2 \theta < 6.76 \cdot 10^{-4}$. The high statistics scenario 2 a) covers a maximum mixing angle of $\sin^2 \theta < 1.38 \cdot 10^{-4}$ but is strongly limited in the sensitivity of the sterile neutrino mass to $m_{\nu_s} < 1.1 \text{ keV}$. Scenario 2 b) covers masses up to $m_{\nu_s} < 5.0 \text{ keV}$ with a maximum mixing of $\sin^2 \theta < 1.87 \cdot 10^{-4}$.

Conclusion

This setting is particularly interesting, if the nominal KATRIN magnetic field setting is required for the experimental operation. The reduction of the source activity and adjustment of the LFCS field is well understood and often practiced. This would allow one to supplement a standard KATRIN measurement campaign with a sterile neutrino search, without any risk.

4.3.3 Intermediate Setting

The third setting combines the two previous settings to an intermediate compromise. In order to increase the adiabatic electron transmission, the source magnetic field strength is moderately reduced to $B_s = 2.0 \text{ T}$ and the LFCS field increased to its maximum value. The corresponding magnetic field rate reduction factor of $f_{\text{red}}^{\text{mag}} = 2.02$ is negligible, which explains why the decrease of the source activity is almost the same as for the previous discussed setting. The reduction of the column density reaches from 7% of the nominal value for the high statistics scenario 3 a) to 1.5% for the deep scan scenario 3 c). To further reduce the signal electron rate, the tritium purity has to be kept at $\epsilon_T = 5.0 \cdot 10^{-3}$. Table 4.3 presents an overview on the parameter settings.

Main Spectrometer Transmission

The reduction of the source and detector magnetic field strength by a factor of 1.8 has a significant impact on the adiabatic transmission. In the high statistics scenario it is possible to measure the spectrum down to energies of 5.5 keV below the endpoint. With a maximum $E_{\text{sur}} = 9.2 \text{ keV}$, the deep scan scenario 3 c) barely differs in its potential compared to scenario 1 c) (maximum $E_{\text{sur}} = 9.4 \text{ keV}$), however, requires only a moderate magnetic field reduction.

Statistical Sensitivity on the keV-scale sterile Neutrino Parameter Space

The strength of the intermediate setting is demonstrated most clearly in the statistical sensitivity (figure 4.14). The moderate reduction of the source and detector magnetic field leads to a significant increase of the adiabatic transmission. The high statistics scenario 3 a) allows one to reach an extended coverage of both parameters. It reaches a maximum mixing sensitivity of $\sin^2 \theta < 2.84 \cdot 10^{-4}$ which is only by a factor of two less compared to scenario 2 a) and slightly better than scenario 1 a) (with $\sin^2 \theta < 3.27 \cdot 10^{-4}$). Scenario 3 b) accesses a large mass parameter space of $m_{\nu_s} < 7.9 \text{ keV}$ by providing an decreased statistical sensitivity due to the limitation of the integrated detector rate to 28 kcps of $\sin^2 \theta < 2.56 \cdot 10^{-4}$.

Table 4.2: In scenarios 2 a) - c), the magnetic field settings are set to the nominal KATRIN values, except the LFCS field. In order to maintain the FPD rate limits, the source strength is significantly reduced.

Parameter	scenario 2 a)	scenario 2 b)	scenario 2 c)
fiducial det. rings	0 – 8	0 – 4	bullseye
maximum rate in kcps	100	52	4
$U_{\text{ret}}^{\text{min}}$ in kV	17.5	13.6	10.0
B_s in T	3.60	3.60	3.60
B_{det} in T	3.58	3.58	3.58
LFCS setting	<i>max.</i>	<i>max.</i>	<i>max.</i>
ρd in cm^{-2}	$5 \cdot 10^{16}$	$1 \cdot 10^{16}$	$5 \cdot 10^{15}$
ϵ_T	0.25	$5.0 \cdot 10^{-3}$	$5.0 \cdot 10^{-3}$

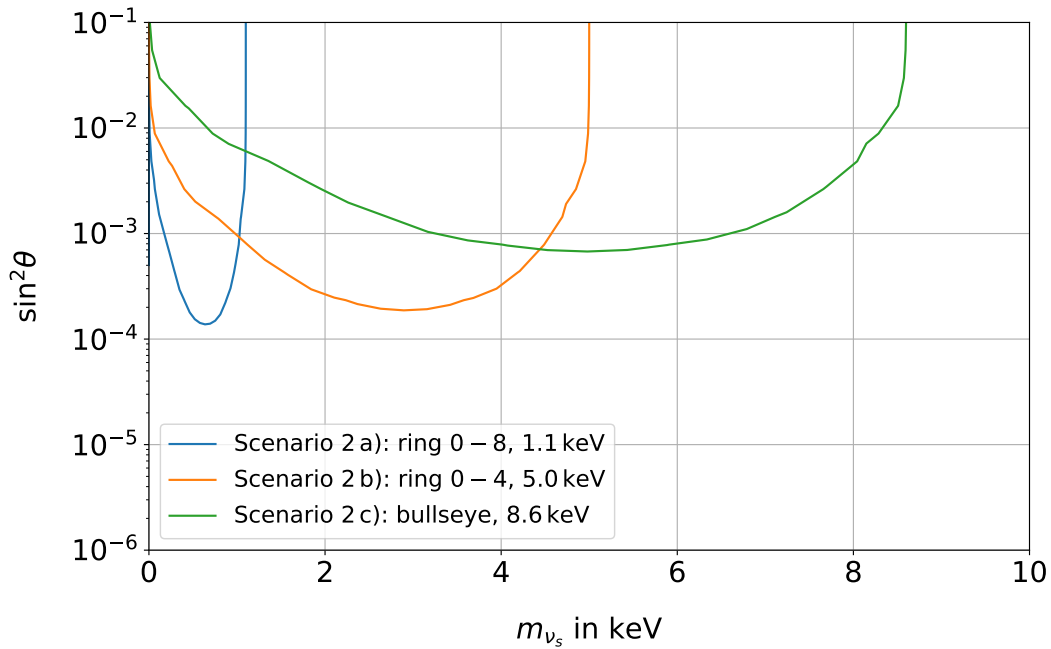


Figure 4.13: Scenario 2 a) uses the technically maximum integrated detector rate of 100 kcps and is therefore most sensitive on the mixing parameter with $\sin^2 \theta < 1.38 \cdot 10^{-4}$. In scenario 2 b), the statistical sensitivity on the mixing is reduced by a factor of 1.3, however, the accessible mass range is approximately 5 times larger.

Table 4.3: In the intermediate setting, the source and detector magnetic fields are reduced to improve the electron transmission through the main spectrometer for electrons with higher surplus energies. As in the two other settings, the LFCS is set to the maximum possible value. Since the signal electron rate reduction is only slightly affected by the lowered source and detector magnetic field, an additional reduction of the source strength is necessary.

Parameter	scenario 3 a)	scenario 3 b)	scenario 3 c)
fiducial det. rings	0 – 8	0 – 2	bullseye
maximum rate in kcps	100	28	4
$U_{\text{ret}}^{\text{min}}$ in kV	13.1	10.7	9.4
B_s in T	2.00	2.00	2.00
B_{det} in T	1.98	1.98	1.98
LFCS setting	<i>max.</i>	<i>max.</i>	<i>max.</i>
ρd in cm^{-2}	$3.5 \cdot 10^{16}$	$1.25 \cdot 10^{16}$	$7.5 \cdot 10^{15}$
ϵ_T	$5.0 \cdot 10^{-3}$	$5.0 \cdot 10^{-3}$	$5.0 \cdot 10^{-3}$

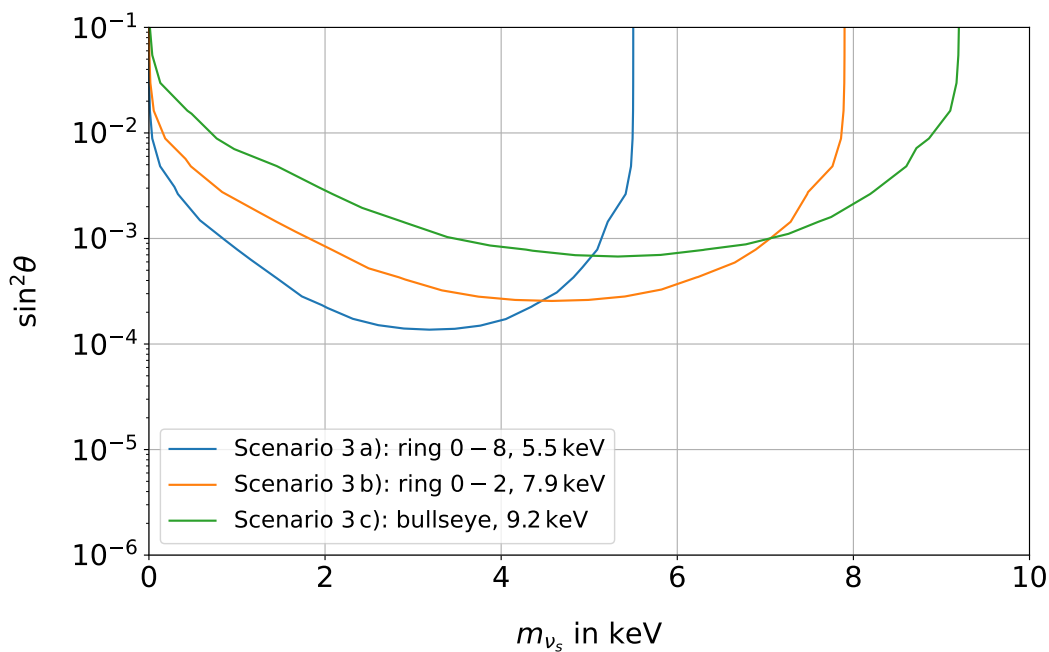


Figure 4.14: The detector bullseye is able to measure surplus energies up to 9.2 keV which is close to the adiabatic setting. The maximum statistical sensitivity on the mixing angle is reached in scenario 3 a) with $\sin^2 \theta < 1.37 \cdot 10^{-4}$, on a comparably large mass range of $m_{\nu_s} < 5.5$ keV. If only the three inner detector rings are used, the spectrum can be measured to values of up to 7.9 keV from the endpoint by only reducing the sensitivity on the mixing angle by a factor of approximately 1.8 compared to the high statistic scenario 3 a).

Conclusion

The intermediate setting proves to be a good compromise to the more conservative nominal field setting, with only modifications of the source strength, and the rather radical adiabatic setting, with the drastic magnetic field reduction. Especially the high statistics scenario 3 a) obtains a good sensitivity coverage with $m_{\nu_s} < 5.5 \text{ keV}$ and $\sin^2 \theta < 1.37 \cdot 10^{-4}$.

The reduction of the source and detector magnetic field by a factor of 1.8 seems realistic within standard KATRIN operations and probably does not require time consuming commissioning.

4.4 Conclusion and Outlook

When the KATRIN experiment is used to search for keV-scales sterile neutrinos, the tritium β -decay spectrum needs to be measured down to several keV below the endpoint. Consequently, the signal rate at the detector increases and exceeds the limit of the FPD at energies of approximately 400 eV below the endpoint. Additionally, the growing surplus energies of signal electrons with respect to the main spectrometer retarding potential lead to transmission losses due to non-adiabaticity.

Both effects can be addressed by an adjustment of the KATRIN magnetic field configuration and by lowering the source activity, which is presented and discussed in sections 4.1 and 4.2.

As a result, three KATRIN settings are derived in section 4.3 which define several scenarios to use the KATRIN experiment, without any hardware modifications, for a keV-scale sterile neutrinos search.

Figure 4.15 illustrates a selection of statistical sensitivities that relate to these settings. By comparing them to the current laboratory limits, they can be set into a context which underlines the potential of a keV-scale sterile neutrino search with the KATRIN experiment. Depending on the scenario, the sensitivity on the mixing angle can exceed the current laboratory limits by up to two orders of magnitude. Scenario 2 a) shows that a large coverage of the parameter space can be studied by the KATRIN experiment, with a setting where the experiment has already been successfully operated with.

The *First Tritium Campaign*, which data is used for a first keV-scale sterile neutrino search with the KATRIN experiment (chapter 6) is one example for a measurement that is comparable to scenario 2 a).

Finally, it is important to point out that all studies show the pure statistical sensitivity. The influence of systematic uncertainties on a keV-scale sterile neutrino search is discussed in detail in the upcoming chapter 5.

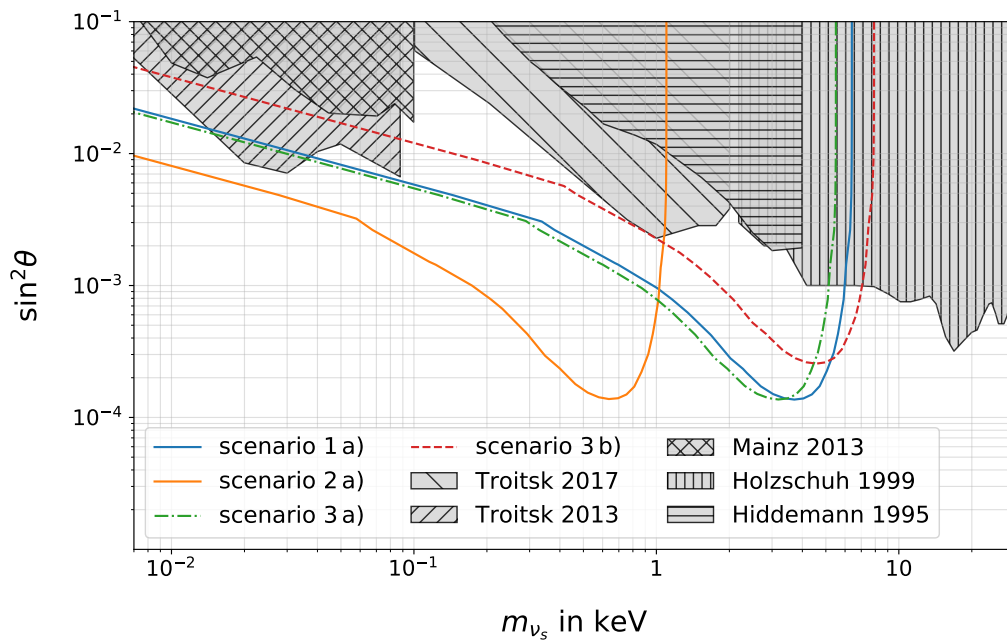


Figure 4.15: Statistical sensitivities of selected scenarios defined in section 4.3 compared to current laboratory limits [244, 245, 246, 247, 248]. Scenarios 1 a, 2 a, and 3 a) cover a large unstudied parameter space, where scenario 2 a and 3 a show similar sensitivity. Scenario 3 b) is less sensitive on the mixing angle, but has the advantage of an increased mass sensitivity.

CHAPTER 5

Systematic Effects of a KATRIN keV-scale sterile Neutrino integral Measurement

The determination of the neutrino mass requires a very good understanding of the tritium spectrum close to the kinematic endpoint E_0 . In order to reach the sensitivity of 0.2 eV (90% C.L.), a systematic uncertainty budget of $\sigma_{\text{syst}} = 0.017 \text{ eV}^2$ is required as shown in the KATRIN design report. [10] A state of the art overview of the KATRIN systematic effects and uncertainties can be found in [249].

If the KATRIN experiment is used to search for keV-scale sterile neutrinos, the entire energy range of the spectrum is of interest. Over the last years, there have been many efforts to study systematic effects related to an integral keV-scale sterile neutrino measurement with the KATRIN experiment. Examples can be found in [12, 16, 98, 259, 260, 47, 261, 262].

This chapter presents the first comprehensive, consistent and therefore comparable overview of all yet known systematic effects that are relevant for an integral keV-scale sterile neutrino measurement. In order to achieve this, many information from existing publications and theses are collected, extended and completed by own investigations with the objective to get an understanding of the scale of the effects and their impact on the sensitivity. Furthermore, open questions are identified and studied to derive recommendations for next steps towards future sterile neutrino measurements. In addition, the results of this chapter find a practical application in the first sterile neutrino analysis of KATRIN data presented in chapter 6.

The chapter is structured as follows: The first section gives an overview of the general analysis strategy when KATRIN is used to search for keV-scale sterile neutrinos and introduces the treatment of systematic uncertainties in the analysis (section 5.1). In the second part, all yet known systematic effects are discussed in detail, quantified, and their influence on the sensitivity of a keV-scale sterile neutrino search is studied (sections 5.2 - 5.8). If possible, countermeasures to reduce the systematic effects are identified and included in the investigation. The last part of the chapter summarizes the effects, concludes the studies, and gives recommendations for the future (section 5.9).

5.1 Analysis Strategy

The KATRIN experiment measures the integral tritium β -decay spectrum. For the analysis, the observed spectrum $N_{\text{obs},i}$ is fit to a predicted model $N_{\text{pre},i}$ by maximizing the likelihood function

$$L(\theta|N_{\text{obs},i}) = \prod_i p(N_{\text{obs},i}|N_{\text{pre},i}(qU_i, \Theta)), \quad (5.1)$$

where Θ are the free fit parameters. For neutrino mass determination, Θ consists of the neutrino mass squared m_ν^2 , the background rate R_{bg} , the endpoint of the spectrum E_0 , and the signal amplitude R_{sig} . [263]

For numerical and technical reasons it is simpler to minimize the negative logarithmic likelihood (referred to as the log-likelihood)

$$-\log L(\theta|N_{\text{obs},i}) = -\prod_i \log p(N_{\text{obs},i}|N_{\text{pre},i}(qU_i, \theta)), \quad (5.2)$$

by solving

$$\left. \frac{d}{d\theta} (-\log L(\theta|N_{\text{obs},i})) \right|_{\theta_{\text{best}}} = 0, \quad (5.3)$$

in order to get the best fit parameters θ_{best} [264]. This procedure requires the assumption of an underlying Poisson distribution of the observed data. If the number of observed events $N_{\text{obs},i}$ is larger than 25, it can be approximated by a Gaussian distribution and the log-likelihood can be expressed in a chi-square function

$$-2\log L \approx \chi^2 = \sum_i \left(\frac{N_{\text{obs},i} - N_{\text{pre},i}(\theta)}{\sigma_i} \right)^2, \quad (5.4)$$

with the statistical uncertainty $\sigma_i \approx \sqrt{N_{\text{pre},i}}$. [263]

Construction of Exclusion Limit

If measured data is used to search for keV-scale sterile neutrinos, the tritium β -decay model is extended by a sterile neutrino mass eigenstate m_{ν_s} and a mixing amplitude $\sin^2 \theta$ as described in equation (3.17) [12].

The sterile neutrino parameter space is binned in a fine grid of $(m_{\nu_s}, \sin^2 \theta)_{i,j}$ combinations. For each tuple, the measured data is fit to the model by minimizing χ^2 . By comparing the resulting $\chi^2(m_{\nu_s}, \sin^2 \theta)_{i,j}$ to that of the fit of the null hypothesis $\chi_{\text{NH}}^2(0, 0)$, parameter space can be excluded by the criterion

$$\Delta\chi_{i,j}^2 = \chi^2(m_{\nu_s}, \sin^2 \theta)_{i,j} - \chi_{\text{NH}}^2 \leq 4.61 \quad (5.5)$$

at 90 % C.L¹. [12, 263]

There are two different ways to include statistical and systematic uncertainties to the χ^2 : The *pull approach* implements an additional constrained fit parameter that increases the χ^2 -function and therefore penalizes it. The *covariance-matrix approach* expresses all systematic effects in a single covariance matrix and is implemented directly in a re-written version of the χ^2 -function. In principle, the two methods can also be combined, since $\chi_{\text{pull}}^2 = \chi_{\text{cov}}^2$ assuming a Gaussian probability distribution function. [265]

¹There are cases where the $\Delta\chi^2$ is calculated with the $\chi_{\text{min}}^2 = \min(\chi^2(m_{\nu_s}, \sin^2 \theta)_{i,j})$ corresponding to the best fit instead of the χ_{NH}^2 , for example in [12]. For small mixing angles, statistical fluctuations can lead to a better fit result than the null hypothesis, but with a small statistical significance. In order to avoid this, the definition of equation (5.5) is chosen in this work.

The following will give a short introduction to both methods. A detailed introduction to the topic can be found in [265, 266].

Pull Approach

In the pull approach, the systematic effects are implemented as additional nuisance fit parameters with the best estimate being $\hat{\zeta}_j$ with its uncertainty σ_{ζ_j} that both have to be gained experimentally, via simulations or calculations [249]. The uncertainty parameters extend the χ^2 -function with penalty terms

$$\chi_{\text{pull}}^2 = \sum_i \left(\frac{N_{\text{obs},i} - N_{\text{pre},i}(\theta)}{\sigma_i} \right)^2 + \sum_j \left(\frac{\hat{\zeta}_j - \zeta_j}{\sigma_{\zeta_j}} \right)^2 \quad [263]. \quad (5.6)$$

The individual treatment of the uncertainties allows one to study their influence on the sensitivity separately. However, additional fit parameters require supplementary computation effort which state a clear disadvantage for example for pixel or run wise multifits. [249]

Covariance Matrix Approach

In the covariance matrix approach the statistical and systematic uncertainties can be combined to one covariance matrix

$$V_{i,j} = \delta_{ij} \sigma_{\text{stat},i} \sigma_{\text{stat},j} + \sum_k \sigma_{\text{sys},i}^k \sigma_{\text{sys},j}^k + \delta_{ij} \sigma_{\text{sys},i} \sigma_{\text{sys},j}, \quad (5.7)$$

where σ_{stat} is the uncorrelated statistical, σ_{sys}^k is the correlated, and σ_{sys} is the uncorrelated systematic uncertainties [249]. In order to calculate a covariance matrix for a systematic effect, the uncertain parameter in the model is varied N -times [267]. The covariance matrix can be extracted from the variance of the spectra \vec{r}

$$V_{i,j} = \frac{1}{N} \sum_n (\vec{r}_i - \langle \vec{r}_i \rangle) \cdot (\vec{r}_j - \langle \vec{r}_j \rangle), \quad (5.8)$$

normalized by N [47].

In order to consider a systematic effect expressed in a covariance matrix in the analysis, the χ^2 -function is extended to

$$\chi_{\text{cov}}^2 = \sum_{i,j} (N_{\text{obs},i} - N_{\text{pre},i}) V_{i,j}^{-1} (N_{\text{obs},j} - N_{\text{pre},j}) \quad (5.9)$$

including the inverse covariance matrix $V_{i,j}^{-1}$. With growing i and j the complexity of inverting $V_{i,j}$ increases. However, the single covariance matrices need to be calculated only once for a certain set of experimental parameters. [249]

Study of systematic Effects

In the following, all yet known systematic uncertainties that are relevant for a keV-scale sterile neutrino search are studied according to the same scheme: after an introduction to the effect, its influence on the spectral shape is calculated. If an analytical description is not possible, approximations or simulations are used. After that, the effect is implemented

in the model and its uncertainty is estimated. The model used in the analysis was developed in the scope of this thesis and is a multithreaded Python code based on the NumPy and SciPy libraries².

The impact of the systematic effects on a sterile neutrino search are studied for a hypothetical *7-day reference measurement*. The total measurement time of one week is equally distributed over the measurement interval from [1.0, 18.575] keV in 100 steps. The maximum integrated rate is 100 kcps (maximum read-out rate of the FPD) which is assumed to be reached at the lowest retarding potential. For the main spectrometer background, a flat distributed rate of 300 mcps is used. It is assumed, that the main spectrometer transmission is fully adiabatic for all tritium β -decay energies. The uncertainties on the systematic effects are considered via the covariance matrix approach as introduced above.

5.2 Backscattering on the Rear Wall

The rear section is located at the up stream end of the source. It consists of the rear wall chamber, a stainless steel housing where the rear wall is located. The rear wall itself is a gold-plated disc with a diameter of 28.6 cm. The main task of the rear wall is to provide a homogeneous starting potential for the source electrons. [142] Furthermore, the rear section is used to monitor the source activity by measuring the characteristic x-ray spectrum of β -electrons that hit the rear wall gold disc and is equipped with an electron gun that can be used to determine the absolute value of the column density and the energy loss function with exceptional precision (see section 5.3) [144].

Electrons that scatter back at the rear wall surface have a non-zero probability to reach the FPD and contribute to the measured spectrum. The influence of rear wall backscattering on a keV-scale sterile neutrino search was first investigated in [259]. The work focused on a scenario with a very small source magnetic field of 0.05 T and quantified the size of the contribution, but did not study the effect on the spectral shape. The work in hand gives a general overview of the effect and shows the dependency on experimental parameters. It introduces a model that is required in analyses and shows how uncertainties influence the sensitivity of a sterile neutrino search.

Transmission and Reflection of Source Electrons

Whether β -electrons that are generated in the source reach the detector or not, is determined by two of their starting conditions:

- Their initial kinetic energy must be sufficient to overcome the electric potential of the main spectrometer $E_{\text{ini}} > qU_{\text{ret}}$.
- Their starting polar angle has to be smaller than the maximum acceptance angle defined by the source and the pinch magnetic field $\theta_s < \theta_{\text{max}} = \sin^{-1} \sqrt{\frac{B_s}{B_{\text{pch}}}}$.

For the nominal magnetic field setting of KATRIN, where $B_s = 3.6$ T and $B_{\text{pch}} = 6.0$ T, the probability for electrons to fulfill the second condition is

$$P_{\text{wgts,fpd}} = \frac{1}{2} \cdot \left(1 - \sqrt{1 - \frac{B_s}{B_{\text{pch}}}} \right) = 0.1837, \quad (5.10)$$

²The basis of the code was developed by Marc Korzeczek, Institute of Experimental Particle Physics, Karlsruhe Institute of Technology

following equations (4.4) - (4.9).

All β -electrons that do not reach the detector directly are guided back to the rear wall gold disc where they undergo elastic and inelastic scattering as well as ionization interactions with the rear wall material [268]. The electrons are either absorbed by the material or scatter back due to angular changing processes. Depending on their scattering angle, some of the backscattered electrons are able to reach the detector with a modified energy distribution caused by the scattering energy loss. [259]

For the KATRIN neutrino mass determination, studies show that electron backscattering at the rear wall is of no concern, since the backscattered electrons loose too much energy to overcome the retarding potential [10, 249]. If the tritium β -decay spectrum is studied over a wider energy range and the retarding potential is lowered, the backscattered electrons can have a significant contribution to the observed spectrum [259].

5.2.1 Influence on the Spectrum

Similar to [259] equations (3.3)-(3.10), the spectrum observed at the detector including the fraction of backscattered electrons can be written as³

$$\Gamma_{\text{with}} = P_{\text{wgts,fpd}} \times \Gamma_{\beta} + (1 - P_{\text{wgts,fpd}}) \cdot P_{\text{BS}} \cdot P_{\text{rw,fpd}} \times \Gamma_{\text{rw}}. \quad (5.11)$$

The unchanged β -spectrum coming from the source Γ_{β} as well as the backscattered spectrum originating at the rear wall Γ_{rw} are weighted with the following probabilities:

- The factor $P_{\text{wgts,fpd}}$ is defined in equation (5.10) and describes the electrons that reach the FPD detector without being magnetically reflected at the pinch magnet.
- P_{BS} is the backscattering probability of tritium β -decay electrons on the rear wall. For the nominal KATRIN magnetic field setting and golden rear wall disc the probability is found to be $P_{\text{BS}} = 0.447$.
- The probability of backscattered electrons to reach the detector $P_{\text{rw,fpd}}$ is determined by the rear wall and detector magnetic field as well as the angular distribution of the backscattered electrons. At nominal magnetic field setting, a fraction of $P_{\text{rw,fpd}} = 0.268$ of the backscattered electrons are able to reach the detector.

The backscattering probability P_{BS} as well as the energy and angular distribution of backscattered electrons have been determined with combined GEANT4 and *KASPER* simulations. Details on the simulations as well as a validation study of GEANT4 backscattering simulations can be found in appendices D and E.

The prefactors of equation (5.11) can be combined to

$$f_{\beta} = P_{\text{wgts,fpd}}, \quad (5.12)$$

$$f_{\text{dist}} = (1 - P_{\text{wgts,fpd}}) \cdot P_{\text{BS}} \cdot P_{\text{rw,fpd}}. \quad (5.13)$$

In order to see the relative influence of the effect on the spectral shape⁴, the ratio of

$$\frac{\int \Gamma_{\text{with}}}{\int \Gamma_{\text{without}}} - 1 = \frac{\int (f_{\beta} \times \Gamma_{\beta} + f_{\text{dist}} \times \Gamma_{\text{rw}})}{\int (f_{\beta} \times \Gamma_{\beta} + f_{\text{dist}} \times \Gamma_{\beta})} - 1 \quad (5.14)$$

as a function of the retarding energy is shown in figure 5.1. The relative influence of the backscattered electrons is large, with values up to 0.339 ($\cong 33.9\%$), in the region

³Electron scattering on hydrogen molecules in the source is not considered here. For a detailed discussion on the influence, see 5.2.

⁴The number of electrons is chosen to be equal for both spectra since only the size of the shape variation is of interest. The total number of electrons is absorbed in the analysis as a normalization by fitting R_{sig} .

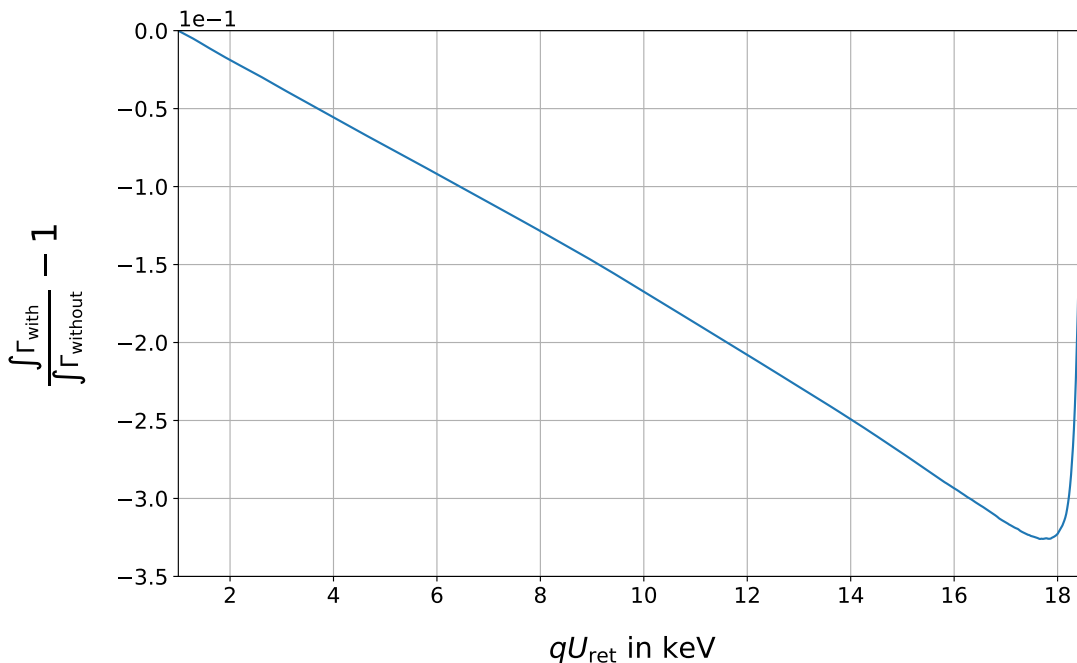


Figure 5.1: The spectral distortion caused by electrons that scattered back at the gold-plated rear wall disc. For lower energies, where the count rates are small, the largest relative deviation of approximately 0.339 is reached.

of the spectrum with low count rate. Modeling such a large effect is challenging, since the uncertainties on the model significantly impact the observed spectrum. Therefore countermeasures are required.

5.2.2 Countermeasures

In order to get a better understanding of the size of the effect, the ratio of both prefactors

$$R_{\text{dist}} = \frac{f_{\text{dist}}}{f_{\beta}}, \quad (5.15)$$

can be used as a direct measure for the distortion caused by backscattered electrons (adapted from [259]).

There are two parameters that influence R_{dist} :

1. **Rear wall magnetic field:** The probability for a backscattered electron to reach the detector depends on the ratio of the rear wall and pinch magnetic field. By lowering B_{rw} , the maximum transmission angle decreases and with it the fraction of electrons that cause the distortion. In addition, the backscattering probability will slightly decrease, since the impact angle θ_{imp} gets flatter if the source magnetic field is kept at the nominal value (see figure D.3 in appendix D). [259] The blue line in the green shaded area of figure 5.2 shows the decrease of R_{dist} as a function of B_{rw} at a fixed source magnetic field of 3.6 T. The rear wall magnetic field is limited to $B_{\text{rw}} \gtrsim 0.16$ T due to the stray field of the source. A further reduction of the magnetic field can only be reached, by a pole reversal of the rear section magnet (orange dashed line), or a simultaneous lowering of the source magnetic field (blue dashed line).

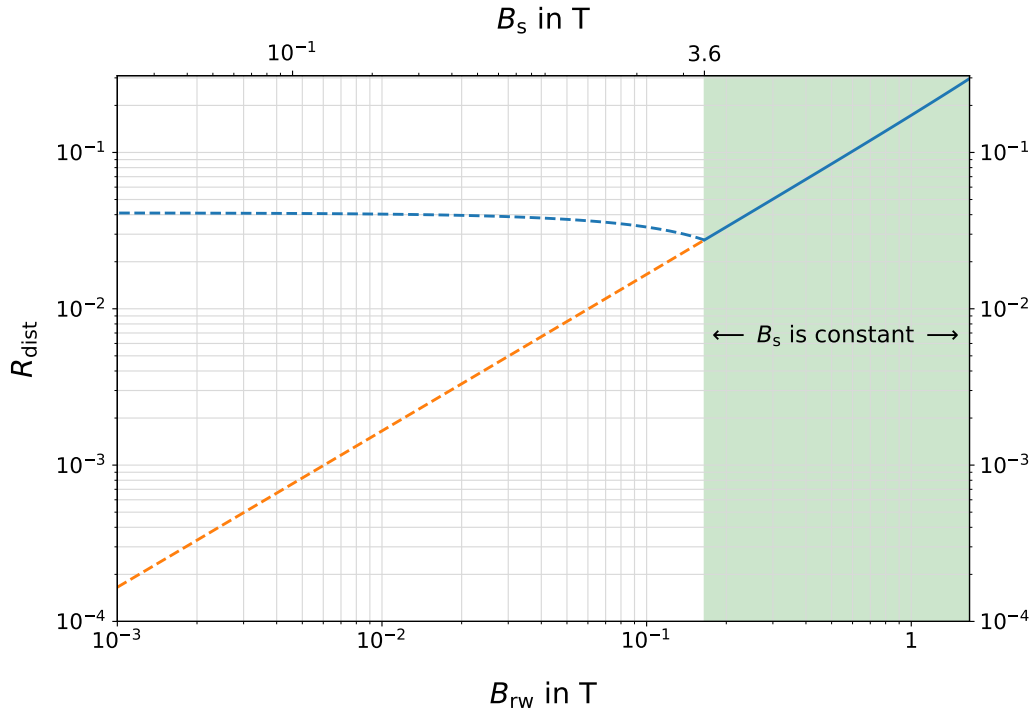


Figure 5.2: If the source magnetic field is kept at its nominal value of 3.6 T, a reduction of the rear wall field leads to a decrease of the contribution of backscattered electrons to the measured spectrum (green shaded area). Due to the stray field of the source, the magnetic field at the rear wall is limited to approximately $B_{rw} = 0.16$ T. If the rear section magnet current would be reversed in polarity, the stray field could be compensated, introducing the opportunity for a large suppression of the effect (orange dashed line). A reduction of the source magnetic field would lead to a small increase of the contribution. After $B_s = 0.5$ T, the ratio would be constant at a value of $4.0 \cdot 10^{-2}$.

2. **Source magnetic field:** A lowering of the source magnetic field leads to an increase of the effect, since the number of magnetically reflected source electrons is enhanced and the number of electrons participating in rear wall backscattering increases [259]. In addition, the contribution of unscattered β -electrons to the measured spectrum is reduced, which can be compensated by simultaneously lowering the rear wall magnetic field.

If the pole of the rear section magnet is not reversed, turning it off while maintaining the source magnetic field at its nominal value gives the setting with the smallest relative contribution of backscattered electrons to the measured spectrum of up to $2.7 \cdot 10^{-2}$.

If for any reason the source magnetic field needs to be lowered, a simultaneous lowering of the rear wall magnetic field is required. If the pole of the magnet is not reversed, the smallest relative contribution is up to $4.1 \cdot 10^{-2}$ [259].

Nominal KATRIN Setting with the Rear Section Magnet turned off

Turning off the rear section magnet has an additional advantage. Figure 5.3 shows two schematic views of the rear section. The blue area displays the magnetic fluxtube that connects the detector and the rear wall. The upper pictures illustrate the magnetic fluxtube at the nominal magnetic field setting of $B_{rw} = 1.66$ T. All field lines are mapped on the gold-plated rear wall disc.

If the rear section magnet is turned off, the fluxtube widens and the field lines do not connect only to the rear wall disc, but also to the stainless steel chamber walls. The

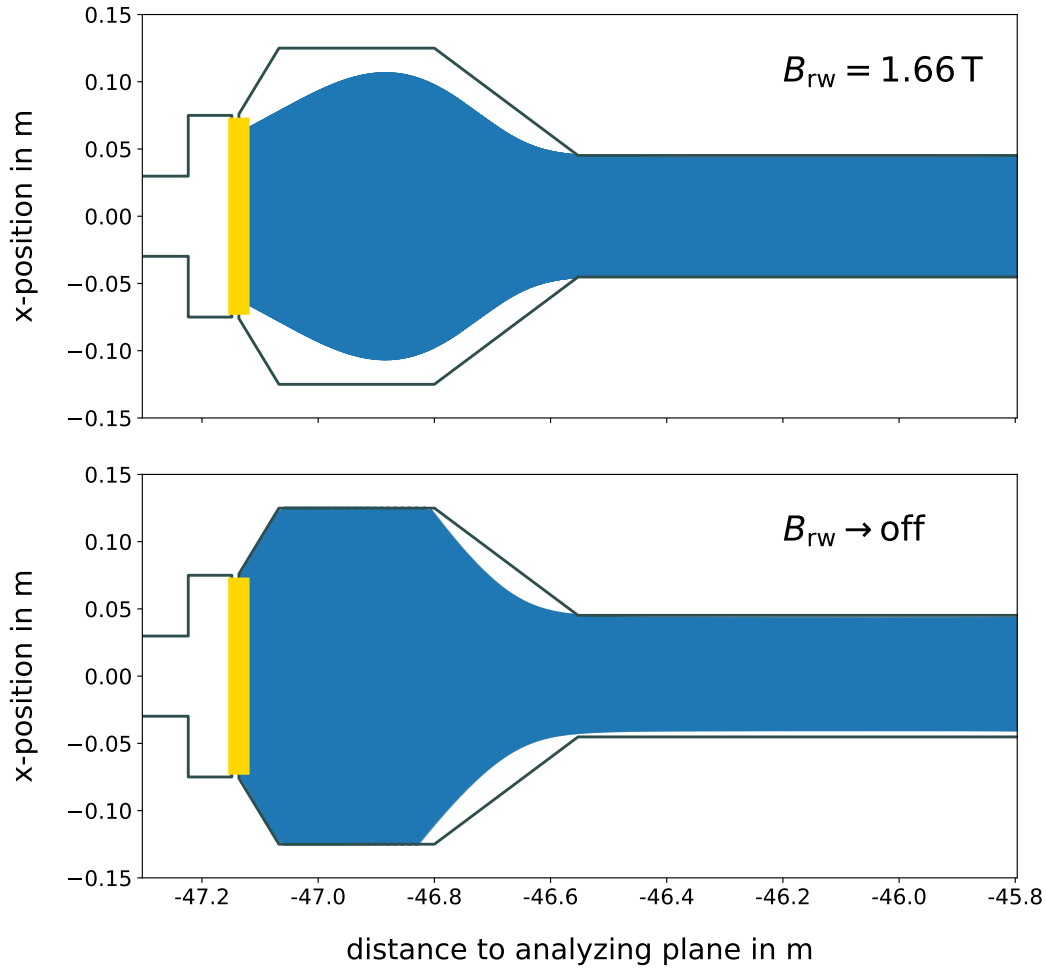


Figure 5.3: The rear wall chamber at two different magnetic field settings. The nominal KATRIN setting (upper illustration) and a scenario where the rear section magnet is turned off (bottom illustration). The blue area shows the magnetic fluxtube that connects the rear wall to the detector. In the nominal setting the field lines all connect to the gold-plated rear wall disc. If the rear section superconducting magnet is turned off, the fluxtube mainly connects to the stainless steel rear wall chamber and only the inner part of the detector observes the rear wall disc. Figure is adapted from [259] figure 3.1.

backscattering probability for stainless steel is smaller by approximately a factor of two compared to gold (for details see appendix D). In combination with the lower rear wall magnetic field, the influence of electron backscattering at the rear wall can be reduced by more than a factor of ten by this experimental modification as can be seen in figure 5.4. [259]

In addition, a distinct radial dependency of the effect is found. Due to a widening of the magnetic fluxtube, the FPD rings observe areas of different B_{rw} , which needs to be considered in the analysis.

5.2.3 Uncertainties and Influence on the Sensitivity

The uncertainties on the model can be divided into two groups: 1. uncertainties on the underlying simulations; 2. influences of simplifications the model is based on. In the following, both are discussed and their impact on the sensitivity of a sterile neutrino measurement is calculated.

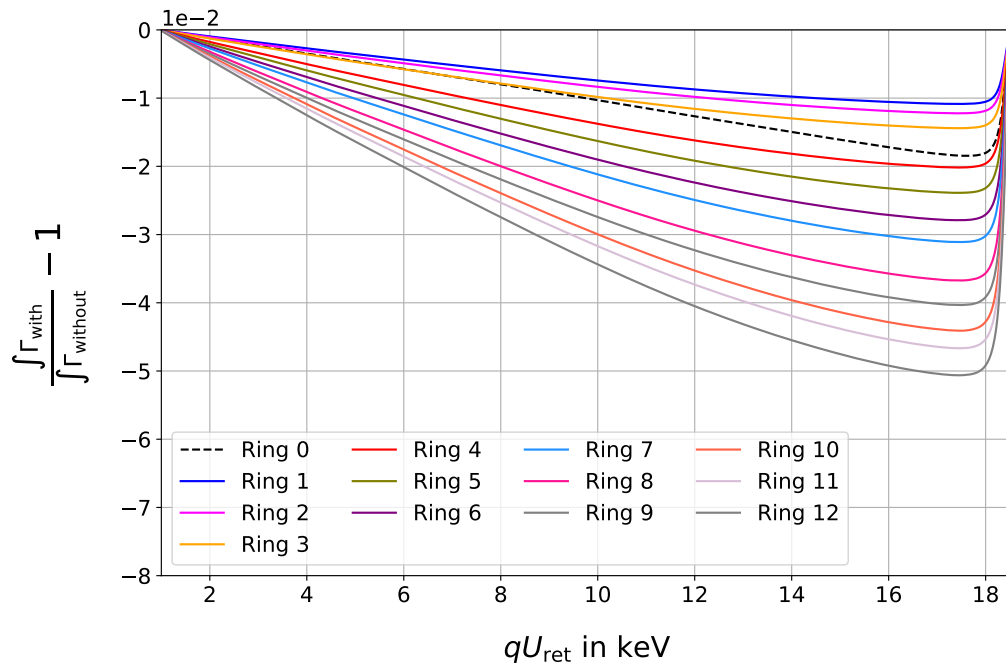


Figure 5.4: If the rear wall magnets are turned off, the distortion is smaller compared to the nominal KATRIN setting (figure D.4). The rear wall magnetic field scales with the radius of the field lines from small values in the center $B_{\text{rw}}^0 = 0.062$ T up to $B_{\text{rw}}^{12} = 0.296$ T for the outermost detector ring. As a consequence, the size of the distortion depends on the detector ring that observes the spectrum. The detector bullseye is the only ring where the field lines connect to the gold-plated rear wall. In all other cases, the electrons scatter back at stainless steel (two times smaller backscattering probability), explaining why the size of the distortion of ring 0 is between the values of ring 3 and 4.

Uncertainty on the underlying Simulations

The modeling of the spectral influence is based on two types of simulations:

1. **Backscattering simulations with *GEANT4*:** The simulations are required to determine the backscattering probability P_{BS} as well as the energy and angular distribution of the backscattered electrons [259]. Appendix E shows a validation study of angular and energy distributions, simulated with *GEANT4* that show deviations from measurements in the order of $\sigma_{geant} < 20\%$. This value is applied as an uncorrelated and energy independent uncertainty on the model.
2. **Magnetic field simulations with *KASPER*:** The simulation of the magnetic field is required to calculate the impact angle θ_{imp} of the electrons on the rear wall surface as well as the coefficients $P_{wgts,fpd}$ and $P_{rw,fpd}$ [259]. There is a large number of experimental validations of *KASPER* magnetic field simulations (for a comprehensive example see [269]). In [270], the uncertainties $\sigma_{B_s} = 2.5\%$ and $\sigma_{B_{pch}} = 0.2\%$ are derived. An uncertainty on the rear wall magnetic field has not been determined yet, but is assumed to be of the same size as the source magnetic field $\sigma_{B_{RW}} = \sigma_{B_s} = 2.5\%$. Their contribution on the uncertainty on the model can be derived by recalculating the effect for a large number of randomly generated fluctuated fields (uncorrelated). The calculations show that the field fluctuations lead to an overall uncertainty of $\sigma_{mag} = 5.6\%$.

Influence of Simplifications

Two major simplifications have been made in the modeling of rear wall backscattering:

1. **Neglecting source scattering:** Only half of the electrons that are generated in the source, propagate directly towards the rear wall. Approximately 31% of the source electrons are emitted in detector direction and magnetically reflected at the pinch magnet. Due to the scattering of electrons on the tritium molecules in the source (reflected electrons have to pass the source up to two times), the energy distribution of the electrons is different to the ones which directly propagate to the rear wall. This effect has an influence on the shape of the backscattered spectrum Γ_{rw} .
2. **Neglecting multiple rear wall scattering:** Backscattered electrons have a probability of $(1 - P_{rw,fpd})$ of being magnetically reflected at the pinch. Reflected electrons will propagate back to the rear wall and undergo a second backscattering process with the probability P_{BS} . This procedure can be repeated until the backscattering angle is small enough to finally reach the detector, or the energy loss is large enough to be blocked by the retarding potential. This leads to an increase of the effective number of electrons that reach the rear wall $P_{rw,fpd} \rightarrow P_{rw,fpd}^*$. Furthermore, a modeling of multiple scattered events has to consider the deviated energy distribution due to the consecutive backscattering as well as the influenced of scattering in the source. In this work, this effect introduces the largest uncertainty on the model and is estimated to be 20%.

Figure 5.5 shows the influence of different model uncertainties on the sensitivity of the 7-day reference measurement. If the rear section magnet is operated at nominal setting, the impact of the uncertainty on the model is large, and leads to a reduction of the sensitivity on the mixing angle $\sin^2 \theta$ of up to a factor 20. For the low field scenario, the impact of the 20% uncorrelated uncertainty is moderate, with a maximum sensitivity reduction of a factor of four. If the model would be improved, and the uncertainty limited to 10% the sensitivity loss can be further reduced to a maximum reduction of a factor of two.

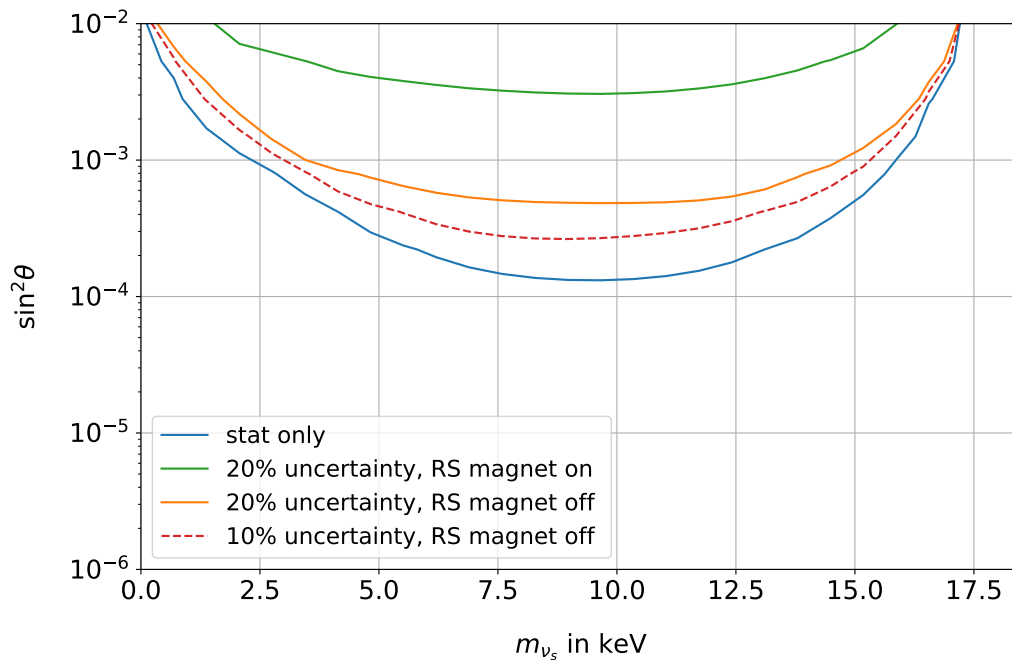


Figure 5.5: The sensitivity of the *7-day reference measurement* including the rear wall backscattering correction. The blue line shows the statistical sensitivity without uncertainties on the correction. The resulting sensitivities for an uncorrelated uncertainty on the model of 20% is shown in the green line (nominal KATRIN setting) as well as the orange line (rear section off). The red dashed line shows the hypothetical case of a reduced uncertainty of the model.

5.2.4 Conclusion

If the endpoint region of the tritium β -decay is studied, electrons that are backscattered at the rear wall are effectively blocked by the retarding potential [249]. By lowering qU_{ret} , the number of backscattered electrons that are able to reach the detector increases, which leads to a distinct deviation of the measured spectrum (maximum relative contribution of 34%) [259].

By lowering the rear wall magnetic field, the effect can be reduced due to the higher magnetic reflection probability of backscattered electrons at the pinch magnet and a widening of the fluxtube. The countermeasure of a reduced rear wall magnetic field is limited by the stray field of the source magnets. [259] An additional reduction can be gained, by reversing the rear section magnet current to generate a compensation field. The option of a new rear wall made of a material with a low backscattering coefficient (for example ${}^4\text{Be}$) is discussed in section 7.3.

By implementing the effect in the model, the impact on the sterile neutrino search was investigated. The uncertainties on the underlying simulations as well as the simplifications that have been made in order to determine the shape of the effect introduce a relative large systematic uncertainty of 20%, which reduces the sensitivity by up to a factor of 20 (nominal KATRIN setting) or a factor of four if the rear section magnet is turned off.

The large uncertainty on the model can be reduced by considering source scattering as well as multiple scattering on the rear wall. One approach for a new model is presented in

section 7.4. Furthermore, simulations can be validated with dedicated measurements as, for example, proposed in [16].

5.3 Electron Scattering in the Source

While electrons propagate from their point of generation to the detector, they have a probability to undergo several scattering processes mainly on hydrogen molecules in the WGTS. As a consequence, the probability for electrons to overcome the retarding potential does not only depend on their starting energy, but also on the numbers of scatterings they underwent in the source and the corresponding energy loss. [10]

This probability is expressed in the KATRIN response function which has been developed over many years of collective work, with focus on energies in the endpoint region of the tritium β -decay spectrum (see for example [10, 138, 124]).

If lower energy ranges of the tritium β -spectrum are measured, which is required for a keV-scale sterile neutrino search, the validation of the response function has to be studied over the full energy scale.

5.3.1 Influence on the Spectrum

In a MAC-E filter system, the rate of transmitted electrons depends on the retarding potential qU_{ret} and is given by

$$\frac{dN(qU_{\text{ret}})}{dt} \propto \int_{qU_{\text{ret}}}^{E_0} \frac{d^2N}{dEdt}(E_0, m_{\nu_e}^2) \cdot T(E, qU_{\text{ret}}) dE, \quad (5.16)$$

where the differential tritium β -decay spectrum is $\frac{d^2N}{dEdt}(E_0, m_{\nu_e}^2)$ [124]. The transmission function $T(E, qU_{\text{ret}})$ describes the probability of an electron to pass the MAC-E filter electrostatic barrier. In the case of tritium β -decay with an isotropic starting angular distribution, $T(E, qU_{\text{ret}})$ is given by

$$T(E, qU_{\text{ret}}) = \begin{cases} 0 & E - qU_{\text{ret}} < 0 \\ \frac{1 - \sqrt{1 - \frac{E - qU_{\text{ret}}}{E} \cdot \frac{B_s}{B_a}}}{1 - \sqrt{1 - \frac{B_s}{B_{\text{pch}}}}} & 0 \leq E - qU_{\text{ret}} \leq \Delta E \\ 1 & E - qU_{\text{ret}} > \Delta E \end{cases}, \quad (5.17)$$

with the energy resolution ΔE as derived in equation (2.8). [10]

The energy loss of electrons caused by scattering has a first order contribution to the observed rate. In order to take this into account, equation (5.16) can be written as

$$\frac{dN(qU_{\text{ret}})}{dt} \propto \int_{qU_{\text{ret}}}^{E_0} \frac{d^2N}{dEdt}(E_0, m_{\nu_e}^2) \cdot R(E, qU_{\text{ret}}) dE, \quad (5.18)$$

where the transmission function $T(E, qU_{\text{ret}})$ is replaced by the response function of the experiment $R(E, qU_{\text{ret}})$, additionally describing the energy loss of the electrons. [124]

The energy loss ϵ of an inelastic scattering process is described by the energy loss distribution

$$f(\epsilon) = \frac{1}{\sigma_{\text{inel}}} \cdot \frac{d\sigma}{d\epsilon}, \quad (5.19)$$

where σ_{inel} is the inelastic scattering cross section [10].

The shape of the energy loss function has been measured and parameterized for electron

kinetic energies of 18 keV, assuming a constant inelastic scattering cross section of $(3.40 \pm 0.07) \cdot 10^{-18} \text{ cm}^2$:

$$f(\epsilon) = \begin{cases} A_1 \cdot \exp\left(-2 \cdot \left(\frac{\epsilon - \epsilon_1}{\omega_1}\right)^2\right) & \epsilon < \epsilon_c \\ A_2 \cdot \frac{\omega_2^2}{\omega_2^2 + 4(\epsilon - \epsilon_2)^2} & \epsilon \geq \epsilon_c \end{cases}, \quad (5.20)$$

with the parameters $A_1 = 0.204 \pm 0.001$, $A_2 = 0.0556 \pm 0.0003$, $\omega_1 = 1.85 \pm 0.02$, $\omega_2 = 12.5 \pm 0.1$, $\epsilon_1 = 12.6 \text{ eV}$, $\epsilon_2 = 14.30 \pm 0.02$, and $\epsilon_c = 12.6 \text{ eV}$ [124, 271].

The parameterization⁵ consists of two components: The energy loss caused by excitation is expressed as a Gaussian distribution with its peak at ϵ_1 . The energy loss due to ionization of tritium molecules is represented in a Lorentzian tail that occurs only for energy losses $\epsilon \geq \epsilon_c$. [124, 271]

The response function is given by the convolution of the transmission function with the energy loss distribution

$$R(E, qU_{\text{ret}}) = \bar{P}_0 \cdot T(E, qU_{\text{ret}}) + \bar{P}_1 \cdot T(E, qU_{\text{ret}}) \otimes f(\epsilon) + \bar{P}_2 \cdot T(E, qU_{\text{ret}}) \otimes [f(\epsilon) \otimes f(\epsilon)] + \dots, \quad (5.21)$$

with the mean probability of scattering n -times \bar{P}_n [124]. The first four contributions of the energy loss function are displayed in figure 5.6.

The scattering probabilities P_n for an electron generated at the position z with an initial polar angle θ are given by a Poisson distribution

$$P_n(z, \theta) = \frac{(\lambda(z, \theta) \cdot \sigma_{\text{inel}})^n}{n!} \cdot \exp(-\lambda(z, \theta) \cdot \sigma_{\text{inel}}), \quad (5.22)$$

with the effective column density

$$\lambda(z, \theta) = \frac{1}{\cos \theta} \int_z^L \rho(z') dz', \quad (5.23)$$

where $\rho(z)$ is the density profile. The limits of the integral state the position of generation z as well as the length of the source L . [124]

For an isotropic electron distribution limited by the maximum acceptance angle θ_{max} , the mean scattering probability as a function of z can be calculated by

$$\bar{P}_n(z) = \frac{1}{1 - \cos \theta_{\text{max}}} \int_{\theta=0}^{\theta=\theta_{\text{max}}} \sin \theta \cdot P_n(z, \theta) d\theta \quad [124]. \quad (5.24)$$

The scattering probabilities used in equation (5.21) are given by integrating over the source length $2L$

$$\bar{P}_n = \frac{1}{\rho d} \cdot \frac{1}{1 - \cos \theta_{\text{max}}} \cdot \int_{-L}^L \int_0^{\theta_{\text{max}}} \rho(z') P_n(z', \theta) \sin \theta d\theta dz' \quad [263]. \quad (5.25)$$

Figure 5.7 shows the resulting response function for up to four scatterings.

The response function has been experimentally validated and shows good agreement for energies close to the endpoint [272]. If the model is extended to lower energies, one major modification is required: The inelastic scattering cross section can no longer be regarded as energy independent [273]. For a study of the influence of an energy independent cross section on the KATRIN neutrino mass determination please see [273].

⁵A new energy loss parameterization has been established recently [272]. The analysis of the *First Tritium Campaign* data in chapter 6 includes the new parameterization. For the scope of this study, the deviation between the models is negligible.

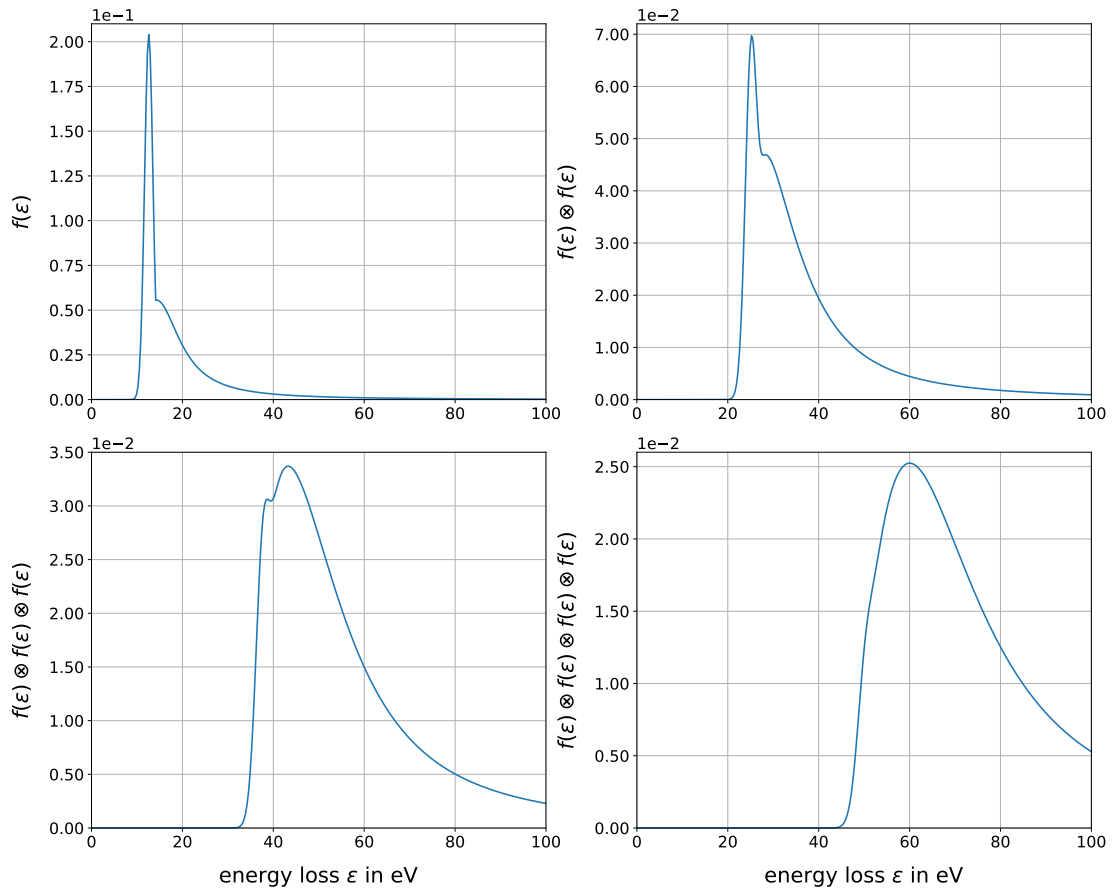


Figure 5.6: The first four contributions of the energy loss to the KATRIN response function. The minimum energy loss for inelastic scattering is 10 eV. As a consequence, the energy loss function is zero for values smaller than n -times 10 eV. The energy loss probability (y -axis) decreases with the number of scatterings n . Figure is adapted from [138] figure 5.5.

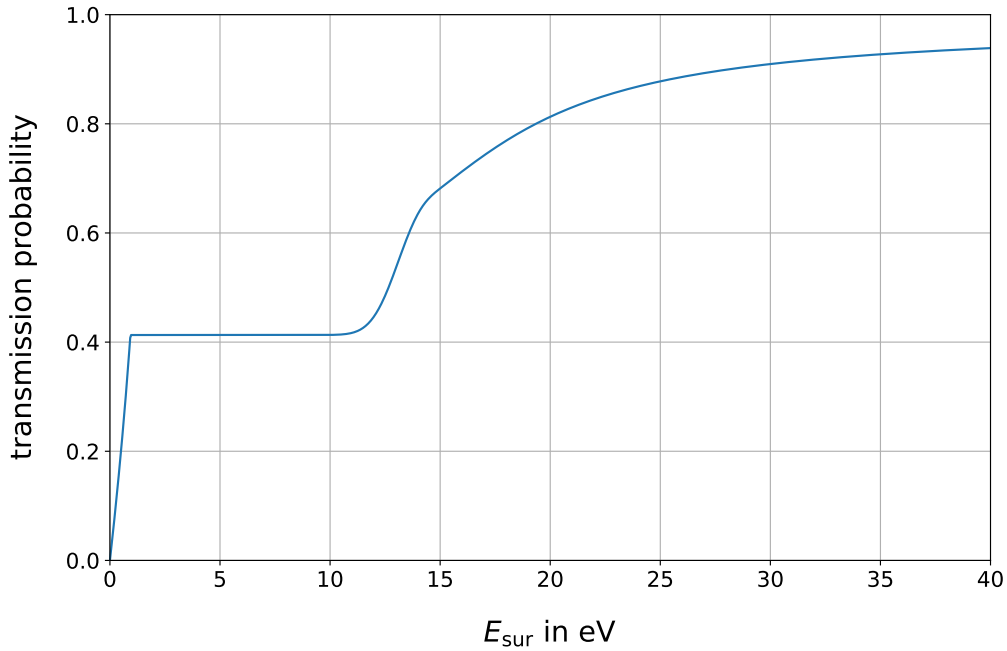


Figure 5.7: The KATRIN response function derived for the nominal column density of $\rho d = 5 \cdot 10^{17} \text{ cm}^{-2}$ and a constant inelastic scattering cross section of $\sigma_{\text{inel}} = 3.4 \cdot 10^{-18} \text{ cm}^2$. Approximately 41% of the electrons leave the source without scattering. At surplus energies larger than 10 eV the first scattered electrons are transmitted.

Energy dependent Cross Section

For relativistic electrons, the energy dependent cross section is given by

$$\sigma_{\text{inel}}(E) = \frac{4\pi a_0^2}{T(E)/R} \left[M_{\text{tot}}^2 \left[\ln \left(\frac{\beta^2(E)}{1 - \beta^2(E)} \right) - \beta^2(E) \right] + \frac{\gamma_{\text{tot}}(E)}{T(E)/R} + C_{\text{tot}} \right], \quad (5.26)$$

where the kinetic energy of the electrons is

$$T(E) = \frac{1}{2} \cdot m_e \cdot \beta^2(E), \quad (5.27)$$

the relativistic factor is

$$\beta(E) = \sqrt{1 - \frac{1}{(E/m_e + 1)^2}}, \quad (5.28)$$

the Rydberg Energy R , the Bohr radius a_0 , and the electron rest mass m_e [274]. The numerical constants M_{tot}^2 , C_{tot} , as well as γ_{tot} depend on the hydrogen isotopologues participating in the scattering process. A detailed derivation of the parameters for H_2 are given in [274, 275, 276]. Their values are:

$$M_{\text{tot}}^2 = 1.5497 \quad (5.29)$$

$$C_{\text{tot}} = 17.502 \quad (5.30)$$

$$\gamma_{\text{tot}}(E) = 2 \cdot \left[-\frac{7}{4} + \ln \left(\frac{E_{\text{ion}}}{T(E)} \right) \right], \quad (5.31)$$

with the ionization energy of molecular hydrogen $E_{\text{ion}} = 15.45 \text{ eV}$.

A visualization of the energy dependent cross section can be seen in the bottom panel of

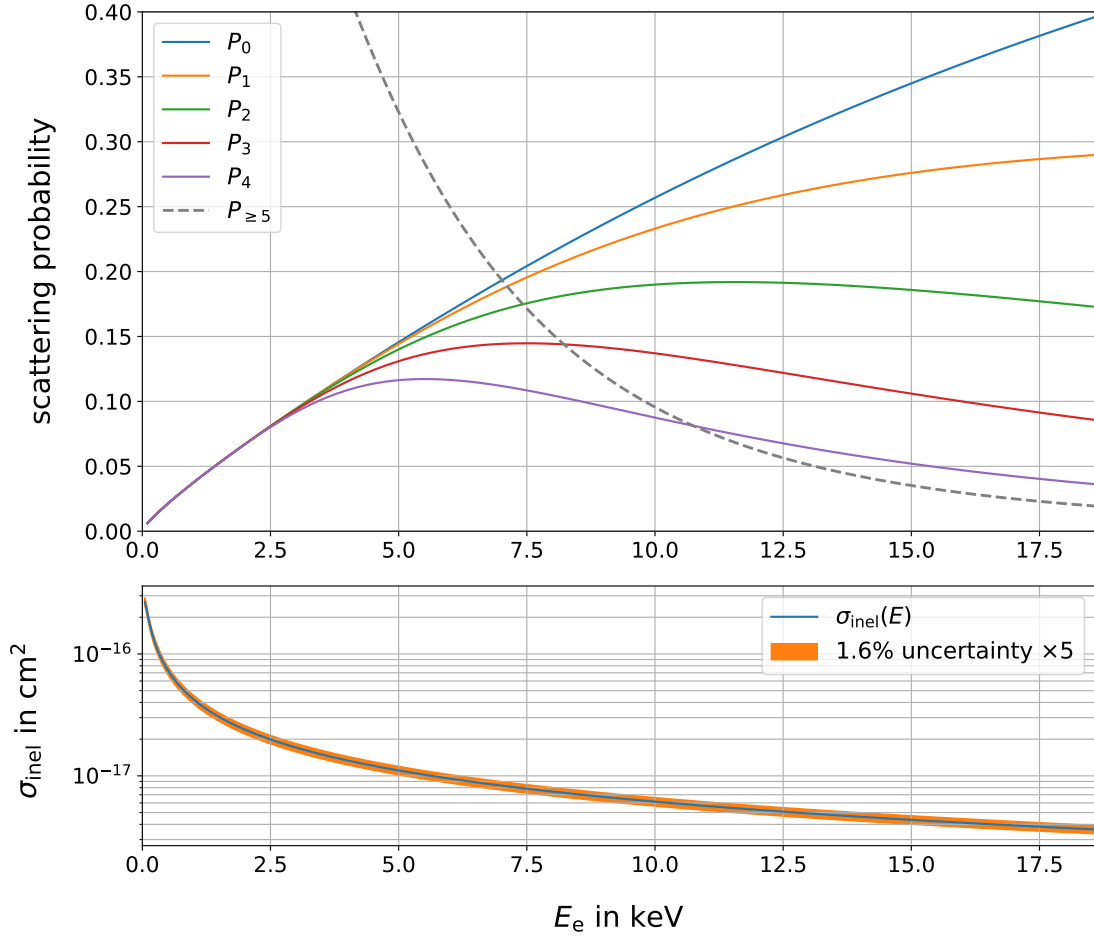


Figure 5.8: Upper panel: By replacing $\sigma \rightarrow \sigma(E)$ in equation (5.22) the energy dependent probabilities $P_n(E)$ for an electron to scatter n -times during its propagation through the WGTS can be calculated. As the cross section for inelastic scattering increases for lower energies, the probability for multiple scattering increases as well. The grey dashed line shows the summation over all scattering probabilities from 5 to ∞ scatterings. **Lower panel:** The relativistic total inelastic scattering cross section increases for lower energies. The relative uncertainty on the cross section is stated as 1.6% and increased by a factor of five for better visualized (orange band) [277].

figure 5.8. The cross section increases for lower electron energies and shows variations of up to two orders of magnitude over the β -decay energy range.

By replacing the constant with an energy dependent cross section in equation (5.22), the scattering probabilities can be calculated as a function of the electron energy. The results are displayed in the top panel of figure 5.8. With smaller electron incident energy, multiple scatterings are more likely while passing the source section. If KATRIN is used to measure the tritium β -decay spectrum over a wider energy range, it is important to consider a high number of scatterings in the analysis.

To study the influence of electron scattering in the source on the spectral shape, the response function stated in equation (5.21) has been implemented in the model. For the calculations, it can be chosen to be constant or energy dependent.

Figure 5.9 shows the relative deviation between two spectra including source scattering and a spectrum without. For the spectra with source scattering a distinction is made between a case with a constant cross section and an energy dependent.

The relative influence of source scattering on the spectral shape is large and reaches values up to 14 % close to the endpoint in both cases. At retarding potentials $qU_{\text{ret}} < 16.0 \text{ keV}$ both scenarios start to divide on a level of 10^{-2} . If an energy dependent cross section is used, the probability for multiple scatterings increases for lower energies which leads to an increased electron loss and a deviation from the calculations assuming a constant cross section.

5.3.2 Countermeasures

By lowering the column density, the number of scatterings can be reduced. If the source is operated at 1 % of the nominal column density, the number of electrons that leave the source unscattered increases from 41 % (nominal ρd) to 98.4 %. Calculations show that the overall contribution of electron scattering to the spectrum is reduced by two orders of magnitude compared to the nominal setting shown in figure 5.9.

5.3.3 Uncertainties and Influence on the Sensitivity

There are three main parameters whose uncertainties have a direct influence on the response model [10]:

- The column density ρd : The forward beam monitor (FBM) and the β -induced x-ray system (BIXS) performs in situ monitoring of the column density from which the systematic uncertainty can be derived for each measurement [249]. For the KATRIN first neutrino mass campaign *KNM1*, an average uncertainty on ρd of 1.03 % has been calculated and used in the analysis [278]⁶.
- The inelastic scattering cross section σ_{inel} : The uncertainty on σ_{inel} has been estimated in [277] with 1.6 % for energies close to the endpoint. There is no obvious reason, why the uncertainty should vary with the energy, therefore the same uncertainty is assumed for the full energy scale.
- The magnetic field in the analyzing plane B_a : The uncertainty on the magnetic field in the analyzing plane was determined in a high-precision magnetometer measurement and is found to be 1 % [281].

Another uncertainty is caused by neglecting the energy dependence of the energy loss function. The energy loss function can be measured using a mono energetic electron

⁶During the *KNM1 Campaign* the absolute column density and the uncertainty on the value has been derived via the throughput of the gas into the WGTS [279]. For the *KNM2 Campaign*, the uncertainty on ρd was reduced to 0.65 % [280]. An even further reduction is expected in the future.

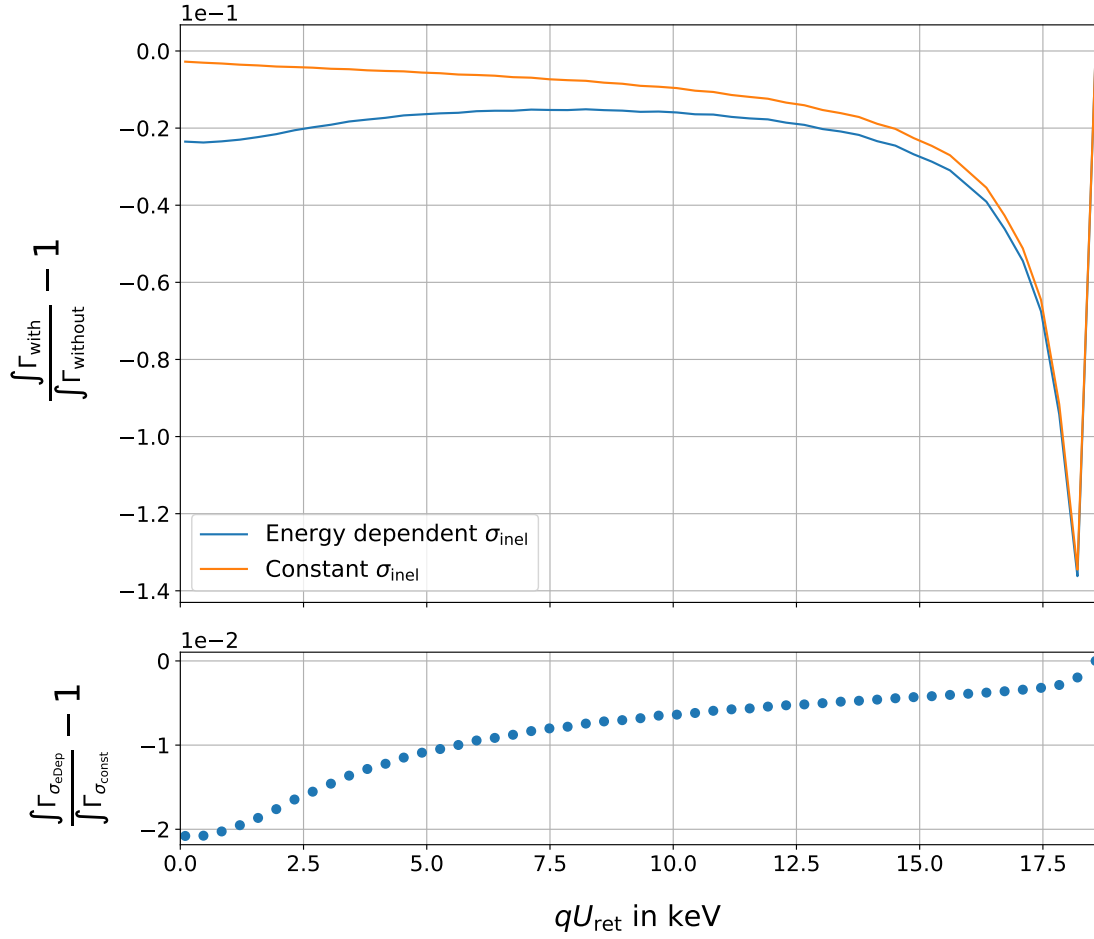


Figure 5.9: The relative influence of electron scattering in the source on the spectrum is large. For energies close to the endpoint, deviations of up to 0.14 ($\cong 14\%$) appear. For energies lower than 16.0 keV the influence is larger if an energy dependent scattering cross section is considered in the model. The increasing probability of multiple scatterings leads to a more distinct relative disturbance of the spectral shape. The lower figure shows the comparison of two spectra which include the effect of electron scattering in the source, calculated with and without an energy dependent cross section. For low energies, the deviation of the two models reaches values of up to $2.0 \cdot 10^{-2}$ ($\cong 2\%$). It can be concluded that if the spectrum is measured on a wider energy range, an energy dependent cross section has to be considered.

source either by an integral measurement [282] or via a time-of-flight measurement [283]. So far, the function has only been measured for energies close to the kinematic endpoint. Recent measurements hint that the energy loss model is also valid for deviating values, for example 20.575 keV [284]. In general, the energy loss function needs to be measured for all energies, using the rear wall electron gun and replacing the tritium in the source with deuterium (the latter is required to reach a wider energy range due to the high expected rates when using tritium).

Due to the complexity of the propagation of uncertainties on the energy loss function, they are neglected in the following discussion. For the analysis of the *First Tritium Campaign* data the nominal uncertainties on the parameterization have been used in the analysis (see section 6.5).

Influence on the Sensitivity

The influence of uncertainties on the energy loss model on the sterile neutrino sensitivity is shown in figure 5.10. Uncertainties on the input parameter σ_{inel} and ρd show a significant influence on the sterile neutrino sensitivity compared to B_a . While the uncertainty on the magnetic field can be in the size of 10 % without a significant effect, an uncertainty on the column density of 1 % reduces the sensitivity on the mixing angle by a factor of up to 1.8 for the *7-day reference measurement*.

If the uncertainties on σ_{inel} , ρd , and B_a are chosen to be the same as for the first KATRIN neutrino mass analysis stated in [9] the sensitivity is lowered by up to a factor of 2.8 compared to the pure statistical sensitivity.

If the column density is lowered to 1 % of its nominal value, the influence of uncertainties on the model input parameters is negligible. Even an unrealistically large uncertainty on the column density of 10 % has no impact on the sensitivity of the *7-day reference measurement*. Therefore, small column densities are preferred to minimize the effect of uncertainties on the source scattering for a keV-scale sterile neutrino measurement, which can be reasonably reconciled with the results of chapter 4.

5.3.4 Conclusion

The scattering of signal electrons on hydrogen molecules has an influence of up to 14 % on the measured spectrum. Therefore, it is important to model the effect precisely. The response function and energy loss model has been developed for KATRIN endpoint measurements. In the scope of this work, the validation of the model on the full energy scale was studied.

The first and most important conclusion is that if KATRIN is used for deep scans of the tritium β -decay spectrum, an energy dependent cross section is required in the model. Furthermore, the increased number of multiple scatterings needs to be considered in the analysis.

Due to the large size of the effect, the model is sensitive to uncertainties on the input parameters. In particular uncertainties on the column density as well as on the inelastic cross section influence the sensitivity of a keV-scale sterile neutrino search up to a factor of 2.8 within the statistics studied here.

By reducing the column density the scattering probability, and thus the influence of the effect on the measured spectrum, decreases. If the source is operated at a low column density of 1 % even an unrealistically large uncertainty of 10 % on the absolute value of the column density does not decrease the sensitivity, assuming that the same amount of statistics are collected as for the nominal case.

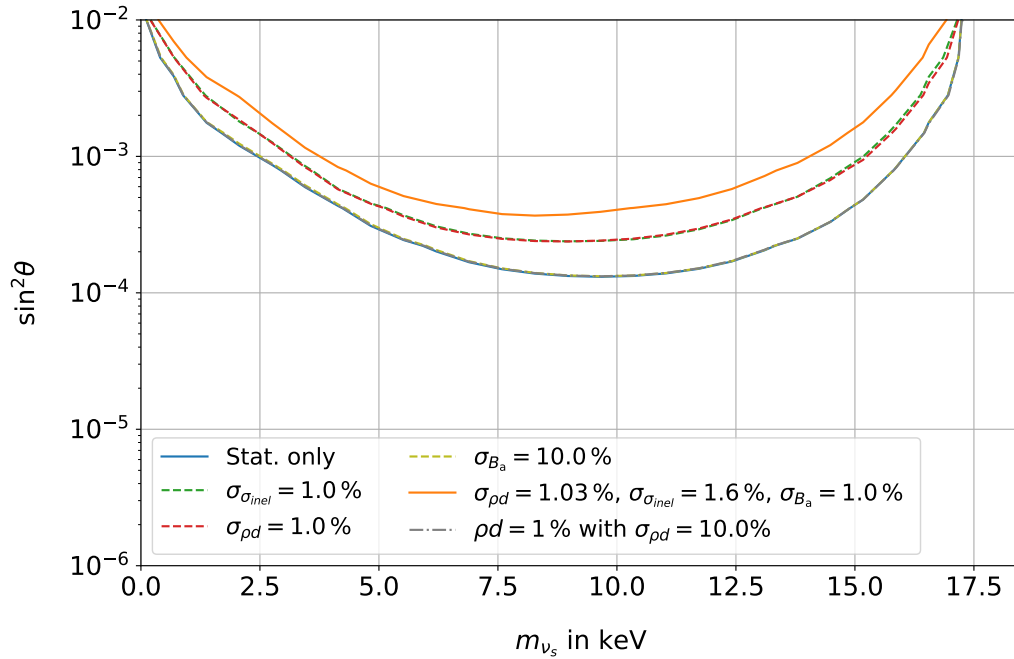


Figure 5.10: The influence of electron scattering in the source on the sterile neutrino sensitivity for the *7-day reference measurement*. The uncertainty on the analyzing plane magnetic field is negligible (dashed yellow line is congruent with the *stat. only* sensitivity), however, the uncertainty on the column density as well as the inelastic cross section has a significant impact on the sensitivity. If the uncertainties from [9] are applied, the sensitivity on the sterile neutrino mixing angle would be decreased by up to a factor of 2.8. If the column density is lowered to 1% even a large uncertainty of 10% on the column density would not lead to a reduction of the sensitivity on the sterile neutrino parameters within the statistics studied here.

Finally, it is important to mention that the energy loss function has only been experimentally validated for energies close to the kinematic endpoint yet. Even though first simulations show no significant energy dependence, it is strongly recommended to measure the energy loss function for smaller energies, if the tritium β -spectrum is observed on a wider energy range. By operating the source at lower column density, the influence of an unconsidered energy dependence of the energy loss model can be minimized.

5.4 Magnetic Traps in the Source

The magnetic field in the WGTS is not homogeneous. As displayed in figure 5.11 there are magnetic field minima at the pump ports (number 1, 2, 5, and 6) and two small minima at the center of the source (number 3 and 4). Electrons that are generated inside the volume of the magnetic field minima can be magnetically trapped. Trapped electrons eventually escape the traps due to elastic and inelastic scattering on hydrogen molecules. The energy loss caused by scattering leads to a distorted energy distribution of the escaped electrons (see section 5.3). A small but non-negligible fraction of these electrons is able to reach the detector. [10]

The effect of magnetic trapping in the KATRIN source was subject of various studies and found to be negligible for the neutrino mass determination, see for example [10, 249]. Its influence on a sterile neutrino search has been studied in [260], but only in a qualitative way which allowed for an approximation of the absolute contribution of the effect on the measured spectrum for a specific benchmark scenario⁷. The influence of the effect on the spectral shape was not studied.

In this work, *KASPER* simulations are used to calculate the angular and energy distribution of electrons that escaped the magnetic traps. This is required to model the influence of the effect on the observed spectrum (section 5.4). Several countermeasures are discussed (section 5.4) and the influence of uncertainties on the model on a keV-scale sterile neutrino search is presented (section 5.4).

The Trapping Process

The following formulation is based on [260] equations (3.10)-(3.15).

The ratio of the magnetic field at the point of generation B_{ini} and the field at the border of the trap B_{trap} ⁸ defines a maximum angle under which an β -electron can start without being magnetically reflected

$$\theta_{\text{ini}} \leq \theta_{\text{trap}} = \sin^{-1} \sqrt{\frac{B_{\text{ini}}}{B_{\text{trap}}}} \quad [10, 260]. \quad (5.32)$$

For an isotropic angular distribution, the number of initially trapped electrons can be calculated over the conical solid angle

$$\Omega_{\text{trap}} = 4\pi \cdot \cos \theta_{\text{trap}}, \quad (5.33)$$

which directly corresponds to the trapping probability

$$P_{\text{trap}} = \frac{\Omega_{\text{trap}}}{4\pi} = \cos \theta_{\text{trap}}$$

$$P_{\text{trap}} = \cos \left(\sin^{-1} \sqrt{\frac{B_{\text{ini}}}{B_{\text{trap}}}} \right) = \sqrt{1 - \frac{B_{\text{ini}}}{B_{\text{trap}}}}. \quad [260] \quad (5.34)$$

⁷The scenario studied included a reduced column density of $\rho d = 3 \cdot 10^{15} \text{ cm}^{-2}$ (0.6 % of the nominal value) and a source magnetic field of $B_s = 0.045 \text{ T}$. The absolute contribution of electron scattering to the spectrum was found to be $7.5 \cdot 10^{-4}$. [260]

⁸In an asymmetric trap, the field at the lower border defines B_{trap} .

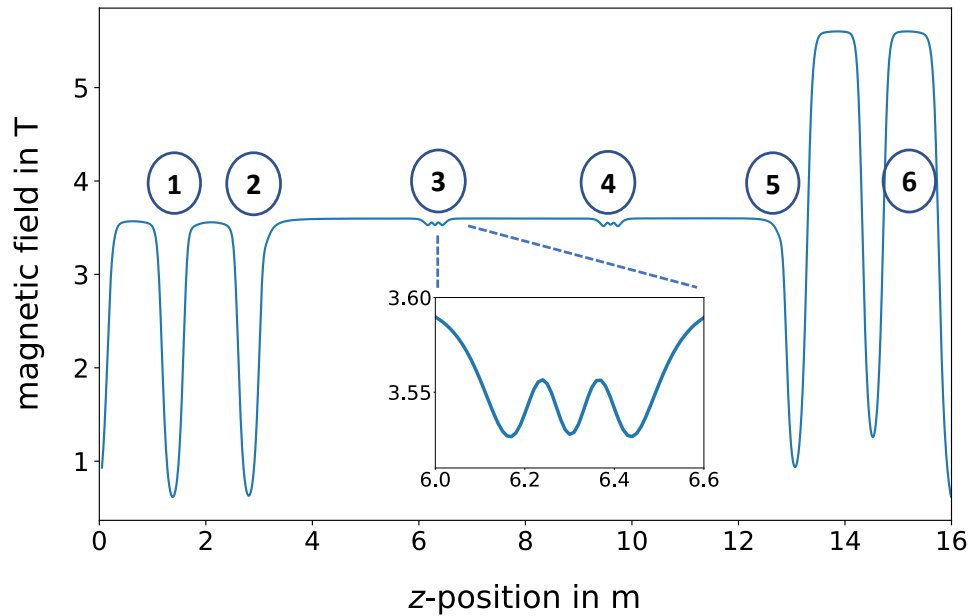


Figure 5.11: An overview of the magnetic field strength in the source. Between the pump ports (trap 1, 2, 5, and 6) the magnetic field drops to small values of less than a third of the mean value. Between the three main coils of the WGTS, compensation coils are installed to avoid the same deep field drops as in the pump port areas. The inner traps are therefore smaller with a corresponding field reduction of approximately 1%. Due to the geometry of the correction coils, the inner minima consist of three further small traps.

Figure 5.12 shows the trapping angle and probability as a function of the electrons' initial position. The trap borders are defined by the local magnetic field minima ± 0.5 m in z -direction. The distance relates to the position where the trapping probability changes back to zero.

The total number of initially trapped electrons does not only depend on the magnetic field but also on the prevailing tritium density ρ in the trap volume [260]. An overview of the nominal density distribution in the WGTS is displayed in figure 5.13. The difference in the density of the inner and the most outer traps is about three orders of magnitude. In total, approximately 27.2% of all electrons start within a trap volume. If the density fractions and the trapping probabilities shown in figure 5.12 are multiplied, the fraction of initially trapped β -electrons can be derived. For the nominal KATRIN setting it is found to be 2.95%.

The initially trapped electrons will escape after a certain time due to a change of their polar angle below θ_{trap} . The angular changes are caused by elastic and inelastic scattering on gas molecules. Inelastic scattering mainly leads to an energy loss and small angular variations. For elastic scattering, it is the other way around. If the angle of escaped electrons is small enough to fulfill equation (2.6) and their remaining energy is bigger than the retarding potential, they are able to reach the detector. Since these electrons undergo a much higher number of scatterings than the electrons that are generated untrapped in the source, they contribute to the signal with a deviated energy distribution. [10]

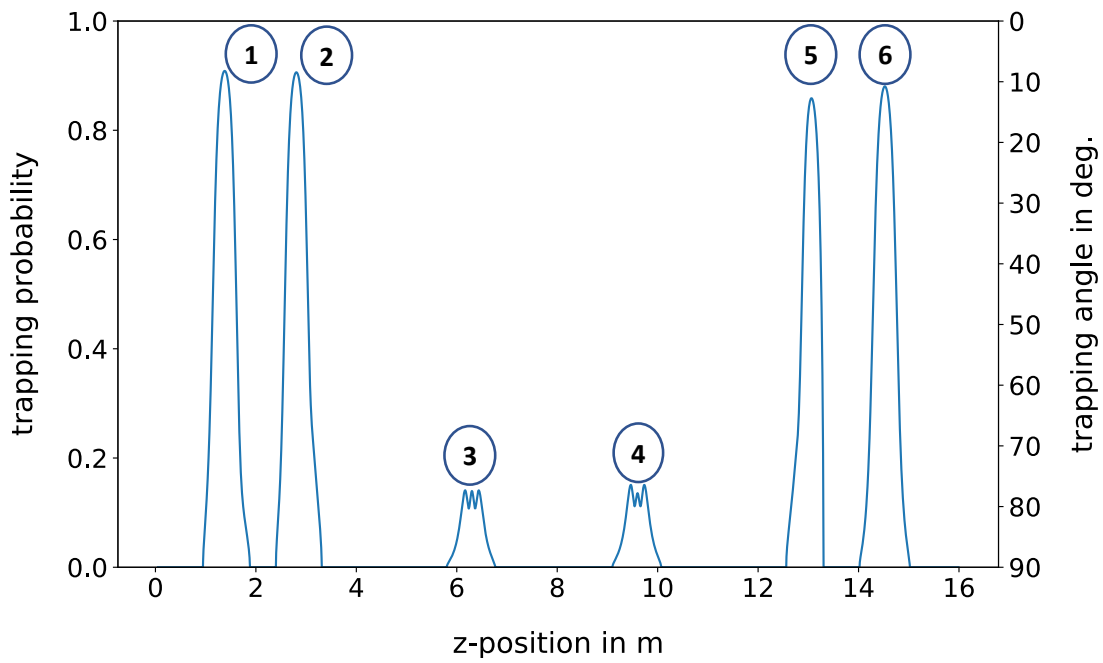


Figure 5.12: If electrons start within the volume of a magnetic trap with an initial polar angle larger than the trapping angle (right ordinate), they will be magnetically reflected at the borders of the trap. The trapping probability is displayed on the left ordinate. Figure is adapted from [260] figure 3.6.

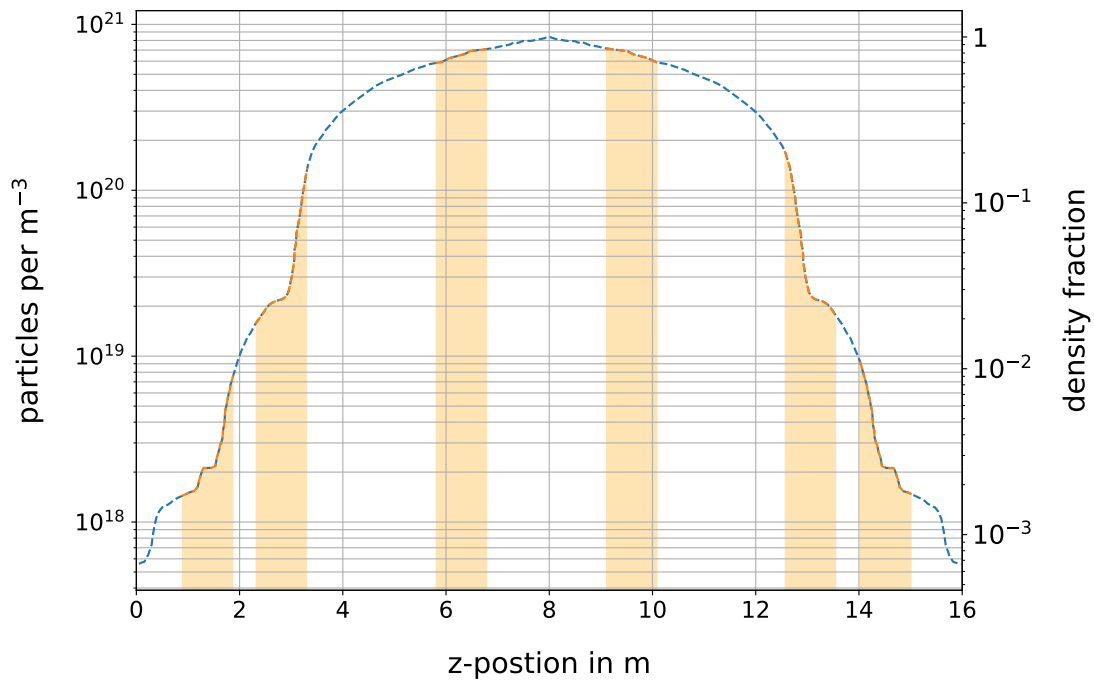


Figure 5.13: The density distribution in the WGTS at nominal setting. The orange shaded areas correspond to the location of the magnetic traps. The right ordinate shows the relative density. The two inner traps are located in an area with a much higher tritium density than the outer traps. In total, the density in the trap volumes accounts for 27.2% of the entire density. The data used in this figure was taken from [285].

Time Evolution of Traps

The time evolution of the magnetic traps is important to consider, since any time dependency would lead to a non steady systematic effect. Furthermore, it allows to study possible charge accumulations caused by temporarily trapped electrons that could lead to a spacial variation of the source electric potential.

The upcoming formulations and calculations are based on [260] equations (F.8)-(F.24). Each trap has a constant filling

$$\Gamma_{\text{fill},i} = \pi r_s^2 \cdot \epsilon_T \cdot \frac{\ln(2)}{t_{1/2}} \cdot \int_{z_{1,i}}^{z_{2,i}} \rho(z) \cdot P_{\text{trap}}(z) dz, \quad (5.35)$$

and escaping rate

$$\Gamma_{\text{esc},i} = \frac{N_i(t)}{\bar{t}_{\text{esc},i}}, \quad (5.36)$$

with the source radius r_s , the tritium purity ϵ_T , the half-life $t_{1/2}$, the number of electrons inside the trap $N_i(t)$ and the mean time required to escape the trap by scattering $\bar{t}_{\text{esc},i}$. [260]

The time evolution of $N_i(t)$ can be expressed by an ordinary first order differential equation

$$\dot{N}_i(t) = \Gamma_{\text{fill},i} - \Gamma_{\text{esc},i} = \Gamma_{\text{fill},i} - \frac{N_i(t)}{\bar{t}_{\text{esc},i}}. \quad [260] \quad (5.37)$$

After separation of the variables, the equation can be written as

$$\int \left(\frac{1}{\Gamma_{\text{fill},i} \cdot \bar{t}_{\text{esc},i} - N_i(t)} \right) dN = \int \frac{1}{\bar{t}_{\text{esc},i}} dt. \quad [260] \quad (5.38)$$

Integrating both sides leads to

$$-\ln(\Gamma_{\text{fill},i} \cdot \bar{t}_{\text{esc},i} - N_i(t)) = \frac{t}{\bar{t}_{\text{esc},i}} + C. \quad [260] \quad (5.39)$$

By rearranging and replacing $C' = e^{-C}$ the number of electrons can be written as a function of time

$$N_i(t) = \Gamma_{\text{fill},i} \cdot \bar{t}_{\text{esc},i} - C' \cdot \exp(-t/\bar{t}_{\text{esc},i}). \quad [260] \quad (5.40)$$

With the initial value $N_i(t=0) = 0$, the constant can be derived

$$C' = \Gamma_{\text{fill},i} \cdot \bar{t}_{\text{esc},i}, \quad (5.41)$$

which leads to the final expression

$$N_i(t) = \Gamma_{\text{fill},i} \cdot \bar{t}_{\text{esc},i} \cdot [1 - \exp(-t/\bar{t}_{\text{esc},i})]. \quad [260] \quad (5.42)$$

The escaping times are derived in a *KASPER* simulation and listed in the first column of table 5.1. Due to the short escaping times, the traps are saturated within a few μs . As a consequence, no time dependent charge effects such as a slow filling over time are expected. The filling rates listed in the second column of table 5.1 are calculated with equation (5.35).

For $t \gg \bar{t}_{\text{esc},i}$ an equilibrium of electrons in the trap is reached

$$\Gamma_{\text{fill},i} = \Gamma_{\text{esc},i}. \quad [260] \quad (5.43)$$

Following the relation

$$\Gamma_{\text{fill},i} = \Gamma_{\text{esc},i} = \frac{N_i(t \gg \bar{t}_{\text{esc},i})}{\bar{t}_{\text{esc},i}}, \quad (5.44)$$

the total number of electrons in the trap in the equilibrium case can be determined [260]. As shown in the last column of table 5.1 these numbers are negligibly small compared to the total decay rate in the source which is on the order of 10^{11} s^{-1} . Therefore, a space charge that could influence the electric potential inside the source can be excluded as well.

Table 5.1: The mean escaping time as obtained by the simulation (first column), the corresponding filling and escaping rate in equilibrium (second column), and the resulting number of trapped electrons (third column). The sum of maximum stored electrons is 1594 for the nominal column density of $\rho d = 5 \cdot 10^{17} \text{ cm}^{-2}$. Therefore, an increased local charge density is not expected.

Trap No.	$\bar{t}_{\text{esc},i}$ in μs	$\Gamma_{\text{fill},i}$ in 10^6 s^{-1}	N_{max}
1	2.21	13.9	31
2	1.54	189.4	292
3	0.67	600.3	401
4	0.69	637.2	439
5	1.84	216.4	398
6	2.17	15.1	33

5.4.1 Influence on the Spectrum

The spectrum including the effect of electrons that escaped the magnetic traps is given by

$$\Gamma_{\text{with}} = P_{\text{wgts,fpd}} \times \Gamma_{\beta} + \sum_{i=1}^6 (P_{\rho,i} \cdot \bar{P}_{\text{trap},i} \cdot P_{qU_{\text{ret}},i} \cdot P_{\theta_{\text{max}},i}) \times \Gamma_{\text{trap},i}, \quad (5.45)$$

with the unchanged β -spectrum from the source Γ_{β} , as well as the deviated spectra of initially trapped and escaped electrons $\Gamma_{\text{trap},i}$, weighted with the following probabilities:

- $P_{\text{wgts,fpd}}$: Analogous to the definition in section 5.2, $P_{\text{wgts,fpd}}$ is the probability of electrons that are generated in the source with an energy larger than qU_{ret} to reach the detector without being magnetically reflected at the pinch magnetic field.
- $P_{\rho,i}$: The density fraction $P_{\rho,i}$ describes the relative amount of decays in a trap volume i , compared to the full integral density of the entire source (see figure 5.13 right ordinate).
- $\bar{P}_{\text{trap},i}$: The mean trapping probability $\bar{P}_{\text{trap},i}$ describes the probability of an electron decaying in a trap, to be initially trapped according to equation (5.32). The product $P_{\rho,i} \cdot \bar{P}_{\text{trap},i}$ is a direct measure of the fraction of source β -electrons that are initially trapped.
- $P_{qU_{\text{ret}},i}$: Whether an electron that escaped the trap is able to reach the detector depends on its kinetic energy E_{esc} and polar angle θ_{esc} . If the kinetic energy is smaller than $E_{\text{esc}} < qU_{\text{ret}}$, the electron can not overcome the retarding potential and does not contribute to the spectral distortion. The probability $P_{qU_{\text{ret}},i}$ describes the fraction of electrons that started with an energy $E_{\text{ini}} > qU_{\text{ret}}$ and are able to overcome the retarding potential after the escape process due to the scattering energy loss.
- $P_{\theta_{\text{max}},i}$: If the polar angle after escape θ_{esc} is larger than the maximum acceptance angle $\theta_{\text{esc}} > \theta_{\text{max}} = \sin^{-1} \sqrt{\frac{B_s}{B_{\text{pch}}}}$, the electron is magnetically reflected at the pinch and therefore unable to reach the detector and contribute to the measured spectrum. The probability $P_{\theta_{\text{max}},i}$ corresponds to the number of electrons that are able to reach the detector without being magnetically reflected.

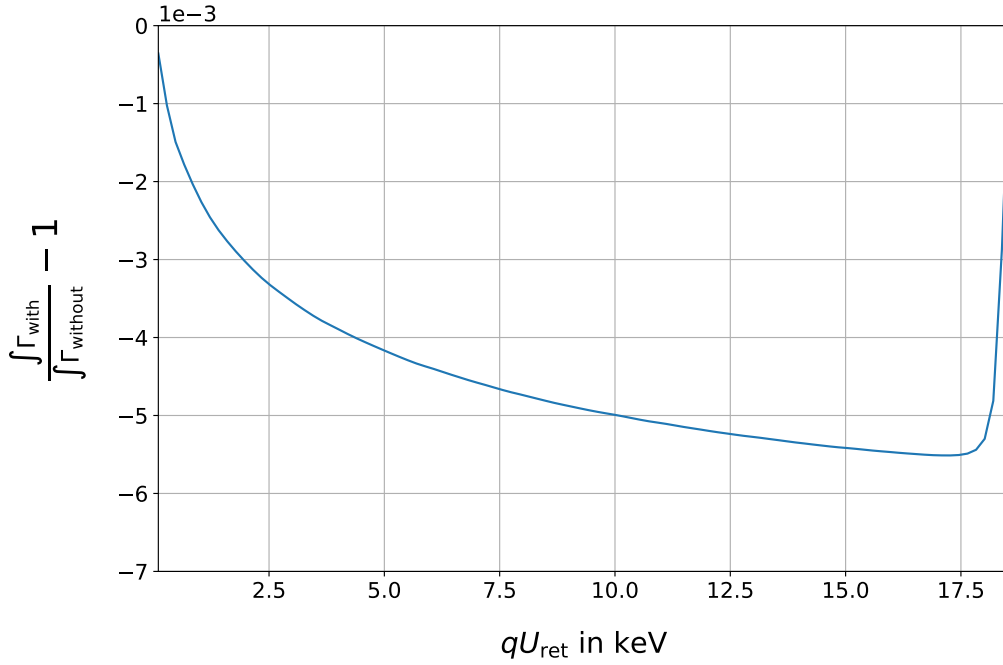


Figure 5.14: The relative influence of magnetic trapping in the source on the shape of an integral spectrum. Close to the endpoint, where the count rate is low, the relative influence of the effect is the largest and reaches values of $5.5 \cdot 10^{-3}$ ($\cong 0.55\%$).

The factors $P_{\text{wgts,fpd}}$, $\bar{P}_{\text{trap},i}$, and $P_{\rho,i}$ can be calculated based on a *KASPER* magnetic field and gas profile simulation⁹.

A determination of $P_{qU_{\text{ret},i}}$, $P_{\theta_{\text{max},i}}$, and $\Gamma_{\text{trap},i}$ requires a *KASPER* simulation of the energy and angular distribution of escaped electrons, including elastic and inelastic scattering of electrons on hydrogen molecules. A description of the simulation settings and analysis can be found in appendix F.

In order to determine the relative influence of the effect on the spectral shape, the ratio

$$\frac{\int \Gamma_{\text{with}}}{\int \Gamma_{\text{without}}} - 1 = \frac{P_{\text{wgts,fpd}} \times \Gamma_{\beta} + \sum_{i=1}^6 (P_{\rho,i} \cdot \bar{P}_{\text{trap},i} \cdot P_{qU_{\text{ret},i}} \cdot P_{\theta_{\text{max},i}}) \times \Gamma_{\text{trap},i}}{P_{\text{wgts,fpd}} \times \Gamma_{\beta} + \sum_{i=1}^6 (P_{\rho,i} \cdot \bar{P}_{\text{trap},i} \cdot P_{qU_{\text{ret},i}} \cdot P_{\theta_{\text{max},i}}) \times \Gamma_{\beta}} - 1, \quad (5.46)$$

is calculated. Figure 5.14 displays the spectral shape deviation caused by magnetic trapping in the source. For higher energy parts of the spectrum, the relative influence of the effect is the largest due to the small count rate. It reaches values of up to $5.5 \cdot 10^{-3}$.

5.4.2 Countermeasures

By lowering the source magnetic field with respect to the pinch magnetic field, the maximum acceptance angle θ_{max} is reduced. As a consequence, the probability $P_{\theta_{\text{max},i}}$ decreases which, however, is partly compensated by the simultaneous decrease of $P_{\text{wgts,fpd}}$. Since the angular distribution of escaped electrons tends to larger angles (for details see appendix F) the reduction of $P_{\theta_{\text{max},i}}$ has a larger effect compared to the decrease of $P_{\text{wgts,fpd}}$ (isotropic distribution). Simulations show that the effect of magnetic trapping on the measured spectrum can be reduced by a factor of 1.7 if the source magnetic field is lowered to $B_s = 1.0$ T and a factor of 6.5 for $B_s = 0.1$ T.

⁹The simulation of the density profile was not performed in the scope of this thesis. The data was taken from [285].

A reduction of the column density does not lead to a decrease of the effect, since the criterion for an escape (large enough angular change) only depends on the mean number of scatterings. A reduced column density would lead to a longer escape time, however, the angular and energy distribution after the trap does not change.

5.4.3 Uncertainties and Influence on the Sensitivity

This section discusses uncertainties on the model as well as their influence on the sensitivity. They are separated in two groups: uncertainties on the simulation as well as uncertainties caused by simplifications.

Uncertainties on the Simulation

In order to study the influence of uncertainties on the *KASPER* simulations, the different parameters whose derivation is based on simulations have been Gaussian fluctuated with a large uncertainty of 30%. The variation leads to a weighted average uncertainty on the model¹⁰ of 8.14%.

Uncertainties based on Simplifications

Two simplifications have been made in the modeling of magnetic trapping in the source:

1. **Neglecting secondary electrons:** Due to ionization, every β -electron that escapes a trap generates ten secondary electrons on average. After escaping the trap, they can contribute to the measured spectrum. The initial energy distribution of the secondary electrons has been simulated with *KASPER*. Most of them (> 99.0%) are generated with energies smaller than $E_{\text{sec}} < 1.0 \text{ keV}$. By choosing $qU_{\text{ret}} = 1.0 \text{ keV}$ as the lowest retarding potential of the measurement, the contribution of secondary electrons can be strongly suppressed.

However, due to the large number of produced secondary particles, they have a non-vanishing probability to contribute to the measured spectrum also for higher energies. Figure 5.15 shows the potential contribution of secondary electrons to the measured spectrum as a function of the retarding potential. Since the maximum energy of secondary particles is $E_{\text{sec,max}} = E_0/2$ the contribution drops to zero at this position of the spectrum [286]. For retarding potentials $qU_{\text{ret}} < 1.0 \text{ keV}$, the contribution gets larger than 0.1 ($\cong 10\%$).

This approach assumes that the secondary electrons have the same probability to reach the detector as the primary particles. Even though secondary electrons are not considered in the model, their influence is covered within the uncertainties of the simulations at this point.

2. **Neglecting source scattering:** This model assumes that electrons that leave a trap have the same probability to scatter on hydrogen molecules while propagating through the source as electrons that are generated free. However, due to the energy and angular deviation caused by the escaping process, the probability could be different. Compared to the overall size of the effect, this contribution is assumed to be small.

In summary, a conservative uncorrelated uncertainty of 10% is used to study the impact of the effect on the sterile neutrino sensitivity.

¹⁰The energy dependent size of the effect was used to weight the average deviation.

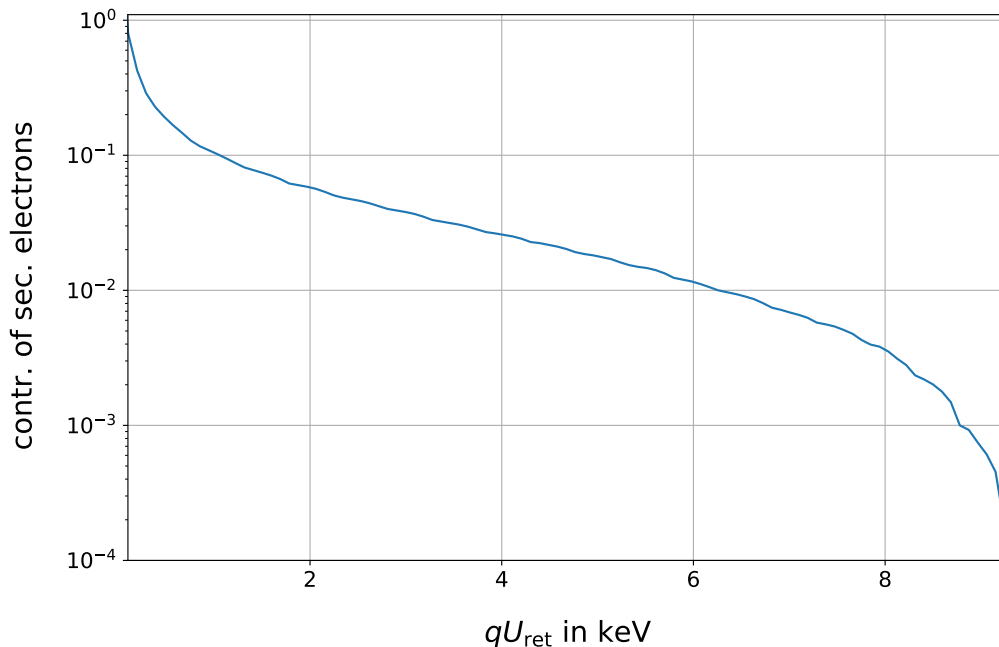


Figure 5.15: The potential contribution of secondary electrons to the measured spectrum. The numbers have been derived by multiplying the ratio of secondary to primary particles (approximately ten) and the fraction of secondaries that have enough energy to overcome the retarding potential. The secondary energy is limited to $E_0/2$ which lead to the drop of the contribution to zero for large retarding potentials.

Influence on the Sensitivity

The influence of magnetic trapping on the sterile neutrino sensitivity of the *7-day reference measurement* is displayed in figure 5.16. The dashed lines show the sensitivity for two different source magnetic field settings and an uncorrelated uncertainty on the model of 10%. The influence of the uncertainty on the sensitivity scales with the size of the magnetic field. For the nominal KATRIN setting, the sensitivity on the mixing angle is reduced by up to a factor of two. If the source magnetic field is set to $B_s = 0.1$ T, the reduction decreases to a factor of only a factor of 1.14.

5.4.4 Conclusion

Local magnetic field minima in the WGTS lead to a trapping of approximately 2.7% of the generated β -electrons. By scattering on hydrogen molecules, the initially trapped electrons leave the trap with a deviated energy and angular distribution [10]. If the spectrum is measured close to the kinematic endpoint, the escaped electrons are unable to overcome the retarding potential due to their energy loss [249]. If the energy range is extended as required for a keV-scale sterile neutrino search, a small but non-negligible fraction of the escaped electrons is able to reach the detector and contributes to a spectral distortion [260].

The relative influence on the spectrum reaches values of up to $5.5 \cdot 10^{-3}$ which makes a consideration of the effect in the analysis necessary. So far, the overall uncertainty on the model is estimated to be 10%, which leads to a reduction of the neutrino sensitivity of up to a factor of two within the studied statistics.

The size of the spectral malformation, as well as the influence of model uncertainties on the sensitivity, can be reduced by lowering the source magnetic field by up to a factor of

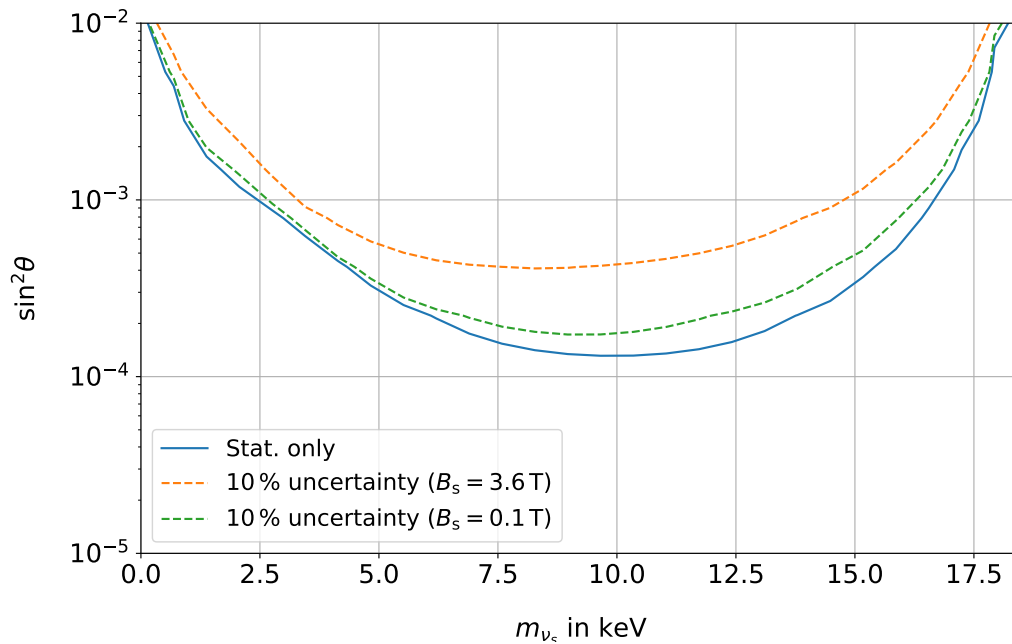


Figure 5.16: The influence of model uncertainties of magnetic trapping in the source on the keV-scale sterile neutrino search. The blue line shows the statistical sensitivity, the dashed line show the influence of an uncorrelated 10% uncertainty on the model for two different source magnetic fields.

five to $B_s = 0.1$ T.

An improvement of the model helps to further reduce the influence of magnetic trapping in the source on the keV-scale sterile neutrino sensitivity. The development of a multi-dimensional convolution model, which is introduced in section 7.4, shows great potential to decrease the influence.

5.5 Source Fluctuations

The total number of tritium atoms in the source N_{tot} is determined by the column density ρd , the tritium purity ϵ_T , and the cross-sectional area of the source A :

$$N_{\text{tot}} = A \cdot \epsilon_T \cdot \rho d. \quad (5.47)$$

It is a direct measure of the source activity. For analyses of KATRIN measurements, the absolute source activity is of minor interest, since it only affects the normalization of the spectrum. However, in an integral measurements, where the count rate as a function of the retarding potential is the relevant observable, unaccounted for fluctuations of N_{tot} have the potential to distort the spectral shape. [131]

This section focuses on source fluctuations and their influence on deep tritium β -scans.

In the first part of this section, the source activity monitoring systems of KATRIN are briefly introduced, and results of current measurements are presented. The second part introduces the influence of source fluctuations on the measured spectrum (section 5.5) as well as countermeasures that take into account the specific time structure of source fluctuations (section 5.5). Finally, the influence of the fluctuations on the sterile neutrino sensitivity is discussed (section 5.5).

Monitoring and Stability

The monitoring of the β -decay rate during a KATRIN measurement is performed by the BIXS and the FBM system (for details see section 2.2.1 and 2.2.2) [249]. Both systems are designed to determine the source activity with a precision of 0.1% on the time scale of hours [143, 158]. Furthermore, the rate stability can be monitored with the FPD, by a steadily repeated measurement at a certain retarding potential [131].

During the first tritium operation it was shown that the β -electron rate was stable on a 0.1%, level at a retarding potential of $qU_{\text{ret}} = E_0 - 1000 \text{ eV}$ in 60 second measurement bins over a total measurement time of 5 hours [131]¹¹.

Not only the rate stability itself, also the stability of the two relevant parameters, the column density ρd and the tritium purity ϵ_{T} can be determined. There are three relevant parameter that are directly connected to the stability of ρd : 1. the pressure of the buffer vessel, that is located right before the inlet valve of the tritium loop system to the source tube; 2. the inlet gas flow itself; 3. the temperature of the source beam tube [131]. The Laser Raman System (LARA) is able to determine ϵ_{T} in situ with a precision of up to 0.034%, depending on the gas composition and pressure setting of the loop system [287]. Throughout the first KATRIN neutrino mass determination campaign (*KNM1*), the variation of ρd and ϵ_{T} during the 2h spectrum scans was found to be $\sigma_{\rho d} = 8.0 \cdot 10^{-3}$ and $\sigma_{\epsilon_{\text{T}}} = 2.0 \cdot 10^{-3}$ [9]. By combining several runs, the uncertainties were further reduced [254].

5.5.1 Influence on the Spectrum

In order to study the influence of source fluctuations on the measured spectrum, the rate per measurement bin is smeared with a Gaussian distribution, where the fluctuation is the standard deviation σ . The smearing was applied bin to bin uncorrelated. Figure 5.17 shows an example with a source fluctuation of $\sigma_{\text{source}} = 10^{-3}$. As expected, the distortion of the spectrum is on the same size as the fluctuation itself.

5.5.2 Countermeasures

The time structure of source fluctuations plays an important role to reduce their influence on a measurement. In order to minimize the uncertainty on the mean source activity, the measurement time distribution can be adjusted accordingly.

A distinction is made between two cases:

- **Long term drifts:** Assuming a long term source activity drift of $\sigma_{\text{drift}} = 10^{-3}$ in 7 days, the measurement time per run has to be in the order of 1 hour and 40 minutes to reach a source stability of $\sigma_{\text{source}} < 10^{-5}$ during one run.
- **High frequency fluctuations:** Fluctuations that occur on short time-scales (sub-run length) require long measurements to collect enough monitoring data points N to reduce the standard error of the mean $\sigma_{\text{mean}} = \frac{\sigma_{\text{fluct}}}{\sqrt{N}}$. Assuming a short scale drift of $\sigma_{\text{drift}} = 10^{-3}$, at least $N = 10^4$ monitoring data points are required to reach $\sigma_{\text{source}} < 10^{-5}$. This can also be reached by combining several runs to one stacked run (see section 6.5) [254].

5.5.3 Uncertainties and Influence on the Sensitivity

Unaccounted source fluctuations can not be implemented in the model that predicts the measured spectrum. The fluctuations themselves are treated as uncorrelated uncertainties.

¹¹This stability is not expected to vary for different retarding voltages since there is no correlation between the voltage setting and the stability of the source activity.

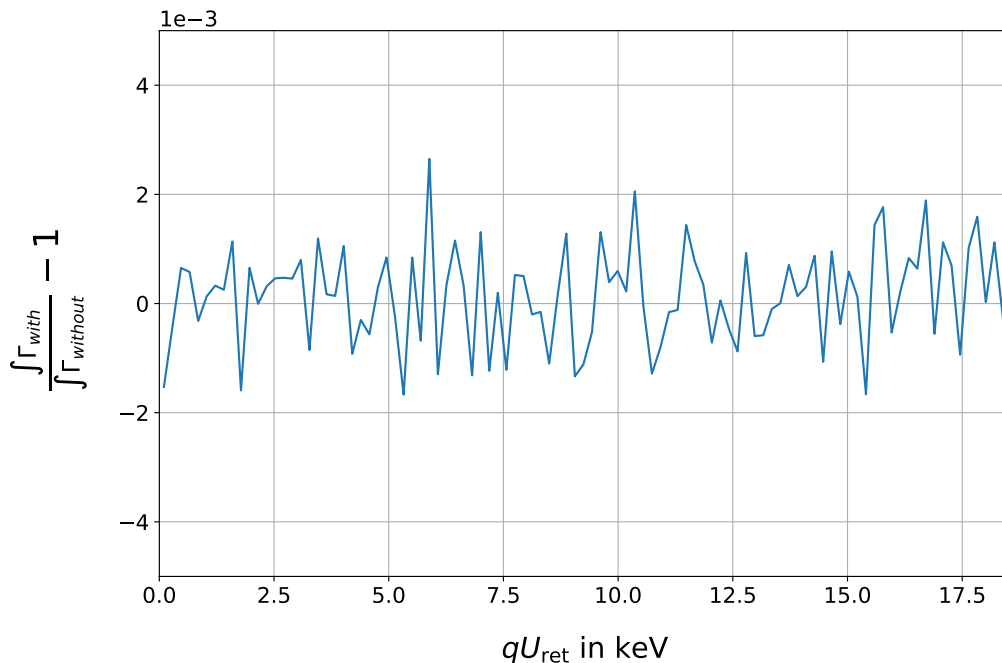


Figure 5.17: The figure shows the relative influence of uncorrelated source fluctuations with a size of $\sigma_{\text{fluct}} = 10^{-3}$ on an integral β -spectrum. The source fluctuations lead directly to bin uncorrelated rate instabilities of the same size.

Figure 5.18 shows the influence of source fluctuations on the keV-scale sterile neutrino sensitivity of the *7-day reference measurement*. A source fluctuation of $\sigma_{\text{fluct}} = 10^{-3}$ would significantly reduce the sensitivity on the mixing angle by up to a factor of four. If the fluctuations are smaller, their influence can be reduced accordingly. For $\sigma_{\text{fluct}} = 10^{-5}$ the influence on the *7-day reference measurement* is negligible.

5.5.4 Conclusion

Unaccounted source fluctuations with an unknown time structure are one of the largest uncertainties if KATRIN is used to search for keV-scale sterile neutrinos. They have to be taken into account as uncorrelated uncertainties which influences the sensitivity significantly as shown in figure 5.18.

KATRIN is equipped with several monitoring systems that can measure the uncertainties. By a combination of the monitoring devices with an optimized scanning procedure and measurement time distribution, the influence of source fluctuations on a keV-scale sterile neutrino search can be minimized.

5.6 Detection Efficiency

A key variable of every detector system is the detection efficiency ϵ that describes the ratio of the true number of electrons arriving at the detector and the number of events that are actually measured. If the value is constant and independent of experimental parameters, the detection efficiency would play a subordinate role in the analysis [250]. However, as measurements and simulations show, the detection efficiency of the FPD is a distinct function of the retarding potential qU_{ret} as well as the detector pixel k (see for example [47]).

Reference [250] defines the FPD detection efficiency as follows

$$\epsilon(qU_{\text{ret}}, k) = \epsilon_{\text{abs}} \cdot \epsilon_{\text{pxl}}(k) \cdot \epsilon_{\text{roi}}(qU_{\text{ret}}, k) \cdot \epsilon_{\text{bs}}(qU_{\text{ret}}) \cdot \epsilon_{\text{pu}}(qU_{\text{ret}}, k), \quad (5.48)$$

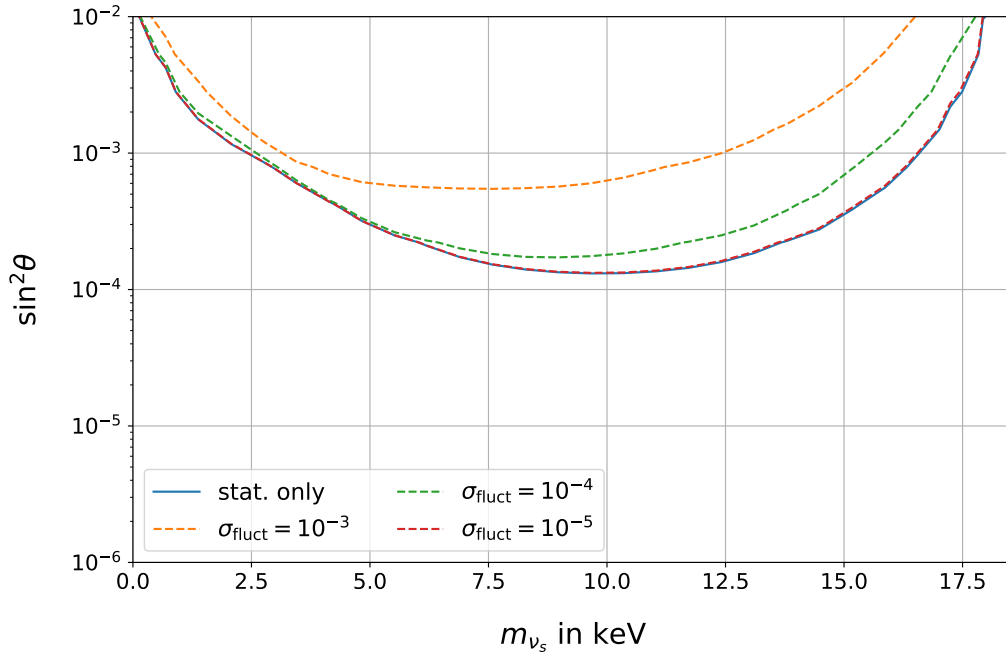


Figure 5.18: In the 7-day reference measurement, a fluctuation of $\sigma_{\text{fluct}} = 10^{-3}$ reduces the sensitivity on the mixing angle by up to a factor of four. Uncertainties of the size $\sigma_{\text{fluct}} = 10^{-5}$ are negligible within the reviewed statistics. In an intermediate case of $\sigma_{\text{fluct}} = 10^{-4}$ the reduction on the mixing angle leads values of up to a factor of two.

with the components:

- ϵ_{abs} : The absolute efficiency is a characteristic value for every detector, caused by technical features. For the FPD it is constant for all pixels and independent of the retarding potential. By fitting the normalization of the spectrum R_{sig} , ϵ_{abs} is absorbed and plays no significant role in the analysis.
- $\epsilon_{\text{pxl}}(k)$: Due to small variations of the energy resolution of the FPD pixels k , ϵ_{abs} needs to be corrected by a pixel dependent factor $\epsilon_{\text{pxl}}(k)$. It can be further used to take into account pixel-correlations, for example of background space structures.
- $\epsilon_{\text{roi}}(qU_{\text{ret}}, k)$: In order to optimize the signal to noise ratio, only parts of the measured detector response are considered in the analysis. The region-of-interest (ROI) is kept constant for all retarding potentials to avoid shifts in the signal to noise ratio. A typical ROI for an endpoint measurement at KATRIN is $14 \text{ keV} \leq E_e \leq 32 \text{ keV}$ (considering the post acceleration $qU_{\text{PAE}} = 10 \text{ keV}$) [131]. If the spectrum is scanned to lower energies, the peak position of the measured detector response shifts to smaller values. This leads to a qU_{ret} dependent event loss. The effect also depends on the pixel k , since the detector response (and thus the peak position) varies for the different segments [47].
- $\epsilon_{\text{bs}}(qU_{\text{ret}})$: Signal electrons are backscattered at the detector surface with a mean probability of approximately 20% [288]. Most of the electrons get backreflected to the detector at the post acceleration potential, retarding potential, or by magnetic reflection at the pinch magnetic field. Electrons with scattering angles smaller than $\theta_{\text{scat}} \leq \sin^{-1} \sqrt{\frac{B_{\text{det}}}{B_{\text{pch}}}} \approx 51^\circ$ (nominal setting) are unlikely to be magnetically reflected. If their energies after scattering are larger than $E_{\text{bs}} > qU_{\text{ret}}$ they are able to overcome

the retarding potential and are lost from the measurement. This electron loss is expressed in the detection efficiency $\epsilon_{\text{bs}}(qU_{\text{ret}})$.

- $\epsilon_{\text{pu}}(qU_{\text{ret}}, k)$: If two signal electrons hit a single pixel within a short time interval, the detector is unable to resolve both events which results in an event loss. This effect is called signal pile-up. A detailed description can be found in section 4.1.1. Signal pile-up is a rate dependent effect that scales with the applied retarding potential qU_{ret} . To second order, it also depends on the observed pixel k due to rate differences measured at each pixel.

For deep tritium β -scans, all retarding potential dependent effects are of particular interest. This section focuses on the backscattering (section 5.6.1) and the pile-up detection efficiency (section 5.6.2). Since $\epsilon_{\text{roi}}(qU_{\text{ret}}, k)$ relies on the specific measurement and analysis window, it will be not discussed here.

All pixel dependencies are of major importance in the data analysis, but have no first order influence on the spectral shape and are therefore not discussed within this work.

The influence of a retarding potential dependent detection efficiency on an integral keV-scale sterile neutrino search with the KATRIN experiment was already topic of different investigations. While [47] mainly focused on $\epsilon_{\text{roi}}(qU_{\text{ret}}, k)$ and $\epsilon_{\text{pu}}(qU_{\text{ret}}, k)$, [98] investigated $\epsilon_{\text{bs}}(qU_{\text{ret}})$ intensively. Almost simultaneously to the work in hand, the thesis [262] was completed that introduced a comprehensive detector response model that goes well beyond the work presented in this chapter.

The following studies combine all available information and extend it with own simulations and calculations. Especially the introductions to section 5.6.1 and 5.6.2 might show some parallelities to [262]. All information or knowledge that has been taken from other works are marked with references.

5.6.1 Electron Loss due to Backscattering

The monolithic silicon wafer of the FPD has a diameter of 125 mm and a thickness of 503 μm , including a non-sensitive dead layer of 100 nm [173]. Signal electrons that hit the detector wafer interact with the silicon medium by inelastic and elastic scattering with a probability of approximately 20% of being backscattered. The backscattering probability P_{bs} depends on the energy and impact angle of the electron with the latter being the dominate parameter. While P_{bs} is almost constant for impact angles between 0° and 18° , it increases fast for larger angles (see also appendix D). [288]

In order to boost the electrons to an energy where a better distinguishability of the signal to the intrinsic detector background is given, the signal electrons are focused towards the detector wafer with the post acceleration electrode (PAE) with a nominal potential of $qU_{\text{PAE}} = 10 \text{ keV}$ [174]. As a side effect, the impact angle and respectively the backscattering probability decreases.

Electrons that scatter back at the detector are likely to be backreflected at either the detector magnetic field itself, the post acceleration potential, the pinch magnetic field, or the retarding potential of the main spectrometer [98]. Figure 5.19 shows the distribution of the turning z -position for backreflected electrons simulated with *KASPER*.

The simulations performed in this study show that the backreflection happens on a very short time scale, and that most of the backscattered events are not resolved by the detector time resolution. Furthermore, the backscattered electrons do not necessarily hit the same pixel again. Depending on their angle and the magnetic field at the detector (size of the *Larmor* radius) they can also hit a nearby pixel. Regardless of whether they hit the same pixel again, multiple crossings of the non sensitive dead layer lead to a reduced deposited

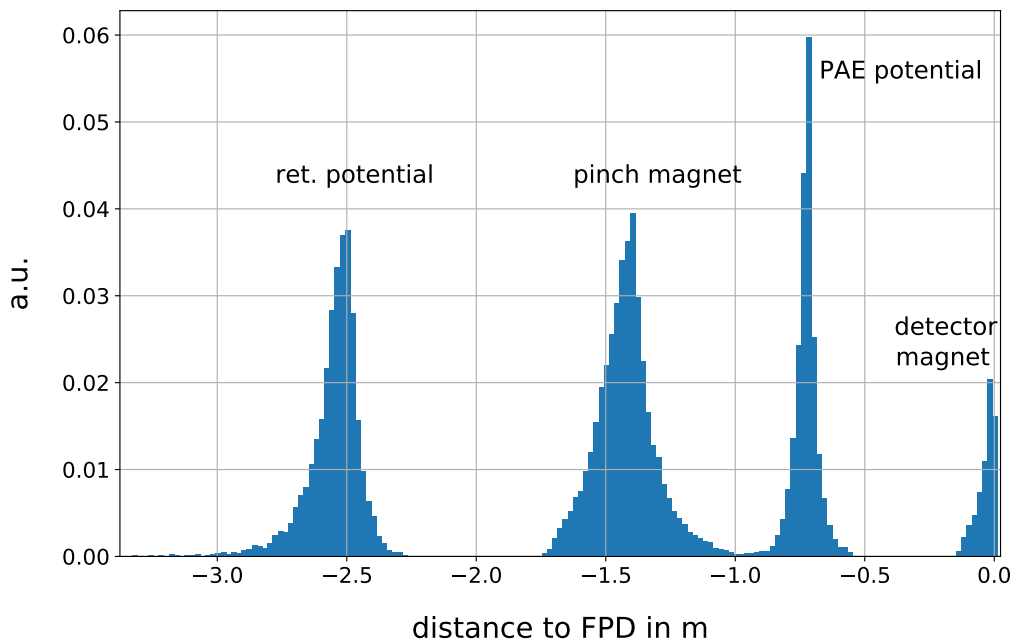


Figure 5.19: The points of backreflection of electrons that scattered back at the detector surface as simulated with *KASPER*. The electrons have β -distributed initial energies of $E_{\text{ini}} = [18.475, 18.575]$ keV. The retarding potential was set to $qU_{\text{ret}} = 18.475$ keV. Depending on their energy and scattering angle, the electrons are reflected back to the detector either on the magnetic field of the detector itself, the post acceleration electrode potential, the field of the pinch magnet, or the retarding potential of the main spectrometer.

energy. This confirms results of [262] and [98].

All these effects are independent of the retarding potential and well understood for the purpose of KATRIN. With the *KESS* software package, developed in 2011, the detector response function can be simulated with a high precision and has been cross checked with measurements [288].

Further details on the detector response modeling can be found in [262].

In an integral measurement, the fraction of electrons that are lost after backscattering scales with the retarding potential qU_{ret} . Electrons with an initial energy E_{ini} that deposited an amount of energy ΔE at the first hit of the detector, are able to pass the spectrometer potential when

$$E_{\text{ini}} - \Delta E > qU_{\text{ret}} \quad (5.49)$$

is fulfilled. By lowering qU_{ret} the number of backscattered electrons that fulfill the condition increases. These electrons propagate back to the source and are lost from the measurement. As a consequence, the detection efficiency is reduced.

5.6.1.1 Influence on the Spectrum

In order to derive $\epsilon_{\text{bs}}(qU_{\text{ret}})$ in the scope of this work, the detector response was simulated on a single-event base for 19 retarding potentials between $qU_{\text{ret}} = [0.457, 18.475]$ keV with a total of 10^5 initial electrons for each setting. The β -electrons were started in front of the main spectrometer with an isotropic angular distribution. When the initial electrons hit the detector, a new track was generated allowing exact comprehension of the backscattering process. Thereby, the number of backscattered electrons as well as the number of electrons

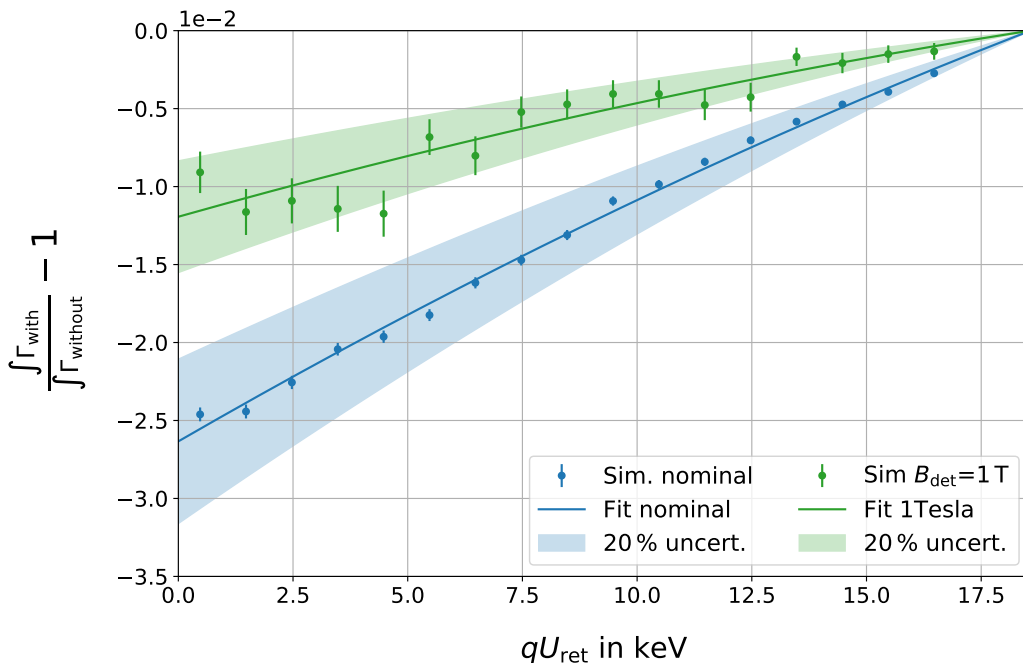


Figure 5.20: The influence of backscattering induced electron loss on the tritium β -decay spectrum simulated with *KASPER*. The effect has an overall size on the percent-level. The size of the effect depends on the detector magnetic field B_{det} . By reducing B_{det} , the number of electrons that are magnetically reflected at the pinch magnet increases, which suppresses the number of electrons that are able to reach the retarding potential [98]. The corrections were parameterized with a second degree polynomial (state in equation (5.51)). The larger errorbars of the simulation shown in green are caused by the ten times less statistics in the simulation.

that overcome the retarding potential after backscattering was determined. The detection efficiency was derived for each simulated retarding potential by

$$\epsilon_{\text{bs}}(qU_{\text{ret}}) = 1 - \frac{N_{\text{lost}}}{N_{\text{hit}}}, \quad (5.50)$$

with the number of electrons that hit the detector surface N_{hit} and the number of electrons that overcome the retarding potential and are lost N_{lost} . This procedure shows analogies to [98, 262].

The detection efficiency has been implemented in the model with a second degree polynomial

$$\epsilon_{\text{bs}}(qU_{\text{ret}}) = a \cdot (qU_{\text{ret}} - E_0)^2 + b \cdot (qU_{\text{ret}} - E_0) + 1.0, \quad (5.51)$$

with a fixed value at the endpoint of $\epsilon_{\text{bs}}(qU_{\text{ret}} = E_0) = 1.0$.

Figure 5.20 illustrates the influence of $\epsilon_{\text{bs}}(qU_{\text{ret}})$ on the measured spectrum. The blue line and markers correspond to the nominal KATRIN magnetic field setting. The errorbars on the markers are the statistical uncertainties of the simulation.

The number of lost electrons increases if the retarding potential is lowered. If no potential is applied, approximately 2.5% of all initial electrons are lost.

5.6.1.2 Countermeasures

The energy loss due to backscattering can be reduced by lowering the detector magnetic field B_{det} in relation to the pinch magnetic field B_{pch} . In this case, the number of backscattered electrons that are magnetically reflected at the pinch magnetic field increases, which

corresponds to a reduction of the number of electrons that are able to reach the retarding potential and overcome it. [98]

The green markers and line in figure 5.20 show the influence of $\epsilon_{\text{bs}}(qU_{\text{ret}})$ on the integral spectrum for a setting with $B_{\text{det}} = 1.0 \text{ T}$. Compared to the nominal setting, the influence of a retarding potential electron loss is reduced by approximately a factor of 2.5.

5.6.1.3 Uncertainties and Influence on the Sensitivity

The deviation of the backscattering loss detection efficiency is based completely on simulations. Due to their high required computation time, the influence of uncertainties on the input parameter, for example magnetic field variations, could not be studied within this work. Furthermore, the simulation is based on simplifications, for example the starting angular distribution of the electrons at the entrance of the main spectrometer is assumed to be isotropic. As a consequence, a rather large and uncorrelated uncertainty of 20% was assumed on the model (the value approximately corresponds to the 1σ error on the polynomial fit).

Figure 5.21 shows the influence of the backscattering electron loss on the *7-day reference measurement* sensitivity. Due to the size of the effect, uncertainties on the model have a large influence on the result. For the nominal setting, the sensitivity on the mixing angle decreases by up to 1.5 orders of magnitude. A reduction of the detector magnetic field leads to no significant improvement on the sensitivity within a uncorrelated uncertainty of 20%.

If the uncertainty are improved in the future, the sensitivity loss could be reduced. However, for an uncertainty of 5% it is still significantly large with deviations from the statistical sensitivity by up to one order of magnitude.

5.6.1.4 Conclusion

Electrons scatter back at the FPD with a mean probability of 20% [288]. Most of the electrons are electrically or magnetically backreflected within times smaller than the detector time resolution. Electrons with a backscattering angle smaller than $\theta_{\text{scat}} \leq \sin^{-1} \sqrt{\frac{B_{\text{det}}}{B_{\text{pch}}}}$ and a high remaining energy of $E_{\text{BS}} \geq qU_{\text{ret}}$ overcome the retarding potential, which leads to a reduced detection efficiency. [98] The probability for the electron loss increases when the retarding potential is lowered. This effect has a major influence on the integral spectrum of up to 2.5%. Consideration in the analysis is therefore required.

The electron loss can not be measured directly which makes simulations necessary. It is strongly recommended to validate the underlying *KESS/KASPER* simulations in a separate test experiment. A first outline has been presented in [16].

Due to the size of the effect, the impact on a keV-scale sterile neutrino search is large. Assuming a 20% uncorrelated uncertainty on the model leads to a reduction on the sensitivity of 1.5 orders of magnitude for the *7-day reference measurement*.

The effect can be slightly diminished by lowering the detector magnetic field in respect to the pinch magnetic field (by a factor of up to 2.5 for $B_{\text{det}} = 1.0 \text{ T}$) [98]. However, the field reduction only leads to an improvement of the sensitivity by up to a factor of two. The strongest potential lays within the improvement of the modeling and therefore the reduction of the uncertainty on the model.

5.6.2 Rate dependent Pile-up Loss

The FPD data acquisition has a characteristic shaping length L . If two electrons hit the same pixel within this time interval, they are counted as one event. [173] Assuming that both electrons have the same energy E_e , the recorded energy varies between E_e (long interval) and $2E_e$ (short interval). This effect is called signal pile-up and is introduced in

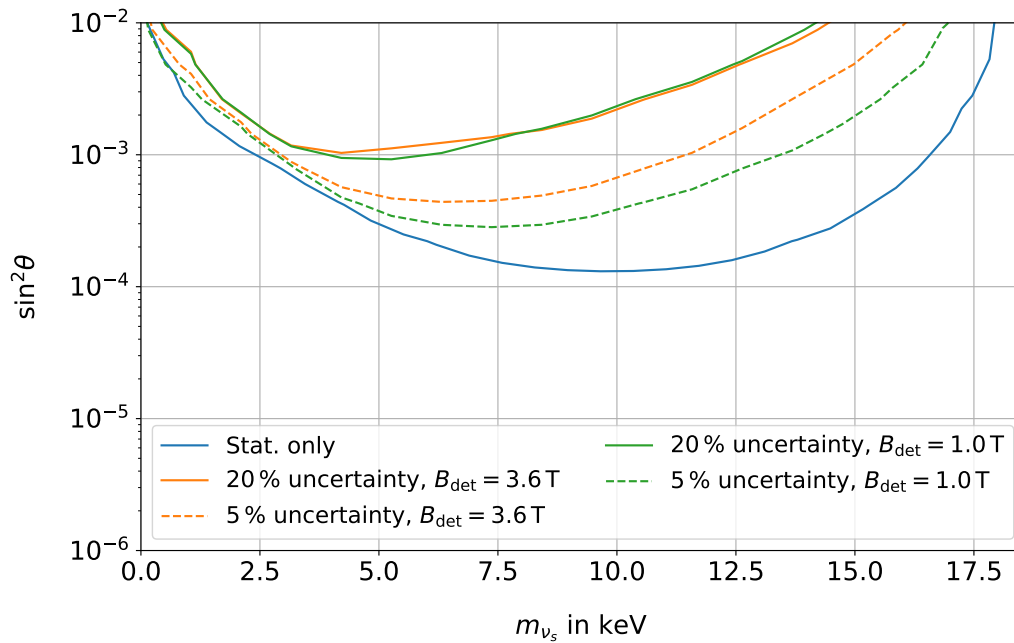


Figure 5.21: The influence of backscattering energy loss on the keV-scale sterile neutrino search is large. For an uncertainty of 20% on the model, the sensitivity of the *7-day reference measurement* at the nominal magnetic field setting would be reduced by up to 1.5 orders of magnitude. Lowering the detector magnetic field leads to a reduction of the effect which, however, has only an influence on the sensitivity if simultaneously the uncertainty on the modeling is reduced. A decrease of the uncertainty to 5% would lower the sensitivity reduction, but is also limited to a reduction to one order of magnitude.

detail in section 4.1.1. For the analysis of the detector data, most of the pile-up events are not considered, since they occur outside the ROI. However, this effect leads to a reduction of the detection efficiency accordingly. [250]

The following section introduces a model to estimate the pile-up loss and calculates the influence on the measured spectrum (section 5.6.2.1). Subsequently, a countermeasure is introduced (section 5.6.2.2) and uncertainties on the model as well as their impact on the sensitivity of a keV-scale sterile neutrino search is studied (section 5.6.2.3).

5.6.2.1 Influence on the Spectrum

The effect of pile-up depends on the signal rate at the detector and respectively on the retarding potential of the main spectrometer. In order to estimate the effect of event loss due to pile-up, a two-fold random coincident model is used. The idea and the model is taken from [250]. It is based on two major assumptions: 1. The signal rate is Poisson distributed; 2. All events that pile-up are lost and will not be counted.

At a given rate $R(qU_{\text{ret}})$, the time intervals Δt between two events are exponentially distributed with the probability density function

$$P_{\Delta t} = R \cdot \exp(-R\Delta t). \quad (5.52)$$

The probability of two electrons to hit the detector within the shaping time L (with the coincident window $2L$) can be described by

$$P_{\text{pu}}(R) = \int_0^{2L} R \cdot \exp(-R\Delta t) d\Delta t = 1 - \exp(-2LR), \quad (5.53)$$

which directly leads to the pile-up detection efficiency

$$\epsilon_{\text{pu}}(qU_{\text{ret}}) = 1 - P_{\text{pu}}(R) = \exp(-2LR(qU_{\text{ret}})) \cdot [250] \quad (5.54)$$

Figure 5.22 shows the influence of $\epsilon_{\text{pu}}(qU_{\text{ret}})$ on the integral tritium β -spectrum, for a scenario with a maximum integrated count rate of $R_{\text{max}} = 10^5$ cps reached at the lowest retarding potential. A shaping length of the FPD trapezoidal filter of $L = 1.6 \mu\text{s}$ was used for the calculations.

Compared to $\epsilon_{\text{bs}}(qU_{\text{ret}})$, the influence of pile-up loss to the spectrum is one order of magnitude smaller, and reaches a maximum deviation of approximately $2.1 \cdot 10^{-3}$ if no retarding potential is applied.

5.6.2.2 Countermeasures

Since the number of pile-up events is directly proportional to the rate at the detector, the influence on the measured spectrum can be reduced by lowering the overall rate. Techniques to experimentally achieve lower rates can be found in section 4.1.

Figure 5.22 shows that the influence on the spectrum can be reduced by one order of magnitude, if the maximum integrated rate at the detector is lowered to $R_{\text{max}} = 10^4$. However, if the measurement time is not increased accordingly, the statistical sensitivity will be reduced.

5.6.2.3 Uncertainties and Influence on the Sensitivity

There are two major uncertainties in the model that have been identified in [250] for energies close to the endpoint which are applied for lower electron energies in this study.

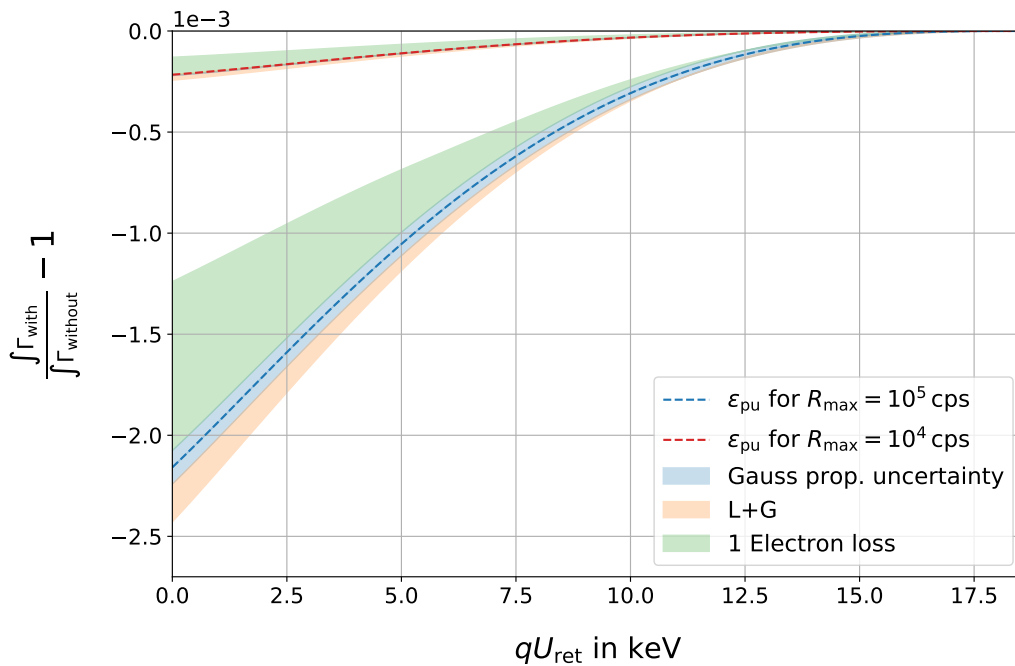


Figure 5.22: The contribution of electron loss due to pile-up on an integral spectrum calculated with equation (5.54). The blue dashed line shows a scenario with a maximum integrated signal rate of $R_{\max} = 10^5$ cps. The underlying model that is used to calculate the pile-up electron loss has two major uncertainties: by choosing the coincident time window too short, the electron loss is underestimated (orange area), while the assumption that all pile-up electrons are automatically lost, leads to an overestimation (green area) [250]. A simple Gaussian propagation of the uncertainty on the rate causes a symmetric uncertainty (blue area) [47]. The red dashed line shows a scenario with a maximum integrated rate of $R_{\max} = 10^4$ cps. The contribution to the integral spectrum reduces by one order of magnitude compared to the other displayed scenario.

- **Event window length:** The model described in equation (5.54) assumes that the coincidence window exactly equals the shaping length of the detector L . However, the time between two filter responses is neglected. This so-called gap length G is a characteristic parameter of the trapezoidal filter and is in the order of 200 ns (for more details see section 4.1.1). The actual coincident window time is between L and $L + G$. Using $L + G$ instead of L in equation (5.54) leads to a further reduction of the detection efficiency. The orange error band in figure 5.22 shows the difference between the results for L and $L + G$ as the coincident window.
- **Loss of all pile-up events:** The model assumes that both electrons that take part in the pile-up are lost. However, two electrons with the energy E_e that pile-up result in an event with the energy between $[E_e, 2E_e]$, with a uniform probability distribution [251]. With a nominal upper bound of 32 keV, not all of the pile-up events will be outside the ROI. Events with a smaller energy will be counted as one electron instead of zero. This effect can be corrected by calculating the probability for electrons with different initial energies (distributed in a tritium β -decay shape) to be measured inside the ROI, and count these events as one electron. The resulting uncertainty has been calculated for the full energy range. It is large and reaches a value of almost 40% for lower energy parts of the spectrum (marked as the green area in figure 5.22).

As proposed in [47], a simple Gaussian propagation of equation (5.54) was applied in order to account for the uncertainty of the rate and time resolution (marked blue in figure 5.22) which is, however, dominated by both other uncertainties.

The impact of pile-up electron loss on a keV-scale sterile neutrino search is displayed in figure 5.23. The relatively large uncertainties of up to 40% caused by the simplifications of the model, lead to a sensitivity reduction of up to a factor of 3.5 in particularly for higher m_{ν_s} . Assuming that the model would be improved in a way that the only uncertainty is the Gaussian error on the rate, the effect could be neglected within the statistical sensitivity studied here.

A reduction of the maximum rate by a factor of ten would improve the statistical sensitivity by approximately a factor of $\sqrt{10} \approx 3.16$ over the entire mass scale (assuming the same total measurement time of 7 days). However, due to the reduction of the pile-up loss, the relative uncertainty on the model does not lower the sensitivity any further.

5.6.2.4 Conclusion

High count rates at the detector lead to signal pile-up. Events that pile-up are likely to be outside the ROI and therefore rejected from the measurement [251]. The probability for pile-up increases with the rate and respectively by lowering the retarding potential. As a consequence, the detection efficiency needs to be corrected for the pile-up event loss [251]. The contribution of pile-up electron loss to the total detection efficiency is approximately a factor of ten smaller compared to that from backscattering electron loss. Even if the uncertainties on the model are rather large, the sensitivity reduction of the *7-day reference measurement* is moderate with a sensitivity loss on the mixing angle up to a factor of 3.5. By lowering the absolute signal rate at the detector, the effect can be effectively suppressed. However, if the rate reduction is not combined with an increase of the total measurement time, the statistical significance decreases accordingly.

The DRIPS software is a tool that can help to improve the pile-up model. It has been developed with the purpose to simulate the electronic response of the FPD for high detector rates and can provide a more reliable calculation for energy ranges lower than the endpoint region in the future. [251]

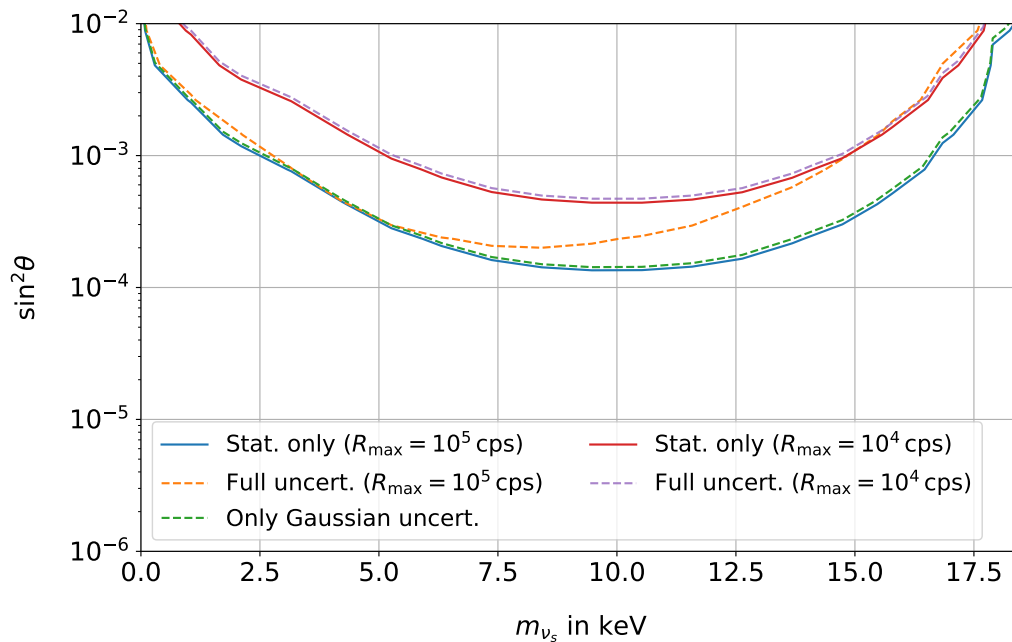


Figure 5.23: Compared to backscattering, the influence of pile-up electron loss on a keV-scale sterile neutrino search is small. Even the relative large uncertainties on the model lead only to a reduction of a factor of 3.5 for higher sterile neutrino masses. If the maximum rate is reduced to $R_{\max} = 10^4$, the influence of uncertainties on the model can be neglected. However, the statistical sensitivity is reduced on the full mass scale compared to the *7-day reference measurement* ($R_{\max} = 10^5$).

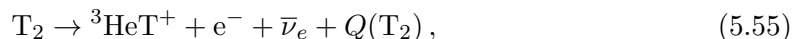
5.7 Theoretical Corrections of the Spectrum

If the tritium β -decay is used to study fundamental physical quantities such as the neutrino mass or the existence of an additional sterile mass eigenstate, the simple description of equation (1.45), needs to be extended [289]. Over the last decades there have been many efforts to precisely describe the tritium β -spectrum with focus on the endpoint region, for example in [133, 290, 291, 289].

If KATRIN is used to search for keV-scale sterile neutrinos, corrections of the spectral shape over the entire energy range are of importance as shown, for example, in [12]. This section discusses all major modifications to the β -decay spectrum, starting with the final state distribution (section 5.7.1) and followed by several other theoretical correction terms (section 5.7.2).

5.7.1 Final State Distribution

KATRIN observes the β -decay of tritiated hydrogen molecules with different isotopological compositions, in the nominal setting mainly T_2 [10]. After the decay



due to the recoil of the outgoing electron, the daughter molecule ${}^3\text{HeT}^+$ can be left in an excited state which requires a correction of the released energy $Q(T^2)$ [121, 289]. As a consequence, the neutrino phase space shown in equation (5.61) needs to be corrected

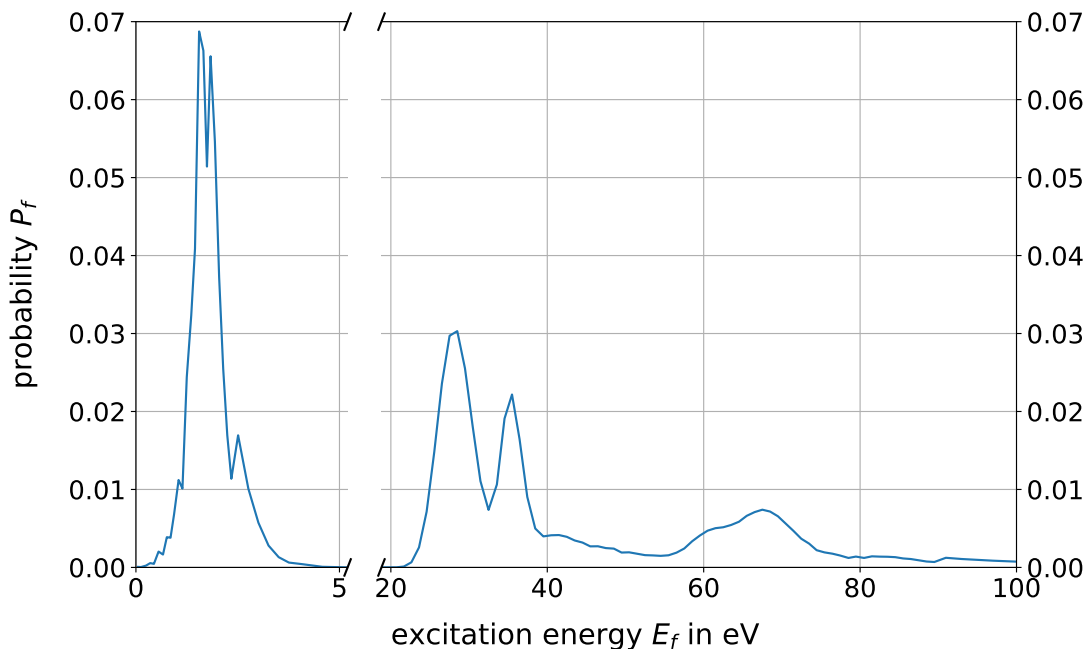


Figure 5.24: The excitation energies of the HeT^+ ion show several peaks between 0 and 100 eV. All excitation energies $E_f < 5$ eV relate to rotational and vibrational excitations of the ground state and have a mean value of $\bar{E}_f \approx 1.75$ eV. For energies above 20 eV, electronic excitations occur. [133] The distribution is taken from [293]. It corresponds to an outgoing electron with $E_e = 18.6$ keV and T_2 molecule with an initial angular momentum of $J = 0$.

by the Final State Distribution (FSD) with excitation energies E_f and the corresponding probabilities P_f

$$(E_0 - E_e) \cdot \sqrt{(E_0 - E_e)^2 - \sum_i |U_{ei}|^2 m_i^2} \rightarrow \quad (5.56)$$

$$\sum_f P_f \cdot (E_0 - E_e - E_f) \cdot \sqrt{(E_0 - E_e - E_f)^2 - \sum_i |U_{ei}|^2 m_i^2} \quad [121]. \quad (5.57)$$

As can be seen in this equation, the FSD has an influence on the spectral shape and the kinematic endpoint position. Therefore, the sensitivity of a neutrino mass measurement depends crucially on a precise knowledge of the FSD [292].

Figure 5.24 shows the FSD of the decay stated in equation (5.55) for an outgoing electron with $E_e = 18.6$ keV [293]. The first peak corresponds to the electronic groundstate ($E_f \approx 2$ eV), broadened by rotational and vibrational excitations, followed by electronic excitation states ($E_f > 20$ eV) and the electronic continuum [294]. The spectrum has been derived for excitation energies up to $E_f < 240$ eV in [293, 294].

Since only the energy of the electron can be measured, while the energy of the neutrino and the remaining energy in the daughter nucleus are undetected, the final-state distribution of the daughter nucleus requires a theoretical determination. The FSDs for all hydrogen isotopologues, including different initial states in terms of angular momentum, have been precisely calculated for energies close to the kinematic endpoint, using the so-called *sudden approximation approach* [134, 294].

Since the recoil energy, and respectively the average excitation energy, of the daughter

molecule decreases with the energy of the outgoing β -electron, the FSDs are energy dependent [133]. So far, no calculations of the FSDs for lower tritium β -decay energies haven been made. However, first approaches to estimate the energy dependence are presented for example in [133]. The following paragraph introduces a model that has been developed recently in [295] and discusses the influence of energy dependent FSDs on the tritium β -decay spectrum and the impact on a keV-scale sterile neutrino search.

Model for an Energy dependent Ground State

The model that is studied here, was developed in [295] and mainly follows the idea of [133]. It approximates the FSD ground states with a Gaussian distribution whose width and position scales with the recoil energy of the daughter molecule.

The recoil energy of the daughter molecule with mass M_{DN} is a function of the kinetic energy $E_{e/\nu}$, momentum $\vec{p}_{e/\nu}$, and mass $m_{e/\nu}$ of the outgoing leptons, as well as the angle between the neutrino and electron momenta $\theta_{e\nu}$

$$E_{\text{rec}}(E_e) = \frac{1}{M_{\text{DN}}} [(E_e^2 + 2E_e m_e) + 2|\vec{p}_e||\vec{p}_\nu| \cdot \cos \theta_{e\nu} + (E_\nu^2 - m_\nu^2)] \quad [133]. \quad (5.58)$$

As displayed on the left side of figure 5.25, the maximum recoil energy $E_{\text{rec}}^{\text{max}} = 1.72 \text{ eV}$ is reached at the kinematic endpoint of the tritium β -decay.

The ground state can be approximated by a Gaussian distribution with the standard deviation of

$$\sigma_{\text{gs}} = \sqrt{\frac{2\mu}{M_{\text{T}}} \cdot E_{\text{rec}} \cdot E_{\text{zp}}}, \quad (5.59)$$

with the reduced mass of the recoiling system μ and the mass of the tritium atom M_{T} [295]. In order to express the energy dependent broadening of the ground state due to rotational and vibrational excitation, the daughter molecule is described as a one-dimensional harmonic oscillator with the zero-point energy of

$$E_{\text{zp}} = \frac{1}{2} \hbar \omega_c - a \left(\frac{1}{2} \hbar \omega_c \right)^2, \quad (5.60)$$

with $\hbar \omega_c = 0.5320 \text{ eV}$ [133]. The second term describes a small anharmonic correction with the coefficient $a = -0.0537 \text{ eV}^{-1}$. Both values have been derived in [133] using data from [296]. The right side of figure 5.25 shows the approximations of different ground states for various electron energies.

The modeling of the excited states as well as the electronic continuum is more complex and requires time consuming computation. However, the energy dependence of the excited states is found to be rather small compared to the ground state. [295] Therefore, the simplified energy dependent FSD model used in this study assumes the same excited states and electronic continuum for all energies calculated in [293].

5.7.1.1 Influence on the Spectrum

The illustration on the top panel of figure 5.26 shows the relative influence of a constant as well as an energy dependent FSD on the spectrum. Both have a large influence on the spectral shape which increases significantly for energies close to the endpoint. The constant FSD was calculated with the approximation of a fixed electron energy $E_e = 18.6 \text{ keV}$.

The bottom panel shows the comparison of two spectra: One calculated with a constant FSD and the other with an energy dependent one. The spectra deviate up to values of $4.9 \cdot 10^{-2}$ in the region close to the endpoint. The divergences reduces for higher energies to a level of 10^{-3} .

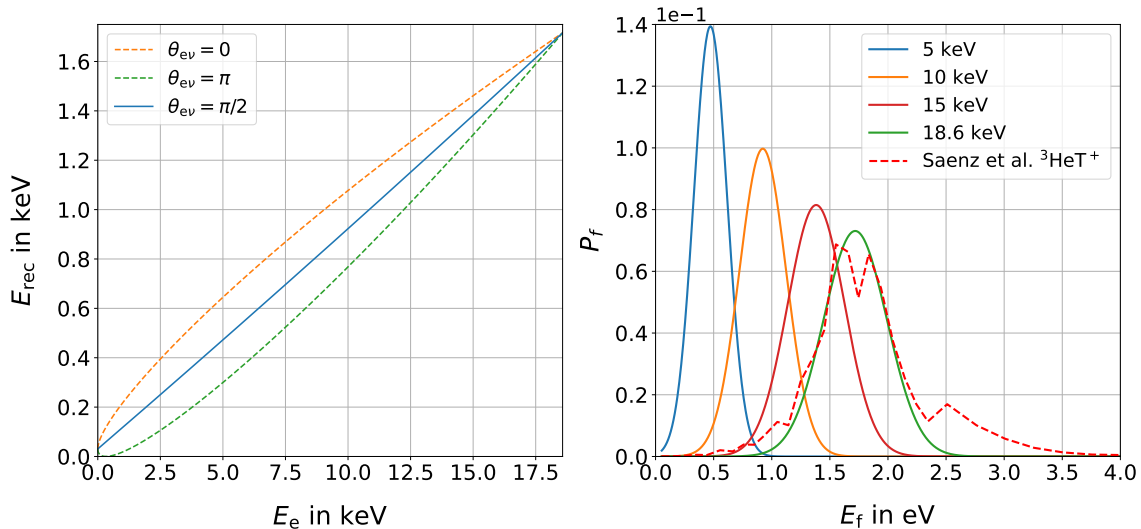


Figure 5.25: The left figure shows the recoil energy of the daughter nucleus as a function of the kinetic energy of the outgoing electron calculated by equation (5.58). Beside the energy, it also scales with the angle between the outgoing lepton momenta. If the recoil energy is varied, the FSD of the daughter molecule changes. The model studied in this section approximates the ground state probabilities with a Gaussian distribution. The right figure shows the ground state distribution for different electron energies for $\theta_{e\nu} = \pi/2$. The dashed line shows the ground state precisely calculated with the sudden-approximation [293]. The figures are adapted from [295] figure 3.2 and 3.3.

5.7.1.2 Uncertainties and Influence on the Sensitivity

In order to get an understanding on the possible impact of an energy dependent FSD on a keV-scale sterile neutrino search, a general uncertainty of 30% on the FSD was assumed in the model. Figure 5.27 shows the result of the sensitivity study which reveals a reduction of up to a factor of six on the mixing angle.

It is important to mention that this model is only an approximation. It was developed to get a first understanding of the influence of an energy dependent FSD on the full energy scale of the tritium β -spectrum and should not be used for data analysis.

5.7.1.3 Conclusion

The FSD of the daughter molecule has a large influence on the neutrino mass determination as well as on a keV-scale sterile neutrino search. The energy required for the excitation is gained by the recoil of the outgoing electron, which leads to an energy dependence of the FSDs [133]. In this work, a first assumption of the impact of an energy dependent FSD on the full energy scale of the tritium β -decay spectrum was made. It shows, that the influence is significantly large and can reach relative spectral deviations of up to $4.9 \cdot 10^{-2}$. This implies consideration of the energy dependent FSD in the analysis of spectral scans of several keV below the endpoint.

The model used in this work includes only an approximation of the ground state energy dependence. All excited states as well as the electronic continuum is assumed to be energy independent. It is highly recommended to either analytically recalculate the FSD for a wider energy range, or improve the approximation of [295] used in this study.

5.7.2 Other theoretical Corrections

The following list contains several atomic and nuclear corrections on the tritium β -decay spectrum, for which the impact on the full energy range has first been discussed in the

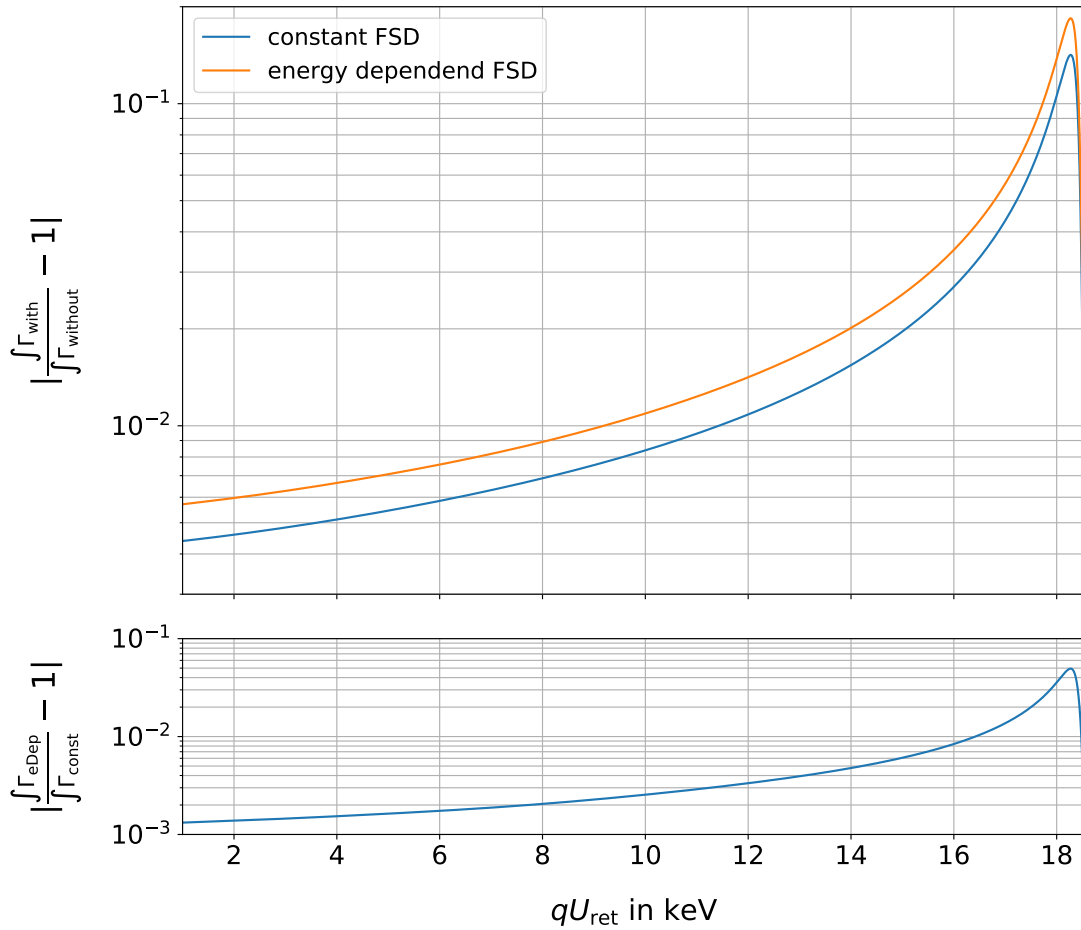


Figure 5.26: If the energy dependent FSD is used to correct the spectrum, the relative influence increases compared to the fixed FSD. A comparison of both cases can be found in the bottom panel. In particular for high electron energies they show a deviation of up to $4.9 \cdot 10^{-2}$.

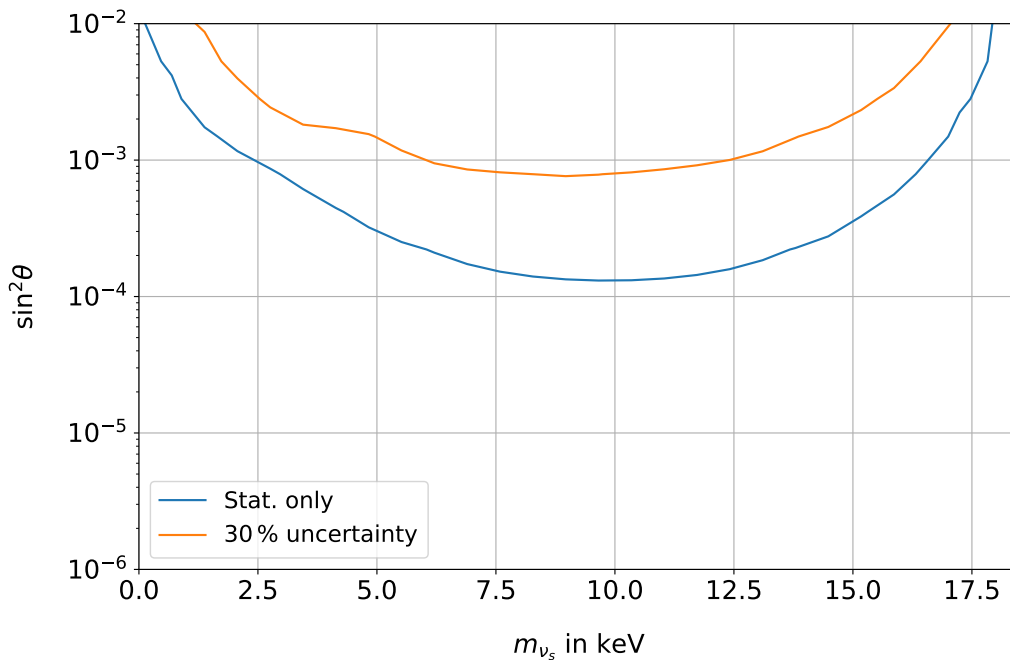


Figure 5.27: The impact of a general uncertainty of 30% on a simplified energy dependent FSD model on the sensitivity of the *7-day reference measurement*. It reduces by up to a factor of six for the mixing angle.

context of a KATRIN sterile neutrino search in [12]. For the impact of the theoretical corrections on the neutrino mass determination, the reader is referred to [289].

After reviewing different corrections, their influences on the spectrum are presented (section 5.7.2.1). In section 5.7.2.2, the uncertainties of the effects are estimated and their impact on a sterile neutrino search is studied.

All correction terms are a function of the energy of the outgoing electron E_e and the atomic number of the daughter nucleus Z (here $Z = 2$). The formulas used to calculate the following correction terms are documented in appendix G:

- The Fermi function $F(E_e, Z)$ used in equation (5.61) is often approximated by an empirical non-relativistic parameterization that can be found in [297]. For the required accuracy a more precise **relativistic Fermi function** $F_{\text{rel}}(E_e, Z)$ is calculated in [298].
- The Fermi function itself must be corrected by a factor $S(E_e, Z)$ which describes the **screening of the daughter nucleus Coulomb field** caused by the remaining 1s-orbital electron [299].
- The 1s-orbital electron does not only screen the nucleus Coulomb potential, but also interacts with the outgoing β -electron. In extreme cases it can be ejected and the β -electron takes its place. The influence of the **interaction with the 1s-orbital electron** is introduced by a multiplicative correction term $I(E_e, Z)$ which is derived in [290] and [300].
- Considering the recoil of the daughter molecule leads to a **changed phase space** as well as **weak-magnetism**, and **V-A interferences**. All three effects can be combined to the recoil correction term $R(E_e, E_0, M)$, where E_0 is the kinematic endpoint and M the mass of the nucleus, as described for instance in [290, 298, 301].

- If the daughter nucleus is not handled as a point-like charge but as a charge distribution with a **finite extension**, the Coulomb field no longer scales with $1/r^2$, which leads to a correction term $L_0(E_e, Z)$. In addition, the wave function of both leptons needs to be reevaluated due to the spatial extension of the nucleus which is considered in the factor $C(E_e, Z)$. [302]
- The finite mass M of the nucleus leads to another required correction $Q(E_e, Z, M)$. Due to the combined momenta of the emitted leptons the **recoiling nucleus Coulomb field** is no longer stationary [302].
- Electrons that are emitted in a Coulomb field can interact with virtual as well as soft real photons which requires **radiative corrections** $G(E_e, E_0)$ [301].

Analogue to equation (12) in [289], the resulting differential β -decay spectrum can be formulated as

$$\frac{dN}{dE_e} = \frac{G_F}{2\pi^3} \cdot \cos^2 \Theta_C \cdot |M|^2 \cdot F_{\text{rel}}(E, Z) \cdot S \cdot I \cdot C \cdot L_0 \cdot p_e \cdot (E_e + m_e) \cdot \sum_f P_f \cdot (E_0 - E_e - E_f) \cdot R \cdot Q \cdot G \cdot \sqrt{(E_0 - E_e - E_f)^2 - \sum_i |U_{ei}|^2 m_{\nu_i}^2}. \quad (5.61)$$

All corrections that are connected to the recoil of the daughter nucleus (R , Q , and G) are a function of the endpoint energy and a specific final state which requires a summation over all final states [289].

5.7.2.1 Influence on the Spectrum

In order to study the influence of the theoretical corrections on the spectral shape, the corresponding correction terms have been separately implemented in the β -decay model. Figure 5.28 shows the results for all corrections. Three of them dominate: the relativistic Fermi function, the screening of the 1s-orbital electron, and the radiative corrections. Even though they scale only slightly with the energy, their overall contribution is in the order of 10^{-3} . Effects such as the finite radius of the nucleus, the nucleus recoil, and the weak interaction corrections scale almost linearly with the energy (or are almost constant) and are in the order of $10^{-4} - 10^{-5}$. Compared to the other correction terms, their potential influence on a full energy spectrum measurement is relatively small. However, depending on the desired sensitivity of the keV-scale sterile neutrino measurement, all correction terms have to be considered in the analysis.

5.7.2.2 Uncertainties and Influence on the Sensitivity

The uncertainties on the correction terms are taken into account by two different methods:

1. Parameters that go into the calculations of the correction terms, were varied within their known uncertainties:
 - The screening potential $V_0 = 76 \text{ eV}$ can be experimentally determined and has an uncertainty of 17.01 % [303].
 - The ratio between axial and vector coupling constants $\lambda_t = (1.265 \pm 0.004)$ as well as the uncertainty on it is derived from the half-life of tritium [291].
 - The radius of the nucleus R_n as well as the FSD required to calculate the exact endpoint E_0 were approximated with an uncertainty of 10 % (a constant FSD was used in the calculations).

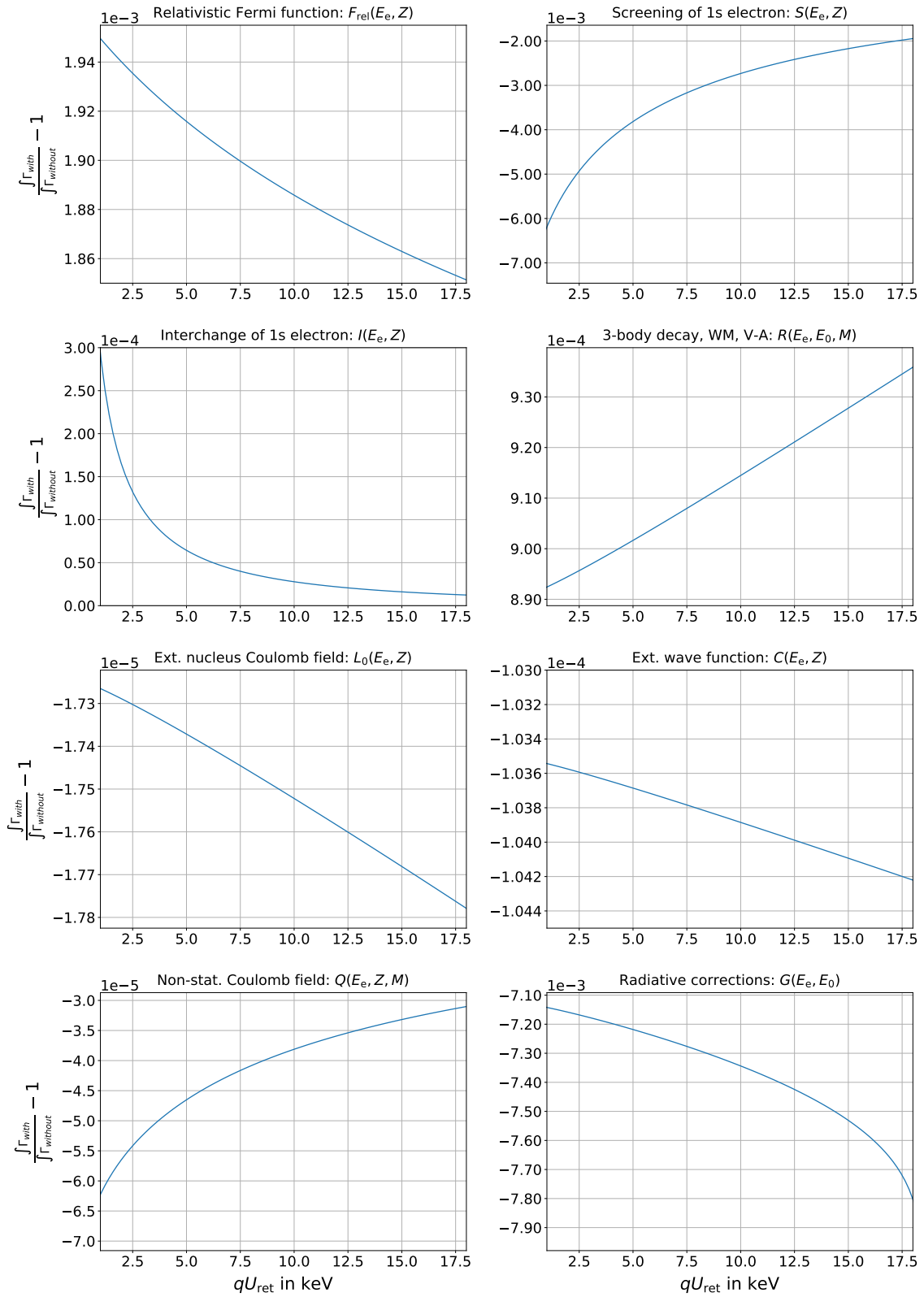


Figure 5.28: The relative influence of the correction factors on the full integral tritium β -decay spectrum. The formulas of the individual corrections can be found in appendix G. The figure is adapted from [12] figure 5.

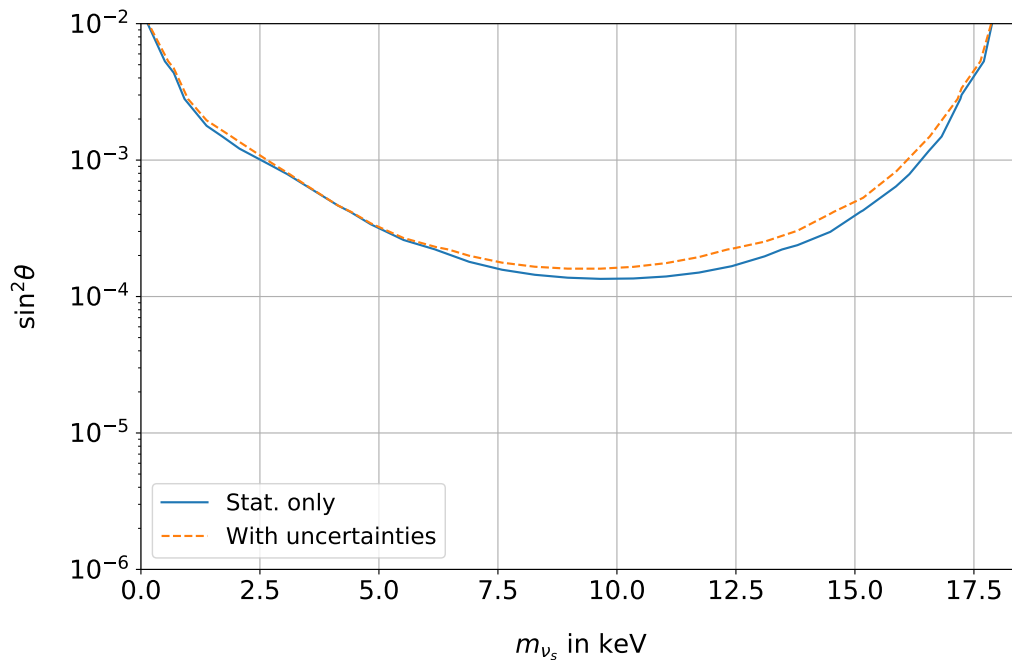


Figure 5.29: The influence of uncertainties on theoretical corrections is small. The sensitivity is only slightly reduced for the *7-day reference measurement*, up to a factor of 1.18.

- The uncertainties on the nucleus M , electron mass m_e , the magnetic moment μ of the nucleus, as well as the Sommerfeld finestructure parameter α were assumed to be negligible.
2. In order to emulate an overall uncertainty of the effect itself, a general error δ_T on the correction term $T(Z, W)$

$$T(Z, W)' \rightarrow T(Z, W) \cdot (1 + \delta_T), \quad (5.62)$$

was assumed with an overall uncertainty of $\delta = 1\%$.

Figure 5.29 shows the resulting sensitivity on the sterile neutrino parameter space for the *7-day reference measurement*. The influence of the theoretical corrections on the sensitivity is very small, and shows a maximum reduction by approximately a factor of 1.18.

5.7.2.3 Conclusion

If the tritium β -decay is used to search for sterile neutrinos in the keV mass range, a precise knowledge of the spectral shape is required. In this section, the influence of different theoretical nuclear and atomic corrections was studied. It was found that depending on the statistical sensitivity of the respective measurement, the corrections need to be taken into account. Furthermore the uncertainties on the correction terms were studied and it was shown that their influence on the sensitivity is small within the here studied statistical sensitivity.

5.8 Minor Effects

The following section describes five systematic effects that are of high relevance for the KATRIN neutrino mass determination measurement, but are found to be negligible for a keV-scale sterile neutrino search within the statistical sensitivity discussed in this work. For a high statistics sterile neutrino measurement as proposed in [12], they may have to be reconsidered.

5.8.1 Retarding Potential Dependent Background Rate

Depending on the experimental setting and the time since the last bake-out of the main spectrometer, the expected background rate for retarding potentials close to the endpoint varies between 0.2–0.5 cps [304, 305]. A recent overview of background causing effects and their influence on the neutrino mass determination measurement can be found in [177, 306].

If the tritium β -decay spectrum is scanned on a wide energy range, the signal rates exceed the expected spectrometer background rate by many orders of magnitude and seem negligible on the first order. However, there are measurements that imply a dependency of the measured background rate on the applied retarding potential over large energy ranges [177, 307]. The energy dependent component of the background is caused by Rydberg atoms [177]. For small retarding potentials the Rydberg component decreases by almost a factor of five (see figure 5.30) [177, 306].

The background rate as a function of the retarding potential can be measured and modeled with an empirical function as formulated in [177]

$$R_{\text{bkg}}(qU_{\text{ret}}) = p_0 \cdot \exp\left(\frac{p_1}{qU_{\text{ret}} + p_2}\right), \quad (5.63)$$

with $p_0 = 0.552 \pm 0.004 \text{ s}^{-1}$, $p_1 = -325.9 \pm 10.5 \text{ V}$, and $p_2 = 174.015 \pm 7.575 \text{ V}$ and is displayed in figure 5.30. In order to study the influence of a retarding potential background on the full tritium β -spectrum, it has been implemented in the model.

It was found, that the retarding potential dependency of the background rate has no impact on a keV-scale sterile neutrino search within the statistical sensitivity of the *7-day reference measurement*. Even if an unrealistically large uncertainty on the slope of 100% is assumed in the Monte Carlo data, the model is able to fit the measurement with a constant background rate, without losing any sensitivity.

It should to be mentioned that for future high statistics sterile neutrino measurements the background rate could be even further reduced by an adjusted LFCS setting (for example by an increase as discussed in section 4.2) or a lowering of the detector magnetic field. Both effects reduce the radius and therefore the volume of the observed magnetic fluxtube inside the main spectrometer, which lowers the background rate accordingly.

5.8.2 HV Instabilities

A stable high-voltage (HV) supply for the main spectrometer retarding potential is an essential requirement for the KATRIN experiment, since long term instabilities and voltage dependent non-linearity would lead to fluctuations on the absolute energy scale on the same level [308]. In order to reach the desired sensitivity on the effective antineutrino mass, the energy scale needs to be stable on a level of down to 3 ppm which corresponds to a HV stability of 60 meV at a retarding potential of $qU_{\text{ret}} = 20 \text{ keV}$ [10]. Since the first commissioning of the main spectrometer, it was shown in several measurements that the demanded accuracy is reached, and in fact exceeded, for example in [308, 309, 310].

In order to study the influence of HV instabilities on a keV-scale sterile neutrinos search, inaccuracies of the retarding potential setpoint have been implemented in the model. The inaccuracies translate to a random rate fluctuation of the same order.

Due to the small size of the instabilities, they are found to be negligible within the statistical significance of the *7-day reference measurement*. Only an exaggerated large HV-instability of 1 V would lead to a small reduction of the sterile neutrino sensitivity of approximately a factor of two.

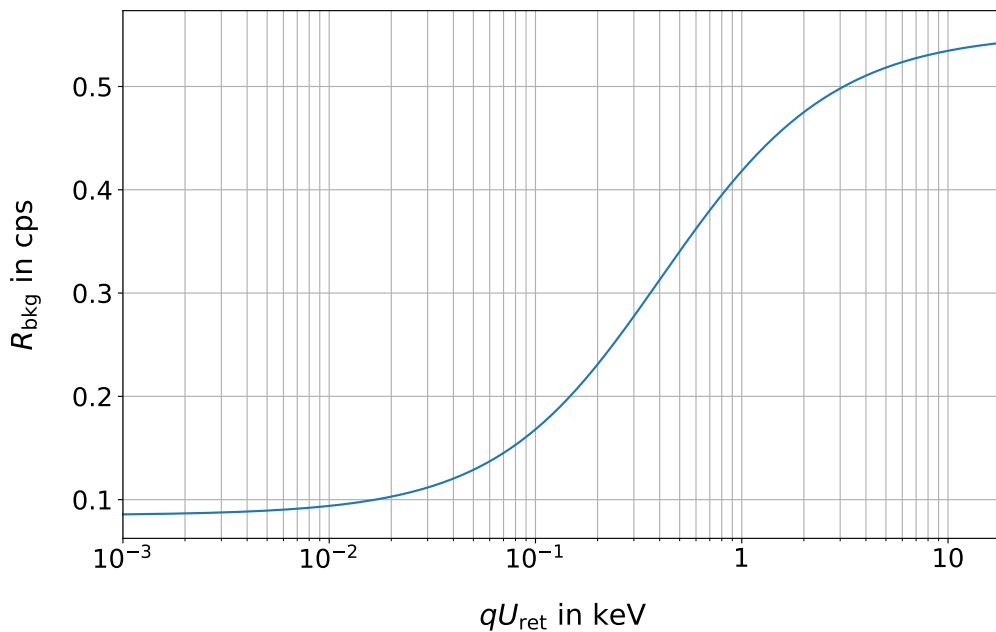


Figure 5.30: The main spectrometer background as a function of the applied retarding potential, calculated with the parameterization from equation (5.63). It increases up to a factor of 5, from a very low retarding potential of $qU_{\text{ret}} = 1 \text{ eV}$ to the highest retarding potential of $qU_{\text{ret}} = 20.0 \text{ keV}$. The absolute values of the background rate depend on the time since the last main spectrometer bake-out as well as on the magnetic field settings.

5.8.3 Doppler Broadening

The thermal motion of the decaying tritium molecules causes a Doppler broadening of the outgoing β -electrons [10]. The effect is slightly enhanced by the finite bulk velocity of gas flow in the source. Depending on the directional movement of the decaying molecule and the emitted electron, the effect can increase or decrease the electron's energy. [289] As derived in [289] by using approximations from [138, 311], the energy and temperature dependent Doppler broadening of the electron spectrum can be approximated by

$$\sigma_E = \sqrt{(E_{\text{CMS}} + 2m_e) \cdot E_{\text{CMS}} \cdot \frac{k_B T}{M}}, \quad (5.64)$$

with the temperature of the decaying molecule T , the molecule mass M and the center of mass energy E_{CMS} . The broadening σ_E as a function of the electron energy is illustrated in figure 5.31. For the mass of the T_2 molecule $M_{\text{T}_2} = 5.618 \text{ GeV}$ and the nominal temperature in the WGTS of $T = 30 \text{ K}$, the broadening of the electron spectrum reaches its maximum at the endpoint with $\sigma_E \approx 94 \text{ meV}$ and decreases for lower energies. For an endpoint analysis, the effect of Doppler broadening is significant [249, 289]. For a keV-scales sterile neutrino measurement it can be neglected due to its small size and smooth progression.

5.8.4 Synchrotron Radiation

Electrically charged particles emit synchrotron radiation when they propagate in cyclotron motion in magnetic fields which leads to an energy loss. In the KATRIN experiment, electrons are magnetically guided from their point of generation to the detector and are therefore vulnerable to synchrotron losses, especially in region with high magnetic field strength

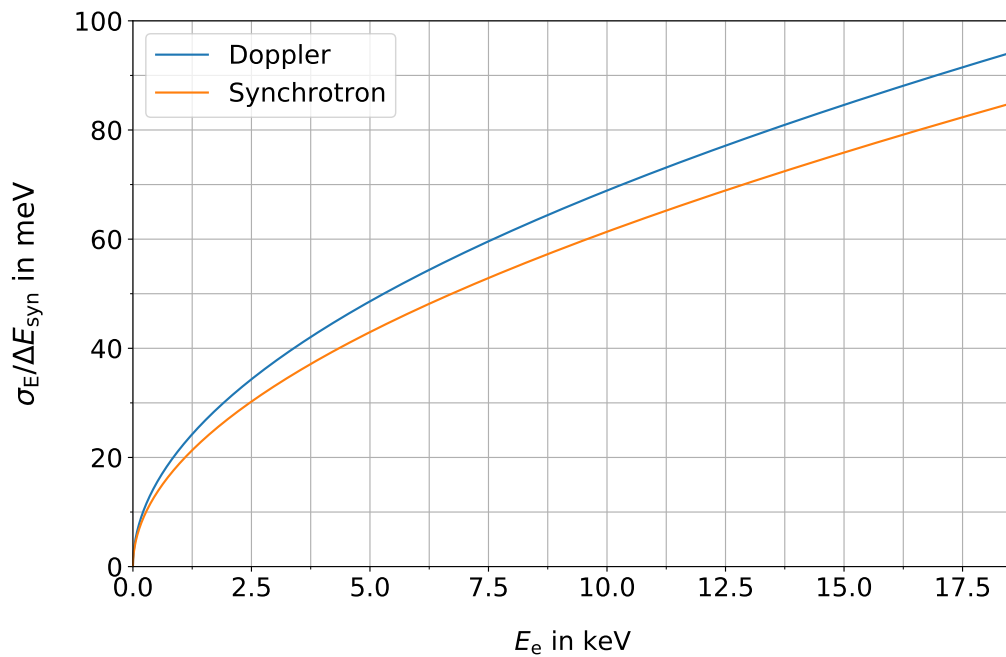


Figure 5.31: The energy broadening of the emitted electron caused by the Doppler effect (blue line) and the maximum energy shift caused by synchrotron radiation loss (orange line). The synchrotron loss was calculated with equation (5.64) and corrected by the results gained in [124] based on detailed simulations of the magnetic geometry. Both effects are significantly large at the endpoint and require consideration in the analysis for the neutrino mass determination [249, 289]. For a keV-scale sterile neutrino search both effects can be neglected within the statistical sensitivity of the *7-day reference measurement*.

namely in the source with $B_s = 3.6$ T and the transport section with $B_{\text{trans}} = 5.6$ T. The radiated energy scales with the polar angle of the electron and goes to zero for small angles. [10]

An approximation of the electron energy loss caused by synchrotron radiation can be found in [124] and is derived for a constant magnetic field B that acts on an electron over the length s

$$\Delta E_{\text{syn}} = \frac{-\mu_0 e^4}{3\pi m_e^3} \cdot B^2 \cdot \sin \theta \cdot E_e \cdot \gamma \cdot \frac{s}{\cos \theta \cdot v}, \quad (5.65)$$

with the vacuum permeability μ_0 , the electron's energy E_e , charge e , mass m_e , polar angle θ , speed v and Lorentz-factor γ .

Analogous to the Doppler broadening, the energy loss of synchrotron radiation is maximal for high energies, which causes a neutrino mass shift and makes it relevant for the neutrino mass determination [249, 289]. For the calculations shown in figure 5.31 the maximum starting angle for the nominal KATRIN setting of $\theta_{\text{max}} = 50.77^\circ$ was assumed. The size of the energy loss is approximately of same size as the Doppler broadening and can be neglected in a keV-scale sterile neutrino search as well.

5.8.5 Plasma Potential

Together with the positive ions, the secondary electrons generate a plasma which potential influences the energy offset of the emitted electrons between the source and the analyzing plane [285]. The source potential is dominated by the rear wall, however, various geometrical parameters can cause local deviations. A steady plasma concentration would cause a constant potential offset which shifts the electron spectrum by a negligible value and can be absorbed in the analysis by fitting the endpoint E_0 . Inhomogeneities in the space and time location of the plasma, however, can lead to spectral distortions. [249] Detailed plasma simulations in [285] estimate the radial and longitudinal potential variations to be on the order of 60 meV. The energy variations are small enough to be neglected for a keV-scale sterile neutrino search with KATRIN. With a lowered source activity, as suggested in section 4.1.3, the effect can be even further reduced.

5.9 Summary and Conclusion

This chapter presents the first study that comprehensively examines all so far known systematic effects that are relevant for a keV-scale sterile neutrino search with the KATRIN experiment, partly based on former works and further developed and unified with own calculations and simulations. For each effect, the influence on the shape of the integral spectrum has been derived. If possible, the shape correction has been implemented in the model and an uncertainty on the correction term was estimated. The impact of the uncertainties on a sterile neutrino sensitivity has been studied within the statistical significance of a *7-day reference measurement*. If countermeasures could be identified, they were discussed and the reduction of the effect was calculated.

The systematic effects can be divided in three categories:

Category 1: Effects that can be fully treated by a consideration in the model (all theoretical uncertainties except the FSD).

Category 2: Effects that can be modeled, but with relative large uncertainties, where an improvement of the model is recommended (for example rear wall backscattering).

Category 3: Effects that have a large impact on a sterile neutrino measurement and require a precise quantification beforehand and a careful consideration in the measurement strategy (for example source fluctuations).

The results of the studies, including the categorization, are summarized in table 5.2. The review of the systematic effects lead to the following conclusion: all effects that were studied can be controlled within reasonable uncertainties. No effect has been identified that makes a search for keV-scales sterile neutrinos with the KATRIN experiment impossible.

However, there are certain recommendations for each studied effect investigations should be focusing on regarding future measurements.

Rear wall backscattering: The contribution of electrons backscattering on the rear wall disc or rear section chamber surface is one of the leading systematic effects that has been studied in this chapter. With combined *GEANT4* and *KASPER* simulations, the influence of the spectrum has been calculated (section 5.2). In order to estimate an uncertainty on the correction, the simulation results have been cross checked with measurements (section E) and the influence of simplifications has been discussed (section 5.2). As a result, a relatively large uncorrelated uncertainty of 20% was found. An improvement of the model that takes into account the influence of electron scattering in the source on the effect is an important step that needs to be taken in order to minimize the uncertainty. Furthermore, the treatment of the uncertainty as fully uncorrelated has a large impact on the sterile neutrino sensitivity. An improved modeling can help to find reasonable correlations.

The option of a beryllium rear wall disc that could be installed between the source and rear section was first documented in [259] and is discussed in section 7.3. It shows that the lower backscattering probability can lead to a reduction of the effect by up to a factor of 45. It is recommended to further discuss the technical feasibility of such an extension.

Source scattering: If the KATRIN experiment is used to search for sterile neutrinos without hardware modifications, the source activity has to be lowered in order to increase the accessible parameter space (section 4.1). This requires a reduction of the column density ρd . A major benefit of operating the WGTS with a reduced amount of gas is the reduction of the scattering of signal electrons on hydrogen molecules. The studies in section 5.3 showed that if the WGTS is operated at 1% of the nominal column density, uncertainties on the electron scattering model can be neglected.

If the KATRIN experiment is used for a high statistics sterile neutrino search as proposed for example in [17], an improvement of the source scattering model is recommended. One open question that could not be answered in the scope of this work, is the possible energy dependence of the energy loss function. However, the KATRIN experiment is equipped with tools and techniques to validate the energy loss parameterization for different electron energies.

Magnetic traps in the source: Another systematic effect is the contribution of electrons that escape magnetic traps in the source with a modified energy distribution (section 5.4). Their influence on the spectral shape has been studied with an extensive *KASPER* simulation and is found to be up to approximately $5.2 \cdot 10^{-3}$. The underlying simplifications lead to an estimated uncorrelated uncertainty of 10% on the derived model. Analogous to the effect of rear wall backscattering, an improvement of the model is recommended in order to minimize the uncertainty as well as to find correlations that help to reduce the impact on the sterile neutrino analysis. A convolution model that takes into account the double differential scattering cross section was first proposed in [312]. This new approach could help to take into account the interplay of different systematic effects with a higher precision. Details can be found in section 7.4.

Source fluctuations: Unaccounted for fluctuations of the source activity can lead to uncorrelated uncertainties which have a large impact on the sterile neutrino sensitivity

Table 5.2: Summary of all systematic effects that have been studied in this chapter. The effect description is followed by the maximum contribution of the effect on the measured β -spectrum. For the source fluctuations (indicated by **), the value depends on the specific measurement setting, data taking and analysis strategy. Hence, a range is given instead of a fixed value. If countermeasures (CM) could be identified, they are listed in the third column. The absolute uncertainty is derived by multiplying the size of the effect with its relative uncertainty. For absolute uncertainties indicated by *, the derivation assumes that the countermeasure is applied. For each effect examined, a recommendation for the next steps to be taken are summarized in the penultimate column.

Effect	Max. Contr.	CM	Abs. Uncert.	Cat.	Next Steps	Section
Rear Wall Backscattering	$3.2 \cdot 10^{-1}$	lower B_{RS}	$6.4 \cdot 10^{-3*}$	2	1. Improve model 2. Install Be-rear wall	5.2
Source Scattering	$1.4 \cdot 10^{-1}$	lower ρd	$< 5.0 \cdot 10^{-6*}$	2	1. Improve model 2. Use $\sigma_{inel}(E)$ 3. Meas. E-Loss	5.3
Magnetic Traps	$5.2 \cdot 10^{-3}$	lower B_s	$5.2 \cdot 10^{-4}$	2	Improve model	5.4
Source Fluctuations	$(10^{-3} - 10^{-5})^{**}$	-	-	3	1. Commissioning 2. Adjust meas. strategy	5.5
Detection Efficiency						5.6
Backscattering	$2.5 \cdot 10^{-2}$	lower B_{det}	$5.0 \cdot 10^{-3}$	2	Improve model	
Pile-Up	$2.1 \cdot 10^{-3}$	lower rate	$8.4 \cdot 10^{-4}$	2	Improve model	
Theoretical Corrections						5.7
E. dep. FSD	$5.0 \cdot 10^{-2}$	-	$1.5 \cdot 10^{-2}$	3	1. Calculate for lower E_e 2. Improve model	
Other corr.	$< 8.0 \cdot 10^{-3}$	-	negligible	1	Consider in model	

(section 5.5). In order to avoid this, the experiment should only be operated in a setting that has been commissioned and found to be stable at the required level (depending on the desired sensitivity of the measurement). This is especially important if the WGTS is operated at low column densities and tritium purities as proposed in section 4.1.

Furthermore, it is shown that the data taking strategy has a large influence on the monitoring precision of the source activity [254]. An adjustment of the measurement time distribution and the (sub-)run length is recommended in order to reduce the influence of source activity fluctuations on the systematic uncertainty budget.

Detection efficiency: Two effects that lead to a retarding potential dependent reduction of the detection efficiency have been studied in section 5.6. The influence of electrons that scatter back on the FPD surface and overcome the retarding potential is found to be a factor of ten larger than the event loss caused by signal pile-up.

The effect of backscattering electron loss was modeled with a *KASPER*/KESS simulation with an estimated uncorrelated uncertainty of 20%. Lowering the detector magnetic field reduces the influence of the backscattering loss only slightly (up to a factor of 2.5 for $B_{\text{det}} = 1.0 \text{ T}$). An improvement of the model that includes a measurement to validate the simulations is recommended [16]. In [262] a new comprehensive model on detector effects has been developed that shows potential to reduce the uncertainty of the detection efficiency modeling.

Furthermore, the DRIPS software provides a strong tool to increase the precision on the modeling of pile-up electron loss [251]. It is important to mention that the influence of signal pile-up can be effectively reduced by lowering the rate at the detector, however, this comes in hand with a reduced statistical sensitivity if the total measurement time is not increased accordingly.

Theoretical corrections: In order to increase the precision of the β -decay model used in the analysis, the underlying theoretical description of the spectrum needs to be extended (section 5.7). It was found that most of the theoretical corrections do not influence the sensitivity significantly, as long as they are taken into account in the model. However, one extension that has a large influence on the spectral shape is the FSD. The FSD has been precisely calculated for the purpose of the KATRIN experiment for electron energies close to the kinematic endpoint [293]. However, the FSDs scale with the recoil energy of the outgoing electron which requires consideration if the spectrum is measured at energies several keV below the endpoint [133]. In the study presented in section 5.7.1 it was found that the energy dependence of the ground state probabilities already leads to a large relative influence on the spectral shape of up to $5 \cdot 10^{-2}$. The model that has been adapted from [295] allows for an approximation. It is strongly recommended to improve the model and, if possible, to precisely calculate the FSD for electron energies several keV below the endpoint.

Besides the medium- to long-term recommendations, the information gained in this chapter are required for the analysis of the first keV-scale sterile neutrino measurement with the KATRIN experiment, presented in the next chapter. In combination with this acquired experience, an optimized KATRIN setting for a future measurement is presented in section 7.5.

CHAPTER 6

Search for keV-scale sterile Neutrinos with KATRIN during the 2018 First Tritium Campaign

The *First Tritium Campaign* took place in 2018 and was the first operation of the KATRIN experiment with tritium. Besides the successful commissioning of the tritium circulation system, the source stability requirement of 0.1 % on the time scale of hours could be demonstrated. The recorded tritium spectra have been mainly studied down to an energy of $qU_{\text{ret}} = E_0 - 100 \text{ eV}$ and showed excellent agreement with the theoretical model. This laid an essential groundwork for all following neutrino mass measurements.[131]

During the campaign, the source was operated at a tritium purity of $\epsilon_T = 5.0 \cdot 10^{-3}$ which enabled the opportunity to extend the narrow measurement window of KATRIN to a wider range of down to $qU_{\text{ret}} = E_0 - 1.6 \text{ keV}$ [131]. This provides the first possibility to search for keV-scale sterile neutrinos with KATRIN data¹.

This chapter presents the first and preliminary results. The analysis of the data was a group effort, mainly carried out by Prof. S. Mertens, C. Köhler (both Technical University Munich and Max Planck Institute Munich), M. Korzeczek, Leonard Köllenberger (both Karlsruhe Institute of Technology), A. Lokhov (Westfälische Universität Münster, Institute for Nuclear Research of Russian Academy of Sciences) and the author of this thesis. The focus of the author's work laid on the derivation of the additional model corrections (section 6.4) as well as the collection, study and documentation of other the systematic effects and uncertainties (section 6.5). A detailed and more in depth analysis will follow in a separate publication.

The chapter is structured as follows: The first section 6.1 gives an introduction of the KATRIN settings during the *First Tritium Campaign*, followed by the data taking, selection, and analysis strategy (section 6.2). The information gained in chapter 5 are used to extend the KATRIN tritium β -decay model which is optimized for the endpoint analysis by two additional effects that become relevant in the wider measurement window (section 6.4). Furthermore, all systematic effects are reviewed for the specific measurement setting and their influence on the sensitivity is calculated in a Monte Carlo study (section 6.5).

¹Parts of the data have been used in two master's theses: In [313], a reduced amount of the *First Tritium Campaign* data (27 runs) was analyzed to search for light sterile neutrinos on the eV-scale. However, with a model that assumed a simulated instead of a measured energy loss function and the FSD calculated for T_2 instead of DT. Furthermore, a simplified systematic treatment was used, neglecting for example the detection efficiency correction due to backscattering as well as the effects of rear wall backscattering and magnetic trapping. In [261] a single 3 hour scan was used to search for keV-scale sterile neutrinos, however, as well with an incomplete and simplified treatment of systematic effects.

The result and conclusion is presented in section 6.6.

Details on the measurement campaign and the results can be found in [131]. The following three sections summarize the most important information about the measurement campaign with focus on the relevance for a keV-scale sterile neutrino search.

6.1 The 2018 First Tritium Campaign

During the *First Tritium Campaign*, the source was mainly operated at a nominal column density of $\rho d = 4.46 \cdot 10^{17} \text{ cm}^{-2}$ and for safety reasons at a reduced tritium purity of $\epsilon_T = 5.0 \cdot 10^{-3}$. This was achieved by a mixture of 1% DT and pure deuterium as carrier gas. As a result of the reduced source activity, the spectrum could be measured down to an energy of 1.6 keV below the endpoint within the detector rate limits. [131]

In addition to the reduced source strength, the KATRIN setup had two deviations from the nominal setting: 1. all magnets were operated at 70% of the nominal values²; 2. compared to the final experimental configuration, the rear section was not available and the WGTS rear end was locked by a stainless steel valve. [131]

One major achievement of the *First Tritium Campaign* was the demonstration of the source stability at the 0.1% level on a time-scale of hours. Besides the monitoring of all relevant slow control parameters (e.g. the beam-tube temperature and the buffer vessel pressure), the stability was measured with the FPD. At a fixed retarding potential of $qU_{\text{ret}} = E_0 - 1 \text{ keV}$ the rate was found to be stable on a 0.1% level for 60 second measurement bins over a time period of 5 hours. [131]

In addition, the recorded tritium spectra were used to test the analysis software and to compare several data taking and analysis strategies. It was shown that the fit parameters were independent of the fitting range³, column density, scanning strategy and were constant over time. [131]

6.2 Data taking Strategy

168 hours of tritium data were collected throughout the campaign, mainly divided in $\sim 3 \text{ h}$ up and down scans. In the scans, the spectrum was recorded on an energy interval of $E_0 - 1600 \text{ eV} \leq qU_{\text{ret}} \leq E_0 + 30 \text{ eV}$ at 26 different retarding potentials. [131]

The measurement time distribution (MTD) shown in figure 6.1 was optimized to obtain approximately the same statistical uncertainty for each measurement point on the first 200 eV below the endpoint. The majority of the measurement time is spend at an energy range of $qU_{\text{ret}} > E_0 - 100 \text{ eV}$. The three measurement points above E_0 were used to monitor the background rate. [131]

During the measurement, up and down scans were combined in alternating order to minimize the influence of possible slow-control parameter drifts and high voltage set time. The up and down scans were supplemented by random scans in order to study time-correlated effects for example on the background rate. [131, 315]

²During the commissioning phase of the full KATRIN superconducting magnet chain in 2018, the magnet module M7 of the CPS had a training quench close to its designed field strength. For safety reasons, all magnets along the magnet chain are now operated at 70%, which only has a minor influence on the sensitivity or stability of the KATRIN experiment. [314]

³In reference [131], three different fitting ranges have been studied using the covariance matrix approach, with lower limits of $qU_{\text{ret}} \leq E_0 - 100/200/300 \text{ eV}$.

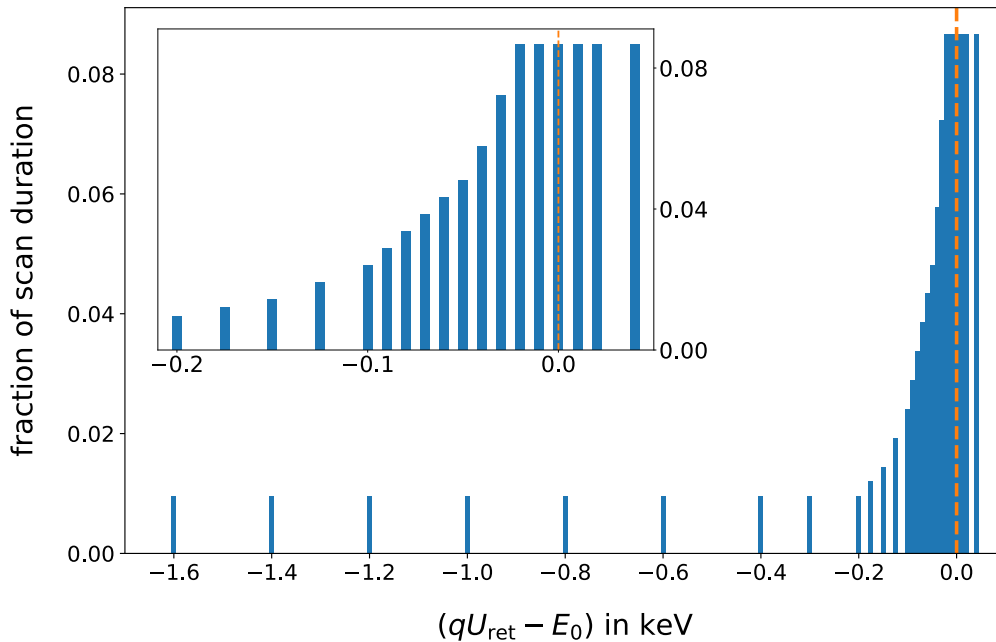


Figure 6.1: The MTD shows the fraction of the scan duration spent at each retarding potential. Close to the endpoint, where the signal rate is small, the most time of the measurement is spent. Three additional measurement points with energies larger than the endpoint energy E_0 are required to determine the background contribution to the signal rate. The orange vertical line shows the position of the endpoint. The figure is adapted from [131] figure 3.

6.3 Data Selection and Analysis

From the total 116 recorded tritium spectra, a selection of 82 are used for the sterile neutrino analysis. All other scans are excluded because they were performed at a different column density, measurement time distribution, or further reduced tritium purity. The data was recorded with all 148 pixels of the detector. Due to the fluxtube alignment and the shadowing of the forward beam monitor, the two most outer rings, as well as three pixels of ring 9 and 10 are excluded in the analysis [131]. The rates recorded by the single pixels are averaged and combined to one effective pixel rate. All 82 scans are then combined to one measured spectrum. The error that is caused by the stacking is negligible [131].

Spectral Analysis

As explained in section 5.1, the data is used to calculate an exclusion limit on the $(m_{\nu_s}, \sin^2 \theta)$ sterile neutrino parameter space.

To do so the modeled spectrum $N_{\text{pre},i}(E)$ is fitted to the measured data $N_{\text{obs},i}(E)$ for predefined combinations of m_{ν_s} and $\sin^2 \theta$, by minimizing the χ^2 function

$$\chi^2 = \sum_{i,j} (N_{\text{obs},i} - N_{\text{pre},i}) V_{i,j}^{-1} (N_{\text{obs},j} - N_{\text{pre},j}). \quad (6.1)$$

The kinematic endpoint E_0 , the amplitude R_s , and the background rate R_{bgk} are free fit parameters. The effective neutrino mass $m_{\nu_e}^2$ is set to zero.

Statistical and systematic uncertainties are included via covariance matrices $V_{i,j}$.

In order to construct the 90% C.L. exclusion limit on the sterile neutrino parameter

space, the procedure is repeated on a predefined grid of $(m_{\nu_s}, \sin^2 \theta)$ combinations. By determining the $\Delta\chi^2 = \chi^2(m_{\nu_s}, \sin^2 \theta) - \chi_{\text{NH}}^2 \leq 4.61$ contour, parts of the studied sterile neutrino parameter space can be excluded. The χ_{NH}^2 corresponds to the fit of the null hypothesis ($m_{\nu_s} = 0.0, \sin^2 \theta = 0.0$).

6.4 Additional Model Corrections

Based on the results of chapter 5, the nominal KATRIN tritium β -decay model is extended by two additional correction terms for the keV-scale sterile neutrino analysis⁴.

Rear Wall Backscattering: Electrons that scatter back at the rear wall, have a non-zero probability to reach the FPD and contribute to the observed spectrum (see section 5.2) [10, 259]. During the *First Tritium Campaign*, the rear section was not installed yet. The WGTS was terminated by a stainless steel valve on the rear side and the rear section magnet was turned off. [131] Since the effect of rear wall backscattering scales with the size of the rear wall magnetic field as well as the material, both deviations from the nominal KATRIN setting are advantageous for the sterile neutrino measurement (see section 5.2). Using the techniques developed in section 5.2, the size of the effect is found to be $2.25 \cdot 10^{-3}$ at 1.6 keV below the endpoint. The derived correction term is displayed in figure 6.2 as the orange line and uncertainty band. Based on the discussion in section 5.2, a relative uncertainty of 20 % (uncorrelated) on the correction is assumed in the analysis.

Magnetic Traps in the Source: Electrons that start in local magnetic field minima in the source can be magnetically trapped. Due to scattering interactions with source gas, the initially trapped electrons are able to escape after a few μs , however, with a modified energy distribution. Depending on their polar angle, escaped electrons can reach the detector and distort the measured spectrum. [10, 260] Based on the procedure developed in section 5.4, the contribution of escaped electrons is found to be $5.32 \cdot 10^{-3}$ at 1.6 keV below the endpoint. The corresponding correction term is displayed in figure 6.2 as the blue line. Following the discussion in 5.4, a relative uncertainty of 10 % (uncorrelated) on the correction is assumed in the analysis.

Figure 6.3 shows the null hypothesis fit ($m_{\nu_s} = 0.0, \sin^2 \theta = 0.0$) of the 82 stacked spectra with and without the additional corrections. Only the statistical uncertainty is taken into account. The fit displayed in the blue line is based on the model that was developed for the KATRIN endpoint analysis. It includes for example the effects of energy loss due to source scattering, the FSD, and the detection efficiencies. If the model is used to fit data on a wider energy range, the data and fit show deviations, especially for energies of $qU_{\text{ret}} < E_0 - 0.4 \text{ keV}$. The deficit is evident in large residuals of up to 9.3σ and a reduced chi-squared of $\chi_{\text{red}}^2 = 15.085$.

If the two additional correction terms presented in this section are applied, the fit result improves significantly as can be seen in the green marked residuals of figure 6.3. The reduced chi-squared improves to $\chi_{\text{red}}^2 = 1.721$. The residuals do not show any structure or trend and fluctuate around zero with a maximum of 2.75σ .

The model and data show excellent agreement already for a spectral analysis that only considers the statistical uncertainty. This underlines the strength of the new derived corrections. In combination with the already existing model it is shown that it is possible to reconstruct KATRIN data on an extended energy window.

⁴Technically, the derived correction terms are applied on the data before the model is fitted. However, this does not change the results or the meaning of the following discussion.

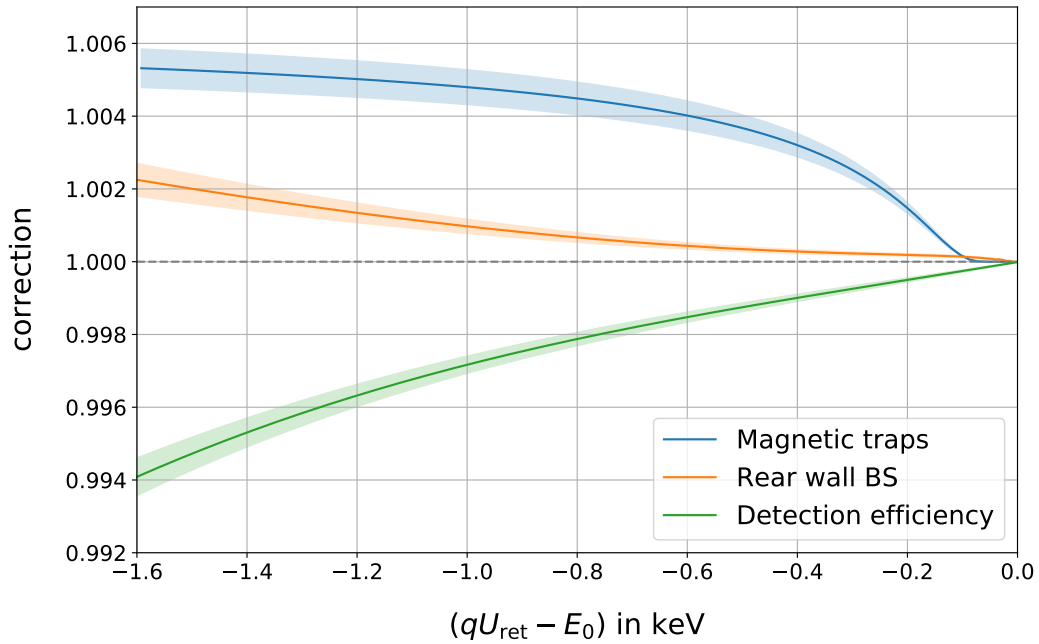


Figure 6.2: As a result of the studies presented in chapter 5, two additional correction terms are derived. The correction terms for the effect of magnetic trapping (blue) as well as rear wall backscattering (orange) lead to an increase of signal electrons on the observed energy range. The corresponding uncertainties on the correction terms are displayed in the colored uncertainty bands. For comparison, the detection efficiency correction, as derived in [262], is displayed in green. The three detection efficiencies that are considered in the analysis (pile-up, backscattering and region of interest loss) are combined to an overall detection efficiency correction. Contrary to the two other corrections, all detector effects, except the backscattering loss, have been considered in the endpoint analysis of the *First Tritium Campaign* data as well [131].

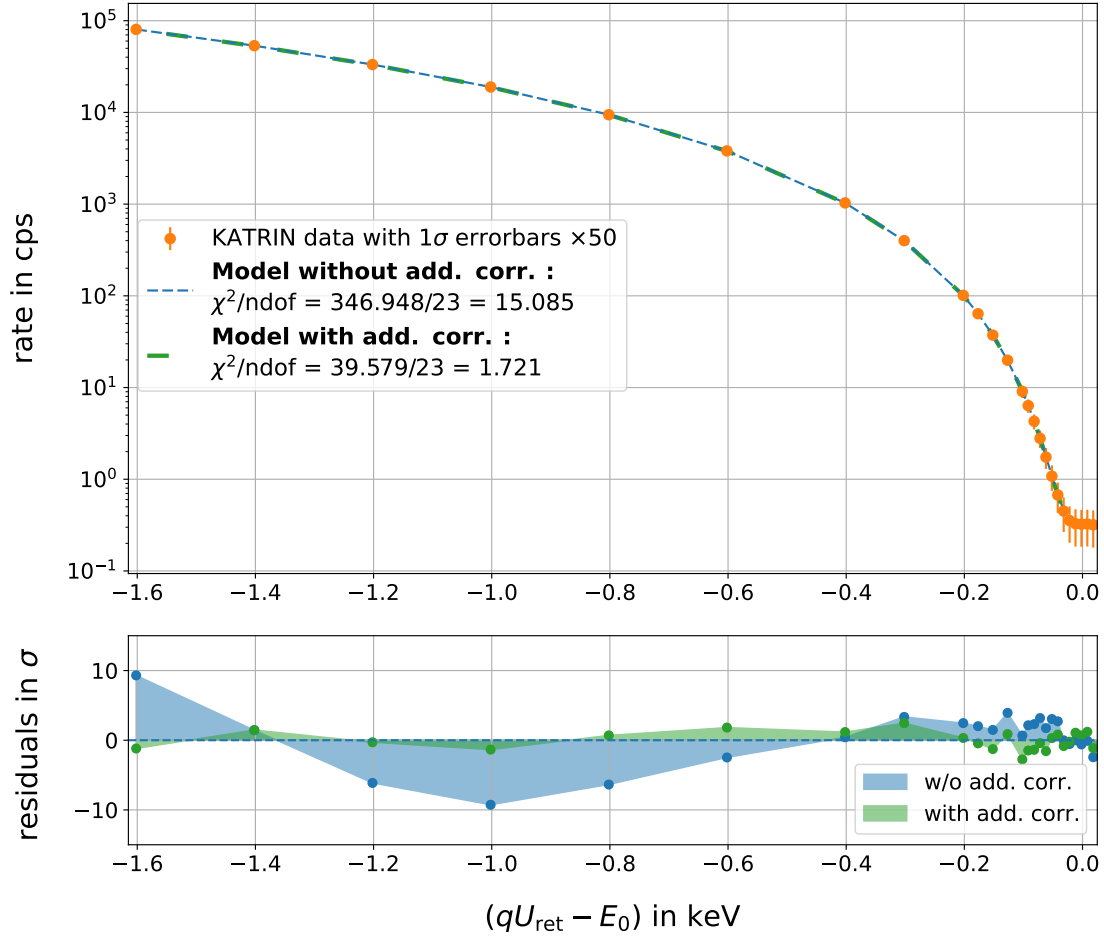


Figure 6.3: The figure shows the null hypothesis fits to the measured spectrum based on the KATRIN β -decay model, with and without the additional corrections applied. The errorbars state the statistical uncertainty on the measured data and are increased by a factor of 50 for better visibility. The residuals are normalized and expressed in standard deviation σ . If no additional corrections are applied, the reduced chi-squared is large with $\chi^2/\text{ndof} = 346.948/23 = 15.085$. If the effects of rear wall backscattering, and magnetic trapping are taken into account, the goodness of fit increases significantly to $\chi^2/\text{ndof} = 39.579/23 = 1.721$. The data extraction and analysis was performed with the KAFIT module of the KASPER framework [263] and kindly provided by Leonard Köllenberger (Karlsruhe Institute of Technology). The figure is adapted from [131] figure 7.

6.5 Systematic Effects and Uncertainties

For the data analysis, all systematic effects discussed in chapter 5 were reevaluated for the specific KATRIN settings during the *First Tritium Campaign*. A comprehensive overview of the parameters can be found in table 6.1 as well as in figure 6.4.

In the following, a short review of all considered systematic effects and uncertainties are presented.

Source Scattering

The scattering probability of electrons in the source are taken into account via the response function (see section 5.3). The most important input parameters for the determination of the response function, as well as their uncertainties during the measurement, are the following:

- **Column Density ρd :** The column density can be determined via a high precision measurement with an electron gun, which is installed at the rear section of the experiment [249]. According to [131] the column density was derived via simulations due to the absence of the rear section during the measurement. The uncertainty on the value stated in [131] as 3% .
- **Inelastic Scattering Cross Section σ_{inel} :** Due to the results of section 5.3 an energy dependent inelastic cross section is used in the analysis. The uncertainty on the value is based on [275] and estimated to be 2%.
- **Magnetic Field Strengths:** The uncertainties on the magnetic field strength at the source B_s , analyzing plane B_a , and pinch B_{pch} have been derived in magnetic field measurements and simulations [316]. In the analysis, uncertainties of $\sigma_{B_s} = 2.5\%$, $\sigma_{B_a} = 1.0\%$ and $\sigma_{B_{\text{pch}}} = 0.2\%$ are assumed.
- **Energy Loss Function:** The parameterization of the energy loss function as well as the uncertainties on it were determined in an electron gun measurement after the campaign [272]. The correlated uncertainties on the empirical model are listed in table 6.1. Within the here studied analysis window, the energy loss function is not expected to show a relevant energy dependence.

Source Fluctuations

As shown in 5.5 sub-run to sub-run fluctuations of the source activity lead to uncorrelated systematic uncertainties and are of harm for the neutrino mass determination as well as for the keV-scale sterile neutrino search (see section). As stated in [131], the relative small tritium purity of $\epsilon_T = 5.0 \cdot 10^{-3}$ leads to a large uncertainty of approximately 1% of the LARA monitoring measurements. If all runs that are used in the analysis are combined, the uncertainty can be reduced to 0.08% [254].

Non-Adiabatic Electrons Transmission

During the *First Tritium Campaign*, the LFCS was operated at nominal values (with $B_a = 6.3 \cdot 10^{-4}$ T). Only data recorded with detector rings $n_{\text{ring}} \leq 10$ are considered in the analysis [131]. In a high statistics Monte Carlo simulation based on 10^7 events, the influence of non-adiabatic electron transmission in the main spectrometer has been derived. At the highest surplus energy that is reached in this measurement, the transmission loss

averaged over all detector rings is found to be $(8.70 \pm 1.45) \cdot 10^{-5}$, with the error being the statistical uncertainty of the simulation.

Detection Efficiency

The detection efficiency of the FPD is composed of an absolute efficiency, as well as retarding potential dependent components (see equation (5.48)). The absolute detection efficiency has only an influence on the total statistics that are gained during a measurement and is therefore of secondary interest for the analysis. However, all detection efficiency contributions that scale with the retarding potential have to be considered. [250]

As introduced in detail in section 5.6, three effects are important for the keV-scale sterile neutrino analysis of KATRIN data:

1. Electrons scatter back at the FPD surface with an approximate probability of 20%. If the remaining energy of the backscattered electron is large enough, they have the chance to overcome the retarding potential and are missing in the spectrum. By lowering the retarding potential, this probability increases which requires a correction of the detection efficiency. [262] The effect has been derived for the *First Tritium Campaign* analysis in [262] and is found to be $1 - \epsilon_{bs} = 1.72 \cdot 10^{-3}$ at 1.6 keV below the endpoint with an uncertainty of 20%.
2. Two electrons that arrive at the detector within a time interval smaller than the shaping length L are piled-up and rejected for the analysis, or counted as a single event. The effect scales with the count rate at the FPD which leads to a dependence on the retarding potential. [250] The size of the electron loss at 1.6 keV below the endpoint is $1 - \epsilon_{pu} = 2.11 \cdot 10^{-3}$ with an uncertainty of 18% [262].
3. A third effect that leads to a retarding potential dependent detection efficiency is caused by the fixed region of interest (ROI) that is used in the KATRIN data acquisition. In order to determine the signal electron rate at a given retarding potential, the events in an energy window of $14 \text{ keV} \leq E_e + qU_{PAE} \leq 32 \text{ keV}$ are counted (with the post acceleration electrode potential $qU_{PAE} = 10 \text{ keV}$). If the retarding potential is lowered, the peak of the detector response shifts to lower energies, which results in a loss of signal electrons caused by the fixed ROI. This electron loss is expressed in the ROI detection efficiency $\epsilon_{roi}(qU)$. [47] The size and shape can be determined with a reference measurement and is derived in [262] with a value of $1 - \epsilon_{roi} = 2.05 \cdot 10^{-3}$ at 1.6 keV below the endpoint. Since the effect can be measured, the uncertainty on the value is relatively small with 0.16% [131].

All effects are combined to one resulting detection efficiency correction that is applied in the analysis. The correction term is displayed in figure 6.2 as the green line.

Theoretical Corrections

As described in section 5.7, the predicted tritium β -decay model is based on the Fermi theory extended by certain corrections. One major extension is the consideration of the final state distribution (FSD): After the decay, the daughter molecule ${}^3\text{HeD}^+$ can be left in an excited state, which requires a correction of the released energy of the decay. As a consequence, the kinematic energy of the β -decay electron is broadened by the energies E_f of the final states. [289] For both, the neutrino mass determination as well as a sterile neutrino analysis, a precise knowledge of the FSD is of high relevance [131]. As shown in section 5.7.1, a particularity of the sterile neutrino search is that if a larger energy range is studied, the influence of an energy dependence of the FSD becomes more important. In

order to take into account the missing energy dependence, considerably large uncertainties are applied (see table 6.1).

Additional theoretical corrections introduced in section 5.7.2 are reviewed for the energy range of the *First Tritium Campaign* measurement. Three effects are relevant within the statistical significance of this measurement. The model used to analyze the data considers the relativistic Fermi function, the correction terms due to the screening of the 1s orbital electron, and radiative corrections. All effects have a relative contribution of $\sim 10^{-3}$ on the spectrum. They scale with the energy on the order or of a few percent within the observed range. The uncertainties on the correction terms are negligibly small and are not considered in the analysis.

Summary of Systematic Effects

Table 6.1 gives an overview of the systematic uncertainty budget for the sterile neutrino analysis of the *First Tritium Campaign* data. The absolute uncertainties on the rear wall backscattering, magnetic trapping, and detection efficiency corrections are derived by multiplying the size of the effect with the relative uncertainty. Source fluctuations can not be modeled. Their full size is taken into account as an uncorrelated absolute uncertainty.

Figure 6.4 displays the absolute uncertainties of the four effects and compares them to the statistical uncertainty. For energies larger than $qU_{\text{ret}} = 18.3 \text{ keV}$ the statistical uncertainty dominates. On the remaining energy scale, the uncertainty on the DT concentration states the largest uncertainty. The uncertainties on the modeling of the magnetic trapping, rear wall backscattering as well as the detection efficiency increase with the distance to the endpoint. At 1.6 keV below the endpoint they are approximately on the same order of $5.0 \cdot 10^{-4}$.

The final null hypothesis fit of the 82 stacked spectra is displayed in figure 6.5. All systematic effects shown in table 6.1 are taken into account via covariance matrices. The orange markers correspond to the measured data with the total uncertainty increased by a factor of 50. The lower figure shows the residuals of the spectrum relative to the 1σ uncertainty band of the null hypothesis fit model. The systematic uncertainty dominates the total error for all energies smaller than $qU_{\text{ret}} < E_0 - 0.2 \text{ keV}$. The null hypothesis fit and data show excellent agreement over the full 1.6 keV energy interval with a reduced chi-squared of $\chi_{\text{red}}^2 = 0.885$ and a corresponding p-value of 0.623.

Influence on the Sterile Neutrino Sensitivity

For a better plausibility of the measurement results, as well as for future improvement, it is important to study the influence of the different systematic effects on the sterile neutrino sensitivity. For this purpose, the exact parameters of the measurement (rate, measurement time distribution, and experimental settings) are simulated with the model that has been developed in the course of chapter 5. For every effect, a covariance matrix is generated and taken into account in the analysis.

Figure 6.6 shows the results of the scans. The uncertainty on the DT concentration has the largest impact on the sensitivity. The second largest contribution comes from the uncorrelated uncertainties on the detection efficiency, rear wall backscattering, and magnetic trapping correction which are all of comparable size. The uncertainty on the parameters that are used to determine the energy loss due to source scattering (dominated by ρd and σ_{inel}) have a low impact for higher masses, but are dominant for $m_{\nu_s} < 0.055 \text{ keV}$. The black dashed contour shows the resulting sensitivity of the Monte Carlo data set, including

Table 6.1: The systematic uncertainty budget for the sterile neutrino analysis of the *First Tritium Campaign* data. The effect description is followed by the size of the contribution to the β -spectrum at 1.6 keV below the endpoint. The last column states the relative uncertainties of the correction terms, or of the parameters that are required to derive the correction in the model. The uncertainties on the FSD relate to the relative normalization 1 %, the variance of the ground state distribution 1 %, and the excited state distribution 3 % [131]. The reference for all other uncertainties are stated in the text.

Effect	Parameter/comment	Size at $E_0 - 1.6$ keV	Uncertainty
Rear Wall Backscattering	In model	$2.25 \cdot 10^{-3}$	
	Correction term		20 %
Electron Scattering/ Transmission	In model	$6.01 \cdot 10^{-2}$	
	ρd		3 %
	σ_{inel}		2 %
Energy Loss Function	$A_{1,2,3}$		6.14 %/0.47 %/0.65 %
	$\mu_{1,2,3}$		0.15 %/0.03 %/0.05 %
	$\sigma_{1,2,3}$		7.58 %/0.81 %/2.62 %
Magnetic Field Stability	$B_s/B_a/B_{\text{pch}}$		2.5 %/1.0 %/0.2 %
Source Fluctuations	Uncorrelated	$8.00 \cdot 10^{-4}$	
	DT Conc.		0.08 %
Magnetic Traps	In model	$5.32 \cdot 10^{-3}$	
	Correction term		10.0 %
Non-Adiabaticity	Negligible	$1.38 \cdot 10^{-5}$	
Detection efficiency	In model	$5.87 \cdot 10^{-3}$	
	Backscattering		20.0 %
	Pile-up		18.0 %
	Region of interest		0.16 %
Theoretical Corrections	In model	$4.45 \cdot 10^{-2}$	
	Final State Dist.		1 %/1 %/3 %
	Rel. Fermi Fct.		Negligible
	Screening		Negligible
	Radiative Corr.		Negligible
Statistical Uncertainty		$4.54 \cdot 10^{-5}$	

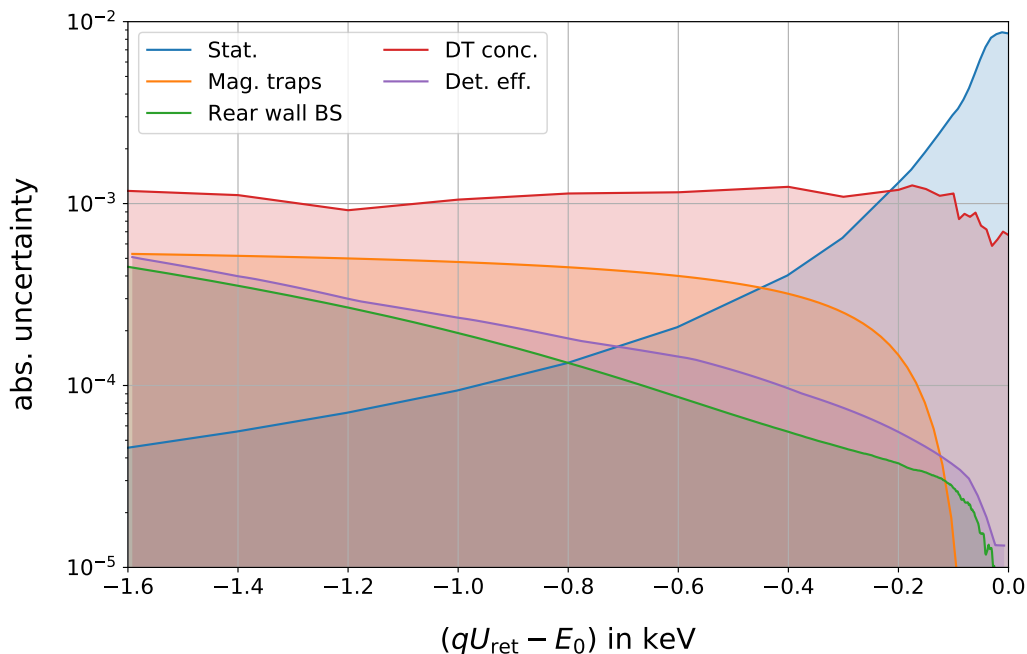


Figure 6.4: The figure shows an overview of the systematic and statistical uncertainties for different retarding potentials. In the endpoint region, the uncertainty budget is dominated by the statistical uncertainty. The fluctuation of the DT concentration is the most relevant uncertainty on the remaining energy scale. All other uncertainties have a maximum contribution at the lowest retarding potential of approximately $5 \cdot 10^{-4}$.

the statistical and all systematic uncertainties. It covers a parameter space that has not yet been excluded by any laboratory experiment.

6.6 Results

The measured spectra were analyzed mainly by Leonard Köllenberger (Karlsruhe Institute of Technology) with the KAFIT module of the KASPER software framework⁵.

For the sterile neutrino analysis, the model is extended with the two additional systematic effects derived in this work. The red line in figure 6.7 shows the 90% C.L. exclusion limit for the data set of the 82 stacked spectra. The difference of the predicted sensitivity (based on Monte Carlo data) and the exclusion limit can be explained by the different models used for the Monte Carlo study (own model) and the model used for the data analysis (KAFIT).

No sterile neutrino signal is found in the data. The minimum mixing amplitude that can be excluded is $\sin^2 \theta < 2.33 \cdot 10^{-3}$ reached at approximately $m_{\nu_s} = 0.3$ keV.

Comparing the exclusion limit with current laboratory limits shows an improvement by up to a factor of eight on a mass range of approximately $0.10 \text{ keV} \leq m_{\nu_s} \leq 0.76 \text{ keV}$.

6.7 Conclusion and Outlook for Future Measurements

This chapter presents the preliminary results of the first keV-scale sterile neutrino measurement with the KATRIN experiment. The sterile neutrino parameter space was studied

⁵For the neutrino mass analysis the results are cross-checked and validated with two independent data analysis tools, the FITRIUM and SAMAK software [317, 266]. The analysis results shown here have been reviewed by Christoph Köhler (Technical University Munich and Max Planck Institute Munich) with the FITRIUM software and showed only minor deviations.

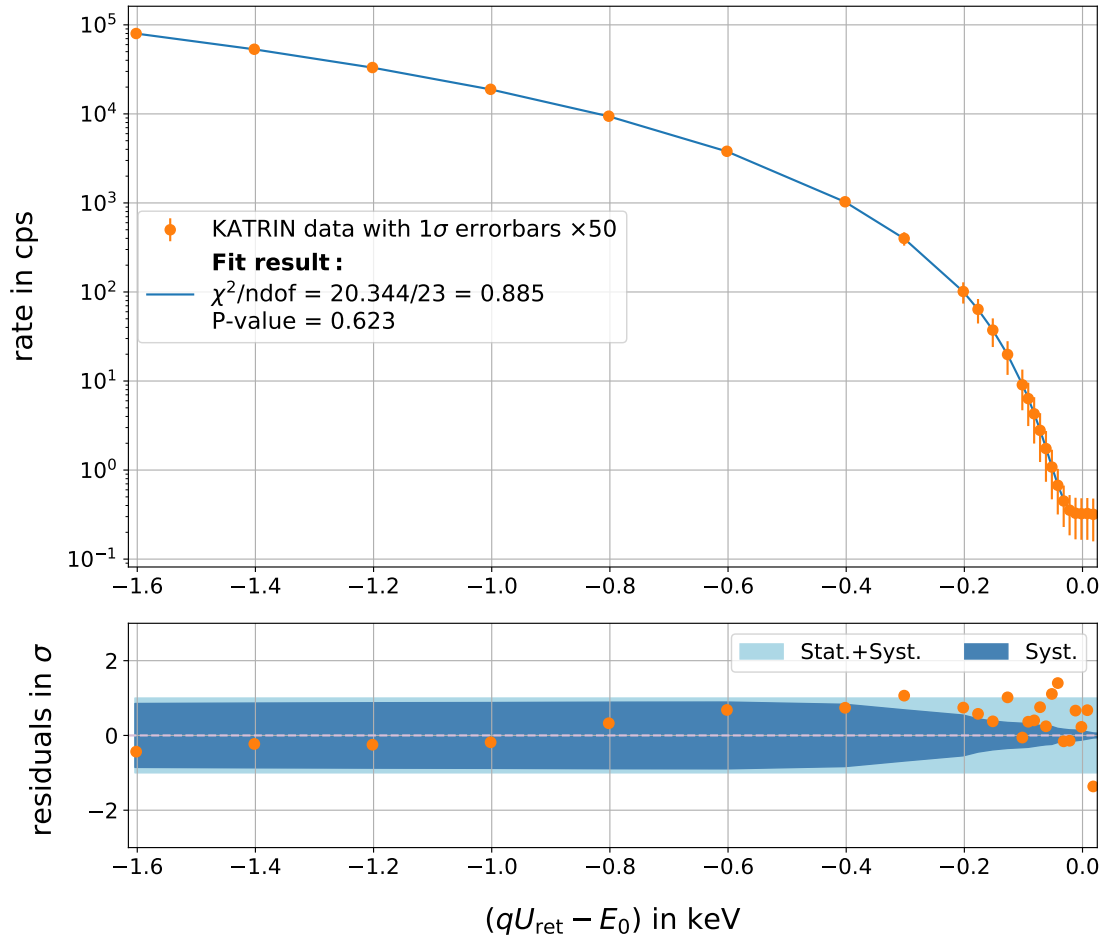


Figure 6.5: The null hypothesis fit of the 82 stacked spectra for the full studied energy range. The errorbars state the total uncertainty on the data (statistical and systematical) and are increased by a factor of 50 for better visibility. The residuals are normalized and expressed in standard deviation σ . The goodness-of-fit is $\chi^2/\text{ndof} = 20.344/23 = 0.885$ with a corresponding p-value of 0.623. The measured data was extracted and analyzed with the KAFIT module of the KASPER framework [263] and kindly provided by Leonard Köllenberger (Karlsruhe Institute of Technology). The figure is adapted from [131] figure 7.

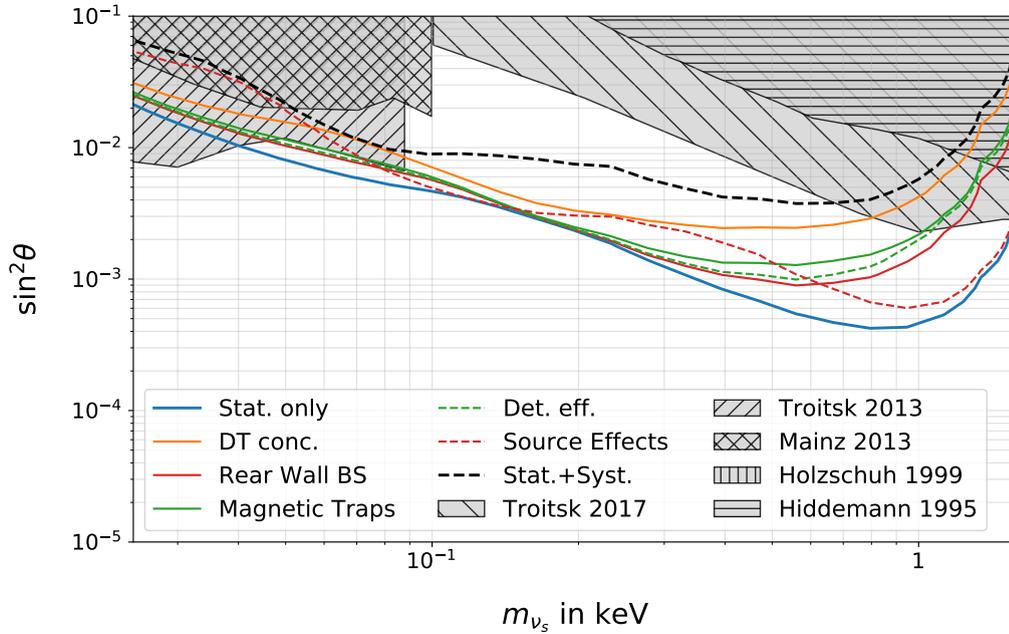


Figure 6.6: The sensitivity contours for a Monte Carlo data set. The different contours correspond to the systematic uncertainties listed in table 6.1. The black dashed line shows the resulting sensitivity including all systematic uncertainties. For comparison, the current laboratory limits on the sterile neutrino parameter space are displayed [244, 245, 246, 247, 248].

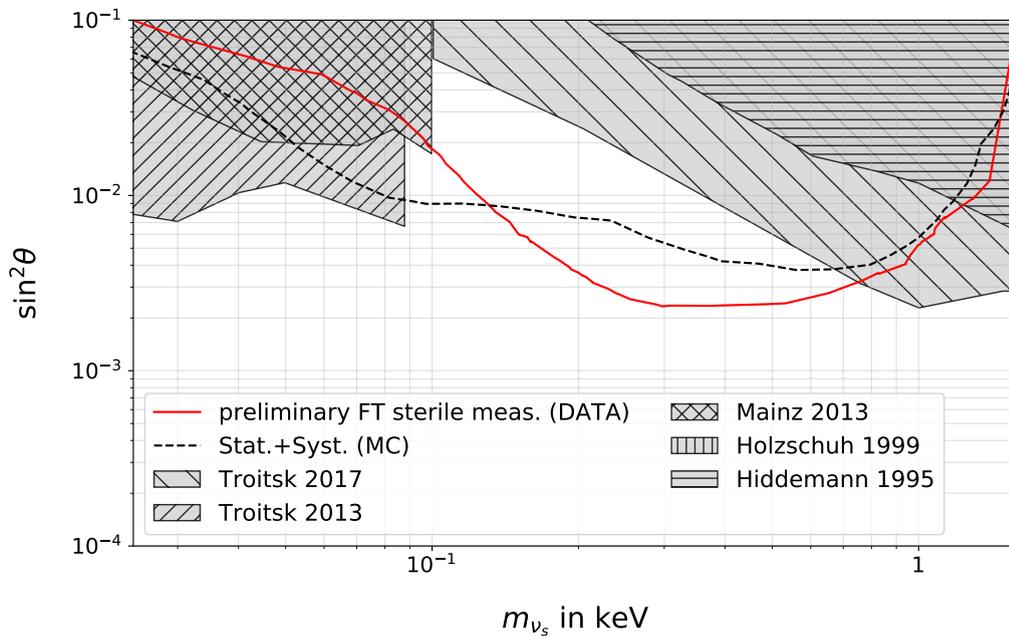


Figure 6.7: With the data taken during the *First Tritium Campaign*, the current laboratory limits on the sterile neutrino mass and mixing amplitude can be improved by up to a factor of eight on a mass range of approximately $0.10 \text{ keV} \leq m_{\nu_s} \leq 0.76 \text{ keV}$ (red solid line). The figure also shows the expected sensitivity based on Monte Carlo data (black dashed line) derived with the model developed in chapter 5. For comparison, the current laboratory limits on the sterile neutrino parameter space are displayed [244, 245, 246, 247, 248].

on a mass range of $0.0 \leq m_{\nu_s} < 1.6$ keV. Compared to the neutrino mass determination, the tritium β -decay model used to fit the measured data, was extended by two additional systematic effects. Both effects have been derived in the scope of this work (chapter 5). With this additional corrections, the measured spectrum and model show excellent agreement on the full studied energy range (see figures 6.3 and 6.5).

The systematic uncertainties have been reviewed and considered in the analysis via covariance matrices. The fluctuation of the DT concentration could be identified as the dominant uncertainty of this measurement. The second largest influence was found for the uncertainties on the correction terms displayed in figure 6.6. Their relative large impact on the sterile neutrino sensitivity can be traced back to their strict treatment as fully uncorrelated.

No sterile neutrino signal was found in the measurement, however, with the obtained exclusion limit, the current laboratory limits on the active-to-sterile mixing amplitude could be improved by up to a factor of eight on a mass range of $0.10 \text{ keV} \leq m_{\nu_s} \leq 0.76 \text{ keV}$.

Outlook

The results of the sterile neutrino measurement presented in this chapter are expected to improve in the upcoming months. There are currently two investigations ongoing which aim to reduce the systematic uncertainty budget:

1. Attempts are being made to reduce the uncertainty on the DT concentration by either a combination of LARA and FBM data, or by using a part of the deep-spectral measurement points to determine the source activity directly with the measured rate at the FPD.
2. The high impact of the rear wall backscattering, magnetic traps, and detection efficiency correction terms on the sterile neutrino sensitivity are related to the treatment of their uncertainties as fully uncorrelated. Studies to quantify and apply correlations are still ongoing.

The updated systematic uncertainty budget as well as the improved resulting exclusion limit will be object of a separate publication that is currently under preparation.

CHAPTER 7

Future Strategies

The KATRIN experiment has the primary goal to determine the effective electron antineutrino mass with a sensitivity of 0.2 eV at 90 % C.L. This is achieved by observing the tritium β -decay in close vicinity to the kinematic endpoint E_0 , typically on an energy interval of [18.475, 18.575] keV. [10] If the experiment is used to search for keV-scale sterile neutrinos, the energy interval needs to be extended by several keV which leads to different challenges. One challenge arises because the rate increases rapidly if the spectrum is observed at lower energies. As shown in section 4.1.1, the FPD is limited to a maximum integrated rate of 10^5 cps. By lowering the source activity (section 4.1.2) as well as adjusting the magnetic field settings (sections 4.1.3 and 4.1.4), the rate at the detector can be effectively reduced. However, the reduction of the signal rate comes at the cost of a reduced statistical significance.

The TRISTAN detector is a novel detector system which is designed to resolve high count rates of up to 10^8 cps. It is currently under development with the main objective to extend the KATRIN setup enabling a search for keV-scale sterile neutrinos with a high statistical significance. [17] In section 7.1, an overview of the general design and the state of development of the TRISTAN detector system is presented.

Another challenge that arises, if the measurement range of the KATRIN experiment is extended, is the loss of transmission in the main spectrometer caused by non-adiabatic transport conditions (section 4.2.1). An increase of the LFCS magnetic field is found to be an effective countermeasure (section 4.2.2). Recently, an upgraded LFCS system was installed at the main spectrometer, with the primary objective to reduce the background [127, 318]. For the purpose of a sterile neutrino measurement, it increases the energy range on which the β -decay spectrum can be observed without transmission loss. Details on the LFCS upgrade as well as its impact on the transmission conditions for electrons with several keV surplus energy are presented in section 7.2.

Chapter 5 discussed systematic effects and uncertainties that are relevant when the KATRIN experiment is used to search for keV-scale sterile neutrinos. One of the leading systematic effects arises from the contribution of electrons that scatter back at the rear wall and reach the detector with a deviated energy distribution (section 5.2). If no countermeasures are taken, these electrons can contribute to the signal rate by up to 32 %. One way to suppress the number of backscattered electrons is a replacement of the existing with a new beryllium rear wall as first proposed in [259]. Beryllium offers the advantage of a lower backscattering probability compared to gold (factor of 20 less) or stainless steel (factor of 10 less, see figure D.3). Section 7.3 introduces the concept of a new beryllium rear wall and shows its potential to reduce the contribution of backscattered electrons to

the signal rate by upto one order of magnitude.

Furthermore, the studies in chapter 5 showed that it is crucial to extend the current KATRIN tritium β -decay model, and include corresponding systematic effects when the spectrum is measured on a wider energy window.

For the analysis of the *First Tritium Campaign* data (chapter 6), the model was already supplemented by two additional corrections. Besides the effect of rear wall backscattering, the contribution of electrons originating from magnetic traps in the source have been considered in the analysis (section 5.4). These extensions to the model showed excellent agreement with the measured data as can be seen in figure 6.5. In order to reduce the influence of uncertainties on the model, a further improvement is important.

In reference [312] a new KATRIN tritium β -decay model is proposed that focuses on the requirements of a keV-scale sterile neutrino search. The *SSC-Sterile Model* uses a multi-dimensional convolution approach to precisely account for the systematic effects introduced in chapter 5. In section 7.4, the new approach is presented and its future perspectives are discussed.

The last part of this chapter, section 7.5, combines all the information gained in this thesis and presents a measurement proposal for a future keV-scale sterile neutrino measurement with the current experimental setup. With a total measurement time of 40 days, it assumes that an entire KATRIN measurement campaign is dedicated to a keV-scale sterile neutrino search.

7.1 The TRISTAN Project

The high and stable decay rate of tritium in the WGTS gives the KATRIN experiment a unique opportunity to perform a laboratory keV-scale sterile neutrino search with a high statistical sensitivity of up to $\sin^2\theta < 10^{-8}$ assuming a three year measurement at full source strength [12]. As discussed in section 4.1.1, the FPD is limited by the read out speed and signal pile-up to a total integrated count rate of 10^5 cps. Therefore, a new detector system is required to make use of the high luminosity of the WGTS.

With the ability to resolve count rates of up to 10^8 cps, the TRISTAN detector is designed to achieve a sensitivity of $\sin^2\theta < 10^{-6}$ on the active-to-sterile mixing amplitude after three years of data taking. Besides that, the new detector system intends to have an energy resolution of 300 eV at 30 keV electron energy, enabling the possibility of a differential measurement.[17] This has a distinct advantage: If the tritium spectrum is measured in an integral measurement, all electrons with energies smaller than the retarding potential are not counted. In order to increase the statistical sensitivity for a given total measurement time, a differential measurement is therefore favored.

Both measurement modes are sensitive to different systematic uncertainties. Studies showed that the combination of both operation types can help to reduce the systematic uncertainty budget [319].

This section gives a brief introduction on the design of the new detector system (section 7.1.1), as well as an overview of the prototype stages and commissioning phases (section 7.1.2).

7.1.1 Purpose and Design

The requirements of a high count rate and energy resolution lead to the design of the TRISTAN detector which is shown in figure 7.1.

It foresees a 3486-pixel Silicon Drift Detector (SDD) with a diameter of approximately

20 cm [17]. In order to optimize systematic effects caused by backscattering and charge-sharing, the pixels are of hexagonal shape with a diameter of about 3 mm [98]. The detector is organized in 21 modules each containing 166 pixels. This design has the goal to cover a maximum possible area of the magnetic fluxtube by minimizing the dead area between the pixels. [320] In order to gain the desired energy resolution, a thin dead layer of ≤ 100 nm is required which poses a new production challenge to SDD techniques. The detector array and its assembly are designed in such a way so that backscattered signal electrons can be identified, which additionally leads to the requirement of a low energy threshold of about 1 keV. [17]

In order to reduce the noise, the read-out system consists of a junction gate n-channel field-effect transistor (nJFET) directly integrated at the SDD. The challenges for the back-end part of the read-out chain are the ability for high sample rates in order to reduce signal pile-up, as well as a high ADC linearity. [17] Both requirements can be met by using a waveform digitizing ADC with a high sampling frequency of about 100 Hz [178, 321].

7.1.2 Prototype Measurements and Schedule

In order to study the requirements described above, several 7-pixel prototypes of different pixel sizes and layouts have been characterized in laboratories at the Max-Planck institute in Munich and at the Karlsruhe Institute of Technology. Calibration measurements using ^{55}Fe and ^{241}Am as x-ray sources confirmed a high energy resolution (139 eV FWHM at 5.9 keV) and an ADC-linearity with a maximum deviation of 0.1 % on an energy range of approximately [11.0, 60.0] keV [17, 322].

Measurements using electron sources are still ongoing but first studies with ^{83}Kr conversion electrons from a evaporated rubidium-krypton source have been performed at the Max-Planck institute in Munich. An energy resolution of about 380 eV at an energy of 17.8 keV was determined, however, at ambient temperature with a setup which was not yet optimized against sources of noise. [323]

The 7-pixel prototype has also been operated at the TROITSK nu-mass experiment in Russia [8]. The program at the KATRIN predecessor experiment consisted of three measurement campaigns which were used to characterize the detector prototype, study systematic effects, and develop analyzing techniques at a real MAC-E filter tritium experiment [324, 325].

Besides the detector characterization, the data taken during the second and third measurement campaign was analyzed to set upper limits on the keV-scale sterile neutrino mass and mixing [324, 325]. For the first time, a differential tritium spectrum was successfully used in such an analysis [326]. For the sterile neutrino analysis, detailed Monte Carlo simulations of the experimental setup were performed with the KASPER simulation framework. In appendix H the implementation of the TROITSK nu-mass experiment to KASPER is described and transmission simulations are shown.

In 2019, the FBM PIN diode detector was replaced by a 7-pixel TRISTAN prototype with the objective of increasing the sensitivity of the monitoring device and further characterizing the prototype in-situ at the KATRIN beamline with tritium operation. During the *KNM2 campaign* the new assembly showed an excellent statistical uncertainty on the rate stability measurement of 0.1 %, on a time scale of hours. [327]

The current schedule foresees to operate the TRISTAN detector at the KATRIN experiment from 2025 [17].

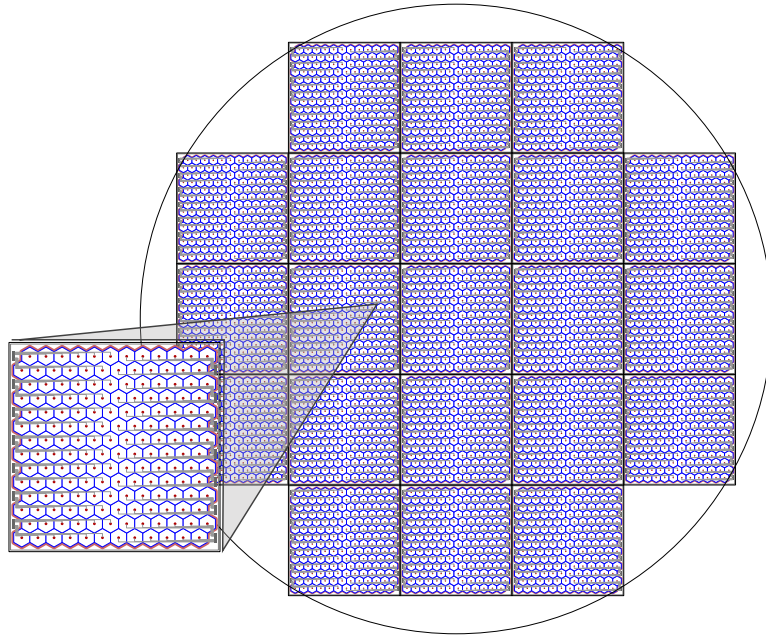


Figure 7.1: The final design of the TRISTAN detector array consists of 21 modules each with 166 pixels. The modules are arranged in a way that a maximum area of the magnetic fluxtube at the detector position is covered (grey circle). All pixels are bonded with a small wire to set the steering electrodes to the same potential. [17] The figure is based on images from [320].

7.2 Upgraded LFCS

Energy dependent transmission losses in the main spectrometer set strong limits on the accessible parameter space when KATRIN is used to search for keV-scale sterile neutrinos (section 4.2.1). Increasing the magnetic field inside the main spectrometer is an effective countermeasure (section 4.2.2). This can be achieved by an increase of the LFCS coil current, which is, however, technically limited to the *max. LFCS* setting shown in table A.1. A further enhancement requires either an increase of the number of turns of the coils or a supplement of new coils to the LFCS.

In fall 2019, an upgrade of the LFCS system was installed at the main spectrometer. It includes five additional coils, as well as an extension of all single to double layer coils. [318] All coils can be operated with a maximum current of 120 A [328].

The main purpose of the upgraded LFCS is the reduction of the main spectrometer background [127]. For a sterile neutrino search, it increases the energy range over which the β -decay spectrum can be observed without transmission loss.

In the following section, the upgraded LFCS is briefly introduced (section 7.2.1), and its transmission properties are studied (section 7.2.2).

7.2.1 Purpose and Design

In order to reach the desired sensitivity on the neutrino mass of 0.2 eV at 90% confidence level, the KATRIN experiment requires a background rate of approximately 10 mcps in the region of interest [10], which is currently exceeded by approximately one order of magnitude [131]. One of the largest background contributions comes from decaying Rydberg atoms [177]. These emitted low energy electrons are distributed almost uniformly in the volume of the spectrometer. By using a specific configuration of the LFCS, the so-called Shifted

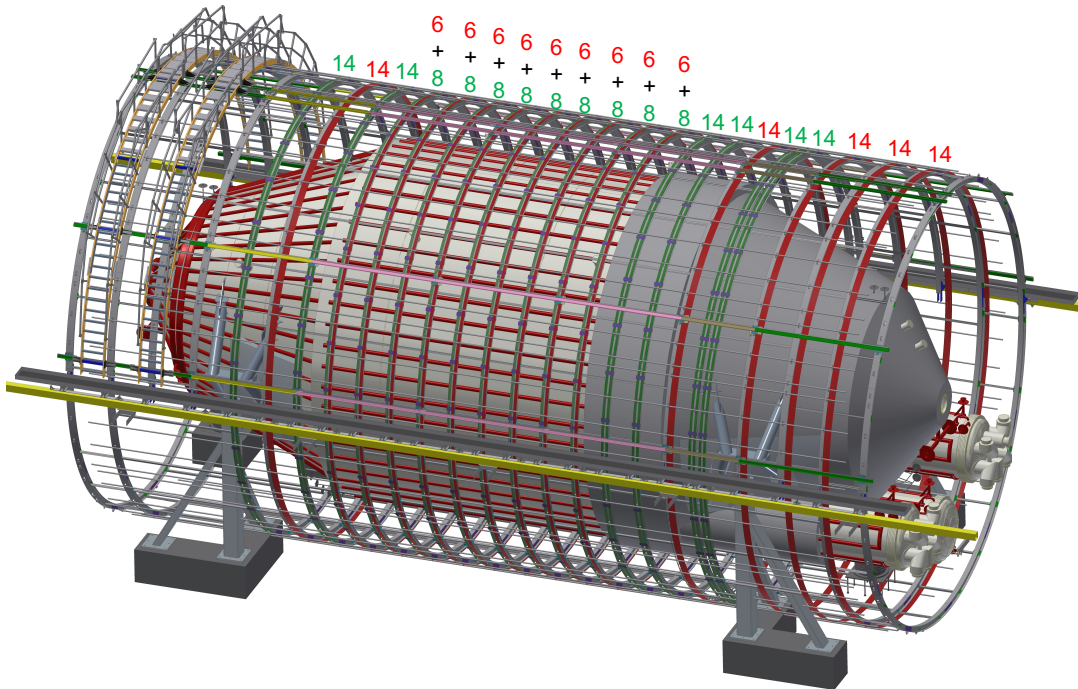


Figure 7.2: A schematic view of the KATRIN main spectrometer and the air coil system. The LFCS before the upgrade is marked in green, the additional coils in red. All coils contain of 14 turns and can be operated with a maximum current of 120 A [328]. The figure was kindly provided by Steffen Lichter (Karlsruhe Institute of Technology).

Analyzing Plane (SAP) setting, the size of the fluxtube inside the main spectrometer is reduced. As a consequence, the background rate can be decreased while simultaneously the high energy resolution is maintained. The SAP procedure was successfully tested with a gaseous krypton source in May 2019. [127]

The upgraded LFCS is displayed in figure 7.2.

7.2.2 Transmission Properties

With the upgraded LFCS system, the transmission conditions for electrons with high surplus energies show a significant enhancement compared to the old *max. LFCS* setting defined in table A.1. Figure 7.3 displays the transmission probability as a function of the surplus energy for the old *max. LFCS* setting (blue markers) and the the upgraded LFCS system (orange markers).

For the upgraded LFCS, the transmission loss exceeds the 0.1 % level at surplus energies larger than $E_{\text{sur}} = 7.8 \text{ keV}$. This is a distinct improvement compared to the old *max. LFCS* setting that already had a loss exceeding 0.1 % at $E_{\text{sur}} = 3.8 \text{ keV}$. When only the detector bullseye is used, the full energy spectrum can be measured without any transmission loss as shown in figure 7.4 .

According to equation (4.26), the best statistical sensitivity can be reached in a measurement, when at least eight detector rings are active. With the upgraded LFCS system, an energy range down to 9.0 keV below the endpoint can be measured for $n_{\text{rings}} = 8$. This is an additional improvement to the old LFCS which only allowed measurement down to 1.1 keV below the endpoint with eight detector rings.

All stated values correspond to an statistical uncertainty of 10^{-4} .

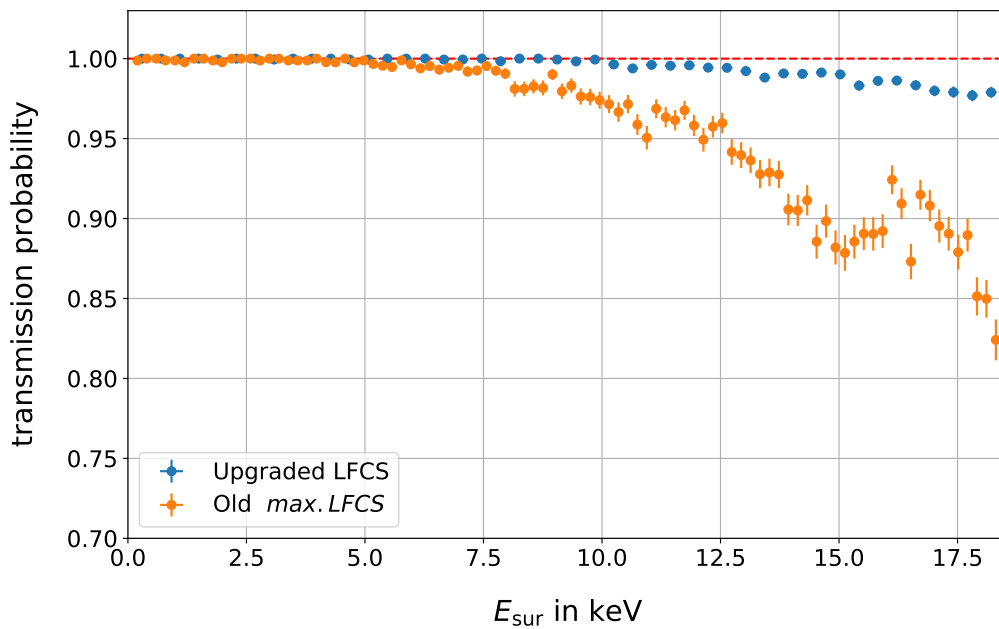


Figure 7.3: The transmission probability as a function of the surplus energy, averaged over all detector rings is shown. With the upgraded LFCS system the transmission probability for electrons with high surplus energies enhances up to 20% compared to the current system at an optimized setting.

7.3 Beryllium Rear Wall

One result of chapter 5 is that β -decay electrons that scatter back off the rear wall surface and reach the detector cause one of the most dominant systematic effects when KATRIN is used to search for sterile neutrinos. As first pointed out in [259], there are two effective countermeasures: a reduction of the rear wall magnetic field or a replacement of the current rear wall setup by a beryllium structure. According to the results of investigations presented in section 5.2, the first countermeasure already decreases the influence of rear wall backscattering by up to one order of magnitude.

As shown in the following, a replacement of stainless steel valve between the source and rear section by a removable beryllium disc, additionally reduces the relative influence of backscattered electrons to the measured spectrum by up to a factor of 45.

Following [259] a distinction between two different magnetic field settings is made.

High and Low Field Scenario

Figure 7.5 illustrates the rear wall chamber with a new beryllium rear wall and the simulated magnetic fluxtube that is observed by the FPD. Two different scenarios are presented:

1. For the simulation shown on the top panel. the rear wall magnet is operated at 65% of its nominal value, in order to assure that all magnetic field lines connect to the beryllium disc. Thus, the advantage of the reduced backscattering probability applies for all field lines observed by the detector. The blue solid line in figure 7.6 shows the resulting distortion of the integral spectrum, derived analogously to the procedure introduced in section 5.2. Compared to the optimized nominal KATRIN rear wall setting (orange solid line), the effect is reduced by up to a factor of 15.

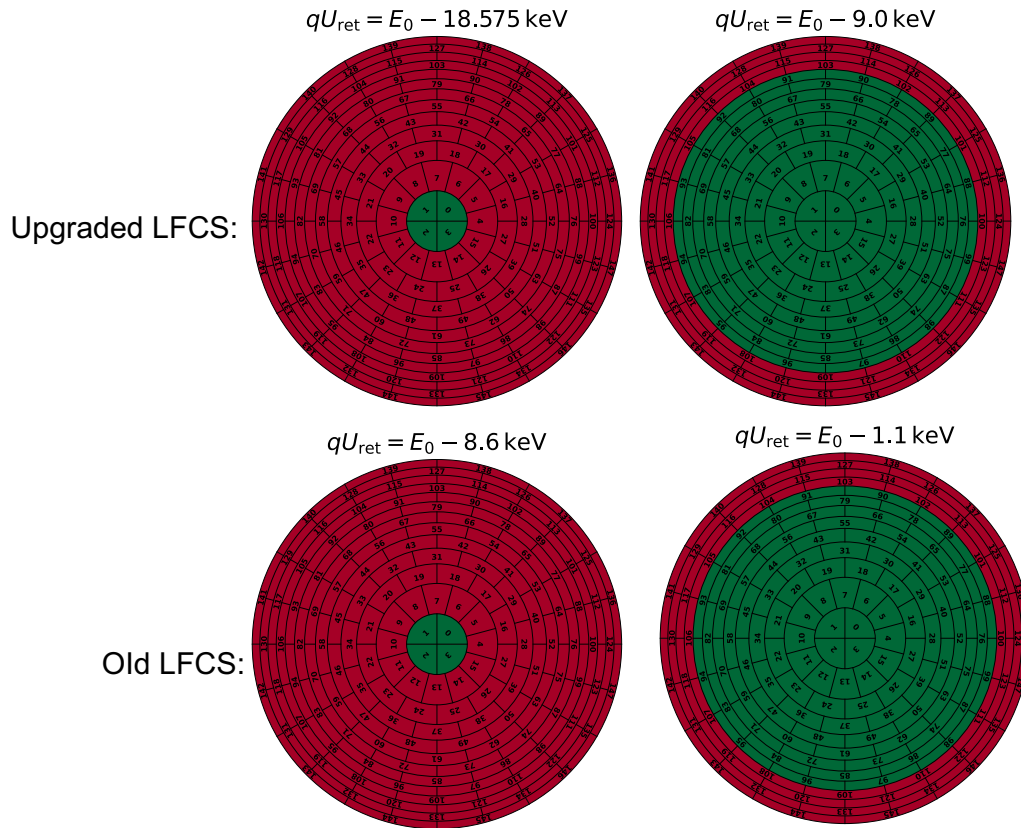


Figure 7.4: The fiducial area of the focal plane detector (green) and the detector rings where transmission losses are expected (red) for different applied retarding potentials qU_{ret} . Compared to the old *max. LFCS* setting (bottom figures), the upgraded LFCS (upper figures) shows a distinct improvement in terms of an adiabatic electron transport. By using only the inner ring of the detector, the full tritium β -decay energy range can be observed within an uncertainty of 10^{-4} . For a measurement of down to 9.0 keV below the endpoint, all inner detector rings up to ring number eight observe a fully-adiabatic transmission. For the old LFCS, only energies down to 8.6 keV below the endpoint were accessible for the bullseye and 1.1 keV for $n_{\text{rings}} = 8$.

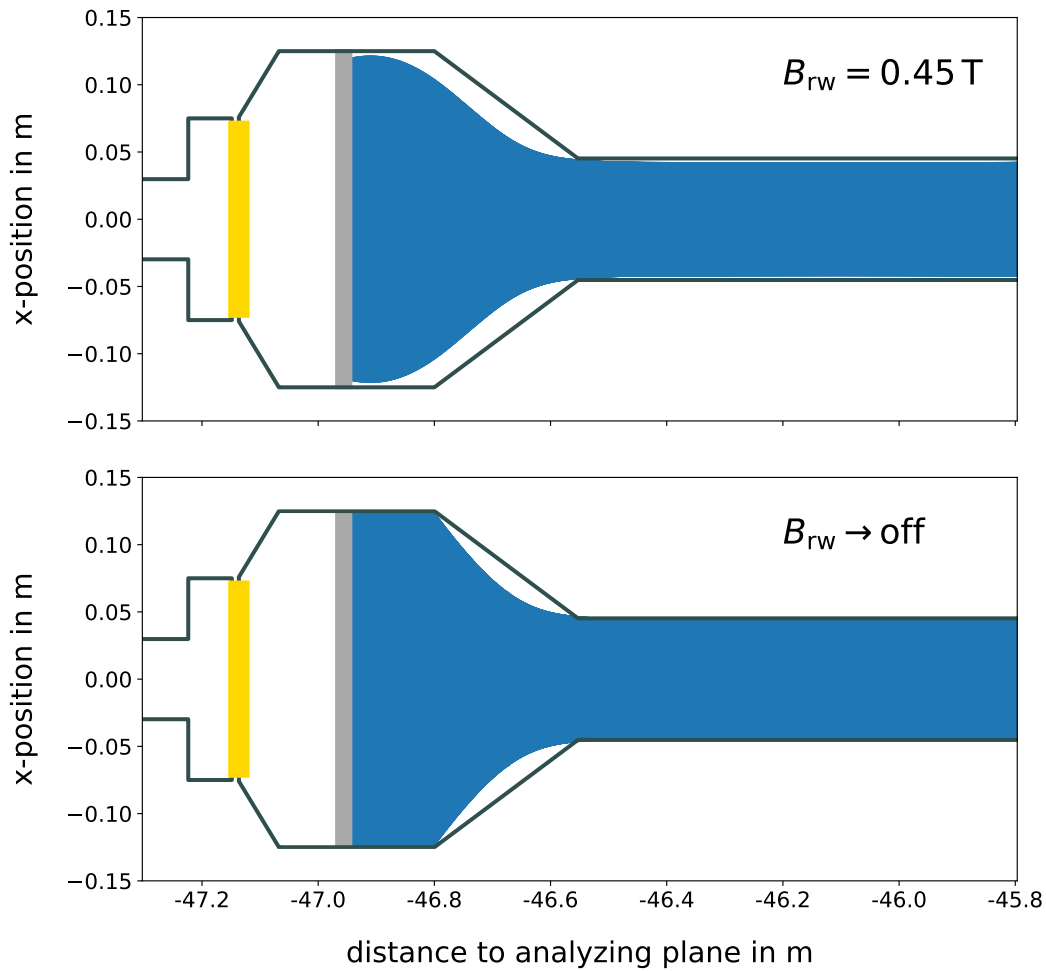


Figure 7.5: The rear wall chamber, including the beryllium rear wall, at two different magnetic field settings. For the top scenario, the magnetic field at the rear section is chosen in such a way, that all magnetic field lines observed by the detector (blue area) connect to the beryllium disc. If the rear section magnet is turned off (bottom illustration), a part of the fluxtube observed by the FPD connects to the stainless steel housing. Figure is adapted from [259] figure 3.1.

2. The figure on the bottom shows a scenario where the rear section magnet is turned off. As a consequence, the fraction of backscattered electrons that are able to reach the detector decreases (see section 5.2). In addition, the lowering of the field causes parts of the observed fluxtube to connect with the stainless steel walls. As can be seen in figure D.3, the backscattering probability of stainless steel is approximately a factor of ten higher compared to beryllium. For electrons that scatter back on the stainless steel housing, the lowered magnetic field is not able to compensate the increased backscattering probability. As a consequence, this low field scenario leads to a worsening of the effect by up to a factor of ten for all FPD rings $n_{\text{rings}} > 5$. However, the inner five detector rings observe field lines that still connect to the beryllium disc and additionally benefit from the lower magnetic field compared to the first scenario. The blue dashed line in figure 7.6 shows the influence on the spectral shape for the low field scenario. For the inner five detector rings, the effect can be further reduced by a factor of 3.

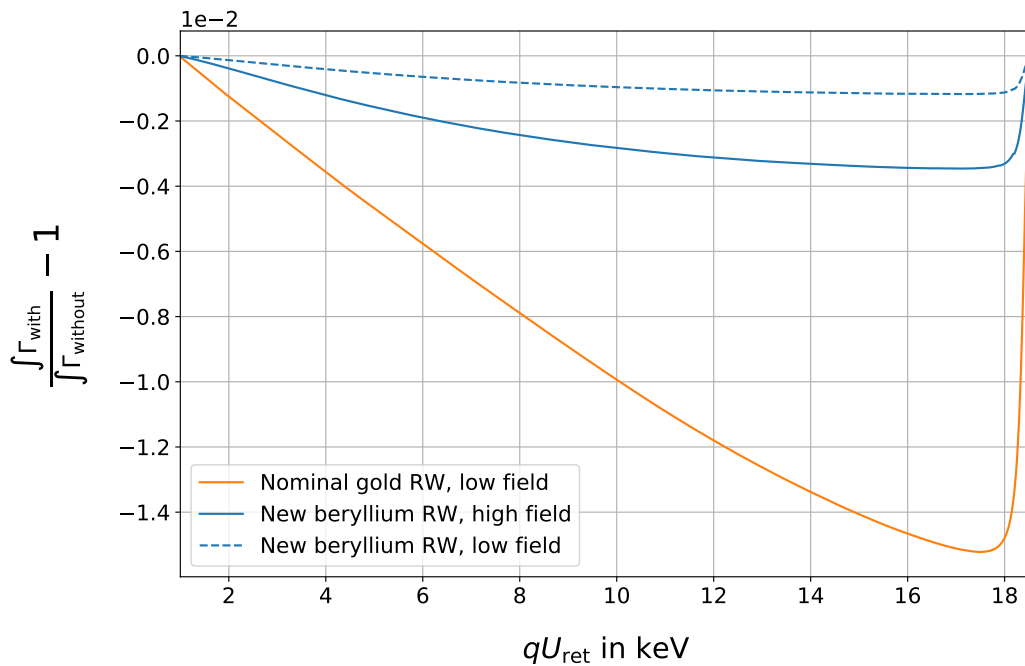


Figure 7.6: Distortion of the integral spectrum caused by backscattered electrons on a beryllium rear wall, averaged over all detector rings. By installing a new beryllium rear wall (solid blue) the overall effect can be reduced by up to a factor of 15 compared to the best case scenario with the current KATRIN rear wall setting (orange solid line). If the rear wall magnet is turned off, the magnetic field is generated by the stray field of the source magnets. Since the flux tube radius exceeds the rear wall, the detector rings 5 - 12 observe the backscattered spectrum of the stainless steel rear wall chamber. The five inner rings benefit from the lower backscattering probability and the reduced magnetic field strength (blue dashed line). Compared to the optimized (low field) nominal KATRIN setting, this scenario reduces the effect of rear wall backscattering by up to a factor of approximately 45.

7.4 SSC-Sterile: A new β -Decay Model for sterile Neutrino Searches

The systematic effect studies presented in chapter 5 revealed that the current KATRIN tritium β -decay model needs to be extended. Two modifications of the model have already been successfully applied in the *First Tritium Campaign* analysis shown in chapter 6. However, a high statistics measurement possible with the TRISTAN detector, requires more detailed modeling to reduce the influence of uncertainties on the sterile neutrino sensitivity.

The *SSC-Sterile Model*¹ follows a multi-dimensional convolution approach [312]. It is currently under development, however, the underlying method was already successfully applied for the analysis of TRISTAN prototype measurements at the Troitsk nu-mass experiment [324, 325, 326].

The following section introduces the basic concept, status, and outlook for the new tritium β -decay model.

The Concept of a multi-dimensional Convolution Model

The concept and main development of the *SSC-Sterile Model* were carried out by Martin Slezák² and Alexey Lokhov³. It was further advanced for example by [47, 329].

The spectrum observed by the detector is gained by convolving the theoretical spectrum S_{theo} with all spectral distorting effects. This allows for individual treatment of the underlying effects as well as a convenient way of studying their impacts on the observation. The resulting spectrum M_{res} observed at the detector is given by

$$M_{\text{res}} = S_{\text{theo}} \otimes R_k = S_{\text{theo}}^T \otimes R_1 \otimes R_2 \otimes \dots, \quad (7.1)$$

where the response matrices R_k are calculated for each effect. [47]

The response matrices do not only take into account the variation of the β -decay energy but additionally the change of the angular distribution. The four dimensional matrices contain the redistribution from $(m \times n)$ initial to $(i \times j)$ final energy and angular bins. Each $(i \times j)$ final distribution is calculated for an initial set of parameter tuple (m, n) individually:

$$R_{mn} = \begin{bmatrix} R_{mn11} & R_{mn12} & \cdots & R_{mn1j} \\ R_{mn21} & R_{mn22} & \cdots & R_{mn2j} \\ \vdots & \vdots & \ddots & \vdots \\ R_{mni1} & R_{mni2} & \cdots & R_{mnij} \end{bmatrix}. \quad (7.2)$$

The resulting response matrix is

$$R = \begin{bmatrix} R_{11} & R_{12} & \cdots & R_{1n} \\ R_{21} & R_{22} & \cdots & R_{2n} \\ \vdots & \vdots & \ddots & \vdots \\ R_{m1} & R_{m2} & \cdots & R_{mn} \end{bmatrix}. \quad (7.3)$$

where the R_{mn} sub-matrices are the elements of the 4-dimensional response matrix. [47]

¹The term *SSC-Sterile* refers to the original KATRIN model code *SSC* which is an abbreviation for **S**ource and **S**pectrum **C**alculation.

²Max-Planck-Institute, Munich

³Institute for Nuclear Research Moscow and Institut für Kernphysik, Westfälische Wilhelms-Universität Münster.

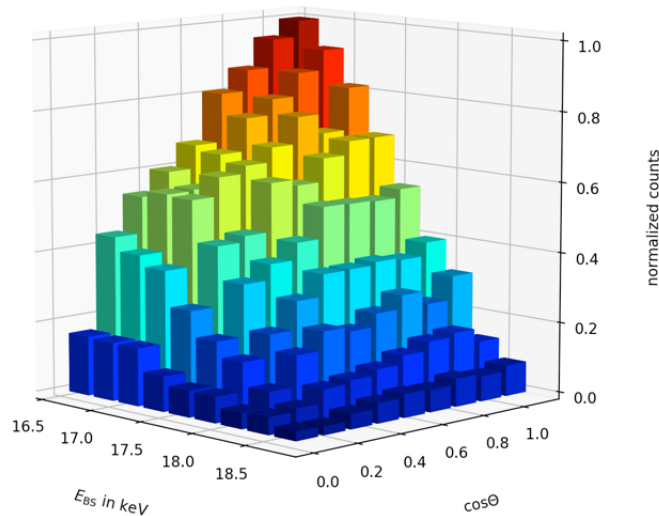


Figure 7.7: Visualization of a (10×10) sub-matrix of backscattered electrons from the rear wall. A total of 10^6 electrons with initial energies $E_{\text{ini}} = [18.375, 18.575]$ keV and a starting angular distribution of $\cos\theta_{\text{ini}} = [0.9, 1.0]$ were used for the simulation. The final energy E_{BS} and angular distribution $\cos\theta$ is stored in a 2-dimensional histogram. By repeating the procedure for different starting energy and angle tuples (m, n) , the matrix in equation (7.3) is calculated.

Figure 7.7 shows the visualization of a typical sub-matrix R_{mn} of electrons backscattered at the rear wall. Due to the energy loss, the energy distribution is smeared to lower energies and the angular distribution is broadened.

Status and Outlook

The *SSC-Sterile Model* was implemented to the FITRIUM analysis software and made public to the KATRIN collaboration. It includes the option of considering individual responses for backscattering at the rear wall, scattering in the source, the electro magnetic fields, and the detector response including backscattering on the detector, pile-up, and dead-layer energy losses [330, 47, 329]. The C++ code allows automatic construction of the response matrices, as well as read-in of matrices calculated externally. In order to reduce the computation time, parts of the calculations are performed by GPUs.

The further development of *SSC-Sterile* requires the comparison of the model with data taken at the KATRIN experiment. A further study of the systematic effects that are implemented will help to improve the precision of the model

7.5 Using KATRIN without Hardware Modifications in the Future

As introduced in section 7.1, the objective of the new TRISTAN detector system is to undertake a high statistics keV-scale sterile neutrino search with the KATRIN experiment. After three years of data taking a sensitivity of $\sin^2\theta < 10^{-6}$ can be reached. [17] This would enable the opportunity to study a sterile neutrino parameter space that is close to the cosmological allowed region in a laboratory and model-independent measurement.

Until TRISTAN is ready to be built in (earliest 2025), it is important to use the KATRIN

experiment as often as possible to record spectra on an extended measurement window. The gained data does not only allow to set new laboratory limits on the sterile neutrino parameter space, it also enables the opportunity to steadily test and improve the tritium β -decay model for energies several keV below the endpoint.

This section proposes a measurement with the current KATRIN setup that studies the tritium β -decay spectrum down to 4.5 keV below the endpoint. It assumes a full KATRIN measurement campaign dedicated only to a keV-scale sterile neutrino search with a total measurement time of 40 days. All systematic effects and uncertainties identified in chapter 5 are considered, to calculate a realistic sensitivity of the measurement.

Settings for the 40 Day Sterile Campaign

In order to reduce the signal rate at the detector, the column density is set to 1% of its nominal value and the tritium purity is reduced to $\epsilon_T = 0.05$. The latter can be obtained by different gas compositions. All magnetic fields are operated at 70% of their design values except the pinch magnet. In order to further reduce the signal rate at the detector (by a factor of 1.6) the pinch magnet is operated at $B_{\text{pch}} = 6.0$ T. The increased ratios between the pinch and the source/detector magnet field have additional benefits. They reduce the systematic effect of magnetic trapping in the source as well as backscattering loss at the detector (sections 5.4 and 5.6). In order to minimize the spectral contribution of electrons backscattering at the rear wall, the rear section magnet is turned off (section 5.2).

The upgraded LFCS is operated at maximum coil currents to avoid transmission loss caused by non-adiabaticity (section 4.2). Furthermore, only the inner eight rings of the FPD are used in the measurement.

The total measurement time of 40 days is divided in 960 scans of 1 hour duration, at 30 different retarding potentials between $qU_{\text{ret}} = [14.075, 18.575]$ keV. The measurement time per sub-run is equally distributed (2 minutes per retarding potential)⁴.

Table 7.1 gives an overview of the parameters.

Uncertainty Budget

In order to calculate the sensitivity that could be reached within such a campaign, all systematic effects identified in chapter 5 have been taken into account in the study.

The following list gives a short overview on the assumed systematic uncertainty budget:

- **Rear wall backscattering/ magnetic traps/ detection efficiencies:** In chapter 5, relatively large uncorrelated uncertainties on the modeling of the three effects have been derived (see table 5.2). An improvement of the model, for example with the approach introduced in section 7.4, is able to reduce the large uncertainties and apply correlations in the analysis on a medium time scale.

Therefore, the sensitivity study displayed in figure 7.8 distinguishes between two scenarios. The best case scenario assumes that all uncertainties are reduced by a factor of two compared to the current values (see table 5.2) and treats them as fully correlated in the analysis. The worst case scenario describes the current treatment with the full uncorrelated, relatively large uncertainties.

⁴This simplified measurement time distribution does not consider measurement points in the background region ($qU_{\text{ret}} > E_0$), or a higher measurement point density for energies close to the endpoint (due to the lower count rate). Since the nominal duration of a KATRIN campaign is 60 days, it is assumed that the additional time that could be required by an extended measurement time distribution is covered within the remaining 20 days.

Table 7.1: The KATRIN settings of the proposed measurement. Details can be found in the text.

Component	Setting
<u>Source:</u>	
ρd	$5.0 \cdot 10^{15} \text{ cm}^{-2}$
ϵ_T	0.05
<u>Magnets:</u>	
B_{pch}	6.0 T
B_{rs}	off
LFCS	maximum
all others	70 %
<u>Scan strategy:</u>	
lowest qU_{ret}	$E_0 - 4.5 \text{ keV}$
num. of meas. points	30
scan duration	1 hour
num. scans	960
total meas. time	40 days

- **Source scattering:** Due to the reduced column density, the influence of uncertainties on the parameters relevant to model source scattering (ρd , σ_{inel} , and the energy loss parameterization), are small (section 5.3). They are taken into account in the sensitivity study assuming the same uncertainties as for the *First Tritium Campaign* (see table 6.1).
- **Source activity fluctuations:** In the *First Tritium Campaign*, a reduced tritium purity of $\epsilon_{\text{T}} = 5.0 \cdot 10^{-3}$ leads to a run-wise uncertainty on the source activity of approximately 1%. By combining all 82 runs, the error on the mean is reduced to a mean value of 0.08% [131].
At the moment, attempts are being made to further reduce the run-wise uncertainty of the source activity by either a combination of LARA and FBM data, or by using a part of the deep-spectral measurement points to determine the source activity directly with the measured rate at the FPD.
In the sensitivity study shown in figure 7.8, the impact of two source activity fluctuations are compared: a run-wise uncertainty of 0.1% and 0.5%. Both values are scaled down by the total number of runs following the discussion in section 5.5.
- **Non-adiabaticity:** With the upgraded LFCS, no transmission loss is expected for the eight inner rings of the FPD on the studied energy range.
- **Theoretical corrections:** The same theoretical corrections as for the *First Tritium Campaign* are considered in the model. It is assumed that the FSD is valid on the full energy range within the uncertainties stated in table 6.1.

Sensitivity

The results of the sensitivity study are displayed in figure 7.8. The statistical limit on the mixing angles reaches a maximum at $\sin^2 \theta = 6.0 \cdot 10^{-5}$. Including systematic uncertainties, the smallest mixing amplitude that can be excluded is $\sin^2 \theta < 2.8 \cdot 10^{-4}$ assuming a run-wise activity fluctuation of $\sigma_{\text{activity}} = 0.1\%$ and $\sin^2 \theta < 6.1 \cdot 10^{-4}$ for $\sigma_{\text{activity}} = 0.5\%$ (best case scenario). If large uncorrelated uncertainties on the rear wall, magnetic trapping, and detection efficiency corrections are taken into account (worst case scenario), the sensitivity on the mixing angle is limited to $\sin^2 \theta < 8.8 \cdot 10^{-4}$ for $\sigma_{\text{activity}} = 0.1\%$ and $\sin^2 \theta < 9.4 \cdot 10^{-4}$ for $\sigma_{\text{activity}} = 0.5\%$.

Conclusion

The proposed measurement uses the KATRIN experiment with a reduced source activity to measure the tritium β -decay spectrum over an extended energy interval down to 4.5 keV below the endpoint. It uses the experiment in a setting, where the systematic uncertainties are expected to be well understood.

With a total measurement time of 40 days, it is proposed to dedicate an entire KATRIN measurement campaign to a keV-scale sterile neutrino search. In the best case scenario, the current laboratory limits on the active-to-sterile mixing amplitude could be improved on a mass scale of approximately $0.10 \text{ keV} \leq m_{\nu_s} \leq 4.10 \text{ keV}$ by up to a factor of 11. If large uncorrelated uncertainties on the rear wall backscattering, magnetic traps, and detection efficiency correction are taken into account, an improvement on the mixing angle of up to a factor of 2.8 could still be reached on a mass range of $0.10 \text{ keV} \leq m_{\nu_s} \leq 2.64 \text{ keV}$.

Following the great success of the sterile neutrino analysis of the *First Tritium Campaign* data, this measurement would be the next major milestone towards a high statistics sterile neutrino search of the KATRIN experiment with the TRISTAN detector.

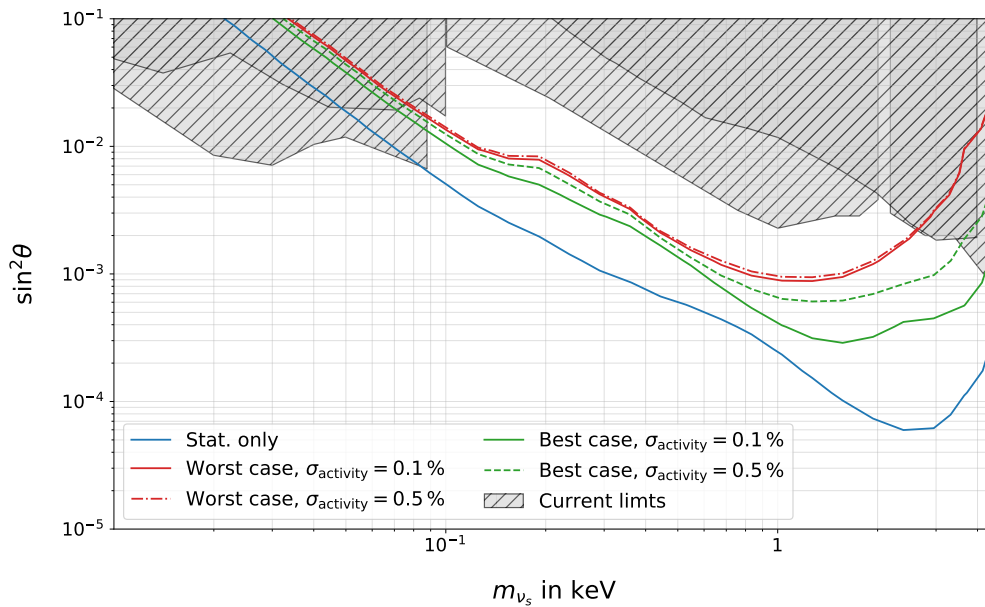


Figure 7.8: The sensitivity of a 40 day sterile neutrino measurement with only statistical uncertainty (blue line) and different systematic uncertainty scenarios. The red solid and dashed line display the worst case scenario as defined in the text. It is subdivided in two cases that assume different run-wise activity fluctuations. The best case scenario is shown in green. The predicted sensitivity is compared to the current laboratory limits from [244, 245, 246, 247, 248].

7.6 Conclusion

The KATRIN experiment is designed to determine the effective electron antineutrino mass by measuring the tritium β -spectrum in close vicinity to the endpoint. If the narrow measurement interval is extended, it provides the opportunity to search for keV-scale sterile neutrinos.

Chapter 4, 5, and 6, described how the KATRIN experiment can be used for such a measurement without any hardware modifications, and by only adjusting experimental parameters such as the source activity. This sort of measurement has the potential to improve the current laboratory limits on the sterile neutrino parameter space by up to one order of magnitude.

Further improvement of the sensitivity would require several hardware modifications which are presented in this chapter.

One important extension would be a new detector system that is able to resolve high count rates. The TRISTAN detector, which is introduced in section 7.1, is designed to measure count rates of up to 10^8 cps with an energy resolution of 300 eV at an electron energy of 30 keV [17]. These features would start to probe a sterile neutrino parameter space of cosmological interest with the KATRIN experiment.

With the currently installed LFCS upgrade introduced in section 7.2, the accessible parameter space of a sterile neutrino search can be additionally extended. With the new air coil system, the transmission for electrons with high surplus energies increases significantly. For electrons that enter the main spectrometer close to the symmetry axis (observed by the FPD bullseye), the entire tritium β -decay energy range can be studied without an

expected transmission loss (within a statistical uncertainty of 10^{-4}).

In order to reduce another leading systematic uncertainty, a new beryllium rear wall is discussed in section 7.3. Electrons backscattering from the rear wall can contribute to the measured spectrum with up to 32% if no countermeasures are taken. By installing a removable beryllium disc between the source and the rear section, the effect can be reduced by up to a factor of $2.7 \cdot 10^2$ to a maximum contribution to the measured spectrum of $1.2 \cdot 10^{-3}$.

The studies of chapter 5 showed that it is important to extend the current KATRIN tritium β -decay model for a keV-scale sterile neutrino search. The *SSC-sterile model* introduced in section 7.4 presents a new multidimensional-convolution approach that treats systematic effects as response matrices. The underlying method was already successfully applied in the analysis of tritium β -decay data [324, 325, 326]. However, a further development of the code is required for a high statistics sterile neutrino search.

Finally in section 7.5, a sterile neutrino measurement is proposed that takes into account all the information gained in this thesis. It is assumed that an entire KATRIN measurement campaign is dedicated to a sterile neutrino search with a total measurement time of 40 days. By reducing the source activity, the tritium β -decay spectrum is measured down to 4.5 keV below the endpoint.

Depending on the systematic budget, a sensitivity on the active-to-sterile mixing angle of up to $\sin^2 \theta < (2.8 - 9.4) \cdot 10^{-4}$ can be reached which would lead to an improvement of the current laboratory limits on the active-to-sterile mixing amplitude of up to a factor of 11 on a mass range of $0.10 \text{ keV} \leq m_{\nu_s} \leq 4.10 \text{ keV}$.

CHAPTER 8

Summary and Outlook

As shown in chapter 1, the experimental discovery of neutrino oscillation proved conclusively that neutrinos have to be massive. This finding stands in fundamental contradiction to the SM in which neutrinos are formulated as massless. One way to introduce neutrino masses to the SM within a minimal extension is described by the seesaw mechanism. There are many different seesaw models that all have one thing in common: they require the introduction of right-handed neutrinos. These particles would predominantly be uncharged under any SM gauge symmetry (*sterile*), however, mix with active neutrinos via mass eigenstate oscillation.

In principle, the mass of the sterile neutrinos can take any value, but there are several preferred scales. One of them is the keV mass scale. Sterile neutrinos in the keV-range could act as Warm Dark Matter and help to solve several open questions about the structure formation of our Universe. They would manifest via active-to-sterile mixing as a kink like distortion in β -decay spectra, enabling a search for sterile neutrinos in laboratory experiments.

The KATRIN experiment, as described in detail in chapter 2, has the goal to determine the effective electron antineutrino mass with an unprecedented sensitivity of 0.2 eV (90 % C.L.). In order to achieve this, the tritium β -decay spectrum is measured close to its kinematic endpoint. In its first four-week tritium measurement campaign (*KNMI*), the current limit on $m_{\bar{\nu}_e}$ could be improved by already a factor of two, to a new upper limit of $m_{\bar{\nu}_e} < 1.1$ eV (90 % C.L.).

In order to gain a high statistical significance, the KATRIN experiment is equipped with a highly luminous tritium source. The daily tritium throughput of 40 g results in an activity of 100 GBq, stable on the permille level.

In chapter 3 it is shown that this feature can be used to extend the physics reach of the KATRIN experiment and search for keV-scale sterile neutrinos in a model-independent laboratory experiment. Previous works show that such a measurement has the potential to reach a high statistical sensitivity on the active-to-sterile mixing amplitude of up to $\sin^2 \theta < 10^{-8}$. This would allow to study a parameter space of cosmological interest.

In order to achieve this high statistical significance, a new detector system is required. The TRISTAN detector is currently under development and is planned to be available for a sterile neutrino measurement with the KATRIN experiment earliest in 2025.

This thesis presents the idea of using the KATRIN experiment without any hardware modifications for a first sterile neutrino measurement. One result of this work is that even with reduced statistics, the KATRIN experiment is able to improve the current laboratory

limits on the sterile neutrino parameter space by more than one order of magnitude on a mass range of several keV.

In order to achieve this, the tritium β -decay spectrum needs to be measured on an extended energy range. In chapter 4 it was found that two major challenges arise, when the retarding potential is lowered accordingly:

1. The signal rate at the detector increases rapidly and exceeds the limits of the FPD already at 400 eV below the endpoint.
2. The growing surplus energy of the signal electrons with respect to the retarding potential leads to a transmission loss due to non-adiabaticity.

In the scope of this work, several countermeasures that address both problems were identified. It was found that by lowering the source activity (either by reducing the column density or the tritium purity), as well as by a modification of the source and detector magnetic field, the full energy range of the β -spectrum can be measured within the FPD limits (section 4.1).

In section 4.2 the cause of the non-adiabatic transmission loss was studied and it was noted that the effect scales with the distance of the electron's propagation path to the main spectrometer symmetry axis. This information was used to find effective countermeasures. By either increasing the LFCS or reducing the detector magnetic field, the magnetic fluxtube inside the main spectrometer that is observed by the detector can be decreased. This leads to an improvement of the transmission probability. Furthermore, the radial dependency of the effect was used to define fiducial detector segments, depending on the specific electromagnetic setting.

All information obtained is incorporated to define three measurement scenarios that enable a keV-scale sterile neutrino search with the KATRIN experiment without hardware modifications (section 4.3).

If the β -decay spectrum is observed further away from the endpoint, specific systematic effects become relevant. This work presents the first comprehensive study of all yet known systematic effects of a keV-scale sterile neutrino search with the KATRIN experiment. In chapter 5 each effect was studied following the same procedure: the relative influence of the effect on the full tritium β -decay spectrum was derived, either analytically or by Monte Carlo simulations. If possible, the effect was modeled in order to take it into account in data analysis. Uncertainties on the modeling were discussed and their impact on a sterile neutrino measurement was studied along a hypothetical 7-day reference measurement (Monte Carlo data set).

The studied systematic effects were divided in three categories, depending on their size and uncertainty. No effect was found that would make a search for keV-scale sterile neutrinos with the KATRIN experiment impossible.

Finally, a comprehensive list of recommendations for the next steps was developed. It suggests action points for short and mid term improvements that are required both for a high statistics sterile neutrino search and a sterile neutrino search without hardware modifications.

With the *First Tritium Campaign* that took place in 2018, the KATRIN experiment achieved a major milestone on its way towards the neutrino mass determination. The first operation of the experiment with tritium demonstrated impressively that the KATRIN experiment fulfills the high requirements that are necessary to reach this ambitious goal. During the campaign, the source was operated at a reduced tritium activity. This enabled a first sterile neutrino search with KATRIN on a mass range of $0.0 \leq m_{\nu_s} < 1.6$ keV. With the information gained in chapter 5, the KATRIN β -decay model which is opti-

mized for an endpoint analysis, could be extended by several systematic effects. Including the additional corrections, the measured data showed excellent agreement with the model which states one of the greatest achievements of this thesis.

As a result, the current laboratory limit on the active-to-sterile mixing amplitude was improved by up to a factor of eight on a sterile neutrino mass range of $0.10 \leq m_{\nu_s} \leq 0.76$ keV. All information on the campaign as well as the analysis can be found in chapter 6.

In the last part of this thesis (chapter 7), future strategies and perspectives for a keV-scale sterile neutrino search with the KATRIN experiment were developed. The general design and the current status of the TRISTAN project was presented. Furthermore, two additional hardware modifications were introduced. One of them is an upgrade of the LFCS which has already been installed at the KATRIN main spectrometer. It was shown that with the upgrade, the effect of non-adiabatic transmission can be further reduced. When only the most inner detector ring is used, the entire tritium β -decay energy range can be measured without any transmission loss.

Furthermore, a multi-dimensional convolution approach was presented which shows the potential to significantly improve the tritium β -decay model on the full energy range. All systematic effects that have been derived in this thesis can be modeled as individual response matrices and combined to one overall response matrix that takes correlations between the individual effects into account.

In the last section, all information gained in this thesis are incorporated into a measurement proposal for a 40 day sterile neutrino measurement with the current KATRIN setup. The predicted sensitivity of the campaign includes a realistic uncertainty budget and shows the potential to improve laboratory limits on the active-to-sterile mixing amplitude up to a factor of 11 on a mass range of $0.10 \leq m_{\nu_s} \leq 4.10$ keV.

The results of this thesis made clear that the KATRIN experiment has the opportunity to play a significant role in direct laboratory Dark Matter searches due to its unique features. The results provide comprehensive recommendations that lead the way towards a high statistics sterile neutrino measurement. Especially the result of the *First Tritium Campaign* should strongly encourage the KATRIN collaboration to continue on the chosen path.

Appendix

A Transmission Studies with the KATRIN Simulation Framework *KASPER*

The *KASPER* simulation framework is a software to simulate electron motion in complex electro magnetic and geometrical structures [331]. It was developed by members of the KATRIN collaboration with the purpose to provide high precision simulations for the KATRIN experiment (see for example [124, 332]). Since its public release in 2017 [331], *KASPER* simulations have been used in several other experiments, for example XENON [333], Darwin [334], Project-8 [335] or the Troitsk nu-mass experiment [324, 326] (for the latter see also appendix H). *KASPER* consist of several packages. For the work presented in this thesis, the following modules are of relevance:

- The particle tracking module *KASSIOPEIA* calculates the electron trajectories in electro magnetic fields by solving the Lorentz equation. In order to safe computation time, the degree of precision can be adjusted. [124]
- The *KGeoBag* package provides geometrical shapes that are used for field calculations, particle navigation and interaction [336].
- The field calculation is done by *KEMField*, a tool to calculate electro magnetic fields for complex geometrical structures on large scales [331].
- Backscattering of electrons on silicon is simulated with *KESS* [288]. The former stand alone software has been implemented to the *KASPER* framework in order to simulated electron backscattering on the FPD (section 5.6).

The simulations are configured via XML-files, where the user can chose the component that should be simulated and the starting and terminating conditions for the events. The precision of the trajectory calculation can be chosen from exact tracking where the Lorentz equation is solved for every step of the particle (with a pre-defined step length), adiabatic tracking where the equation of motion is only derived at the guiding center position, and magnetic tracking where only the magnetic field lines are calculated [124]. The simulation output is stored in root histograms.

Detailed information on the *KASPER* framework can be found in [331].

Transmission Studies with *KASPER*

For the transmission studies presented in sections 4.2, 6.5, and

Analysis of the Simulations

The generated electrons propagate towards the FPD and are terminated if they fulfill one of the following conditions

- **Terminator max-z:** Electrons that pass the main spectrometer and the pinch magnet are terminated at the position of the detector.
- **Terminator min-z:** Electrons that are reflected due to non-adiabatic motion were terminated after they passed their starting position with direction to the source.
- **Terminator trapped:** If an electron is trapped inside the main spectrometer and is repeatedly reflected at both entries it is terminated after 10 turns.

Since the initial magnetic field inside the PS-2 magnet scales with the radius, only electrons that fulfill the conditions

$$r_{\text{ini}} \leq r_{\text{det}} \cdot \sqrt{\frac{B_{\text{det}}}{B_{\text{ini}}}}, \quad (8.1)$$

$$\theta_{\text{ini}} \leq \sin^{-1} \sqrt{\frac{B_{\text{pch}}}{B_{\text{ini}}}}, \quad (8.2)$$

are considered in the analysis of the simulation. [16]

The transmission probability is calculate for each energy bin i by forming the ratio of the electrons started $n[i]$ and passed the main spectrometer $t[i]$

$$T[i] = \frac{t[i]}{n[i]}. \quad (8.3)$$

The uncertainty on the transmission probability is derived in [337] and given by

$$\sigma[i] = \sqrt{\frac{(t[i] + 1)(t[i] + 2)}{(n[i] + 2)(n[i] + 3)} - \frac{(t[i] + 1)^2}{(n[i] + 2)^2}}}. \quad (8.4)$$

The uncertainty caused by the energy binning is calculated by the standard deviation of the mean. [16]

Table A.1 shows the LFCS settings used in the course of section 4.2.

B Relation between Non-Adiabaticity and Chaos

Electrons with high surplus energy with respect to the retarding potential experience a high magnetic field gradient inside the main spectrometer which can lead to non-adiabatic angular transition (for details see section 4.2.1). This causes a large transmission loss of up to 60 % for the nominal KATRIN magnetic field settings, if no countermeasures are taken.

In [125] it is found, that the effect varies substantially for small differences of the starting conditions which is related to the chaotic nature of the problem This section proves, that the non-adiabatic electron movements fulfill the properties of a *chaotic system* after the definition that can be found in [338]. The study closely follows [125].

Figure B.1 shows the comparison of the propagation paths of two electrons that move inside the main spectrometer for two scenarios, simulated with *KASPER*:

1) Adiabatic Scenario (left figure):

Both electrons had a surplus energy of $E_{\text{sur}} = 100 \text{ eV}$ above the retarding potential. They are generated in the center of the main spectrometer on the symmetry axis with a radial distance of 10^{-14} m . Their initial polar angel is $\theta_{\text{ini}} = 5^\circ$ which leads to a magnetic reflection on both ends of the main spectrometer according to equation (4.4). As a consequence, both electrons are trapped. During their propagation through the spectrometer,

Table A.1: Overview of the LFCS settings used in the study shown in section 4.2. The applied coil current is shown for each coil number for three settings. The values for the nominal setting are taken from [125].

setting:	Nominal	<i>max. LFCS</i>	400 A
Coil no.	I_{coil} in A	I_{coil} in A	I_{coil} in A
1	99.2	95	400
2	4.0	95	400
3	18.3	120	400
4	40.3	120	400
5	5.4	120	400
6	92.1	120	400
7	46.0	120	400
8	86.4	120	400
9	57.0	120	400
10	17.5	120	400
11	30.4	120	400
12	69.6	95	400
13	1.0	95	400
14	8.5	95	400
15	8.5	95	400

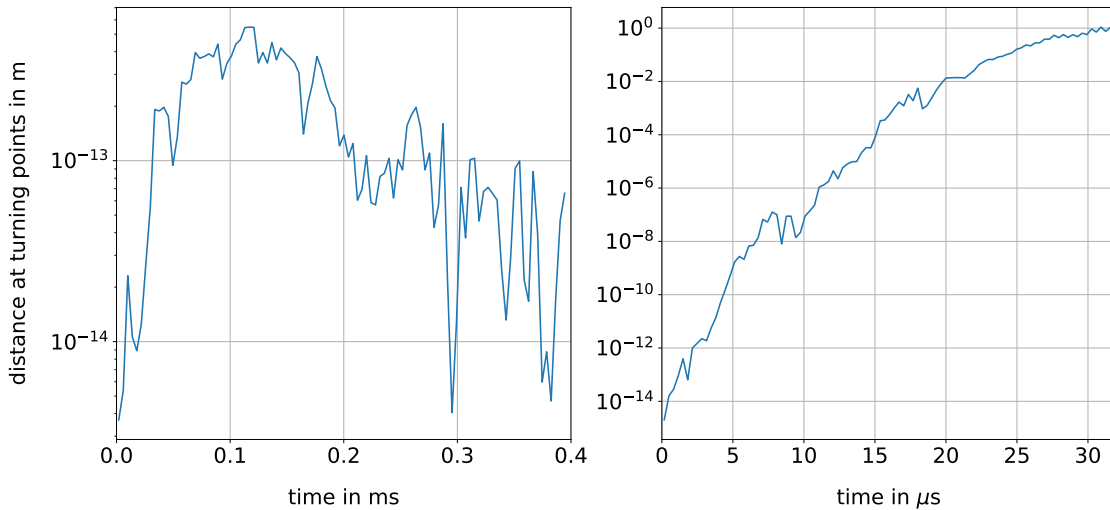


Figure B.1: Both graphs show the dependency of two electron trajectories on a small variation of the starting condition of 10^{-14} m. The left panel shows an example of an adiabatic propagation of two trapped electrons. The distance of the trajectories is small and stays within two orders of magnitude which can be explained by the fluxtube widening. For electrons with non-adiabatic transmission conditions (right panel) the small variation of the starting conditions leads to an exponential increase in the distance of the trajectories. After 30μ s the electrons show a distance of approximately 1 m. This behavior is a strong indication for a chaotic system [338]. The figure as well as the idea of this study is adapted from [125] appendix figure 12.

their distance increases by up to two orders of magnitude, which can be explained by the widening of the fluxtube. After approximately 0.4 ms both electrons turned 100 times inside the main spectrometer and the calculation was terminated. The small variation of the starting condition had no significant influence on the trajectory of the electrons.

2) Non-Adiabatic Scenario (right figure):

In the second scenario, both electrons had a large surplus energy of $E_{\text{sur}} = 15$ keV. Otherwise, the same starting conditions were chosen for the simulation as for scenario 1. Unlike the previous case, the small variation of the starting position causes a fast and exponential increase of the distance of the two electrons. Because of their high surplus energy and respectively velocity, 100 turns were already reached after 32μ s. At the end of the simulation, the distance of both particles is in the order of meters. The 10^{-14} variation of the initial position had a major influence on the resulting electron trajectories, which indicates a chaotic behavior of the motion [338].

The assumption that the chaotic behavior is in fact a numerical artifact of the simulation itself, caused by the large number of iterations that are required to calculate the step-wise trajectory, was already disproved by [125]. There it was shown that the influence of numerical instabilities on the simulation result would scale with the number of steps per gyration, which was ruled out by an ensemble of about 1000 separate simulations.

C Simulation of secondary Photon Emission at the Detector Chamber

If the retarding potential is lowered in order to observe a wider energy range of the tritium β -decay spectrum, the count rate at the detector increases rapidly and exceeds the FPD limitations (section 4.1.1). One way to reduce the signal electron rate is to lower the detector magnetic field with respect to the source magnetic field. As a consequence, the fluxtube widens up and the fraction of electrons that are observed by the FPD decreases accordingly (see section 4.1.4).

Figure C.2 illustrates the results of a *KASPER* field line simulation of a scenario where the detector magnet was turned off and the pinch magnet was operated at its nominal value of $B_{\text{pch}} = 6.0$ T. A large part of the magnetic fluxtube connects to the detector housing. Electrons that hit the stainless steel surface are either absorbed or backscattered. During both processes, the electrons can create secondary γ -emission via bremsstrahlung [268]. The backscattering and secondary emission probabilities can be derived with *GEANT4* and *KASPER* Monte Carlo simulations.

Due to their electric charge, backscattered electrons will propagate always along their original field line and can not reach the detector. The electrically chargeless photons, however, contribute to the detector γ -background.

The following derivation gives an estimate of the detector background increase caused by photon emission of β -decay electrons due to a widened fluxtube.

Electron induced γ -Background at the Detector

The contribution of the γ -background to the β -electron signal is

$$R_{\gamma\text{-bgk}} = \frac{\Gamma_{\gamma}^{\text{det}}}{\Gamma_{\beta}^{\text{det}}}, \quad (8.5)$$

where $\Gamma_{\gamma}^{\text{det}}$ is the photon and $\Gamma_{\beta}^{\text{det}}$ is the signal electron rate observed by the detector. The photon rate is given by

$$\Gamma_{\gamma}^{\text{det}} = \Gamma_{\beta}^{\text{wall}} \cdot f_{\gamma} \cdot f_{\text{bs}} \cdot f_{\Omega_{\gamma}}, \quad (8.6)$$

with the following factors:

- $\Gamma_{\beta}^{\text{wall}}$: The rate of β -electrons that hit the detector chamber walls.
- f_{γ} : The probability for an β -electron to emit a photon due to bremsstrahlung.
- f_{bs} : The backscattering multiplication factor, that takes into account electrons that hit the chamber walls multiple times due to backscattering and backreflection.
- $f_{\Omega_{\gamma}}$: The fraction of photons that are in the direct line of sight of the detector and therefore contribute to the γ -background.

Combining equations (8.5) and (8.6) gives

$$R_{\gamma\text{-bgk}} = \frac{\Gamma_{\beta}^{\text{wall}}}{\Gamma_{\beta}^{\text{det}}} \cdot f_{\gamma} \cdot f_{\text{bs}} \cdot f_{\Omega_{\gamma}}. \quad (8.7)$$

Assuming a radial homogeneous tritium density profile in the WGTS, the ratio of β -electrons that hit the wall or the detector wafer is given by the size of the corresponding fluxtube in the source that is mapped on both components

$$\frac{\Gamma_{\beta}^{\text{wall}}}{\Gamma_{\beta}^{\text{det}}} = \frac{r_2^2 - r_1^2}{r_1^2} = 1.79, \quad (8.8)$$

with the inner and outer radius of the fluxtube connected to the chamber $r_1 = 0.335$ cm and $r_2 = 0.559$ cm (according to equation 4.15).

The conversion factor f_γ is derived in a combined *GEANT4* and *KASPER* Monte Carlo simulation. The *KASPER* simulation is used to calculate the magnetic field in the detector chamber and the impact angle of the electrons. With *GEANT4*, f_γ and the energy spectrum of the photons are simulated. Taking only photons with energies bigger than the post acceleration electrode potential of $qU_{\text{PAE}} = 10.0$ keV into account, leads to $f_\gamma = 1.22 \cdot 10^{-5}$.

Not all of the generated photons are able to reach the detector wafer. Only photons that are generated at the wall of the post acceleration electrode chamber that is marked yellow in figure C.2 are in the direct line of sight to the wafer.

Assuming an isotropic photon emission, the probability for a photon generated at position z to reach the detector wafer can be calculated analogous to equations (5.33) and (5.34)

$$P_{\Omega_\gamma}(z) = \cos \left[\tan^{-1} \left(\frac{2r_{\text{waf}}}{z} \right) \right] = \frac{1}{\sqrt{\left(\frac{2r_{\text{waf}}}{z}\right)^2 + 1}}, \quad (8.9)$$

with the radius of the FPD wafer r_{waf} .

By integrating over the post acceleration electrode length l_{PAE} , the factor f_{Ω_γ} can be derived

$$f_{\Omega_\gamma} = \int_{l_{\text{PAE}}} \frac{1}{\sqrt{\left(\frac{2r_{\text{waf}}}{z}\right)^2 + 1}} dz = 9.0 \cdot 10^{-2}. \quad (8.10)$$

The simulations show, that 27% of the electrons that hit the detector chamber scatter back. Backscattered electrons are likely to be backreflected at the pinch magnet or the retarding potential. The multiple impacts on the stainless steel consequently leads to multiple emitted photons. Assuming that all backscattered electrons are backreflected to the chamber walls, the multiplicity factor is given by

$$f_{\text{bs}} = \sum_{n=1}^{\infty} 0.27^n = \frac{1}{1 - 0.27} = 1.37. \quad (8.11)$$

Combining all the factors lead to a background contribution of

$$R_{\gamma\text{-bgk}} = 2.69 \cdot 10^{-6}, \quad (8.12)$$

which is neglectable.

D Backscattering Probability and Energy Distribution of backscattered Electrons

Electrons that scatter back at the rear wall have a non-zero probability to reach the detector and contribute to the measured spectrum [10]. For a KATRIN sterile neutrino search, this states one of the most dominant systematic uncertainties (see chapter 5). In order to find effective countermeasures, it is important to understand the dependency of the backscattering on different parameters.

The following section presents a study, where the influence of different materials, impact angles and incident electron energies on the backscattering probability and the energy distribution of backscattered electrons is studied with *GEANT4* simulations.

Electrons that penetrate solid matter undergo different interactions on the surface and inside the material, causing energy and direction changes. Due to the angular changing

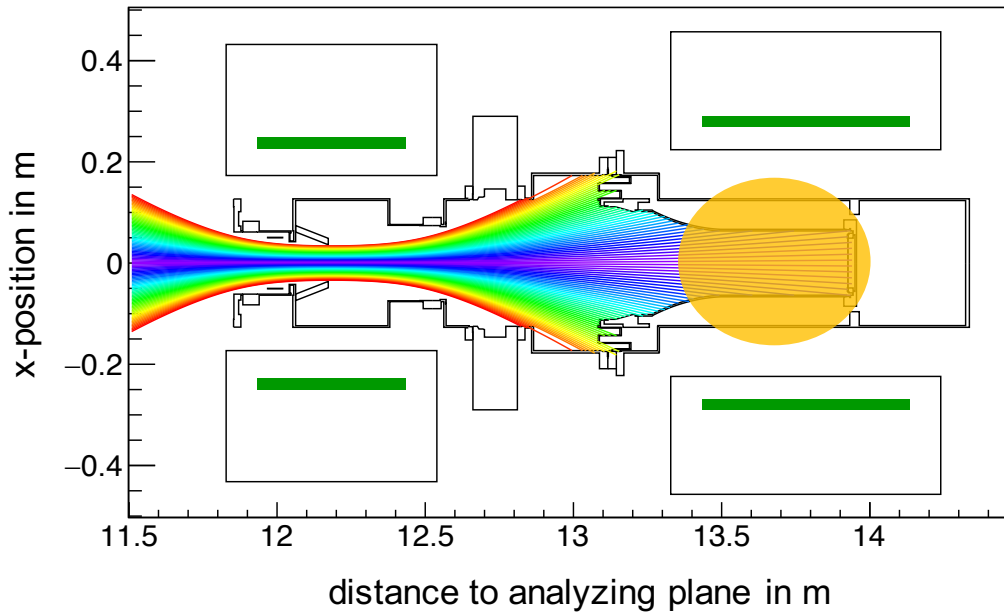


Figure C.2: If the detector magnet is turned off, the fluxtube widens (rainbow colored area). Only a small fraction of the signal electrons are observed by the detector wafer. The other field lines connect with the stainless steel wall of the detector chamber. Those electrons can cause photon emission. If the photons are generated in an area close to the detector (yellow area), they contribute to the detector background.

processes (mainly elastic scattering) the electrons have the probability P_{BS} to scatter back. [288] The backscattering probability as well as the shape of the backscattered spectrum depends on three different factors:

- **Material:** Rutherford's theory of scattering predicts that the total scattering cross section is proportional to the atomic number in first approximation $\sigma(Z) \propto Z^2$ [339]¹. The left graph in figure D.3 shows the backscattering probability as a function of Z . For boron ($Z = 5$) the backscattering probability is more than ten times smaller as for gold ($Z = 79$). This can be explained by the different penetration depths which lead to a reduced backscattering probability as well as a broader backscattering energy distribution (see figure D.4) [341].
- **Impact angle:** The impact angle is defined in a way that $\theta_{imp} = 0.0^\circ$ corresponds to a perpendicular impact. P_{BS} grows with the impact angle θ_{imp} of the incident electrons (figure D.3, middle graph). For electrons hitting the surface with angles close to 90° , the backscattering probability becomes almost 1.0. The shape of the spectrum varies in the height and width of the peak for different θ_{ini} (see figure D.4).
- **Incident energy:** The backscattering probability increases only slightly with the initial energy E_{ini} as can be seen on the right graph in figure D.3. For typical tritium β -decay energies the difference is in the order of a few percent. The peak height of the energy distribution scales with the incident energy, while the rest of the shape is only slightly affected as displayed in figure D.4.

¹Recent measurements correct it to $\sigma(Z) \propto Z^{1.47}$ [340].

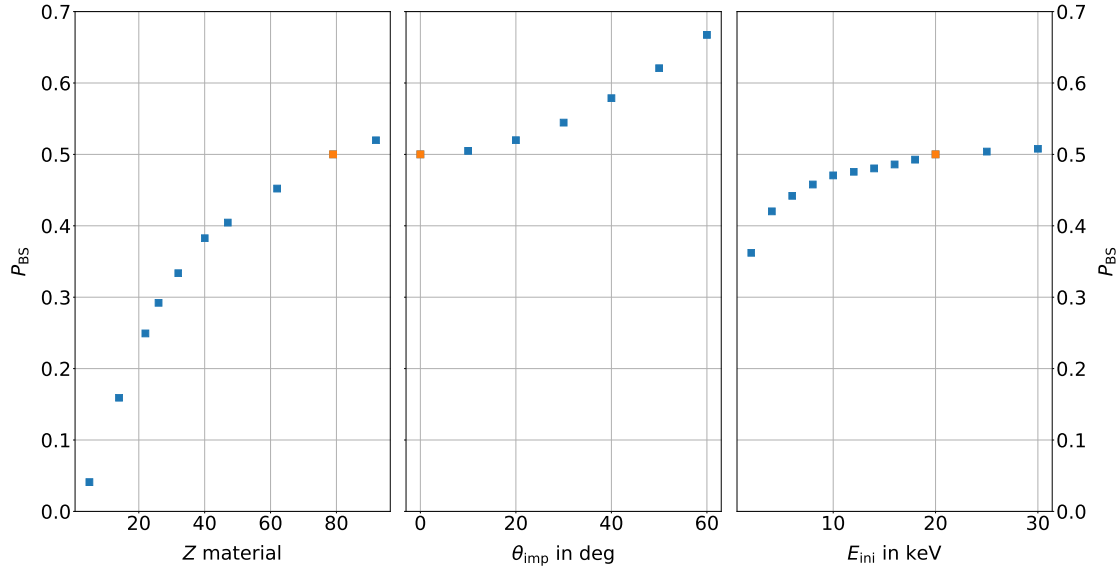


Figure D.3: Backscattering probabilities as a function of material, impact angle, and initial energy. **Left:** P_{BS} strongly depends on the material, and increases with the atomic number. **Middle:** The steeper the impact angle, the higher is the probability for electrons to scatter back at a solid surface. **Right:** On the keV-energy scale, P_{BS} scales only slightly with the energy of the incident electron. All three dependencies can be traced back to the penetration depth of the electron in the the solid. Large penetration depths lead to small backscattering coefficients. [341] The orange marker serves as a reference point which corresponds to the scattering of electrons that impact perpendicular on a gold surface with an initial energy of 20 keV.

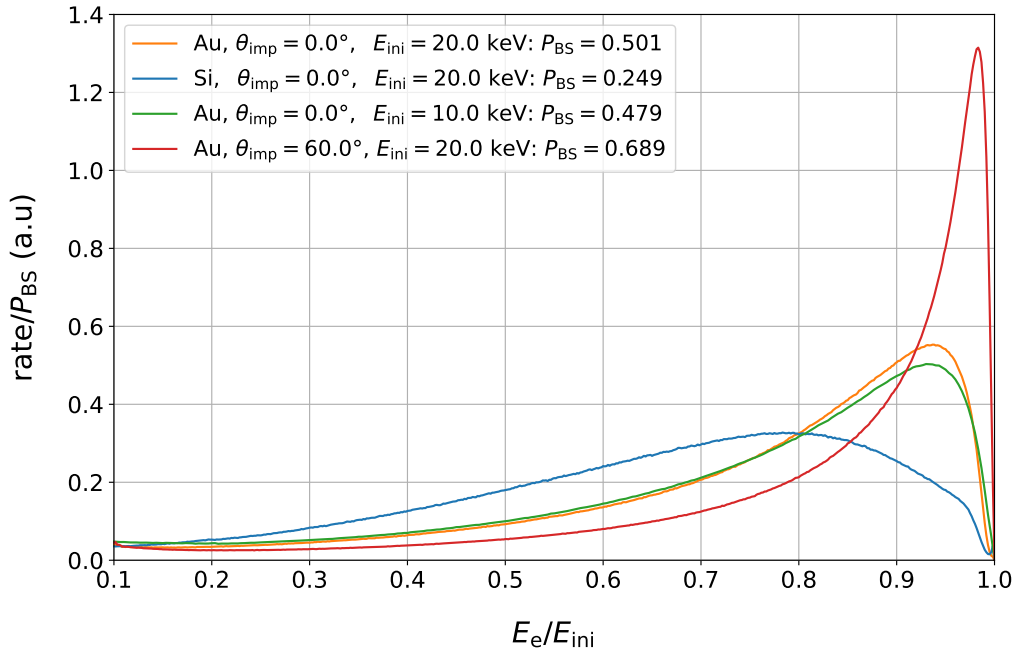


Figure D.4: All spectra are normalized to the backscattering probability and displayed as a function of the energy in units of E_{ini} . The energy distribution of the backscattered electrons varies in shape, especially for different materials and impact angles. A small atomic number as well as a large impact angle lead to a more distinct main peak close to the energy of the incident electrons. The influence on the incident electron energy is small.

E Validation of *GEANT4* Backscattering Simulations and Uncertainty Estimation

Electrons that scatter back at the rear wall, have a non-zero probability to reach the detector with a deviated energy distribution [10]. The effect is one of the leading systematic uncertainties, when the KATRIN experiment is used to search for keV-scale sterile neutrinos (see chapter 5). In order to determine the backscattering probability, as well as the energy and angular distribution of the backscattered electrons, *GEANT4* simulations on a single event basis are used.

The simulations have been compared to a selection of measurements, with the objective of verifying and determining an uncertainty on them. The first and the third study follows mainly the idea of [342], however, adapted to the specific energy range used to simulate the electron backscattering.

Backscattering Probability

In [343], the electron backscattering probability P_{BS} has been measured for 27 different elements using an electron microprobe analyzer. For the comparison of *GEANT4* simulations, 14 different P_{BS} have been selected, all measured at an initial electron energy of $E_{\text{ini}} = 20.2$ keV. Figure E.5 shows the results. The mean deviation between measurement and simulation is found to be 6.28 %. For the backscattering coefficient of gold, as required for the simulations of the rear wall backscattering, the deviation is with 3.26 % close to the 2 % uncertainty of the measured values as stated in [343].

Energy Distribution

In [344], the energy distribution of electrons backscattering on a thick silver surface with an initial energy of $E_{\text{ini}} = 30$ keV, is measured at a fixed scattering angle. Figure E.6 shows the comparison with a *GEANT4* simulation. Two different aspects become apparent when comparing the spectra: 1. the peak of the simulation is shifted to lower energies; 2. in the lower energy part of the spectrum at approximately $E_e = 2.5$ keV, the simulation shows another increase in rate that can not be confirmed by the measurement.

It can be assumed that the thickness of the specimen has an influence on the mean energy loss of backscattered electrons and could therefore cause a shift of the main peak. Unfortunately, the author of [344] does not specify the thickness of the silver specimen used for the measurement. No explanation on the deviation at low energies could be found.

The mean deviation weight with the count rate, was found to be 19.56 % for the full energy range, and 14.84 % if only energies > 5 keV are considered. This states the largest divergence of simulation and measurement that has been found in the scope of this study.

Angular Distribution

Figure E.7 shows the comparison of a simulated and a measured angular distribution of electrons backscattering on a thick gold foil as described in [345]. The electrons had an initial energy of $E_{\text{ini}} = 15.7$ MeV, which is approximately three orders of magnitude larger than the tritium β -decay energies.

The simulations have been performed for two different interaction models used in the *GEANT4* code. While the *emstandard-opt0* package is specialized to simulate interactions in the MeV-range, the *emlivermore* package is designed for keV energies. The latter has been used in the simulations of rear wall backscattering. Both simulations show excellent agreement with the measurement. For the simulation using the *emlivermore* package,

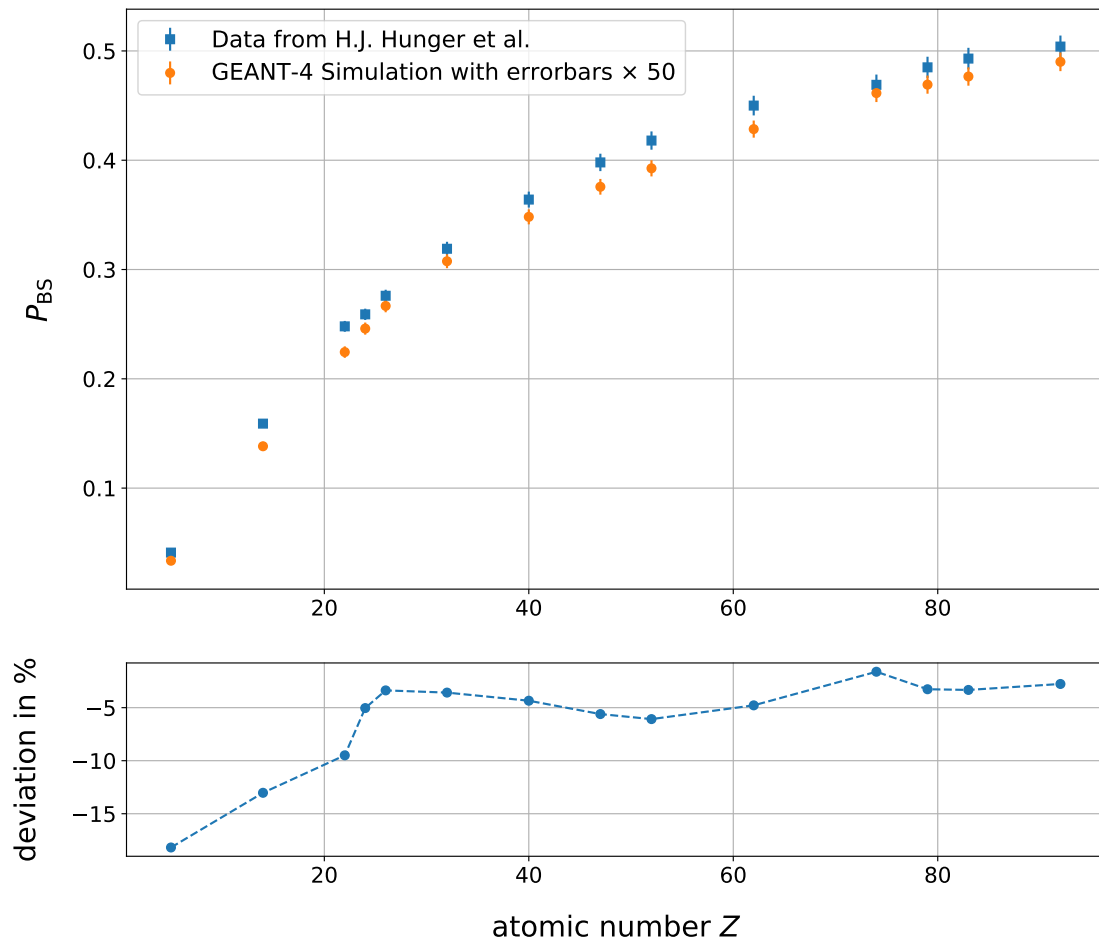


Figure E.5: The figure shows the comparison of measured and simulated backscattering probabilities P_{BS} as a function of the atomic number Z . On the full range, the simulation show good agreement with the measurement. The mean deviation was found to be 6.28%. The largest deviation appears for elements with a low Z . If the mean value is weighed with the backscattering probability, it reduces to 4.76%. The uncertainty on the measurement is indicated with 2% [343]. The error on the simulation is the statistical uncertainty.

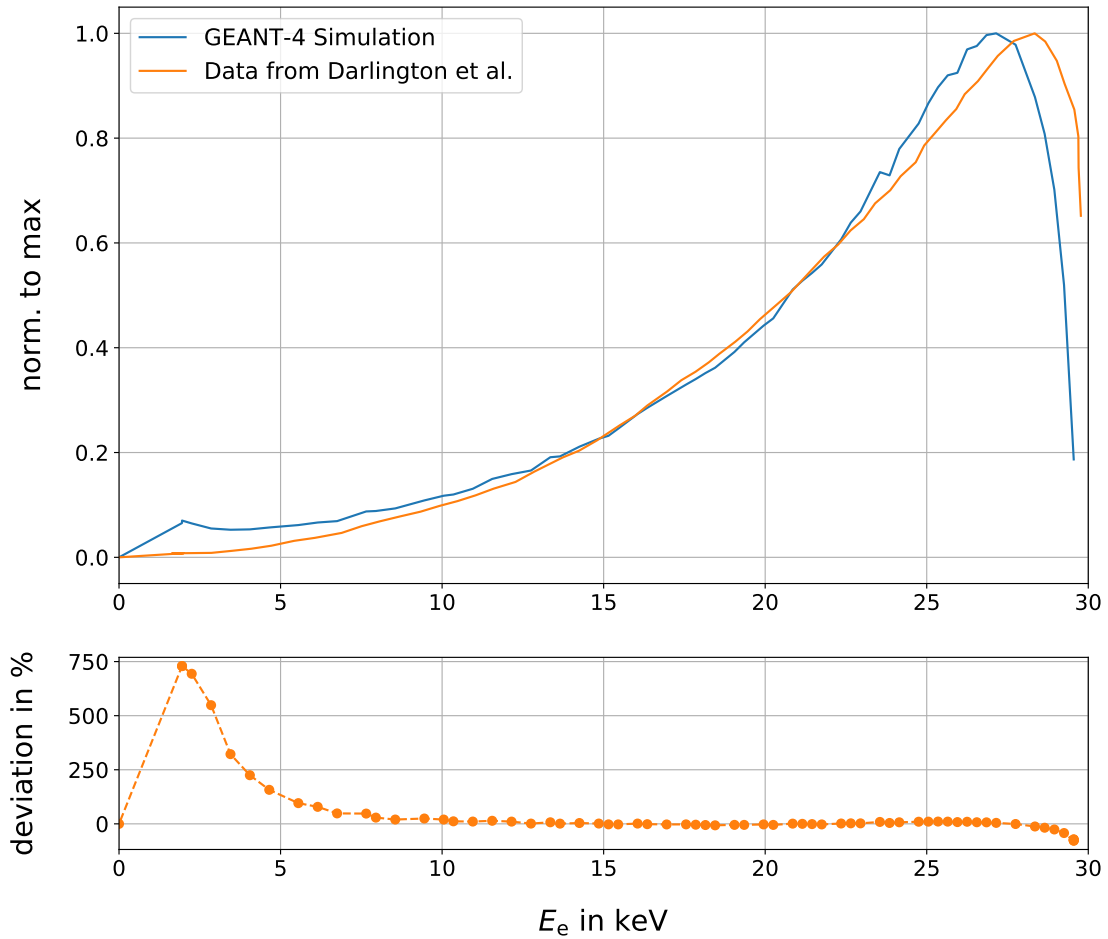


Figure E.6: The comparison of two backscattering spectra: one that has been measured in [344] using a mono energetic electron source (orange) and one the has been simulated with *GEANT4* (blue). The spectra show a deviation of the peak position and in the lower energy part. Apart from that, the shape of both spectra are in good agreement. The weighed average deviation of 19.56 % is the largest uncertainty found in the validation study.

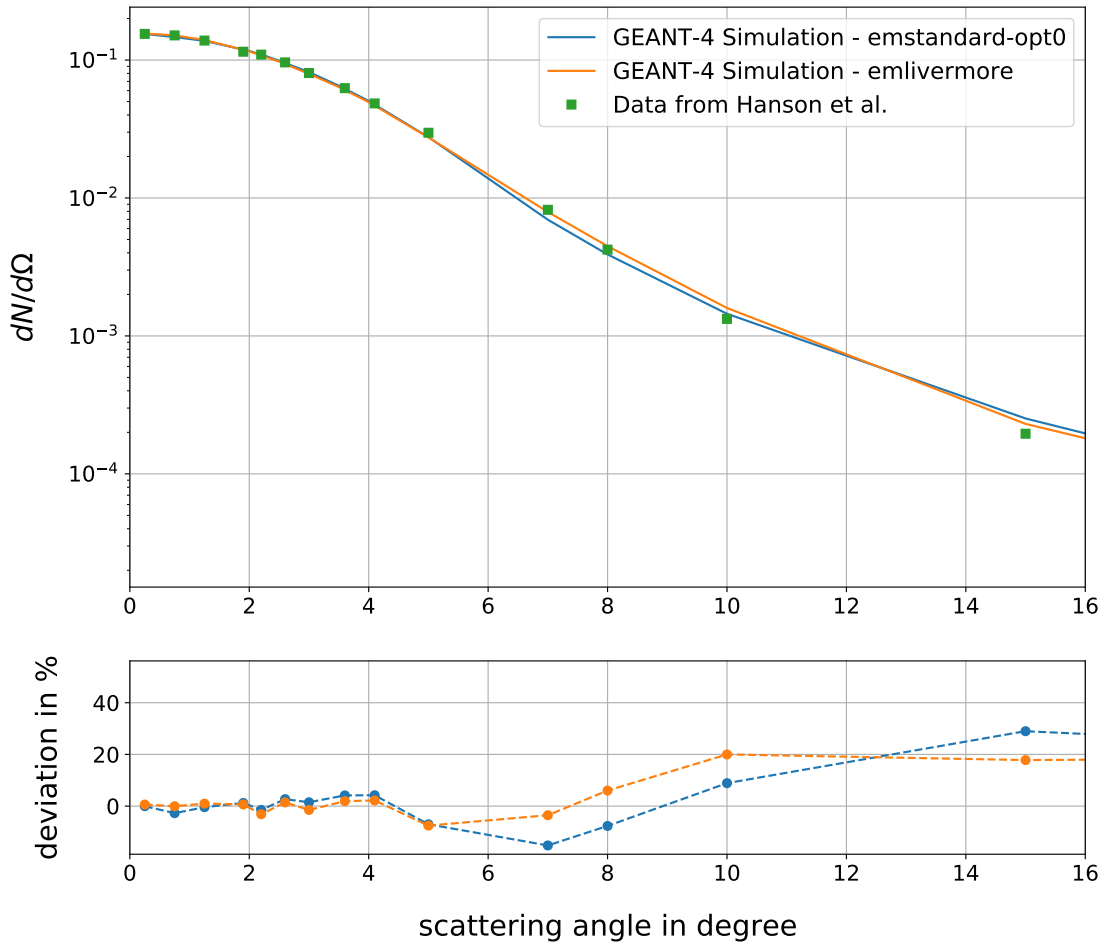


Figure E.7: The figure shows the comparison of a measured and simulated backscattering angular distribution. The simulations have been carried out for two *GEANT4* interaction models. Both simulations show excellent agreement with the measurement with a weighed mean deviation of only 1.43% (*livermore*) and 1.99% (*emstandard-opt0*).

the weighted average deviation is only 1.43%.

Since the low energy interaction package *emlivermore* shows such good agreement for high energies, it is assumed to show the same accuracy for interactions in the designed energy region.

F Simulation of Energy and Angular Distribution of escaped Electrons

Approximately 3% of all β -decay electrons in the WGTS are initially trapped in local magnetic field minima. The trapped electrons undergo elastic and inelastic scattering on hydrogen molecules inside the trap volume and leave the trap eventually with a distorted energy and angular distribution (section 5.4 [10]). In order to calculate the contribution of the escaped electrons to the measured spectrum, *KASPER* simulations are required. The simulations are based on [260], however, have been further developed to fit the requirements of this study.

This section gives an overview of the simulation settings and analysis for the study presented in section 5.4 as well as for the *First Tritium Campaign* analysis in chapter 6.

Electron and Angular Distribution of escaped Electrons

In order to determine the energy and angular distortion caused by multiple scatterings of electrons in magnetic traps, 10^5 mono-energetic electrons were simulated for each magnetic trap displayed in figure 5.11. Their initial energies had a discrete distribution with values between $[0.575, 18.575]$ keV in 1.0 keV steps. By choosing only initial angles larger than the trapping angle $\theta_{\text{ini}} > \theta_{\text{trap}}$, the electrons were all initially trapped.

During the simulation the electrons underwent elastic and inelastic scattering on hydrogen molecules. The gas density was chosen to be constant, determined by the average gas density of the corresponding traps². The simulations were terminated after all electrons left the trap due to the angular changes caused by the scattering.

Figures F.8 and F.9 show simulated energy loss ΔE and angular distributions of escaped electrons θ_{esc} . The distributions vary for the different E_{ini} , which can be explained by the energy dependency of the scattering cross sections (section 5.3).

In order to calculate the distorted spectra of escaped electrons $\Gamma_{\text{trap},i}$, a tritium β -spectrum is folded with the simulated ΔE distributions. The correlation of E_{ini} and the probability of an escaped electron to reach the detector without being magnetically reflected $P_{\theta_{\text{max}},i}$ is also taken into account, by multiplying each of the bins by the corresponding $P_{\theta_{\text{max}},i}$. A comparison of the β -spectrum of the initial electrons as well as the distorted spectrum of escaped electrons can be seen in figure F.10. In order to make the comparison easier, both spectra are normalized to their maximum. The energy distribution after the trap is strongly deviated. However, it is important to mention that the total number of electrons that are able to reach the FPD with a deviated spectrum is about three orders of magnitude smaller than the number of β -electrons with an unchanged spectral shape (section 5.4).

Magnetic Traps during the *First Tritium Campaign*

In order to determine the influence of magnetic trapping in the source during the *First Tritium Campaign*, the same procedure was applied. Due to the relative small energy window of $[16.975, 18.575]$ keV the ΔE and θ_{esc} distributions were assumed to be independent of E_{ini} , which could be shown in a high statistics *KASPER* simulation (with 10^5 initial events).

G Theoretical Correction Terms of the Tritium β -Spectrum

For all correction terms, natural units ($\hbar = c = 1$) are used. The nomenclature is based on [346], where the following quantities are defined:

- Total energy of the electron in units of m_e : $W = (E + m_e)/m_e$.
- Endpoint energy in units of m_e : $W_0 = (E - E_f + m_e)/m_e$.
with the excitation energies of the final-states E_f .
- Electron momentum in units of m_e : $p = \sqrt{W^2 - 1}$.
- Fine structure constant: $\alpha = 1/137$.
- Sommerfeld parameter: $\eta = \alpha ZW/p$.

²Due to their low density, the simulations of the outer traps require time consuming computation (in the order of days for a statistic of 10^4 initial events). In order to avoid this, the density for the outer traps were artificially increased by a factor of 25 (trap 2 and 5) and 250 (trap 1 and 6), which does not lead to a significant variation of the simulation results as shown in [260].

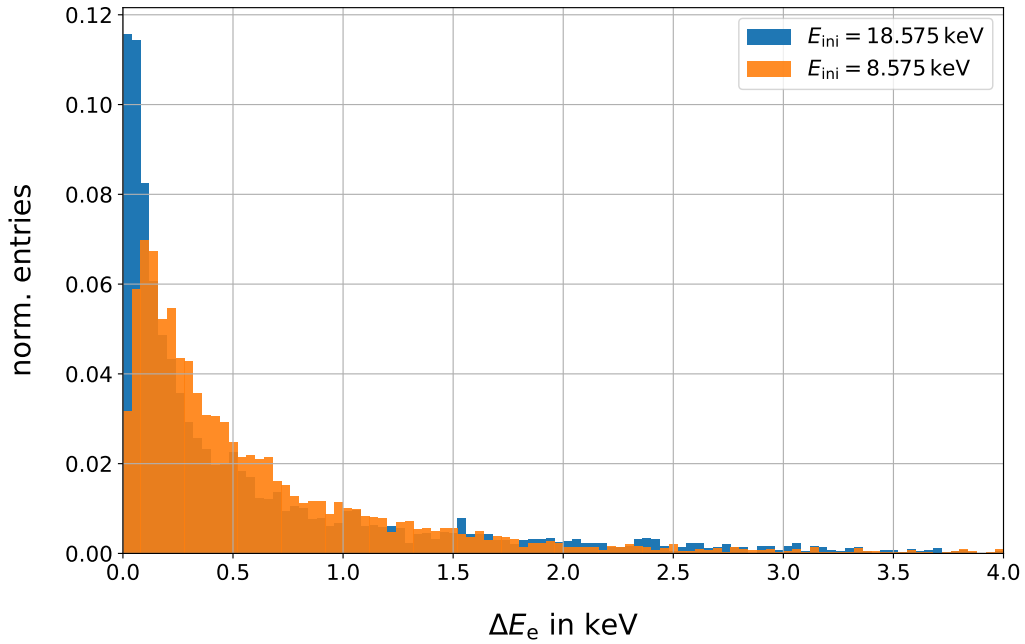


Figure F.8: The simulated energy loss of electrons that started either with a kinetic energy of $E_{\text{ini}} = 18.575$ keV (blue histogram) or $E_{\text{ini}} = 8.575$ keV (orange histogram). For lower electron energies, the tendency to multiple scatterings increases (see section in 5.3) which leads to a broader energy loss distribution. For the sake of clarity, only energy losses up to 4.0 keV are displayed here.

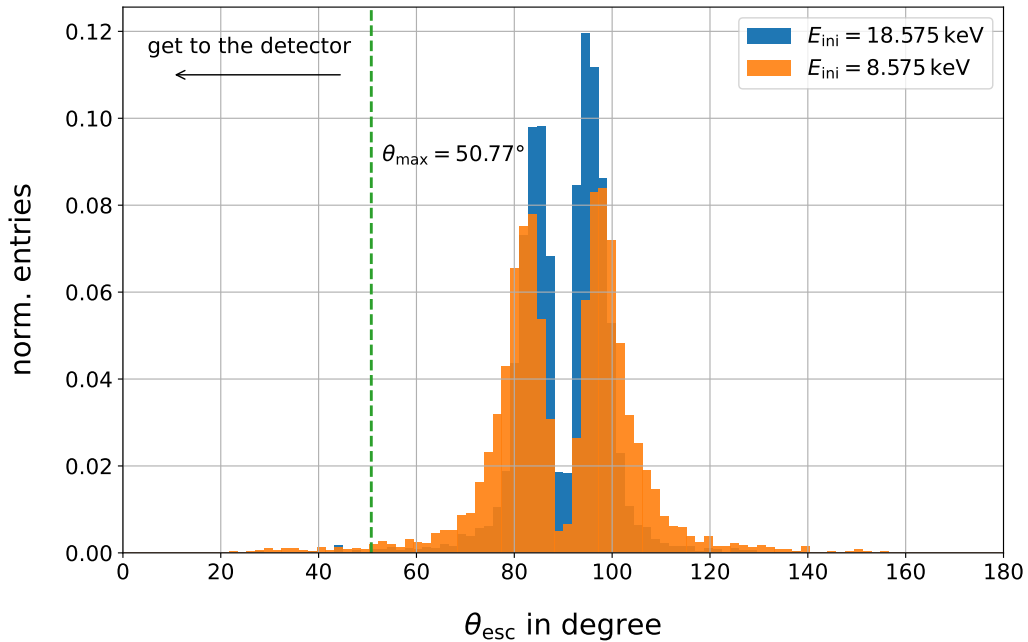


Figure F.9: The polar angle distribution of escaped electrons. The angular changes are mainly caused by elastic scattering. Analog to inelastic scattering, the elastic scattering cross section also increases for smaller energies, which translates to a broadening of the final polar angle distribution. The green line marks the maximum acceptance angle θ_{max} for the nominal magnetic field setting. All electrons that scatter back under an polar angle smaller than the maximum acceptance angle $\theta_{\text{esc}} < \theta_{\text{max}}$, are able to reach the detector if their energy allows to overcome the retarding potential. All other electrons are reflected in direction of the rear wall.

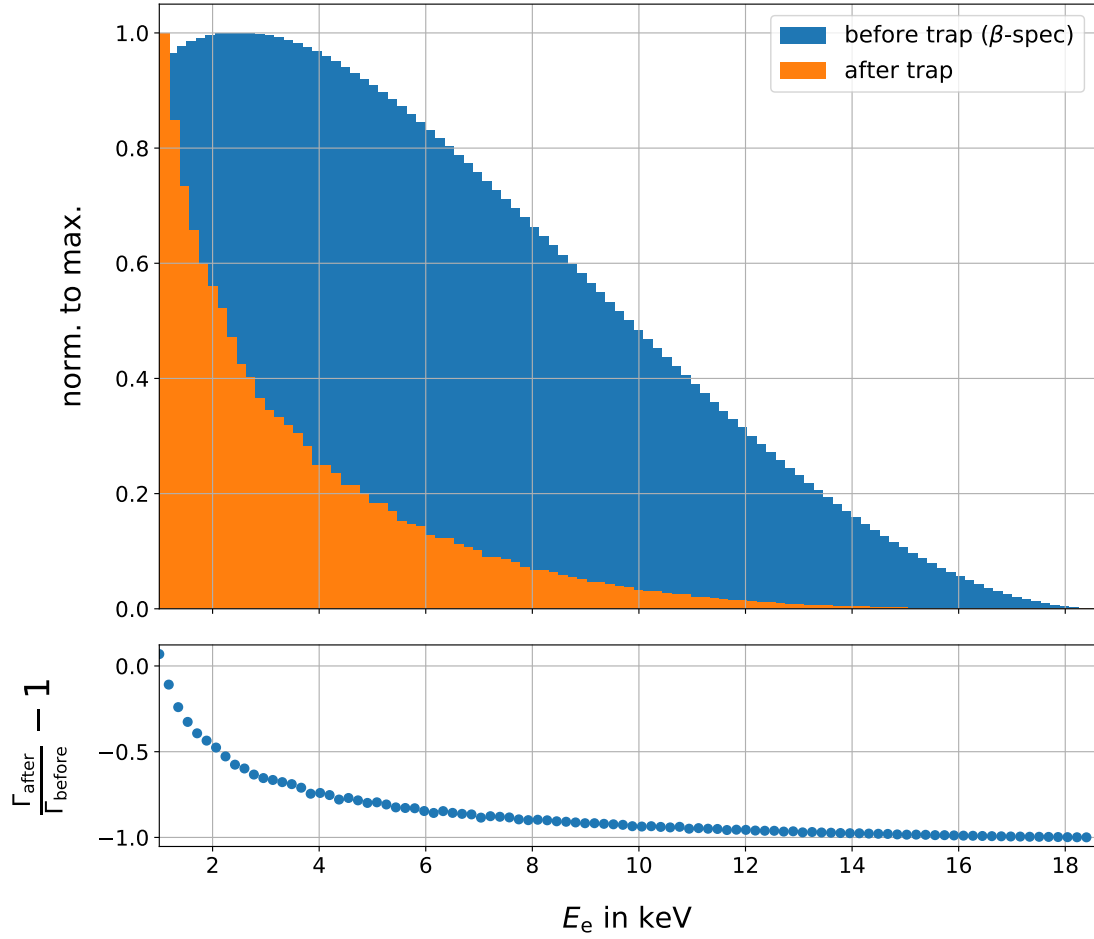


Figure F.10: The normalized spectrum of electrons that escaped the trap (orange histogram) and a β -decay distribution (blue histogram). By folding the β -decay spectrum with the simulated energy loss distributions, the distorted spectrum can be calculated. The spectral shapes strongly deviate, especially for energies close to the endpoint, where the scattering in the magnetic traps has the strongest influence due to the low rate.

- The relativistic Lorentz factor: $\gamma = \sqrt{1 - Z^2\alpha^2}$.
- Nuclear radius of ${}^3\text{He}$ in units of m_e given by the Elton formula [347]:
 $R_n = 2.8840 \cdot 10^{-3} \cdot m_e$.
- Mass of ${}^3\text{He}$ in units of m_e : $M = 5497.885 \cdot m_e$.
- Ratio between axial and vector coupling constants derived in [291]
 $\lambda_t = |g_A/g_V| = 1.265 \pm 0.004$.

Most of the following formulas are from the original references, however, cross-checked with [346] and [12].

Relativistic Fermi Function

The relativistic Fermi function can be found in [290]:

$$F_{\text{rel}}(W, Z) = 4(2pR_n)^{2(\gamma-1)} \cdot \frac{|\Gamma(\gamma + i\eta)|^2}{(\Gamma(2\gamma + 1))^2} \cdot e^{\pi\eta}, \quad (8.13)$$

where Γ is the complex gamma function.

Screening of the Daughter Nucleus Coulomb Field by the Orbital Electron

The correction term is taken from [299]:

$$S(Z, W) = \bar{W}/W \left(\frac{\bar{p}}{p}\right)^{2\gamma-1} \cdot e^{\pi(\bar{\eta}-\eta)} \frac{|\Gamma(\gamma + i\bar{\eta})|^2}{|\Gamma(\gamma + i\eta)|^2}, \quad (8.14)$$

with $\bar{W} = W - V_0/m_e$, $\bar{p} = \sqrt{\bar{W}^2 - 1}$ and $\bar{\eta} = \alpha Z \bar{W} / \bar{p}$.

The screening potential $V_0 = (76 \pm 10)$ eV is derived in [303].

Orbital Electron Exchange

The correction of the effect is derived in [300] and [290]. In [12] the parameterization was renewed and does not only include the transition of the 1s ground state as derived in [290] but also the first 10 excited states of the daughter nucleus ${}^3\text{He}^+$:

$$I(Z, W) = 1 + 2.462 \cdot a^2(\tau) + 0.905 \cdot a(\tau), \quad (8.15)$$

with

$$a(\tau) = \exp \left[2\tau \cdot \arctan \left(-\frac{2}{\tau} \right) \right] \cdot \left(\frac{\tau^2}{1 + \frac{1}{4}\tau^2} \right)^2, \quad (8.16)$$

and $\tau = -2\alpha/p$.

Recoil Effect, Weak Magnetism and V-A Interference

Due to the recoil of the nucleus, the two-body transforms into a three-body decay. Besides the final state distribution, the recoil effect needs to be considered in the calculation of the

coulomb field. It furthermore affects the weak magnetism of the system as well as causes $V - A$ interferences. All corresponding corrections have been derived in [348]:

$$R(W, W_0, M) = 1 + (A \cdot W - \frac{B}{W}) \cdot \frac{1}{C}, \quad (8.17)$$

with

$$A = 2 \frac{(5\lambda_t^2 + 2\lambda_t \cdot \mu + 1)}{M}, \quad (8.18)$$

$$B = 2\lambda_t \frac{(\lambda_t + \mu)}{M}, \quad (8.19)$$

$$C = 1 + 3\lambda_t^2 - B \cdot W_0. \quad (8.20)$$

The difference between the magnetic moment of tritium and helium is given by $\mu = 5.106588$ with a negligible error [12].

Recoil Coulomb Field

The correction factor is taken from [290]:

$$Q(Z, W, W_0) = 1 - \frac{\pi \cdot \alpha \cdot Z}{M \cdot p} \left(1 + \frac{1 - \lambda_t^2}{1 + 3\lambda_t^2} \frac{W_0 - W}{3W} \right). \quad (8.21)$$

Finite Extension of the Nucleus

The finite extension of the decaying nucleus is given by two correction terms: L_0 corrects the coulomb field within the non zero extension of the nucleus and C accounts for the evaluation of the wave functions of the participating leptons through the volume of the nucleus. All equations are taken from [290].

$$L_0(Z, W) = 1 + \frac{13}{60} (\alpha Z)^2 - W \cdot R_n \cdot \alpha \cdot Z \cdot \frac{41 - 26\gamma}{15 \cdot (2\gamma - 1)} \quad (8.22)$$

$$- \alpha \cdot Z \cdot R_n \cdot \gamma \cdot \frac{17 - 2\gamma}{30 \cdot W \cdot (2\gamma - 1)}, \quad (8.23)$$

with the finite size of the weak interaction:

$$C(Z, W) = 1 + C_0 + C_1 \cdot W + C_2 \cdot W^2, \quad (8.24)$$

$$C_0 = -\frac{233}{630} (\alpha \cdot Z)^2 - \frac{1}{5} (W_0 \cdot R_n)^2 + \frac{2}{35} (W_0 \cdot R_n \cdot \alpha \cdot Z), \quad (8.25)$$

$$C_1 = -\frac{21}{35} (R_n \cdot \alpha \cdot Z) + \frac{4}{9} (W_0 \cdot R_n^2), \quad (8.26)$$

$$C_2 = -\frac{4}{9} R_n^2. \quad (8.27)$$

Radiative Corrections

The correction terms are taken from [301].

$$\begin{aligned}
 G(W, W_0) = & (W_0 - W)^{\frac{2\alpha}{\pi} t(\beta)} \cdot \left\{ 1 + \frac{2\alpha}{\pi} \cdot \left[t(\beta) \cdot \left(\ln(2) - \frac{3}{2} + \frac{W_0 - W}{W} \right) \right. \right. \\
 & + \frac{1}{4} (t(\beta) + 1) \cdot \left(2(1 + \beta^2) + 2 \cdot \ln(1 - \beta) + \frac{(W_0 - W)^2}{6W^2} \right) \\
 & \left. \left. - 2 + \frac{1}{2}\beta - \frac{17}{36}\beta^2 + \frac{5}{6}\beta^3 \right] \right\},
 \end{aligned}$$

with

$$t(\beta) = \frac{1}{2\beta} \cdot \ln \left(\frac{1 + \beta}{1 - \beta} \right) - 1. \quad (8.28)$$

H Measurements at Troitsk Nu-Mass Experiment

The Troitsk nu-mass experiment is a MAC-E filter based tritium β -decay experiment that was build and commissioned from 1985 - 1994 [349]. After ten years of data taking, a limit on the neutrino mass of 2.05 eV at 95 % confidence level could be set [8]. In the following years the spectrometer was upgraded and is now used to search for keV-scale sterile neutrinos in a comparable approach as proposed in this thesis [240].

The similarity to the KATRIN experiment, makes the Troitsk nu-mass experiment most suitable to study new technology such as the TRISTAN detector [17]. The first TRISTAN prototype measurement campaign at the Troitsk nu-mass experiment took place in May 2017 (Troitsk-I), followed by two consecutive campaigns in November 2017 (Troitsk-II) and April 2018 (Troitsk-III). The objectives of the measurements were the characterization of the detector prototype, studies of systematic effects, and development of analyzing techniques at a real MAC-E filter tritium experiment [324, 325].

Beside that, the data taken during the second and third measurement campaign was used for a sterile neutrino analysis [324, 325, 326]. For the first time, a differential tritium spectrum was successfully used to search for keV-scale sterile neutrinos [326].

For the analysis of the data, detailed Monte Carlo simulations were required. For this purpose the geometries of the Troitsk nu-mass experiment were implemented in the *KASPER* simulation framework and made available for both, the KATRIN as well as the Troitsk collaboration.

This section gives a short overview on the experimental setup and its implementation to *KASPER* followed by a transmission study used for the Troitsk-I analysis is presented.

The Setup of the Troitsk Nu-Mass Experiment

An overview of the current Troitsk nu-mass setup is illustrated in figure H.11. The experiment is segmented in a source, transport, spectrometer, and detector section. The working principle is the same as that of the KATRIN experiment. Tritium is pumped into the source section where it decays. The energy determination of the signal electrons takes place in the spectrometer that is operated as a MAC-E filter setup with an energy resolution of up to 3 eV. The signal electrons that are able to overcome the retarding potential are counted with a single-pixel (Si)Li pin-diode with a diameter of 17 mm. [8]

The Troitsk nu-mass experiment disposes of a total number of 39 magnets organized in several units. The geometries of the magnets and electrodes, as well as generous support

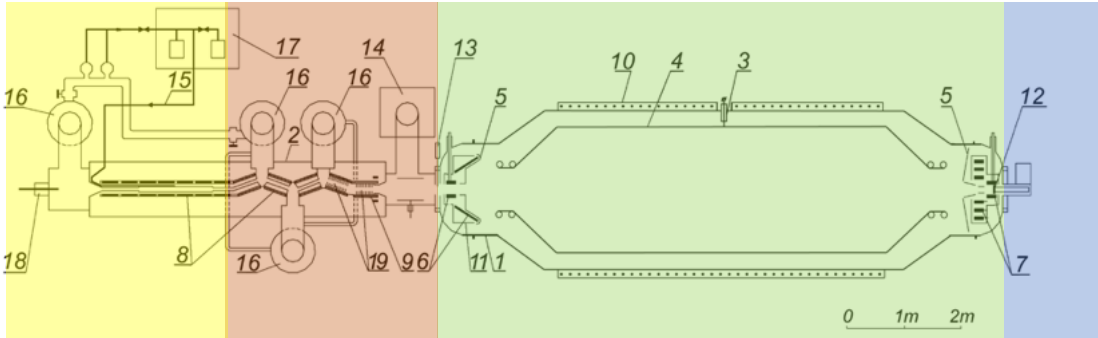


Figure H.11: The Troitsk nu-mass experiment is segmented in four sections: the source section including the windowless gaseous tritium source and an electron gun for calibration (yellow), the transport and pumping section (red), the spectrometer (green), and the detector (blue). The displayed components are: 1) spectrometer tank, 2) source tube, 3) high voltage feed-through, 4) spectrometer high voltage electrode, 5) ground electrode, 6) pinch magnet, 7) detector magnet, 8) and 9) source and transport magnets, 10) spectrometer warm coil, 11) liquid nitrogen jacket of pinch magnet, 12) detector and detector cooling system, 13) shutter gate valve, 14) titanium sublimation pump, 15) tritium loop system, 16) mercury diffusion pump, 17) tritium storage and purification system, 18) electron gun, and 19) cryo argon pump. The figure is adapted from [240, 325].

during the implementation process, were provided by Aino Skasyrskaya³ of the Troitsk collaboration.

The magnetic field as simulated with *KASPER* can be found in H.12. A major difference to the KATRIN setup is that the highest magnetic field (pinch magnet) is placed on the down stream side of the spectrometer. This reduces the spectrometer background caused by electron scattering on residual gas. In order to avoid backscattering at the rear wall, the rear and transport section magnetic field is stronger than the source magnetic field. However, the generated magnetic trap states one of the largest uncertainties of the Troitsk nu-mass experiment. [349]

Transmission Studies for the Troitsk-I Campaign

The TRISTAN detector prototype used during the Troitsk-I measurement campaign consisted of seven hexagonal pixels each with a diameter of 1 mm. The left side of figure H.13 shows a picture of the detector array. The central pixel had a positional offset of 1.8 mm from the spectrometer axis, which was considered in the transmission studies, as well as the individual radial positions of the pixels. All detector pixels observe full transmission for surplus energies up to $E_{\text{sur}} = 8 \text{ keV}$ as can be seen on the right side of figure H.13. Pixel 1, which was the closest to the symmetry axis, shows even a full transmission for all surplus energies. Based on the simulation results, the measurement settings of the Troitsk-II and -III campaigns were chosen. The measurement results did not show any energy dependent rate losses which supports the simulations.

Further use of *KASPER* Simulations of the Troitsk Nu-Mass Experiment

The implementation of the Troitsk nu-mass experiment geometries to the *KASPER* simulation framework has already been required for several tasks:

³Institute for Nuclear Research of Russian Academy of Science, Moscow, Russia

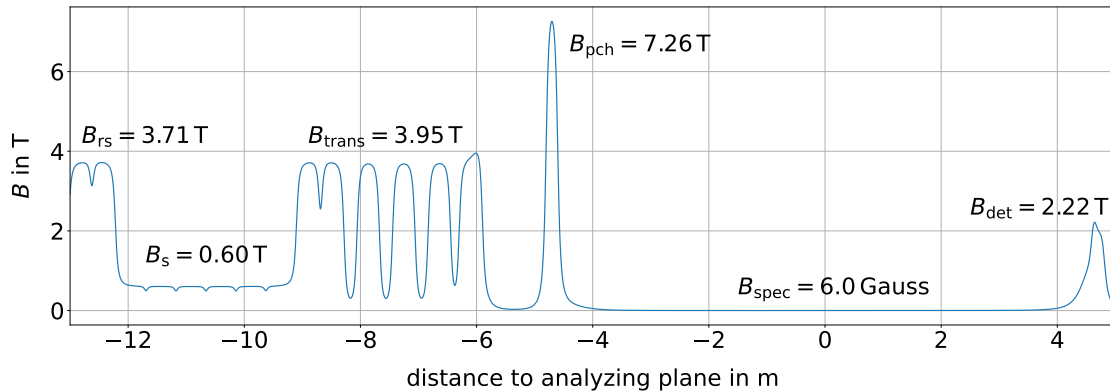


Figure H.12: The magnetic field of the Troitsk nu-mass experiment simulated with *KASPER*. A large magnetic field difference between source and rear section traps most of the electrons in the source. Hence, the electrons do not interact with the rear wall, where they would scatter and distort the spectrum. However, a systematic effect occurs due to the trapping which states one of the largest uncertainties of the Troitsk nu-mass experiment [349]. Other than in the KATRIN setup, the pinch magnet is located in front of the spectrometer.

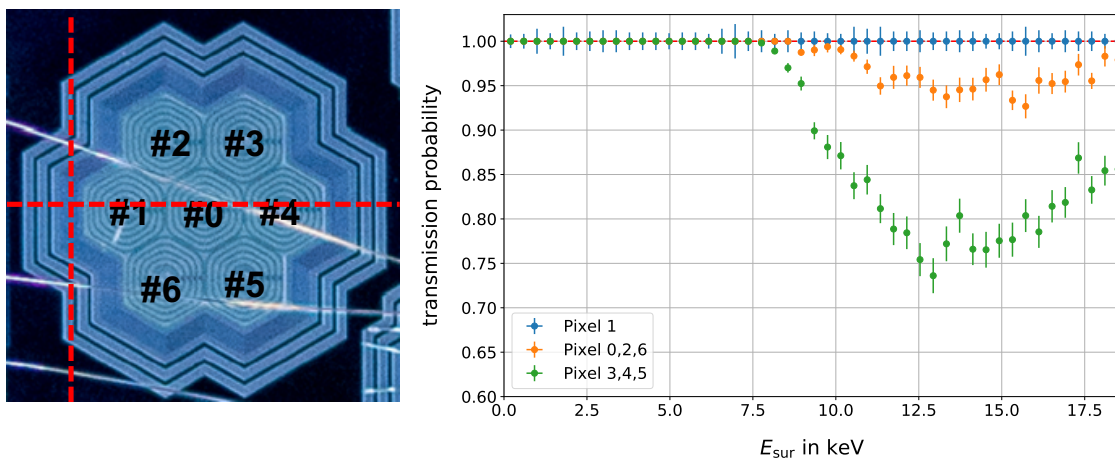


Figure H.13: The detector array had an offset of 1.8 mm to the spectrometer symmetry axis (shown as red dashed line in the left figure). The transmission of the detector shows a fully-adiabatic transport for surplus energies up to 8 keV. Since the transmission probability depends on the distance to the symmetry axis, the transmission loss starts at smaller energies for the outer than for the inner rings.

- Planning of the program of all three Troitsk campaigns, as well as support during the measurements.
- Analysis of the results of Troitsk-I, II and III. Especially the reconstruction of the detector responses showed excellent agreement of the simulations and the calibration measurements [325].
- The *KASPER* simulations of the Troitsk experiment played an essential role in the sterile neutrino analysis of Troitsk-II and III data [324, 326].
- For the Troitsk nu-mas keV-scale sterile neutrino program, under threshold events have been simulated with *KASPER* and improved the so far used approximation which is another leading uncertainty of the experiment [240, 349].

List of Figures

1.1	The Standard Model of Particle Physics	4
1.2	Solar neutrino spectrum	6
1.3	Results from the Daya Bay experiment	9
1.4	Generation of neutrino mass via Yukawa coupling to Higgs	12
1.5	Massparabel and coherent sum of the neutrino masseigenstates	15
1.6	Feynman graphs of single and double β -decays	16
1.7	Spectra of single and double β -decays	18
2.1	Overview of the KATRIN experimental setup	22
2.2	KATRIN tritium loop	23
3.1	Standard Model extended by three right-handed sterile neutrinos	31
3.2	Cosmological limits on the sterile neutrino parameter space	36
3.3	Laboratory limits on the sterile neutrino parameter space	38
3.4	Tritium β -decay spectrum distorted by a fourth sterile mass eigenstate	40
4.1	Schematic representation of signal pile-up	43
4.2	Inlet pressure over time	46
4.3	Lowest retarding potential for different ϵ_T and ρd	46
4.4	Rate reduction due to reduced detector and and source magnetic field	48
4.5	Rate reduction due to reduced column density and source magnetic field	50
4.6	Transmission of the KATRIN main spectrometer as a function of the surplus energy	54
4.7	Transmission probability as a function of the surplus energy for different entrance radii and polar angles	54
4.8	Size of the fluxtube in the main spectrometer	55
4.9	Transmission probability as a function of the surplus energy for different air coil currents	55
4.10	Transmission depending on the surplus energy for different detector magnetic fields	56
4.11	Fiducial areas of the detector for different retarding potentials	58
4.12	Statistical sensitivity adiabatic setting	61
4.13	Statistical sensitivity nominal field setting	63
4.14	Statistical sensitivity intermediate setting	64
4.15	Comparison of selected statistical sensitivities compared to current laboratory limits	66
5.1	Relative influence of rear wall backscattering	72
5.2	Reducing the source and rear wall magnetic field as a countermeasure	73
5.3	Rear wall chamber and field lines for different magnetic field settings	74
5.4	Relative influence of rear wall backscattering with the rear section magnet off	75
5.5	Sensitivity rear wall backscattering	77
5.6	Energy loss function	80

5.7	The response function of KATRIN	81
5.8	Energy dependent inelastic cross section	82
5.9	Relative influence of source scattering	84
5.10	Sensitivity for electron scattering	86
5.11	Overview of the magnetic field in the source	88
5.12	Trapping angle and probability as function of the z-position	89
5.13	Density distribution in the source	89
5.14	Relative influence of magnetic trapping in the source	92
5.15	Contribution of secondaries to the signal	94
5.16	Sensitivity magnetic trapping in the source	95
5.17	Relative influence of source fluctuations	97
5.18	Sensitivity source fluctuations	98
5.19	Points of back reflection of backscattered electrons	100
5.20	Relative influence of backscattering lost electrons	101
5.21	Sensitivity of backscattering electron loss	103
5.22	Relative influence of pile-up loss	105
5.23	Sensitivity pile-up induced electron loss	107
5.24	Final state distribution of a HeT ⁺ ion	108
5.25	A simplified energy dependent fsd model	110
5.26	Relative influence of a final state distribution	111
5.27	Sensitivity energy dependent final state distribution	112
5.28	Relative influence of theoretical corrections	114
5.29	Sensitivity theoretical corrections	115
5.30	Parameterization of the retarding potential depending background	117
5.31	Energy loss due to synchrotron radiation and Doppler broadening	118
6.1	Measurement time distribution First Tritium Campaign	125
6.2	Correction terms applied in the analysis	127
6.3	Combined spectrum with fit and residuals	128
6.4	Absolute statistical and systematic uncertainties	133
6.5	Stacked spectrum with null hypothesis fit and residuals including all systematic uncertainties	134
6.6	Monte Carlo sensitivity study of the different systematic effects	135
6.7	Exclusion of sterile neutrino parameter space based on the measured data	135
7.1	Tristan general design	140
7.2	The upgraded LFCS system	141
7.3	Transmission as function of the surplus energy for the upgraded LFCS system	142
7.4	Fiducial area for the upgraded LFCS system	143
7.5	Rear wall chamber and field lines for different magnetic field settings including a beryllium rear wall	144
7.6	Relative influence of electron backscattering on a beryllium rear wall	145
7.7	Response matrix rear wall backscattering	147
7.8	Sensitivity 40-day sterile campaign	151
B.1	Distance of two particles in a (non-)adiabatic scenario	160
C.2	Widened fluxtube at the FPD	163
D.3	Backscattering probabilities as a function of material, energy and angle	164
D.4	Energy distributions of backscattered electrons	164
E.5	Validation of GEANT4: backscattering probability	166
E.6	Validation of GEANT4: energy distribution	167
E.7	Validation of GEANT4: angular distribution	168
F.8	Energy loss due to scattering in a magnetic trap	170

F.9 Polar angle distribution of escaped electrons	170
F.10 Spectrum before and after trap no.3	171
H.11 Overview of the Troitsk nu-mass experiment	175
H.12 Magnetic field of Troitsk nu-mass	176
H.13 Position of the detector and corresponding transmission	176

List of Tables

1.1	Neutrino oscillation parameter	9
1.2	Parameter of the Λ CDM-Model	14
4.1	Parameter adiabatic setting	61
4.2	Parameter nominal field setting	63
4.3	Parameter intermediate setting	64
5.1	Time development of the traps	91
5.2	Overview of all studied systematic effects	121
6.1	Systematic budget of the First Tritium Campaign	132
7.1	KATRIN settings for the 40-day sterile campaign	149
A.1	Different LFCS settings	159

Bibliography

- [1] W. Pauli, “Offener Brief an die Gruppe der Radioaktiven bei der Gauvereins-Tagung zu Tübingen,” 1930. [Online]. Available: http://www.symmetrymagazine.org/sites/default/files/legacy/pdfs/200703/logbook_letter.pdf
- [2] C. Cowan et al., “Detection of the free neutrino: A Confirmation,” *Science*, vol. 124, pp. 103–104, 1956. [Online]. Available: <http://dx.doi.org/10.1126/science.124.3212.103>
- [3] G. Danby et al., “Observation of High-Energy Neutrino Reactions and the Existence of Two Kinds of Neutrinos,” *Phys. Rev. Lett.*, vol. 9, no. 1, pp. 36 – 44, 1962. [Online]. Available: <http://dx.doi.org/10.1103/PhysRevLett.9.36>
- [4] DONUT Collaboration, “Observation of Tau Neutrino Interactions,” *Phys. Lett. B*, vol. 504, no. 3, pp. 218 – 224, 2001. [Online]. Available: [http://dx.doi.org/10.1016/S0370-2693\(01\)00307-0](http://dx.doi.org/10.1016/S0370-2693(01)00307-0)
- [5] J. Boger et al., “The Sudbury neutrino observatory,” *Nucl. Instrum. Meth. A*, vol. 449, pp. 172–207, 2000. [Online]. Available: [http://dx.doi.org/10.1016/S0168-9002\(99\)01469-2](http://dx.doi.org/10.1016/S0168-9002(99)01469-2)
- [6] K. Zuber, *Neutrino Physics, Second Edition*, T. . Francis, Ed. Series in High Energy Physics, Cosmology and Gravitation, 2011.
- [7] C. Kraus et al., “Final results from phase ii of the mainz neutrino mass search in tritium β decay,” *The European Phys. Journal C*, vol. 40, no. 4, p. 447â468, Apr 2005. [Online]. Available: <http://dx.doi.org/10.1140/epjc/s2005-02139-7>
- [8] V. Aseev et al., “Upper limit on the electron antineutrino mass from the troitsk experiment,” *Phys. Rev. D*, vol. 84, p. 112003, Dec 2011. [Online]. Available: <https://link.aps.org/doi/10.1103/PhysRevD.84.112003>
- [9] M. Aker et al., “Improved upper limit on the neutrino mass from a direct kinematic method by katrin,” *Phys. Rev. Lett.*, vol. 123, no. 22, p. Article: 221802, 2019. [Online]. Available: <http://dx.doi.org/10.1103/PhysRevLett.123.221802>
- [10] J. Angrik et al., “KATRIN design report 2004,” 2005.
- [11] S. Grohmann et al., “Precise temperature measurement at 30-K in the KATRIN source cryostat,” *Cryogenics*, vol. 51, pp. 438–445, 2011. [Online]. Available: <http://dx.doi.org/10.1016/j.cryogenics.2011.05.001>
- [12] S. Mertens et al., “Sensitivity of next-generation tritium beta-decay experiments for keV-scale sterile neutrinos,” *Journal of Cosmology and Astroparticle Physics*, vol. 2015, no. 02, pp. 020–020, feb 2015. [Online]. Available: <https://doi.org/10.1088%2F1475-7516%2F2015%2F02%2F020>
- [13] M. Drewes et al., “A White Paper on keV Sterile Neutrino Dark Matter,” *JCAP*, vol. 01, p. 025, 2017. [Online]. Available: <http://dx.doi.org/10.1088/1475-7516/2017/01/025>

- [14] T. Asaka et al., “The ν msm, dark matter and neutrino masses,” *Phys. Lett. B*, vol. 631, no. 4, pp. 151 – 156, 2005. [Online]. Available: <http://www.sciencedirect.com/science/article/pii/S0370269305013675>
- [15] T. Lasserre et al., “Reactor antineutrino anomaly,” *Phys. Rev. D*, vol. 83, p. 073006, Apr 2011. [Online]. Available: <https://link.aps.org/doi/10.1103/PhysRevD.83.073006>
- [16] A. Huber, “Search for keV-scale sterile neutrinos with KATRIN,” Master’s thesis, Karlsruhe Institut of Technology, 2015.
- [17] S. Mertens et al., “A novel detector system for KATRIN to search for keV-scale sterile neutrinos,” *Journal of Physics G: Nuclear and Particle Physics*, vol. 46, no. 6, p. 065203, may 2019. [Online]. Available: <https://doi.org/10.1088%2F1361-6471%2Fab12fe>
- [18] S-I Tomonaga, J. Schwinger and R. Feynman, “Joint nobel prize of physics 1965 - for their fundamental work in quantum electrodynamics, with deep-ploughing consequences for the physics of elementary particles.” 1965. [Online]. Available: <https://www.nobelprize.org/prizes/physics/1965/summary/>
- [19] S. L. Glashow, A. Salam and S. Weinberg, “Joint nobel prize of physics 1979 - for their contributions to the theory of the unified weak and electromagnetic interaction between elementary particles, including, inter alia, the prediction of the weak neutral current.” 1979. [Online]. Available: <https://www.nobelprize.org/prizes/physics/1979/summary/>
- [20] J. Cronin and V. Logsdon, “Joint nobel prize of physics 1980 - for the discovery of violations of fundamental symmetry principles in the decay of neutral k-mesons.” 1980. [Online]. Available: <https://www.nobelprize.org/prizes/physics/1980/summary/>
- [21] T. Kajita and A. MacDonald, “Joint nobel prize of physics 2015 - for the discovery of neutrino oscillations, which shows that neutrinos have mass.” 2015. [Online]. Available: <https://www.nobelprize.org/prizes/physics/1979/summary/>
- [22] Y. Fukuda et al., “Evidence for oscillation of atmospheric neutrinos,” *Phys. Rev. Lett.*, vol. 81, pp. 1562–1567, Aug 1998. [Online]. Available: <https://link.aps.org/doi/10.1103/PhysRevLett.81.1562>
- [23] M. Gonzalez-Garcia et al., “Phenomenology with Massive Neutrinos,” *Phys. Rept.*, vol. 460, pp. 1–129, 2008. [Online]. Available: <http://dx.doi.org/10.1016/j.physrep.2007.12.004>
- [24] H. Becquerel, “Sur les radiations emises par Phosphorescence,” *Comptes Rendus de l’Academie des sciences: Vol.122*, 1896.
- [25] E. Rutherford, “Uranium Radiation and the Electrical conduction Produced by it,” *Philosophical Magazine and Journal of Science, series 5*, pp. 109 - 163, 1898.
- [26] F. Soddy, “The interpretation of radium,” *John Murray (publisher)*, 1909.
- [27] L. Meitner et al., “Über die Beta-Strahlen des aktiven Niederschlags des Thorium,” *Phys. Z. 12*, pp. 273, 1911.
- [28] J. Chadwick, “Intensitätsverteilung im magnetischen Spektrum der β -Strahlen von Radium B + C,” *Verhandl. Dtsch. phys. Ges.*, vol. 16, p. 383, 1914.
- [29] E. Fermi, “Versuch einer theorie der β -strahlen,” *Zeitschrift für Physik*, vol. 88, no. 3, pp. 161–177, Mar 1934. [Online]. Available: <https://doi.org/10.1007/BF01351864>

-
- [30] M. Perl and F. Reines, “Joint nobel prize of physics 1995 - for pioneering experimental contributions to lepton physics.” 1995. [Online]. Available: <https://www.nobelprize.org/prizes/physics/1995/summary/>
- [31] M. L. Perl et al., “Evidence for anomalous lepton production in $e^+ - e^-$ annihilation,” *Phys. Rev. Lett.*, vol. 35, pp. 1489–1492, Dec 1975. [Online]. Available: <https://link.aps.org/doi/10.1103/PhysRevLett.35.1489>
- [32] D. Decamp et al., “Determination of the Number of Light Neutrino Species,” *Phys. Lett. B*, vol. 231, pp. 519–529, 1989. [Online]. Available: [http://dx.doi.org/10.1016/0370-2693\(89\)90704-1](http://dx.doi.org/10.1016/0370-2693(89)90704-1)
- [33] Planck Collaboration, “Planck 2018 results. VI. Cosmological parameters,” *Astr. and Astrophys.*, 2018.
- [34] O. Philipsen, *Quantenfeldtheorie und das Standardmodell der Teilchenphysik: Eine Einführung*. Springer Spektrum, Berlin, Heidelberg, 2018.
- [35] E. S. Abers et al., “Gauge theories,” *Physics Reports*, vol. 9, no. 1, pp. 1 – 2, 1973. [Online]. Available: <http://www.sciencedirect.com/science/article/pii/0370157373900276>
- [36] E. Noether, “Invarianten beliebiger Differentialausdrücke,” *Nachr. Ges. Wiss. Göttingen, Math.-Phys. Kl.*, pp. 37–44, 1918.
- [37] H. Fritzsch et al., “Advantages of the color octet gluon picture,” *Phys. Lett. B*, vol. 47, no. 4, pp. 365 – 368, 1973. [Online]. Available: <http://www.sciencedirect.com/science/article/pii/0370269373906254>
- [38] C. N. Yang et al., “Conservation of Isotopic Spin and Isotopic Gauge Invariance,” *Phys. Rev.*, vol. 96, no. 1, pp. 191–195, Oct. 1954. [Online]. Available: <http://dx.doi.org/10.1103/PhysRev.96.191>
- [39] R. P. Feynman, “Mathematical formulation of the quantum theory of electromagnetic interaction,” *Phys. Rev.*, vol. 80, pp. 440–457, Nov 1950. [Online]. Available: <https://link.aps.org/doi/10.1103/PhysRev.80.440>
- [40] S. L. Glashow, “Partial Symmetries of Weak Interactions,” *Nucl. Phys.*, vol. 22, pp. 579–588, 1961. [Online]. Available: [http://dx.doi.org/10.1016/0029-5582\(61\)90469-2](http://dx.doi.org/10.1016/0029-5582(61)90469-2)
- [41] S. Weinberg, “A Model of Leptons,” *Phys. Rev. Lett.*, vol. 19, pp. 1264–1266, 1967. [Online]. Available: <http://dx.doi.org/10.1103/PhysRevLett.19.1264>
- [42] A. Salam, “Weak and Electromagnetic Interactions,” *Conf. Proc.*, vol. C680519, pp. 367 – 377, 1968.
- [43] G. Aad et al., “Observation of a new particle in the search for the standard model higgs boson with the atlas detector at the lhc,” *Phys. Lett. B*, vol. 716, no. 1, pp. 1–29, 2012. [Online]. Available: <http://dx.doi.org/10.1016/j.physletb.2012.08.020>
- [44] S. Chatrchyan et al., “Observation of a new boson at a mass of 125 GeV with the cms experiment at the lhc,” *Phys. Lett. B*, vol. 716, no. 1, pp. 30–61, Sep 2012. [Online]. Available: <http://dx.doi.org/10.1016/j.physletb.2012.08.021>
- [45] t. . A.O Sushkov et al.
- [46] L. Bergström and A. Goobar, *Cosmology and Particle Astrophysics*. Springer Verlag, 2003.
- [47] L. Köllenberger, “Model Building and Search for keV-Scale Sterile Neutrino with the KATRIN-Experiment,” Master’s thesis, Karlsruhe Institute of Technology, 2019.

- [48] M. Tanabashi et al., “Rev. of Particle Physics,” *Phys. Rev.*, vol. D98, no. 3, p. 030001, 2018. [Online]. Available: <http://dx.doi.org/10.1103/PhysRevD.98.030001>
- [49] J. Goldstone, “Field Theories with Superconductor Solutions,” *Nuovo Cim.*, vol. 19, pp. 154–164, 1961. [Online]. Available: <http://dx.doi.org/10.1007/BF02812722>
- [50] P. W. Higgs, “Broken Symmetries and the Masses of Gauge Bosons,” *Phys. Rev. Lett.*, vol. 13, pp. 508–509, 1964. [Online]. Available: <http://dx.doi.org/10.1103/PhysRevLett.13.508>
- [51] C. S. Wu et al., “Experimental Test of Parity Conservation in β Decay,” *Phys. Rev.*, vol. 105, pp. 1413–1414, 1957. [Online]. Available: <http://dx.doi.org/10.1103/PhysRev.105.1413>
- [52] M. Goldhaber et al., “Helicity of Neutrinos,” *Phys. Rev.*, vol. 109, pp. 1015–1017, 1958. [Online]. Available: <http://dx.doi.org/10.1103/PhysRev.109.1015>
- [53] H. Yukawa, “On the Interaction of Elementary Particles I,” *Proc. Phys. Math. Soc. Jap.*, vol. 17, pp. 48–57, 1935. [Online]. Available: <http://dx.doi.org/10.1143/PTPS.1.1>
- [54] E. Majorana, “Teoria simmetrica dell’ elettrone e del positrone,” *Nuovo Cim.*, vol. 14, pp. 171–184, 1937. [Online]. Available: <http://dx.doi.org/10.1007/BF02961314>
- [55] J. N. Bahcall, “Solar Neutrino Cross Sections and Nuclear Beta Decay,” *Phys. Rev.*, vol. 135, no. 1B, pp. B137 – B146, 1964. [Online]. Available: <http://dx.doi.org/10.1103/PhysRev.135.B137>
- [56] R. Davis, “Solar neutrinos. ii. experimental,” *Phys. Rev. Lett.*, vol. 12, pp. 303–305, Mar 1964. [Online]. Available: <https://link.aps.org/doi/10.1103/PhysRevLett.12.303>
- [57] K. Lande et al., “Results from the Homestake solar neutrino observatory,” *Conf.Proc., 25th International Conference on High-energy Physics (ICHEP 90)*, pp. 667–675, 1990.
- [58] R. Davis et al., “Solar Neutrinos - a Scientific Puzzle,” *Science*, vol. 191, pp. 264–267, 1976. [Online]. Available: <http://dx.doi.org/10.1126/science.191.4224.264>
- [59] W. Hampel et al., “GALLEX solar neutrino observations: Results for GALLEX IV,” *Phys. Lett.*, vol. B447, pp. 127–133, 1999. [Online]. Available: [http://dx.doi.org/10.1016/S0370-2693\(98\)01579-2](http://dx.doi.org/10.1016/S0370-2693(98)01579-2)
- [60] J. Abdurashitov et al., “Measurement of the solar neutrino capture rate with gallium metal. III: Results for the 2002–2007 data-taking period,” *Phys. Rev. C*, vol. 80, p. 015807, 2009. [Online]. Available: <http://dx.doi.org/10.1103/PhysRevC.80.015807>
- [61] J. N. Bahcall et al., “New solar opacities, abundances, helioseismology, and neutrino fluxes,” *The Astrophys. Journal*, vol. 621, no. 1, pp. L85–L88, jan 2005. [Online]. Available: <https://doi.org/10.1086%2F428929>
- [62] B. Pontecorvo, “Inverse beta processes and nonconservation of lepton charge,” *Zh. Eksp. Teor. Fiz.*, vol. 34, p. 247, 1957.
- [63] ———, “Mesonium and anti-mesonium,” *Zh. Eksp. Teor. Fiz.*, vol. 33, pp. 549 – 551, 1957.
- [64] S. Sakata et al., “Remarks on the unified model of elementary particles,” *Prog. Theor. Phys.*, vol. 28, pp. 870–880, 1962. [Online]. Available: <http://dx.doi.org/10.1143/PTP.28.870>

- [65] M. Kobayashi et al., “Cp-violation in the renormalizable theory of weak interaction,” *Progress of Theoretical Physics*, vol. 49, no. 2, pp. 652 – 657, 1973. [Online]. Available: <https://doi.org/10.1143/PTP.49.652>
- [66] P. Adamson et al., “Electron neutrino and antineutrino appearance in the full MINOS data sample,” *Phys. Rev. Lett.*, vol. 110, no. 17, p. 171801, 2013. [Online]. Available: <http://dx.doi.org/10.1103/PhysRevLett.110.171801>
- [67] K. Abe et al., *Phys. Rev. Lett.*, vol. 112, p. 061802, Feb 2014. [Online]. Available: <https://link.aps.org/doi/10.1103/PhysRevLett.112.061802>
- [68] J. K. Ahn et al., “Observation of reactor electron antineutrinos disappearance in the reno experiment,” *Phys. Rev. Lett.*, vol. 108, p. 191802, May 2012. [Online]. Available: <https://link.aps.org/doi/10.1103/PhysRevLett.108.191802>
- [69] Super-Kamiokande Collaboration, “Atmospheric Results from Super-Kamiokande,” 2014, xXVI International Conference on Neutrino Physics and Astrophysics, Boston, USA, June 2-7.
- [70] F. P. An et al., “New Measurement of Antineutrino Oscillation with the Full Detector Configuration at Daya Bay,” *Phys. Rev. Lett.*, vol. 115, no. 11, p. 111802, 2015. [Online]. Available: <http://dx.doi.org/10.1103/PhysRevLett.115.111802>
- [71] P. F. de Salas et al., “Status of neutrino oscillations 2018: 3σ hint for normal mass ordering and improved CP sensitivity,” *Phys. Lett. B*, vol. 782, pp. 633–640, 2018. [Online]. Available: <http://dx.doi.org/10.1016/j.physletb.2018.06.019>
- [72] J. H. Christenson et al., “Evidence for the 2π Decay of the K_0 Meson,” *Physical Rev. Lett.* vol. 13, pp. 138–140, 1964.
- [73] A. D. Sakharov, “Violation of CP Invariance, C asymmetry, and baryon asymmetry of the universe,” *Pisma Zh. Eksp. Teor. Fiz.*, vol. 5, pp. 32–35, 1967. [Online]. Available: <http://dx.doi.org/10.1070/PU1991v034n05ABEH002497>
- [74] M. Drewes et al., “Matter and Antimatter in the Universe,” *New J. Phys.*, vol. 14, p. 095012, 2012. [Online]. Available: <http://dx.doi.org/10.1088/1367-2630/14/9/095012>
- [75] A. Zee, “A Theory of Lepton Number Violation, Neutrino Majorana Mass, and Oscillation,” *Phys. Lett. B*, vol. 93, p. 389, 1980, [Erratum: *Phys.Lett.B* 95, 461 (1980)]. [Online]. Available: [http://dx.doi.org/10.1016/0370-2693\(80\)90349-4](http://dx.doi.org/10.1016/0370-2693(80)90349-4)
- [76] E. Ma, “Verifiable radiative seesaw mechanism of neutrino mass and dark matter,” *Phys. Rev. D*, vol. 73, p. 077301, Apr 2006. [Online]. Available: <https://link.aps.org/doi/10.1103/PhysRevD.73.077301>
- [77] P. Pérez et al., “On the origin of neutrino masses,” *Phys. Rev. D*, vol. 80, p. 053006, Sep 2009. [Online]. Available: <https://link.aps.org/doi/10.1103/PhysRevD.80.053006>
- [78] C. D. Froggatt et al., “Hierarchy of Quark Masses, Cabibbo Angles and CP Violation,” *Nucl. Phys.*, vol. B147, pp. 277–298, 1979. [Online]. Available: [http://dx.doi.org/10.1016/0550-3213\(79\)90316-X](http://dx.doi.org/10.1016/0550-3213(79)90316-X)
- [79] Y. Chikashige et al., “Are there real goldstone bosons associated with broken lepton number?” *Phys. Lett. B*, vol. 98, no. 4, pp. 265 – 268, 1981. [Online]. Available: <http://www.sciencedirect.com/science/article/pii/0370269381900113>
- [80] G. B. Gelmini et al., “Left-Handed Neutrino Mass Scale and Spontaneously Broken Lepton Number,” *Phys. Lett.*, vol. 99B, pp. 411–415, 1981. [Online]. Available: [http://dx.doi.org/10.1016/0370-2693\(81\)90559-1](http://dx.doi.org/10.1016/0370-2693(81)90559-1)

- [81] G. C. Branco et al., “Relating the scalar flavor changing neutral couplings to the CKM matrix,” *Phys. Lett.*, vol. B380, pp. 119–126, 1996. [Online]. Available: [http://dx.doi.org/10.1016/0370-2693\(96\)00494-7](http://dx.doi.org/10.1016/0370-2693(96)00494-7)
- [82] S. M. Davidson et al., “Lhc phenomenology of a two-higgs-doublet neutrino mass model,” *Phys. Rev. D*, vol. 82, no. 11, Dec 2010. [Online]. Available: <http://dx.doi.org/10.1103/physrevd.82.115031>
- [83] M. Gell-Mann et al., “Complex Spinors and Unified Theories,” *Conf. Proc. C*, vol. 790927, pp. 315–321, 1979.
- [84] P. Minkowski, “ $\mu \rightarrow e\gamma$ at a Rate of One Out of 10^9 Muon Decays?” *Phys. Lett. B*, vol. 67, pp. 421–428, 1977. [Online]. Available: [http://dx.doi.org/10.1016/0370-2693\(77\)90435-X](http://dx.doi.org/10.1016/0370-2693(77)90435-X)
- [85] T. Yanagida, “Horizontal Symmetry and Masses of Neutrinos,” *Prog. Theor. Phys.*, vol. 64, p. 1103, 1980. [Online]. Available: <http://dx.doi.org/10.1143/PTP.64.1103>
- [86] S. Glashow, “The Future of Elementary Particle Physics,” *NATO Sci. Ser. B*, vol. 61, p. 687, 1980. [Online]. Available: http://dx.doi.org/10.1007/978-1-4684-7197-7_15
- [87] R. N. Mohapatra et al., “Neutrino mass and spontaneous parity nonconservation,” *Phys. Rev. Lett.*, vol. 44, pp. 912–915, Apr 1980. [Online]. Available: <https://link.aps.org/doi/10.1103/PhysRevLett.44.912>
- [88] J. Schechter et al., “Neutrino Masses in $SU(2) \times U(1)$ Theories,” *Phys. Rev. Lett. D22*, pp. 2227, 1980.
- [89] T. Lasserre et al., “Reactor antineutrino anomaly,” *Phys. Rev. D*, vol. 83, p. 073006, Apr 2011. [Online]. Available: <https://link.aps.org/doi/10.1103/PhysRevD.83.073006>
- [90] M. Drewes, “The Phenomenology of Right Handed Neutrinos,” *Int. J. Mod. Phys.*, vol. E22, p. 1330019, 2013. [Online]. Available: <http://dx.doi.org/10.1142/S0218301313300191>
- [91] P. Langacker, “Neutrino masses from the top down,” *Annual Review of Nuclear and Particle Science*, vol. 62, no. 1, pp. 215–235, 2012. [Online]. Available: <https://doi.org/10.1146/annurev-nucl-102711-094925>
- [92] C. Athanassopoulos et al., “Evidence for anti-muon-neutrino \rightarrow anti-electron-neutrino oscillations from the LSND experiment at LAMPF,” *Phys. Rev. Lett.*, vol. 77, pp. 3082–3085, 1996. [Online]. Available: <http://dx.doi.org/10.1103/PhysRevLett.77.3082>
- [93] A. Aguilar-Arevalo et al., “Search for electron neutrino appearance at the $\delta m^2 \sim eV^2$,” *Phys. Rev. Lett.*, vol. 98, no. 23, Jun 2007. [Online]. Available: <http://dx.doi.org/10.1103/PhysRevLett.98.231801>
- [94] C. Giunti et al., “Effect of the reactor antineutrino anomaly on the first double-chooz results,” *Phys. Rev. D*, vol. 85, p. 031301, Feb 2012. [Online]. Available: <https://link.aps.org/doi/10.1103/PhysRevD.85.031301>
- [95] J. Conrad et al., “The LSND and MiniBooNE Oscillation Searches at High Δm^2 ,” *Annu. Rev. Nucl. Part. Sci.*, vol. 63, no. arXiv:1306.6494, p. 45, Jun 2013, comments: Posted with permission from the Annual Review of Nuclear and Particle Science, Volume 63. opyright 2013 by Annual Reviews, <http://www.annualreviews.org>. [Online]. Available: <https://cds.cern.ch/record/1558473>

-
- [96] A. De Gouvea et al., “Constraining the (Low-Energy) Type-I Seesaw,” *Phys. Rev.*, vol. D85, p. 053006, 2012. [Online]. Available: 1110.6122
- [97] A. Donini et al., “The minimal 3+2 neutrino model versus oscillation anomalies,” *JHEP*, vol. 07, p. 161, 2012. [Online]. Available: [http://dx.doi.org/10.1007/JHEP07\(2012\)161](http://dx.doi.org/10.1007/JHEP07(2012)161)
- [98] M. Korzeczek, “eV- and keV-sterile neutrino studies with KATRIN,” Master’s thesis, Karlsruhe Institute of Technology, 2016.
- [99] S. Dodelson et al., “Sterile neutrinos as dark matter,” *Phys. Rev. Lett.*, vol. 72, pp. 17–20, Jan 1994. [Online]. Available: <https://link.aps.org/doi/10.1103/PhysRevLett.72.17>
- [100] H. J. De Veg et al., “Model-independent analysis of dark matter points to a particle mass at the keV scale,” *Monthly Notices of the Royal Astronomical Society*, vol. 404, no. 2, pp. 885–894, May 2010. [Online]. Available: <http://dx.doi.org/10.1111/j.1365-2966.2010.16319.x>
- [101] —, “Cosmological evolution of warm dark matter fluctuations I: Efficient computational framework with Volterra integral equations,” *Phys. Rev.*, vol. D85, p. 043516, 2012. [Online]. Available: <http://dx.doi.org/10.1103/PhysRevD.85.043516>
- [102] —, “Observational rotation curves and density profiles versus the Thomas-Fermi galaxy structure theory,” *Mon. Not. Roy. Astron. Soc.*, vol. 442, no. 3, pp. 2717–2727, 2014. [Online]. Available: <http://dx.doi.org/10.1093/mnras/stu972>
- [103] E. Bulbul et al., “Detection of an Unidentified Emission Line in the Stacked X-Ray Spectrum of Galaxy Clusters,” , vol. 789, no. 1, p. 13, Jul 2014. [Online]. Available: <http://dx.doi.org/10.1088/0004-637X/789/1/13>
- [104] A. Boyarsky et al., “Unidentified line in x-ray spectra of the andromeda galaxy and perseus galaxy cluster,” *Phys. Rev. Lett.*, vol. 113, p. 251301, Dec 2014. [Online]. Available: <https://link.aps.org/doi/10.1103/PhysRevLett.113.251301>
- [105] M. Fukugita et al., “Barygenesis without grand unification,” *Phys. Lett. B*, vol. 174, no. 1, pp. 45 – 47, 1986. [Online]. Available: <http://www.sciencedirect.com/science/article/pii/0370269386911263>
- [106] V. De Rome et al., “Sneutrino Dark Matter in Low-scale Seesaw Scenarios,” *JHEP*, vol. 12, p. 106, 2012. [Online]. Available: [http://dx.doi.org/10.1007/JHEP12\(2012\)106](http://dx.doi.org/10.1007/JHEP12(2012)106)
- [107] J. Lesgourgues et al., “Massive neutrinos and cosmology,” *Phys. Rept.*, vol. 429, pp. 307–379, 2006. [Online]. Available: <http://dx.doi.org/10.1016/j.physrep.2006.04.001>
- [108] J. Austin et al., “Beyond the Cosmological Standard Model,” *Phys. Rept.*, vol. 568, pp. 1–98, 2015. [Online]. Available: <http://dx.doi.org/10.1016/j.physrep.2014.12.002>
- [109] S. Hannestad, “Neutrinos in cosmology,” *New J. Phys.*, vol. 6, p. 108, 2004. [Online]. Available: <http://dx.doi.org/10.1088/1367-2630/6/1/108>
- [110] F. Heizmann, “Optimization of a KATRIN source analysis tool and investigations of the potential to constrain the relic neutrino background,” Master’s thesis, Karlsruhe Institute of Technology, 2015.
- [111] S. Alam et al., “The eleventh and twelfth data releases of the sloan digital sky survey: final data from sdss-iii,” *The Astrophys. Journal Supplement Series*, vol. 219, no. 1, p. 12, jul 2015. [Online]. Available: <https://doi.org/10.1088%2F0067-0049%2F219%2F1%2F12>

- [112] C. Weizsäcker, “Zur Theorie der Kernmassen,” *Z. Phys.*, vol. 96, pp. 431–458, 1935. [Online]. Available: <http://dx.doi.org/10.1007/BF01337700>
- [113] M. Goeppert-Mayer, “Double beta-disintegration,” *Phys. Rev.*, vol. 48, pp. 512–516, Sep 1935. [Online]. Available: <https://link.aps.org/doi/10.1103/PhysRev.48.512>
- [114] C. Sáenz et al., “Results of a search for double positron decay and electron-positron conversion of ^{78}Kr ,” *Phys. Rev. C*, vol. 50, pp. 1170–1174, Aug 1994. [Online]. Available: <https://link.aps.org/doi/10.1103/PhysRevC.50.1170>
- [115] G. Racah, “Sulla simmetria tra particelle e antiparticelle,” *Il Nuovo Cimento*, vol. 14, no. 7, p. 322, Jul 1937. [Online]. Available: <https://doi.org/10.1007/BF02961321>
- [116] S. R. Elliott et al., “Double beta decay,” *Annual Review of Nuclear and Particle Science*, vol. 52, no. 1, pp. 115–151, 2002. [Online]. Available: <http://dx.doi.org/10.1146/annurev.nucl.52.050102.090641>
- [117] C. E. Aalseth et al., “The Majorana Experiment,” *Nucl. Phys. Proc. Suppl.*, vol. 217, pp. 44–46, 2011. [Online]. Available: <http://dx.doi.org/10.1016/j.nuclphysbps.2011.04.063>
- [118] A. Gando et al., “Search for majorana neutrinos near the inverted mass hierarchy region with kamland-zen,” *Phys. Rev. Lett.*, vol. 117, no. 8, Aug 2016. [Online]. Available: <http://dx.doi.org/10.1103/PhysRevLett.117.082503>
- [119] M. Agostini et al., “Improved limit on neutrinoless double- β decay of ^{76}Ge from gerda phase ii,” *Phys. Rev. Lett.*, vol. 120, p. 132503, Mar 2018. [Online]. Available: <https://link.aps.org/doi/10.1103/PhysRevLett.120.132503>
- [120] J. Menendez et al., “Disassembling the Nuclear Matrix Elements of the Neutrinoless beta beta Decay,” *Nucl. Phys.*, vol. A818, pp. 139–151, 2009. [Online]. Available: <http://dx.doi.org/10.1016/j.nuclphysa.2008.12.005>
- [121] E. W. Otten et al., “Neutrino mass limit from tritium beta decay,” *Rept. Prog. Phys.*, vol. 71, p. 086201, 2008. [Online]. Available: <http://dx.doi.org/10.1088/0034-4885/71/8/086201>
- [122] G. Beamson et al., “The collimating and magnifying properties of a superconducting field photoelectron spectrometer,” *Journal of Physics E*, vol. 13, no. 1, p. 64, 1980. [Online]. Available: <http://dx.doi.org/10.1088/0022-3735/13/1/018>
- [123] P. Kruit et al., “Magnetic field paralleliser for 2π electron-spectrometer and electron-image magnifier,” *Journal of Physics E: Scientific Instruments*, vol. 16, no. 4, pp. 313–324, apr 1983. [Online]. Available: <https://doi.org/10.1088/0022-3735/16/4/016>
- [124] S. Groh, “Modeling of the Response Function and Measurement of Transmission Properties of the KATRIN Experiment,” *Karlsruhe Institute of Technology*, 2015, doctoral thesis.
- [125] N. Wandkowsky, “Study of background and transmission properties of the KATRIN spectrometers,” *Karlsruhe Institute of Technology*, 2013, doctoral thesis.
- [126] T. Thümmler, “Entwicklung von Methoden zur Untergrundreduzierung am Mainzer β -Spektrometer,” Master’s thesis, Johannes Gutenberg Universität Mainz, 2002.
- [127] A. Lokhov, “Background reduction with the shifted analyzing plane configuration in KATRIN,” *Bad Honnef Conference - massive Neutrinos (Poster and Abstract)*, 2019.

- [128] M. Arenz et al., “The KATRIN Superconducting Magnets: Overview and First Performance Results,” *JINST*, vol. 13, no. 08, p. T08005, 2018. [Online]. Available: <http://dx.doi.org/10.1088/1748-0221/13/08/T08005>
- [129] —, “First transmission of electrons and ions through the KATRIN beamline,” *Journal of Instrumentation*, vol. 13, no. 04, pp. P04 020–P04 020, apr 2018. [Online]. Available: <https://doi.org/10.1088%2F1748-0221%2F13%2F04%2Fp04020>
- [130] M. Hackenjös, “KATRIN First Light - Commissioning and Modelling of the Beamline,” Ph.D. dissertation, Karlsruhe Institute of Technology, 2017.
- [131] M. Aker et al., “First operation of the KATRIN experiment with tritium,” *Submitted to Eur. Phys. J. C*, 2019.
- [132] L. L. Lucas et al., “Comprehensive review and critical evaluation of the half-life of tritium,” *Journal of research of the National Institute of Standards and Technology*, vol. 105, no. 4, pp. 541–549, 08 2000.
- [133] L. I. Bodine et al., “Assessment of molecular effects on neutrino mass measurements from tritium β decay,” *Phys. Rev. C*, vol. 91, p. 035505, Mar 2015. [Online]. Available: <https://link.aps.org/doi/10.1103/PhysRevC.91.035505>
- [134] N. Doss et al., “Molecular effects in investigations of tritium molecule beta decay endpoint experiments,” *Phys. Rev.*, vol. C73, p. 025502, 2006. [Online]. Available: <http://dx.doi.org/10.1103/PhysRevC.73.025502>
- [135] —, “Excitations to the electronic continuum of ${}^3\text{HeT}^+$ in investigations of T^2 β -decay experiments,” *Jour. of Phys. B*, vol. 41, no. 12, 2008.
- [136] T. Bode, “Optimierung des 2-Phasen-Kühlkonzepts für den WGTS-Demonstrator von KATRIN,” *Karlsruhe Institute of Technology*, 2011, diploma thesis.
- [137] S. Grohmann et al., “The thermal behaviour of the tritium source in KATRIN,” *Cryogenics*, vol. 55-56, pp. 5–11, 2013. [Online]. Available: <http://dx.doi.org/10.1016/j.cryogenics.2013.01.001>
- [138] M. Hötzel, “Simulation and analysis of source-related effects for KATRIN,” Ph.D. dissertation, Karlsruhe Institute of Technology, 2012.
- [139] M. Sturm, “Aufbau und Test des Inner-Loop-Systems der Tritiumquelle von KATRIN,” *Karlsruhe Institute of Technology*, 2010, doctoral thesis.
- [140] S. Welte et al., “Experimental performance test of key components of the katrin outer tritium loop,” *Fusion Science and Technology*, vol. 71, no. 3, pp. 316–320, 2017. [Online]. Available: <https://doi.org/10.1080/15361055.2017.1291233>
- [141] M. Schlösser et al., “Accurate calibration of the laser raman system for the karlsruhe tritium neutrino experiment,” *Journal of molecular structure*, vol. 1044, pp. 61–66, 2013, 51.54.01; LK 02. [Online]. Available: <http://dx.doi.org/10.1016/j.molstruc.2012.11.022>
- [142] M. Babutzka, “Design and development for the Rearsection of the KATRIN experiment,” Ph.D. dissertation, Karlsruhe Institute of Technology, 2014.
- [143] M. Röllig, “Tritium analytics by beta induced x-ray spectrometry,” *Karlsruhe Institute of Technology*, 2015, doctoral thesis.
- [144] M. Röllig et al., “Activity monitoring of a gaseous tritium source by beta induced x-ray spectrometry,” *Fusion Engineering and Design*, vol. 88, no. 6, pp. 1263 – 1266, 2013, proceedings of the 27th Symposium On Fusion Technology (SOFT-27); Belgium, September 24-28, 2012. [Online]. Available: <http://www.sciencedirect.com/science/article/pii/S0920379612004632>

- [145] M. Babutzka et al., “Monitoring of the operating parameters of the KATRIN windowless gaseous tritium source,” *New Journal of Physics*, vol. 14, no. 10, p. 103046, oct 2012. [Online]. Available: <https://doi.org/10.1088%2F1367-2630%2F14%2F10%2F103046>
- [146] A. Jansen, “The Cryogenic Pumping Section of the KATRIN Experiment - Design Studies and Experiments for the Commissioning,” Ph.D. dissertation, Karlsruhe Institute of Technology, 2015.
- [147] A. Kosmider, “Tritium Retention Techniques in the KATRIN Transport Section and Commissioning of its DPS2-F Cryostat,” Ph.D. dissertation, Karlsruhe Institute of Technology, 2012.
- [148] X. Luo et al., “Monte Carlo simulation of gas flow through the KATRIN DPS2-F differential pumping system,” *Vacuum*, vol. 80, no. 8, pp. 864 – 869, 2006. [Online]. Available: <http://dx.doi.org/10.1016/j.vacuum.2005.11.044>
- [149] M. Hackenjos, “Die Differentielle Pumpstrecke des KATRIN-Experiments - Inbetriebnahme und Charakterisierung des Supraleitenden Magnetsystems,” *Karlsruhe Institute of Technology*, 2015, master thesis.
- [150] S. Reimer, “Ein elektrostatisches Dipolsystem zur Eliminierung von Ionen in der DPS2-F des KATRIN Experimentes,” *Karlsruhe Institute of Technology*, 2009, diploma thesis.
- [151] M. Klein, “Tritium ions in KATRIN: blocking, removal and detection,” Ph.D. dissertation, Karlsruhe Institute of Technology, 2018.
- [152] A. Windberger, “Berechnungen und Simulationen zum Verhalten von Ionen in der differentiellen Pumpstrecke des KATRIN-Experiments,” Master’s thesis, Karlsruhe Institut of Technology, 2011.
- [153] C. Röttele, “Tritium suppression factor of the katrin transport section,” Ph.D. dissertation, Karlsruhe Institut of Technologie (KIT), 2019, 51.03.01; LK 01. [Online]. Available: <http://dx.doi.org/10.5445/IR/1000096733>
- [154] W. Gil et al., “The Cryogenic Pumping Section of the KATRIN Experiment,” *Applied Superconductivity, IEEE Transactions*, vol. 20, no. 3, pp. 316 – 319, 2010. [Online]. Available: <http://dx.doi.org/10.1109/TASC.2009.2038581>
- [155] M. Babutzka, “Untersuchung eines verfahrbaren Monitor-detektors zur Überwachung der Aktivität des β -Zerfalls in der kryogenen Pumpstrecke bei KATRIN,” *Karlsruhe Institute of Technology*, 2011, diploma thesis.
- [156] B. Beskers, “Messung und Optimierung der Eigenschaften des Monitor-detektors für keV-Elektronen in der kryogenen Pumpstrecke des KATRIN Experiments,” Master’s thesis, Westfälische Wilhelms-Universität Münster, 2010.
- [157] S. Hickford, “The KATRIN forward beam monitor detector,” 2007, 2015 DPG Spring Meeting, Wuppertal (Germany). [Online]. Available: <http://fuzzy.fzk.de/bscw/bscw.cgi/d358586/95-TRP-4250-C1-SWuestling.pdf>
- [158] E. Ellinger et al., “Monitoring the KATRIN source properties within the beamline,” *Journal of Physics: Conference Series*, vol. 888, p. 012229, sep 2017. [Online]. Available: <https://doi.org/10.1088%2F1742-6596%2F888%2F1%2F012229>
- [159] F. Glück et al., “Electromagnetic design of the large-volume air coil system of the KATRIN experiment,” *New Journal of Physics*, vol. 15, no. 8, p. 083025, aug 2013. [Online]. Available: <https://doi.org/10.1088%2F1367-2630%2F15%2F8%2F083025>

- [160] F. M. Fränkle et al., “Penning discharge in the KATRIN pre-spectrometer,” *Journal of Instrumentation*, vol. 9, no. 07, pp. P07 028–P07 028, jul 2014. [Online]. Available: <https://doi.org/10.1088/1748-0221/9/07/P07028>
- [161] M. Prall et al., “The KATRIN pre-spectrometer at reduced filter energy,” *New Journal of Physics*, vol. 14, p. 073054, 2012. [Online]. Available: <http://dx.doi.org/10.1088/1367-2630/14/7/073054>
- [162] M. Aker et al., “Suppression of Penning discharges between the KATRIN spectrometers,” 11 2019.
- [163] K. Hugenberg, “Design of the electrode system of the KATRIN main spectrometer,” *Westfälische Wilhelms-Universität Münster*, 2008, diploma thesis.
- [164] K. Valerius, “Electromagnetic design and inner electrode for the katrin main spectrometer,” *Progress in Particle and Nuclear Physics*, vol. 57, no. 1, pp. 58 – 60, 2006, international Workshop of Nuclear Physics 27th course. [Online]. Available: <http://www.sciencedirect.com/science/article/pii/S0146641005001353>
- [165] —, “Spectrometer-related background processes and their suppression in the KATRIN experiment,” *Westfälische Wilhelms-Universität Münster*, 2009, doctoral thesis.
- [166] M. Zacher, “Electromagnetic design and field emission studies for the inner electrode system of the KATRIN main spectrometer,” *Westfälische Wilhelms-Universität Münster*, 2009, diploma thesis.
- [167] S. Goerhardt, “Background Reduction Methods and Vacuum Technology at the KATRIN Spectrometers,” *Karlsruhe Institute of Technology*, 2014, doctoral thesis.
- [168] T. Thümmel et al., “Precision high voltage divider for the katrin experiment,” *New Journal of Physics*, vol. 11, no. 10, p. 103007, Oct 2009. [Online]. Available: <http://dx.doi.org/10.1088/1367-2630/11/10/103007>
- [169] M. Erhard et al., “High-voltage monitoring with a solenoid retarding spectrometer at the KATRIN experiment,” *JINST*, vol. 9, p. P06022, 2014. [Online]. Available: <http://dx.doi.org/10.1088/1748-0221/9/06/P06022>
- [170] M. Slezak, “The source of monoenergetic electrons for the monitoring of spectrometer in the KATRIN neutrino experiment,” *Charles University in Prague, NPI Rez*, 2011, diploma thesis.
- [171] M. Slezak et al., “Electron line shape of the KATRIN monitor spectrometer,” *Journal of Instrumentation*, vol. 8, p. T12002, 2013. [Online]. Available: <http://dx.doi.org/10.1088/1748-0221/8/12/T12002>
- [172] M. Zboril, “Solid electron sources for the energy scale monitoring in the KATRIN experiment,” Ph.D. dissertation, Westfälische Wilhelms-Universität Münster, 2011.
- [173] J. Schwarz, “The Detector System of the KATRIN Experiment - Implementation and First Measurements with the Spectrometer,” *Karlsruhe Institute of Technology*, 2014, doctoral thesis.
- [174] J. Amsbaugh et al., “Focal-plane detector system for the katrin experiment,” *Nuclear Instruments and Methods in Physics Research Section A: Accelerators, Spectrometers, Detectors and Associated Equipment*, vol. 778, pp. 40 – 60, 2015. [Online]. Available: <http://www.sciencedirect.com/science/article/pii/S0168900215000236>
- [175] F. Harms, “Characterization and Minimization of BackgroundProcesses in the KATRIN Main Spectrometer,” *Karlsruher Institute of Technology*, 2016.

- [176] A. Pollithy, “KNM1 Background - systematics,” *KATRIN internal report*, 2019.
- [177] N. Trost, “Modeling and measurement of Rydberg-State mediated Background at the KATRIN Main Spectrometer,” Ph.D. dissertation, Karlsruhe Institute of Technology, 2018.
- [178] K. Dolde et al., “Impact of adc non-linearities on the sensitivity to sterile keV neutrinos with a katrin-like experiment,” *Nuclear Instruments and Methods in Physics Research Section A: Accelerators, Spectrometers, Detectors and Associated Equipment*, vol. 848, pp. 127 – 136, 2017. [Online]. Available: <http://www.sciencedirect.com/science/article/pii/S0168900216312761>
- [179] M. Shaposhnikov et al., “The ν msm, dark matter and baryon asymmetry of the universe,” *Phys. Lett. B*, vol. 620, pp. 17–26, 2005. [Online]. Available: <http://dx.doi.org/10.1016/j.physletb.2005.06.020>
- [180] G. Jungman et al., “Supersymmetric dark matter,” *Phys. Rept.*, vol. 267, pp. 195–373, 1996. [Online]. Available: [http://dx.doi.org/10.1016/0370-1573\(95\)00058-5](http://dx.doi.org/10.1016/0370-1573(95)00058-5)
- [181] A. Klypin et al., “Where are the missing Galactic satellites?” *Astrophys. J.*, vol. 522, pp. 82–92, 1999. [Online]. Available: <http://dx.doi.org/10.1086/307643>
- [182] G. Torrealba et al., “The feeble giant. discovery of a large and diffuse milky way dwarf galaxy in the constellation of crater,” *Monthly Notices of the Royal Astronomical Society*, vol. 459, no. 3, p. 2370â2378, Apr 2016. [Online]. Available: <http://dx.doi.org/10.1093/mnras/stw733>
- [183] K. Dongwon et al., “Horologium ii: A second ultra faint milky way satellite in the horologium constellation,” *The Astrophys. Journal*, vol. 808, no. 2, p. L39, jul 2015. [Online]. Available: <https://doi.org/10.1088%2F2041-8205%2F808%2F2%2FL39>
- [184] K. Bechtol et al., “Eight new milky way companions discovered in first-year dark energy survey data,” *The Astrophys. Journal*, vol. 807, 03 2015. [Online]. Available: <http://dx.doi.org/10.1088/0004-637X/807/1/50>
- [185] G. Torrealba et al., “At the survey limits: discovery of the aquarius 2 dwarf galaxy in the vst atlas and the sdss data,” *Monthly Notices of the Royal Astronomical Society*, vol. 463, 05 2016. [Online]. Available: <http://dx.doi.org/10.1093/mnras/stw2051>
- [186] D. Homma et al., “Searches for new milky way satellites from the first two years of data of the subaru/hyper supprime-cam survey: Discovery of cetus iii,” *Publications of the Astronomical Society of Japan*, vol. 70, 01 2018. [Online]. Available: <http://dx.doi.org/10.1093/pasj/psx050>
- [187] N. Martin et al., “Hydra ii: a faint and compact milky way dwarf galaxy found in the survey of the magellanic stellar history,” *The Astrophys. Journal*, vol. 804, 03 2015. [Online]. Available: <http://dx.doi.org/10.1088/2041-8205/804/1/L5>
- [188] D. Kim et al., “A Hero’s Dark Horse: Discovery of an Ultra-faint Milky way Satellite in Pegasus,” *Astrophys. J.*, vol. 804, no. 2, p. L44, 2015. [Online]. Available: <http://dx.doi.org/10.1088/2041-8205/804/2/L44>
- [189] —, “Portrait of a Dark Horse: a Photometric and Spectroscopic Study of the Ultra-faint Milky Way Satellite Pegasus III,” , vol. 833, no. 1, p. 16, Dec 2016. [Online]. Available: <http://dx.doi.org/10.3847/0004-637X/833/1/16>
- [190] B. Laevens et al., “Sagittarius II, Draco II and Laevens 3: Three new Milky way Satellites Discovered in the Pan-starrs 1 3π Survey,” *Astrophys. J.*, vol. 813, no. 1, p. 44, 2015. [Online]. Available: <http://dx.doi.org/10.1088/0004-637X/813/1/44>

-
- [191] G. Torrealba et al., “Discovery of two neighbouring satellites in the carina constellation with maglites,” *Monthly Notices of the Royal Astronomical Society*, vol. 475, no. 4, pp. 5085–5097, Jan 2018. [Online]. Available: <http://dx.doi.org/10.1093/mnras/sty170>
- [192] B. Moore et al., “Dark matter substructure within galactic halos,” *The Astrophys. Journal*, vol. 524, no. 1, p. L19âL22, Oct 1999. [Online]. Available: <http://dx.doi.org/10.1086/312287>
- [193] J. D. Simon et al., “The kinematics of the ultra-faint milky way satellites: Solving the missing satellite problem,” *The Astrophys. Journal*, vol. 670, no. 1, pp. 313–331, nov 2007. [Online]. Available: <https://doi.org/10.1086%2F521816>
- [194] S.-H.Oh et al., “Dark and luminous matter in things dwarf galaxies,” *The Astronomical Journal*, vol. 141, no. 6, p. 193, may 2011. [Online]. Available: <https://doi.org/10.1088%2F0004-6256%2F141%2F6%2F193>
- [195] J. Freundlich et al., “How baryonic feedback processes can affect dark matter halos: a stochastic model,” 12 2016.
- [196] J. Navarro et al., “A Universal density profile from hierarchical clustering,” *Astrophys. J.*, vol. 490, pp. 493–508, 1997. [Online]. Available: <http://dx.doi.org/10.1086/304888>
- [197] J. Diemand et al., “Cusps in cold dark matter haloes,” *Monthly Notices of the Royal Astronomical Society*, vol. 364, no. 2, pp. 665–673, 2005.
- [198] W. J. G. de Blok et al., “High-resolution rotation curves of low surface brightness galaxies. II. mass models,” *The Astronomical Journal*, vol. 122, no. 5, pp. 2396–2427, nov 2001. [Online]. Available: <https://doi.org/10.1086%2F323450>
- [199] A. Agnello et al., “A virial core in the sculptor dwarf spheroidal galaxy,” *The Astrophys. Journal*, vol. 754, no. 2, p. L39, Jul 2012. [Online]. Available: <http://dx.doi.org/10.1088/2041-8205/754/2/L39>
- [200] N. C. Amorisco et al., “Dark matter cores and cusps: the case of multiple stellar populations in dwarf spheroidals,” *Monthly Notices of the Royal Astronomical Society*, vol. 419, no. 1, pp. 184–196, Oct 2011. [Online]. Available: <http://dx.doi.org/10.1111/j.1365-2966.2011.19684.x>
- [201] M. G. Walker et al., “A mtehode for measuring slopes of the mass profiles of dwarf spheroidal galaxies,” *The Astrophys. Journal*, vol. 742, no. 1, p. 20, nov 2011. [Online]. Available: <https://doi.org/10.1088%2F0004-637x%2F742%2F1%2F20>
- [202] R. De Naray et al., “Do baryons alter the halos of low surface brightnessgalaxies?” *Astrophys. Jour.*, vol. 741, pp. L29, 2011.
- [203] S. Shao et al., “The phase-space density of fermionic dark matter haloes,” *Monthly Notices of the Royal Astronomical Society*, vol. 430, no. 3, pp. 2346–2357, Feb 2013. [Online]. Available: <http://dx.doi.org/10.1093/mnras/stt053>
- [204] M. Boylan-Kolchin et al., “Too big to fail? the puzzling darkness of massive milky way subhaloes,” *Monthly Notices of The Royal Astronomical Society*, vol. 415, 02 2011. [Online]. Available: <http://dx.doi.org/10.1111/j.1745-3933.2011.01074.x>
- [205] —, “The Milky Way’s bright satellites as an apparent failure of LCDM,” *Mon. Not. Roy. Astron. Soc.*, vol. 422, pp. 1203–1218, 2012. [Online]. Available: <http://dx.doi.org/10.1111/j.1365-2966.2012.20695.x>

- [206] E. Tollerud et al., “M31 Satellite Masses Compared to LCDM Subhaloes,” *Mon. Not. Roy. Astron. Soc.*, vol. 440, no. 4, pp. 3511–3519, 2014. [Online]. Available: <http://dx.doi.org/10.1093/mnras/stu474>
- [207] L. E. Strigari et al., “The cosmic abundance of classical milky way satellites,” *The Astrophys. Journal*, vol. 749, no. 1, p. 75, mar 2012. [Online]. Available: <https://doi.org/10.1088%2F0004-637x%2F749%2F1%2F75>
- [208] A. Brooks et al., “Why baryons matter: The kinematics of dwarf spheroidal satellites,” *Astrophys. Jour.*, vol. 786, pp. 87, 2014.
- [209] E. Kirby et al., “The dynamics of isolated Local Group galaxies,” *Mon. Not. Roy. Astron. Soc.*, vol. 439, no. 1, pp. 1015–1027, 2014. [Online]. Available: <http://dx.doi.org/10.1093/mnras/stu025>
- [210] S. Garrison-Kimmel et al., “Too Big to Fail in the Local Group,” *Mon. Not. Roy. Astron. Soc.*, vol. 444, no. 1, pp. 222–236, 2014. [Online]. Available: <http://dx.doi.org/10.1093/mnras/stu1477>
- [211] —, “Elvis: Exploring the local volume in simulations,” *Mon. Not. Roy. Astron. Soc.*, vol. 438, pp. 2578-2596, 2014.
- [212] A. Boyarsky et al., “A lower bound on the mass of dark matter particles,” *Journal of Cosmology and Astroparticle Physics*, vol. 2009, no. 03, pp. 005–005, Mar 2009. [Online]. Available: <http://dx.doi.org/10.1088/1475-7516/2009/03/005>
- [213] S. Tremaine et al., “Dynamical role of light neutral leptons in cosmology,” *Phys. Rev. Lett.*, vol. 42, pp. 407 - 410, 1979.
- [214] A. A. Meiksin et al., “The Physics of the Intergalactic Medium,” *Rev. Mod. Phys.*, vol. 81, pp. 1405–1469, 2009. [Online]. Available: <http://dx.doi.org/10.1103/RevModPhys.81.1405>
- [215] H. Bi et al., “Evolution of structure in the intergalactic medium and the nature of the $\text{Ly}\alpha$ forest,” *The Astrophys. Journal*, vol. 479, no. 2, pp. 523–542, Apr 1997. [Online]. Available: <http://dx.doi.org/10.1086/303908>
- [216] R. Lynds, “The Absorption-Line Spectrum of 4c 05.34,” *The Astrophys. Journal*, vol. 164, p. L73, Mar 1971. [Online]. Available: <http://dx.doi.org/10.1086/180695>
- [217] V. Narayanan et al., “Constraints on the mass of warm dark matter particles and the shape of the linear power spectrum from the $\text{Ly}\alpha$ forest,” *The Astrophys. Journal*, vol. 543, no. 2, pp. L103–L106, nov 2000. [Online]. Available: <https://doi.org/10.1086%2F317269>
- [218] A. Makarov et al., “Can sterile neutrinos be the dark matter?” *Phys. Rev. Lett.*, vol. 97, no. 19, Nov 2006. [Online]. Available: <http://dx.doi.org/10.1103/PhysRevLett.97.191303>
- [219] L. Benjamin et al., “Natural Suppression of Symmetry Violation in Gauge Theories: Muon - Lepton and Electron Lepton Number Nonconservation,” *Phys. Rev. D*, vol. 16, p. 1444, 1977. [Online]. Available: <http://dx.doi.org/10.1103/PhysRevD.16.1444>
- [220] L. Wolfenstein et al., “Radiative Decays of Massive Neutrinos,” *Phys. Rev. D*, vol. 25, p. 766, 1982. [Online]. Available: <http://dx.doi.org/10.1103/PhysRevD.25.766>
- [221] A. Ibarra et al., “Indirect Searches for Decaying Dark Matter,” *Int. J. Mod. Phys. A*, vol. 28, p. 1330040, 2013. [Online]. Available: <http://dx.doi.org/10.1142/S0217751X13300408>

-
- [222] A. Boyarsky et al., “Checking the dark matter origin of a 3.53 keV line with the milky way center,” *Phys. Rev. Lett.*, vol. 115, p. 161301, Oct 2015. [Online]. Available: <https://link.aps.org/doi/10.1103/PhysRevLett.115.161301>
- [223] J. Tesla et al., “Discovery of a 3.5 keV line in the galactic centre and a critical look at the origin of the line across astronomical targets,” *Monthly Notices of the Royal Astronomical Society*, vol. 450, no. 2, pp. 2143–2152, Apr 2015. [Online]. Available: <http://dx.doi.org/10.1093/mnras/stv768>
- [224] S. Riemer-Sørensen, “Constraints on the presence of a 3.5 keV dark matter emission line from chandra observations of the galactic centre,” *Astronomy & Astrophysics*, vol. 590, p. A71, May 2016. [Online]. Available: <http://dx.doi.org/10.1051/0004-6361/201527278>
- [225] T. Tamura et al., “An x-ray spectroscopic search for dark matter in the perseus cluster with suzaku,” *Publications of the Astronomical Society of Japan*, vol. 67, no. 2, Mar 2015. [Online]. Available: <http://dx.doi.org/10.1093/pasj/psu156>
- [226] T. Takahashi et al., “The astro-h mission,” *Proceedings of the SPIE*, vol. 7732, pp. 18, 2010.
- [227] S. Clark, “Attitude control failures led to break-up of japanese astronomy satellite,” *spaceflight now*, 2016.
- [228] R. Barbieri et al., “Bounds on sterile neutrinos from nucleosynthesis,” *Phys. Lett. B*, vol. 237, no. 3, pp. 440 – 445, 1990. [Online]. Available: <http://www.sciencedirect.com/science/article/pii/037026939091203N>
- [229] E. Aprile et al., “First dark matter search results from the xenon1t experiment,” *Phys. Rev. Lett.*, vol. 119, p. 181301, Oct 2017. [Online]. Available: <https://link.aps.org/doi/10.1103/PhysRevLett.119.181301>
- [230] L. Gastaldo et al., “Light sterile neutrino sensitivity of 163ho experiments,” *Journal of High Energy Physics*, vol. 2016, no. 6, p. 61, Jun 2016. [Online]. Available: [https://doi.org/10.1007/JHEP06\(2016\)061](https://doi.org/10.1007/JHEP06(2016)061)
- [231] K. Fujikawa et al., “Magnetic moment of a massive neutrino and neutrino-spin rotation,” *Phys. Rev. Lett.*, vol. 45, pp. 963–966, Sep 1980. [Online]. Available: <https://link.aps.org/doi/10.1103/PhysRevLett.45.963>
- [232] D. R. O. Morrison, “The rise and fall of the 17-keV neutrino,” *Nature*, vol. 366, no. 6450, pp. 29–32, 1993. [Online]. Available: <https://doi.org/10.1038/366029a0>
- [233] K. Schreckenbach et al., “Search for mixing of heavy neutrinos in the β^+ and β^- -spectra of the ^{64}Cu decay,” *Phys. Lett. B*, vol. 129, no. 3, pp. 265 – 268, 1983. [Online]. Available: <http://www.sciencedirect.com/science/article/pii/0370269383908584>
- [234] J. J. Simpson, “Evidence of heavy-neutrino emission in beta decay,” *Phys. Rev. Lett.*, vol. 54, pp. 1891–1893, Apr 1985. [Online]. Available: <https://link.aps.org/doi/10.1103/PhysRevLett.54.1891>
- [235] T. Ohi et al., “Search for heavy neutrinos in the beta decay of ^{35}S . evidence against the 17 keV heavy neutrino,” *Phys. Lett. B*, vol. 160, no. 4, pp. 322 – 324, 1985. [Online]. Available: <http://www.sciencedirect.com/science/article/pii/037026938591336X>
- [236] V. M. Datar et al., “Search for heavy neutrinos in the beta decay of ^{35}S ,” *Nature*, vol. 318, no. 6046, p. 547548, 1985.

- [237] S. Chatrchyan et al., “Search for heavy lepton partners of neutrinos in proton-proton collisions in the context of the type iii seesaw mechanism,” *Phys. Lett. B*, vol. 718, no. 2, pp. 348 – 368, 2012. [Online]. Available: <http://www.sciencedirect.com/science/article/pii/S0370269312011367>
- [238] K.-H. Hiddeemann et al., “Limits on neutrino masses from the tritium beta spectrum,” *Journal of Physics G: Nuclear and Particle Physics*, vol. 21, no. 5, pp. 639–650, may 1995. [Online]. Available: <https://doi.org/10.1088%2F0954-3899%2F21%2F5%2F008>
- [239] E. Holzschuh et al., “Search for heavy neutrinos in the beta spectrum of Ni-63,” *Phys. Lett.*, vol. B451, pp. 247–255, 1999. [Online]. Available: [http://dx.doi.org/10.1016/S0370-2693\(99\)00200-2](http://dx.doi.org/10.1016/S0370-2693(99)00200-2)
- [240] J. Abdurashitov et al., “First measurements in search for keV-sterile neutrino in tritium beta-decay by Troitsk nu-mass experiment,” *Pisma Zh. Eksp. Teor. Fiz.*, vol. 105, no. 12, pp. 723–724, 2017. [Online]. Available: <http://dx.doi.org/10.1134/S0021364017120013>
- [241] C. Kraus et al., “Limit on sterile neutrino contribution from the mainz neutrino mass experiment,” *The European Phys. Journal C*, vol. 73, 10 2012. [Online]. Available: <http://dx.doi.org/10.1140/epjc/s10052-013-2323-z>
- [242] K. Blaum et al., “The electron capture ^{163}Ho experiment echo,” 2013.
- [243] L. Gastaldo, “Detect sterile neutrinos in electron capture spectra: ECHO and beyond,” 2017, Flavour & Dark Matter Workshop, Heidelberg.
- [244] J. L. Mortara et al., “Evidence against a 17 keV neutrino from ^{35}S beta decay,” *Phys. Rev. Lett.*, vol. 70, pp. 394–397, Jan 1993. [Online]. Available: <https://link.aps.org/doi/10.1103/PhysRevLett.70.394>
- [245] S. Müller et al., “Search for admixture of a 17 keV neutrino beta decay of ^{35}S ,” *Zeitschrift für Naturforschung A*, vol. 49, p. 874, 1994. [Online]. Available: <https://www.degruyter.com/view/j/zna.1994.49.issue-9/zna-1994-0910/zna-1994-0910.xml>
- [246] T. Ohshima et al., “No 17 keV neutrino: Admixture $< 0.073\%$ (95)”, *Phys. Rev. D*, vol. 47, pp. 4840–4856, Jun 1993. [Online]. Available: <https://link.aps.org/doi/10.1103/PhysRevD.47.4840>
- [247] T. Ohi et al., “Search for heavy neutrinos in the beta decay of ^{35}S . evidence against the 17 keV heavy neutrino,” *Phys. Lett. B*, vol. 160, no. 4, pp. 322 – 324, 1985. [Online]. Available: <http://www.sciencedirect.com/science/article/pii/S037026938591336X>
- [248] J. Abdurashitov et al., “First measurements in search for keV sterile neutrino in tritium beta-decay in the troitsk nu-mass experiment,” *JETP Lett.*, vol. 105, no. 12, pp. 753–757, Jun 2017. [Online]. Available: <https://doi.org/10.1134/S0021364017120013>
- [249] H. Seitz-Moskaliuk, “Characterisation of the katrin tritium source and evaluation of systematic effects,” Ph.D. dissertation, Karlsruhe Institute of Technology, 2019.
- [250] S. Enomoto, “Detector Count Corrections for First Tritium,” *Internal KATRIN report*, 2019.
- [251] —, “Simple Analytical Models of Signal Pile-Up,” 2014, internal KATRIN document. [Online]. Available: <https://neutrino.ikp.kit.edu:8080/SDS-Analysis/25>

-
- [252] C. Röttle et al., “Personal communication,” Feb. 2020.
- [253] A. Marsteller, “Personal communication,” Feb. 2020.
- [254] T. Lasserre et al., “Dt fluctuation in first tritium data,” *Internal Report*, 2019.
- [255] L. Chi Sheng and J. Au Kong, *Applied Electromagnetism, Second Edition*. PWS Engineering, 1987.
- [256] M. Born et al., “Beweis des Adiabatenatzes,” *Zeitschrift für Physik*, vol. 51, no. 3-4, pp. 165–180, Mar 1928. [Online]. Available: <http://dx.doi.org/10.1007/BF01343193>
- [257] M. Prall, “Transmission function of the pre-spectrometer and systematic tests of the main-spectrometer wire electrode (phd thesis),” Ph.D. dissertation, 07 2011.
- [258] A. Picard et al., “A solenoid retarding spectrometer with high resolution and transmission for kev electrons,” *Nuclear Instruments and Methods in Physics Research Section B: Beam Interactions with Materials and Atoms*, vol. 63, no. 3, pp. 345 – 358, 1992. [Online]. Available: <http://www.sciencedirect.com/science/article/pii/0168583X9295119C>
- [259] E. Förstner, “Optimization of the KATRIN rear wall for a keV-scale sterile neutrino search,” *Karlsruher Institute of Technology*, 2017, bachelor thesis.
- [260] F. Knapp, “Impacts of Magnetic Traps in theWGTS on a keV-scale Sterile Neutrino Search with KATRIN,” *Karlsruher Institute of Technology*, 2017, bachelors Thesis.
- [261] M. Steven, “Modelling of the tritium β -decay spectrum for sterile neutrino search with katrin and analysis of the first tritium data,” Master’s thesis, Technische Universität München, 2018.
- [262] M. Korzeczek, “Sterile neutrino search with katrin - design of a novel detector system and investigation of detector-related systematic uncertainties,” Ph.D. dissertation, Karlsruhe Institute of Tehcnology, 2020.
- [263] M. Kleesiek, “A Data Analysis and Sensitivity-Optimization Framework for the KATRIN Experiment,” *Karlsruhe Institute of Technology*, 2014, phd thesis.
- [264] L. L. Cam, “Maximum likelihood - an introduction,” *Department of statistics, university of berkeley, technical report no.168 (unpublished)*, 1991.
- [265] G. Fogli et al., “Getting the most from the statistical analysis of solar neutrino oscillations,” *Phys. Rev. D*, vol. 66, p. 053010, 2002. [Online]. Available: <http://dx.doi.org/10.1103/PhysRevD.66.053010>
- [266] L. Schlüter, “Development of new methods to include systematic effects in the first tritium data analysis and sensitivity studies of the katrin experimen,” Master’s thesis, Technische Universität München, 2019.
- [267] A. Franke, “Searching for reactor antineutrino flavor oscillations with the double chooz far detector,” Ph.D. dissertation, Columbia University, 2012.
- [268] H. Krieger, *Grundlagen der Strahlungsphysik und des Strahlenschutzes*, 5th ed. Springer Spektrum, 2017. [Online]. Available: <http://dx.doi.org/10.1007/978-3-662-55760-0>
- [269] M. G. Erhard, “Influence of the magnetic field on the transmission characteristics and the neutrino mass systematic of the katrin experiment,” Ph.D. dissertation, Karlsruher Institut für Technologie (KIT), 2016. [Online]. Available: <http://dx.doi.org/10.5445/IR/1000065003>

- [270] F. Glück, “Uncertainty of the WGTS and PCHmagnetic fields,” *KATRIN Technical Note*, 2018.
- [271] V. N. Aseev et al., “Energy loss of 18 keV electrons in gaseous t and quenched condensed d films,” *The European Physical Journal D - Atomic, Molecular, Optical and Plasma Physics*, vol. 10, no. 1, pp. 39–52, Mar 2000. [Online]. Available: <https://doi.org/10.1007/s100530050525>
- [272] V. Hannen, “New energy loss parameterization,” *Internal KATRIN Report*, 2019.
- [273] F. Leven, “Analysis of Selected Models for Inelastic Electron-Scattering in the KATRIN Gaseous Tritium Source,” Master’s thesis, Karlsruhe Institute of Technology, 2019.
- [274] M. Inokuti, “Inelastic collisions of fast charged particles with atoms and molecules—the bethe theory revisited,” *Rev. Mod. Phys.*, vol. 43, pp. 297–347, Jul 1971. [Online]. Available: <https://link.aps.org/doi/10.1103/RevModPhys.43.297>
- [275] J. W. Liu, “Total cross sections for high-energy electron scattering by h_2 ($^1\Sigma_g^+$), n_2 ($^1\Sigma_g^+$), and o_2 ($^3\Sigma_g^-$),” *Phys. Rev. A*, vol. 35, pp. 591–597, Jan 1987. [Online]. Available: <https://link.aps.org/doi/10.1103/PhysRevA.35.591>
- [276] —, “Total inelastic cross section for collisions of h_2 with fast charged particles,” *Phys. Rev. A*, vol. 7, pp. 103–109, Jan 1973. [Online]. Available: <https://link.aps.org/doi/10.1103/PhysRevA.7.103>
- [277] F. Glück et al., “Inelastic Scattering Cross Section Uncertainty,” *KATRIN internal Report*, 2019.
- [278] F. Block et al., “Systematic Uncertainty of Column Density / Column Density Times Inelastic Scattering Cross-Section,” *Internal KATRIN report*, 2019.
- [279] —, “Katrin knm1 reference report: Systematic uncertainty of column density/column density times inelastic scattering cross-section,” *Internal KATRIN Report*, 2019.
- [280] —, “KATRIN KNM2 Reference Report: Systematic Uncertainty of Column Density/ Column Density Times Inelastic Scattering Cross-Section,” *Internal KATRIN Report*, 2020.
- [281] —, “KATRIN First Tritium Reference Report Systematic Uncertainty of Magnetic Field in the Analyzing Plan,” *Internal KATRIN report*, 2019.
- [282] R. Sack et al., “Eloss measurements in scanning mode,” 2019, talk at 36th KATRIN Collaboration Meeting.
- [283] C. Rodenbeck, “Measuring energy loss with time of flight at fixed voltages,” 2019, talk at 36th KATRIN Collaboration Meeting.
- [284] —, “Eloss Measurements at 100 K,” 2019, presentation during the Analysis Call on 03.12.19.
- [285] L. Kuckert, “The Windowless Gaseous Tritium Source of the KATRIN Experiment - Characterisation of Gas Dynamical and Plasma Properties,” Ph.D. dissertation, Karlsruhe Institute of Technology, 2017.
- [286] A. Lokhov, “Personal communication,” Apr. 2020, 26th April 2020.
- [287] S. Fischer, “Commissioning of the KATRIN Raman system and durability studies of optical coatings in glove box and tritium atmospheres,” Ph.D. dissertation, Karlsruhe Institute of Technology, 2014.

- [288] P. Renschler, “A new Monte Carlo simulation code for low-energy electron interactions in silicon detectors,” *Karlsruhe Institute of Technology*, 2011, doctoral thesis.
- [289] M. Kleesiek et al., “ β -decay spectrum, response function and statistical model for neutrino mass measurements with the katrin experiment,” *The European Phys. Journal / C*, vol. 79, no. 3, p. Article: 2014, 2019, 51.03.01; LK 01. [Online]. Available: <http://dx.doi.org/10.1140/epjc/s10052-019-6686-7>
- [290] D. Wilkinson, “Small terms in the beta-decay spectrum of tritium,” *Nuclear Physics A*, vol. 526, iss. 1, pp. 131-140, 1991.
- [291] A. Faessler et al., “Exact relativistic tritium β -decay endpoint spectrum in a hadron model,” *Phys. Rev. C*, vol. 77, p. 055502, May 2008. [Online]. Available: <https://link.aps.org/doi/10.1103/PhysRevC.77.055502>
- [292] S. Jonsell et al., “Neutrino-mass determination from tritium β decay: Corrections to and prospects of experimental verification of the final-state spectrum,” *Phys. Rev. C*, vol. 60, p. 034601, Jul 1999. [Online]. Available: <https://link.aps.org/doi/10.1103/PhysRevC.60.034601>
- [293] A. Saenz et al., “Improved Molecular Final-State Distribution of HeT^+ for the β .”
- [294] SAGE Collaboration, “Solar Neutrino Flux Measurements by the Soviet-American Gallium Experiment (SAGE) for half the 22-Year Solar Cycle,” *Exp. Theo. Phys.*, vol. 95, pp. 181-193, 2002.
- [295] C. Schätz, “Development of an energy dependent final state distribution for T_2 ,” Master’s thesis, Technical University Munich, 2019.
- [296] G. Dieke, “The molecular spectrum of hydrogen and its isotopes,” *Journal of Molecular Spectroscopy*, vol. 2, no. 1, pp. 494 – 517, 1958. [Online]. Available: <http://www.sciencedirect.com/science/article/pii/002228525890095X>
- [297] J. J. Simpson, “Measurement of the β -energy spectrum of ^3H to determine the antineutrino mass,” *Phys. Rev. D*, vol. 23, pp. 649–662, Feb 1981. [Online]. Available: <https://link.aps.org/doi/10.1103/PhysRevD.23.649>
- [298] A. Faessler et al., “Exact relativistic tritium β -decay endpoint spectrum in a hadron model,” *Phys. Rev. C*, vol. 77, p. 055502, May 2008. [Online]. Available: <https://link.aps.org/doi/10.1103/PhysRevC.77.055502>
- [299] H. Behrens et al., “Electron radial wave functions and nuclear beta decay,” *Oxford University Press*, 1982.
- [300] E. Otten, “Searching the absolute neutrino mass in tritium β -decay -interplay between nuclear, atomic and molecular physics,” *Hyperfine Interactions*, vol. 196, pp. 3–23, 02 2010. [Online]. Available: <http://dx.doi.org/10.1007/s10751-009-0150-2>
- [301] W. W. Repko et al., “Radiative corrections to the end point of the tritium β decay spectrum,” *Phys. Rev. C*, vol. 28, pp. 2433–2436, Dec 1983. [Online]. Available: <https://link.aps.org/doi/10.1103/PhysRevC.28.2433>
- [302] D. Wilkinson, “Evaluation of beta-decay: Ii. finite mass and size effects,” *Nuclear Instruments and Methods in Physics Research Section A: Accelerators, Spectrometers, Detectors and Associated Equipment*, vol. 290, no. 2, pp. 509 – 515, 1990. [Online]. Available: <http://www.sciencedirect.com/science/article/pii/016890029090570V>
- [303] C. K. Hargrove et al., “Measurement of the screening potential in ^3H β decay,” *Phys. Rev. C*, vol. 60, p. 034608, Aug 1999. [Online]. Available: <https://link.aps.org/doi/10.1103/PhysRevC.60.034608>

- [304] D. Hinz, “Background measurements after bake-out and baffle cooling,” 2019, analysis Call 10.09.2019.
- [305] F. Fränkle, “overview on SDS2b results,” 2015, talk at 29th KATRIN Collaboration Meeting.
- [306] D. Hinz, “Ionisation mechanisms of ^{206}Pb induced Rydberg atoms,” Master’s thesis, Karlsruhe Institute of Technology, 2018.
- [307] N. Trost, “Background Investigations Simulation & SDS2b,” 2015, talk at 29th KATRIN Collaboration Meeting.
- [308] C. Rodenbeck, “Calibration and Monitoring of KATRIN’s Precision High Voltage System with First $^{83\text{m}}\text{Kr}$ Measurements,” Master’s thesis, Karlsruhe Institute of Technology, 2018.
- [309] M. Arenz et al., “Calibration of high voltages at the ppm level by the difference of $^{83\text{m}}\text{Kr}$ conversion electron lines at the KATRIN experiment,” *Eur. Phys. J.*, vol. C78, no. 5, p. 368, 2018. [Online]. Available: <http://dx.doi.org/10.1140/epjc/s10052-018-5832-y>
- [310] O. Rest et al., “A novel ppm-precise absolute calibration method for precision high-voltage dividers,” *Metrologia*, vol. 56, no. 4, p. 045007, jul 2019. [Online]. Available: <https://doi.org/10.1088/0026-1361/56/4/045007>
- [311] F. Sharipov, “Numerical calculations of tritium flow through the KATRIN beamline,” *KATRIN internal report*, 2003.
- [312] A. Lokhov et al., “A model for a keV-scale sterile neutrino search with KATRIN: SSC-sterile,” Feb. 2018, talk at 34th KATRIN Collaboration Meeting.
- [313] F. Megias, “ev-scale sterile neutrino investigation with the first tritium katrin data,” Master’s thesis, Technische Universität München, 2019.
- [314] W. Gil, “First operation of the complete katrin superconducting magnet chain,” *IEEE Transactions on Applied Superconductivity*, vol. 28, no. 4, pp. 1–5, 2018.
- [315] S. Mertens et al., “Background due to stored electrons following nuclear decays in thekatrin spectrometers and its impact on the neutrino mass sensitivity,” *Astroparticle Physics*, vol. 41, pp. 52 – 62, 04 2012. [Online]. Available: <http://dx.doi.org/10.1016/j.astropartphys.2012.10.005>
- [316] F. Heizmann, “Analysis tools and methods for tritium data taking with the katrin experiment,” Ph.D. dissertation, Karlsruhe Institut of Technology (KIT), 2019, 51.03.01; LK 01. [Online]. Available: <http://dx.doi.org/10.5445/IR/1000093536>
- [317] C. Karl, “Analysis of first tritium data of the katrin experiment,” Master’s thesis, Technische Universität München, 2018.
- [318] T. Thümmler, “Spectrometer and detector system status update,” Mar. 2020, talk during 38th KATRIN collaboration meeting.
- [319] A. Lokhov et al., “Combined analysis technique to search for sterile neutrinos,” Mar. 2017, talk at 32nd KATRIN Collaboration Meeting.
- [320] Tobias Bode, “TRISTAN Detector R&D,” 2017, talk at 32nd KATRIN Collaboration Meeting.
- [321] K. Dolde, “Detector and read-out development to search for sterile neutrinos with KATRIN,” Master’s thesis, Karlsruhe Institute of Technology, 2016.

-
- [322] D. Sigmann, “Investigation of the Detector Response to Electrons of the TRISTAN Prototype Detectors,” Master’s thesis, Technical University of Munich, 2019.
- [323] X. Pawlowski, “Characterization of the TRISTAN Silicon Drift Detectors with Krypton Conversion Electrons,” 2018, bachelor Thesis.
- [324] K. Altenmüller et al., “Silicon drift detector prototypes for the keV-scale sterile neutrino search at KATRIN: detector characteristics and proof-of-concept analysis of a differential ^3H -spectrum,” *To be published*, 2019.
- [325] K. Altenmüller, “Search for sterile neutrinos in β -decays,” Ph.D. dissertation, Technical University of Munich and University Paris-Saclay, 2019.
- [326] T. Brunst et al., “Measurements with a TRISTAN prototype detector system at the “troitsk nu-mass” experiment in integral and differential mode,” *Journal of Instrumentation*, vol. 14, no. 11, pp. P11 013–P11 013, nov 2019. [Online]. Available: <https://doi.org/10.1088/1748-0221/14/11/P11013>
- [327] E. Ellinger et al., “The tristan forward beam monitor,” Nov. 2019, talk at the 37th KATRIN collaboration meeting.
- [328] F. Glück, “Personal Communication,” 2019, via email on 7th March 2019.
- [329] M. Stevens, “Modelling of the Tritium β -Decay Spectrum for Sterile Neutrino Search with KATRIN and Analysis of the First Tritium Data,” Master’s thesis, Technical University Munich, 2018.
- [330] A. Lokhov et al., “Update on the model for a keV-scale sterile neutrino search with KATRIN: SSC-sterile,” Nov. 2018, talk at 35th KATRIN Collaboration Meeting.
- [331] D. Furse et al., “Kassiopeia: a modern, extensible c++ particle tracking package,” *New Journal of Physics*, vol. 19, no. 5, p. 053012, may 2017. [Online]. Available: <https://doi.org/10.1088/1367-2630/19/5/053012>
- [332] S. Mertens, “Study of Background Processes in the Electrostatic Spectrometers of the KATRIN experiment,” *Karlsruhe Institute of Technology*, 2012, doctoral thesis.
- [333] J. Wulf, “Electrostatic Field Simulations and Low-Temperature Measurements for a Xenon-based Dual-Phase Noble Gas DarkMatter Detector,” Master’s thesis, Karlsruher Institute of Technology, 2014.
- [334] S. Stern, “A setup to investigate mitigation strategies of charging effects at ptfе surfaces for darwin,” Master’s thesis, Karlsruhe Institute of Technology, 2020.
- [335] A. Esfahani et al., “Determining the neutrino mass with cyclotron radiation emission spectroscopy-Project 8,” *J. Phys. G*, vol. 44, no. 5, p. 054004, 2017. [Online]. Available: <http://dx.doi.org/10.1088/1361-6471/aa5b4f>
- [336] D. Hilk, “Electric field simulations and electric dipole investigations at the KATRIN main spectrometer,” Ph.D. dissertation, Karlsruher Institute of Technology, 2017.
- [337] T. Ullrich et al., “Treatment of errors in efficiency calculations,” 2007.
- [338] E. Glasner et al., “Sensitive dependence on initial conditions,” *Nonlinearity*, vol. 6, no. 6, pp. 1067–1075, nov 1993. [Online]. Available: <https://doi.org/10.1088/0951-7715/6/6/014>
- [339] E. Rutherford, “The scattering of α and β particles by matter and the structure of the atom,” *The London, Edinburgh, and Dublin Philosophical Magazine and Journal of Science, Series 6*, pp. 669–688, 1911.

- [340] R. Mayol et al., “Total and transport cross sections for elastic scattering of electrons by atoms,” *Atomic Data and Nuclear Data Tables*, vol. 65, no. 1, pp. 55 – 154, 1997. [Online]. Available: <http://www.sciencedirect.com/science/article/pii/S0092640X97907348>
- [341] A. Bentabet et al., “Backscattering coefficients and mean penetration depths of 1.4 keV electron scattering in solids,” *Applied Physics A: Materials Science & Processing*, vol. 88, no. 2, pp. 353–358, Aug. 2007. [Online]. Available: <http://dx.doi.org/10.1007/s00339-007-3954-4>
- [342] L. Urban, “A model for multiple scattering in geant4,” *Monte Carlo 2005 Topical Meeting*, 01 2005.
- [343] H.-J. Hunger et al., “Measurements of electron backscattering coefficient for quantitative epma in the energy range 4–40 keV,” *physica status solidi (a)*, vol. 56, pp. K45 – K48, 11 1979. [Online]. Available: <http://dx.doi.org/10.1002/pssa.2210560157>
- [344] E. H. Darlington, “Backscattering of 10–100 keV electrons from thick targets,” *Journal of Physics D: Applied Physics*, vol. 8, no. 1, pp. 85–93, Jan 1975. [Online]. Available: <https://doi.org/10.1088/0022-3727/8/1/016>
- [345] A. O. Hanson et al., “Measurement of multiple scattering of 15.7-meV electrons,” *Phys. Rev.*, vol. 84, pp. 634–637, Nov 1951. [Online]. Available: <https://link.aps.org/doi/10.1103/PhysRev.84.634>
- [346] M. Kleesik et al., “ β -Decay Spectrum, Response Function and Statistical Model for Neutrino Mass Measurements with the KATRIN Experiment,” *Eur. Phys. J.*, vol. C79, no. 3, p. 204, 2019. [Online]. Available: <http://dx.doi.org/10.1140/epjc/s10052-019-6686-7>
- [347] L. Elton, “A semi-empirical formula for the nuclear radius,” *Nuclear Physics*, vol. 5, pp. 173 – 178, 1958. [Online]. Available: <http://www.sciencedirect.com/science/article/pii/0029558258900166>
- [348] S. M. Bilenkii et al., “,” *Sov. Phys. JETP* 37, 1960.
- [349] A. Nozik, “Status and Perspectives of Troitsk Nu-Mass experiment,” May 2018, quarks 2018 Conference in Valday, Russia.

Danksagung

Zum Schluss möchte ich mich von Herzen bedanken. Bei allen Menschen die zum Gelingen dieser Arbeit beigetragen und meine vergangenen Jahre in der KATRIN Kollaboration, aber auch jenseits der Physik, zu etwas Einzigartigem gemacht haben. Dabei gilt mein besonderer Dank

- Prof. Dr. Guido Drexlin für die vielen Jahre der Unterstützung und Förderung und insbesondere seine Vorlesungen, die in mir als Student eine Neugierde geweckt haben, die bis heute nicht gestillt ist.
- Dr. habil. Thierry Lasserre für die Übernahme des Korreferats und die vielen Gespräche, in denen er mir als Berater und Mentor zur Seite stand.
- Prof. Dr. Susanne Mertens für die vielen Jahre der Begleitung, die wertvollen Ratschläge und die unzähligen gemeinsamen Stunden der Arbeit aber auch der Freizeit.
- Dr. Alexey Lokhov für sein immer offenes Ohr und seine immense Erfahrung in fast allen Bereichen rund um KATRIN.
- Allen „Sterilen Jägern“ die in den vergangenen Jahren mitgeholfen haben das Sterile Neutrino Programm von KATRIN aufzubauen. Neben den bereits genannten zählen dazu besonders auch: Dr. David Radford, Dr. Ferenc Glück, Dr. Joachim Wolf, Dr. Stefan Groh, Dr. Marc Korzeczek, Dr. Kai Dolde, Tim Brunst, Leonard Köllenberger, Christoph Köhler, Dr. Martin Slezák, Dr. Thibaut Houdy und viele weitere.
- Dr. Stephanie Hickford, Dr. Carsten Röttle und Leonard Köllenberger für das intensive Korrekturlesen der vorliegenden Arbeit und die enge Begleitung während der Vorbereitung auf meine mündliche Prüfung. Ihnen möchte ich auch stellvertretend für alle Kolleginnen und Kollegen für die angenehme und inspirierende Arbeitsatmosphäre am Institut danken.
- Allen KATRIN Young (und manchmal auch Old) Scientists für die unzähligen Dienstreisen, Kollaborations-Meetings, Workshops und Konferenzen die jede für sich betrachtet unvergesslich waren.
- Tim Brunst und Konrad Altenmüller, stellvertretend für alle anderen Beteiligten, für die großartigen Messkampagnen am TROITSK Nu-Mass Experiment sowie Dr. Vlad Pantuev, Dr. Alexander Nozik und Dr. Nikita Titov für die großzügige Gastfreundschaft.
- Der Friedrich-Ebert-Stiftung, dem Graduierten Kolleg 1694, KSETA und KHYS für die finanzielle und ideelle Förderung und die unkomplizierte Unterstützung.
- Den Mitarbeitenden des KIT für die Hilfe rund um Arbeitsverträge, Dienstreisen und andere organisatorische Dinge. Besonders bedanken möchte ich mich bei Katharina Fischer, Marion Behecti und Dr. Markus Steidl.

- Thomas Csabo, Dr. Jan Behrens, Dr. Florian Fränkle und allen anderen Administratoren, für die hervorragende IT-Infrastruktur und die oft kurzfristigen Fehlerhebungen.
- Dr. Moritz Hackenjos, Jan Bondy, Isabel Arnst, Dr. Florian Heizmann, Phillip Gasch, Léonard Gaucher, Frédéric Husser und Prof. Dr. Panagiotis Kotetes für die Freundschaften die das Studium schon lange überdauern.
- Stellvertretend für alle meine Wegbegleiterinnen und Wegbegleiter Hannes Huber, Paul Schumacher, Dr. Jonas Beil und Hauke Löffler für die jahrzehntelangen Freundschaften und das Verständnis für die oft knappe Zeit die zum Pflegen der selben vorhanden ist.
- Vlasta Gracin und Neda Cilinger für die unvergleichliche Gastfreundschaft während meinen „Schreibcamps“ auf Lošinj, in denen fernab des Karlsruher Trubels große Teile dieser Arbeit entstanden sind.

Zum Schluss danke ich meinen Eltern Caterina und Matthias Huber, meinen Geschwistern Hannes, Lisa und Lukas und meiner gesamten Familie für den großen Rückhalt auch jenseits der akademischen Welt und ganz besonders Tonja Čuić für die Geduld und die Aufmunterung in den Phasen des Selbstzweifels.

U znak sjećanja na Nedu Cilinger, arhitekticu svjetlosti.

†10.07.2020